INFORMATION TO USERS

This manuscript has been reproduced from the microfilm master. UMI films the text directly from the original or copy submitted. Thus, some thesis and dissertation copies are in typewriter face, while others may be from any type of computer printer.

The quality of this reproduction is dependent upon the quality of the copy submitted. Broken or indistinct print, colored or poor quality illustrations and photographs, print bleedthrough, substandard margins, and improper alignment can adversely affect reproduction.

In the unlikely event that the author did not send UMI a complete manuscript and there are missing pages, these will be noted. Also, if unauthorized copyright material had to be removed, a note will indicate the deletion.

Oversize materials (e.g., maps, drawings, charts) are reproduced by sectioning the original, beginning at the upper left-hand corner and continuing from left to right in equal sections with small overlaps. Each original is also photographed in one exposure and is included in reduced form at the back of the book.

Photographs included in the original manuscript have been reproduced xerographically in this copy. Higher quality 6" x 9" black and white photographic prints are available for any photographs or illustrations appearing in this copy for an additional charge. Contact UMI directly to order.

UMI

A Bell & Howell Information Company
300 North Zeeb Road, Ann Arbor MI 48106-1346 USA
313/761-4700 800/521-0600

Response of the Upper Ocean to Wind, Wave and Buoyancy Forcing

by

Vadim Dmitri Polonichko
M. Sc. With Honors, Moscow Institute of Physics and Technology, Moscow, Russia, 1988

A Dissertation Submitted in Partial Fulfillment of the
Requirements for the Degree of

DOCTOR OF PHILOSOPHY

in the School of Earth and Ocean Sciences

We accept this dissertation as conforming to the required standard

Dr. D. M. Farmer, Co-supervisor	(School of Earth and Ocean Sciences)
Dr. C. J. R. Garrett, Co-supervisor	(School of Earth and Ocean Sciences, and Department of Physics and Astronomy)
Dr. E. C. Carmack, Department Member	(School of Earth and Ocean Sciences)
Dr. R. Lueck, Department Member	(School of Earth and Ocean Sciences)
Dr. R. Pinkel, External Examiner	(Scripps Institution of Oceanography & University of California San Diego)

Supervisors: Dr. David M. Farmer and Dr. Chris J. R. Garrett

ABSTRACT

At high winds, turbulence in the ocean surface mixed layer is dominated by organized coherent structures in the form of counterrotating helical vortices known as Langmuir cells. While the dynamics of the ocean surface layer has been studied rather extensively at lower wind speeds, the detailed physics at higher winds has remained largely inaccessible because of limited sea-going operations and difficulty conducting *in situ* measurements at high sea states.

In the present thesis new measurement techniques, based on acoustical remote sensing, are described. A freely drifting imaging sonar was employed, which allowed us to follow time-evolving features for an extended period of time. This imaging sonar extends the acoustical approach beyond fixed orientation sonars and covers a full 360° circle on the surface. The full circle capability turns out to be a key addition to the measurements: it allowed quantitative evaluation of the directional properties of Langmuir circulation surface structure. These new methods allow us to sample near-surface circulation and bubble distributions even in extreme conditions, and contribute to our understanding of small scale dynamics in the wind driven surface layer.

Using vertical velocity measurements in the convergent regions of Langmuir circulation and a model scaling, we infer the effective viscosity relevant to cell generation. Matching velocity- and temperature-inferred turbulent viscosities we estimate the depth scale over which the wind-wave forcing is of most importance. The velocity-inferred viscosity compares favorably with the mean model viscosity values evaluated at approximately two significant wave heights below the surface. Combining the effective

viscosity calculated at different depths with the observed Stokes drift and friction velocity we estimate Langmuir numbers La between 0.015 and 0.1. We observe evolving cell patterns at larger La (between 0.02 and 0.05), which indicates that higher viscosity values than previously assumed in the models may be relevant for Langmuir circulation dynamics.

Acoustical observations of the orientation of surface bubble clouds and the directional wave field during several deployments provided an opportunity for comparison of the directional properties of Langmuir circulation with a model that takes into account effects associated with misalignment of the Stokes drift and wind forcing. Model results imply that the growth rate is maximal overall when wind and waves are aligned. For a given angle between the Stokes drift and the wind (the misalignment angle) the direction of the cell axis for maximal growth lies between the Stokes drift and the wind and is mainly determined by (i) the misalignment angle and (ii) the ratio of the Stokes drift shear and mean Eulerian shear. Our ocean observations showed Langmuir cells responding to the changes in wind direction within 15 to 20 min. On two occasions, when the wind changed direction and waves lagged behind, the cells were observed to form in an intermediate direction (between wind and waves) consistent with model predictions.

Observations of the near-surface circulation and thermal structure during a storm motivate analysis in terms of the Froude number derived from the measured vertical density gradient, the turbulent diffusivity which is inferred from the measured temperature distributions, and velocity and spatial structure of the circulation. The results demonstrate inhibition of Langmuir circulation by the presence of warm surface water at the beginning of a storm and provide a test of model description of the balance between wind-driven stirring and buoyant resistance.

To better understand our measurements and the limitations of the approach, based on the acoustical backscatter, a technique for scatter location estimation is proposed. By comparing velocity magnitudes, independently measured with side-looking and upward-

looking sonars, we estimate an effective scattering depth. These results show that the backscatter measured with side-looking sonars originates not right at the surface but at some depth below.

Examiners:

Dr. D. M. Farmer, Co-supervisor	(School of Earth and Ocean Sciences)
Dr. C. J. R. Garrett, Co-supervisor &	(School of Earth and Ocean Sciences, and Department of Physics and Astronomy)
Dr. E. C. Carmack, Department Member	(School of Earth and Ocean Sciences)
Dr. R. Lueck, Department Member	(School of Earth and Ocean Sciences)
Dr. R. Pinkel, External Examiner	(Scripps Institution of Oceanography, and University of California San Diego)

TABLE OF CONTENTS

LIST OF TABLES

LIST OF FIGURES

LIST OF SYMBOLS

Physical Constants

α_T	coefficient of thermal expansion of water, 1.7×10^{-4} K^{-1}at 10°C, 35 psu, 1 atm
γ	adiabatic constant of air, 1.4
κ	von Karman's constant, 0.4
ν	kinematic viscosity of water, 1.3×10^{-6} m^2/s at 0°C
ρ_a	density of dry air, 1.25 kg/m^3 at 10°C, 1 atm
ρ_w	density of sea water, 1027 kg/m^3 at 10°C, 35 psu, 1atm
ϕ_w	surface tension between water and air, 7.3×10^{-2} N/m at 20°C
c	sound speed in water, 1490 m/s at 10°C, 35 psu, 1 atm
C_p	specific heat of water, 4×10^3 J/kg/K at 10°C, 35 psu, 1atm
g	gravitational acceleration, 9.8 m/s^2

Dimensionless Numbers

Ek	Ekman number
FL	Langmuir Froude number
Ho	Hoenikker number
La	Langmuir number
La_{tur}	turbulent Langmuir number
Pr	Prandtl number
Re	Reynolds number
Ri	Richardson number
RS	Reynolds Stokes number
Sr	shear ratio
Su	Stokes drift−friction velocity ratio

General Notation

A	wave amplitude
$A(k_1,k_2)$	2-d Fourier transform of the backscatter intensity
$\mathcal{A}$	cell aspect ratio
a	bubble radius
$a_r(f)$	bubble resonant radius
$a(t)$	instrument vertical acceleration
α	Langmuir cell orientation angle
$\alpha(U_{10},\chi)$, $\Gamma(\omega,U_{10},\chi)$	JONSWAP spectral parameters
$B(\omega)$	spreading parameter
Δb	buoyancy jump
$\beta = \frac{1}{2}\, h_s$	inverse Stokes drift e-folding depth
$C_\tau(t)$	complex covariance at time lag τ
C_D	drag coefficient for the air−sea interface
c_g	group wave speed
c_p	phase wave speed
$\overline{c}_p$	wave effective phase speed
χ	exponential mapping variable
$\mathcal{D}$	cell penetration depth
D_b	bubble cloud depth
d	instrument depth
$\delta(a,f)$	bubble damping coefficient
E_{in}	energy input from the wind
$F(\omega)$	wave height frequency spectrum
f	frequency
f_C	Coriolis frequency
$f_r(a)$	bubble resonance frequency
$\Phi(\omega,\theta)$	directional spreading function
Γ	filter frequency response
$\mathcal{G}$	time scale in CL2 dimensionalization
$H_{1/3}$	significant wave height

h	mixed layer depth
h_m	matching depth for parameterization of the turbulent transfer
h_s	Stokes drift e-folding depth
$h_p(t)$	instrument displacement
η	surface elevation
φ	phase
$I(x,y)$	two-dimensional backscatter matrix
$\mathbf{k} = (k, l, m)$	wavenumber vector
L	number of bits in the code
$\mathcal{L}$	cell spacing
L, M, A	characteristic matrices
$\Lambda(\theta,\alpha,\mathrm{Sr})$	eigenvalue for stability matrix
Λ	growth rate of Langmuir cells
λ	wavelength
M	number of code repetitions
$N(a)$	bubble concentration
$n(a,z)\,da$	bubble size distribution function
ν_e	eddy viscosity
P	hydrostatic pressure
$p(\omega,z)$	wave induced pressure
$p(\theta,\mathrm{r})$	directional intensity
$\bar{p}(\theta)$	average directional intensity
π	quality factor of a bubble
Q	quality factor of a bubble
Q	total heat flux
Θ	dimensionless temperature
θ	wave direction
R_s	range to the imaging sonar to the surface
$\mathcal{R}_1$, $\mathcal{R}_2$	Galerkin residuals
r	range
r_s	slant range
$S(f)$	integral scattering cross-section

$s(a,f)$	scattering cross-section of an individual bubble
$S(\omega,\theta)$	directional wave height frequency spectrum
$S_0 = \|\mathbf{U}_s\|/2$	half magnitude of the surface Stokes drift
σ_r^2	range uncertainty
σ_v^2	lower bound of the single ping velocity variance
σ_η^2	variance of surface elevation
T	temperature
$\mathcal{T}$	wave period
T_p	transmitted pulse length
$T_b = 1/f_s$	code bit length
t	time
τ	time lag
τ_a	wind stress
τ_s	skin friction component of the surface stress
τ_w	wave component of the surface stress
$\mathbf{U} = (U,V)$	mean current
$\mathbf{U}_s = (U_s, V_s)$	Stokes drift
U_{10}	wind speed
$\mathbf{u} = (u,v,w)$	velocity components
u_*	friction velocity
V	Doppler velocity estimate
V_{alias}	Doppler aliasing velocity
$\mathcal{V}$	volume
$W(\omega)$	velocity Fourier transform
w_b	maximum downward velocity in the convergences
w_{max}	bubble rise speed
$\Omega = (\xi,\vartheta,\zeta)$	vorticity components
ω	wave angular frequency
ω_p	wave peak angular frequency
x,y,z	Cartesian coordinates
χ	fetch
ξ	vorticity

ψ	streamfunction
$Z(t)$	complex backscatter amplitude

Mathematical Notation and Abbreviations

$\mathcal{F}$	Fourier transform operator
$\mathcal{F}^{-1}$	inverse Fourier transform operator
$H(\omega)$	transfer function in the Fourier domain
$\mathcal{R}(\theta,k)$	complete Radon transform
rms	root-mean-squared
rhs	right-hand side
lhs	left-hand side
SNR	signal-to-noise ratio
$\langle\,\rangle$	ensemble averaging operator
$*$	convolution operator
$\sim$	dimensional quantity
$'$	perturbation
$\|\,\|$	magnitude
σ^2	variance
bold typeface	denotes vectors and matrices

ACKNOWLEDGMENTS

First of all, I thank Dr. David Farmer for inviting me to join the Acoustics Oceanography Research Group at the Institute of Ocean Sciences (IOS), Sidney, British Columbia and giving me the opportunity to work on this challenging research project. I thank both Drs. Chris Garrett and David Farmer for their encouragement and enthusiasm, insight and guidance in teaching me how to approach solving physics problems. I thank them for generously sharing their time and ideas, for their stimulating discussions and patience during the course of this work which helped greatly to fulfill this project. Both Drs. David Farmer and Chris Garrett provided financial support which is highly appreciated.

I am very grateful for the help offered by my committee members: Dr. Rolf Lueck for his guidance on signal analysis aspects of this work and Dr. Eddy Carmack for motivating discussions on oceanographic issues.

I thank Dr. Johannes Gemmrich, with whom I have shared the office for 5 years, for stimulating discussions on scientific and other matters. Dr. J. Gemmrich also provided valuable input to the work on thermal inhibition: depth-adjusted heat flux data, cooling rate calculations and temperature data, which is gratefully acknowledged.

Thanks are due to Dr. Ming Li, who helped with the formulation of the misalignment model. I am also indebted to Dr. Anand Gnanadesikan and Dr. Pierre Mourad for their help in clarifying the original version of the manuscript on wind-wave misalignment.

I am indebted to Grace Kamitakahara-King and Willi Weichselbaumer for assistance in solving numerous computing problems. Thanks are due to Alan Adrian, Ron Teichrob, and Kim Wallace for designing, building and constantly upgrading the instrumentation and to the crew of *R/V Wecoma* for making data collection under severe conditions

possible. Drs. Rex Andrew and Rich Pawlowicz are thanked for the help with signal analysis problems. Thanks go to all my fellow students and colleagues at the Institute of Ocean Sciences; it has been a pleasure working with you.

I also thank Dr. Jim Edson for the meteorological data for the Marine Boundary Layer and Dr. Mark Trevorrow for helping with the acquisition and processing software design, instrument support and processing of the directional wave field data for the Wecoma I experiment. Geoffrey Dairiki is thanked for meteorological data for the Wecoma I experiment. The editorial assistance of Rosalie Rutka is greatly appreciated. Finally, I thank Maya Iskandar for her support and patience.

Oh how many wonderful discoveries
Spirit of enlightenment is preparing for us
And experience, son of difficult mistakes
And genius, friend of paradoxes ...

A. Pushkin, 1829

О, сколько нам открытий чудных
Готовит просвещенья дух,
И опыт, сын ошибок трудных,
И гений, парадоксов друг ...

А.С. Пушкин, 1829 г.

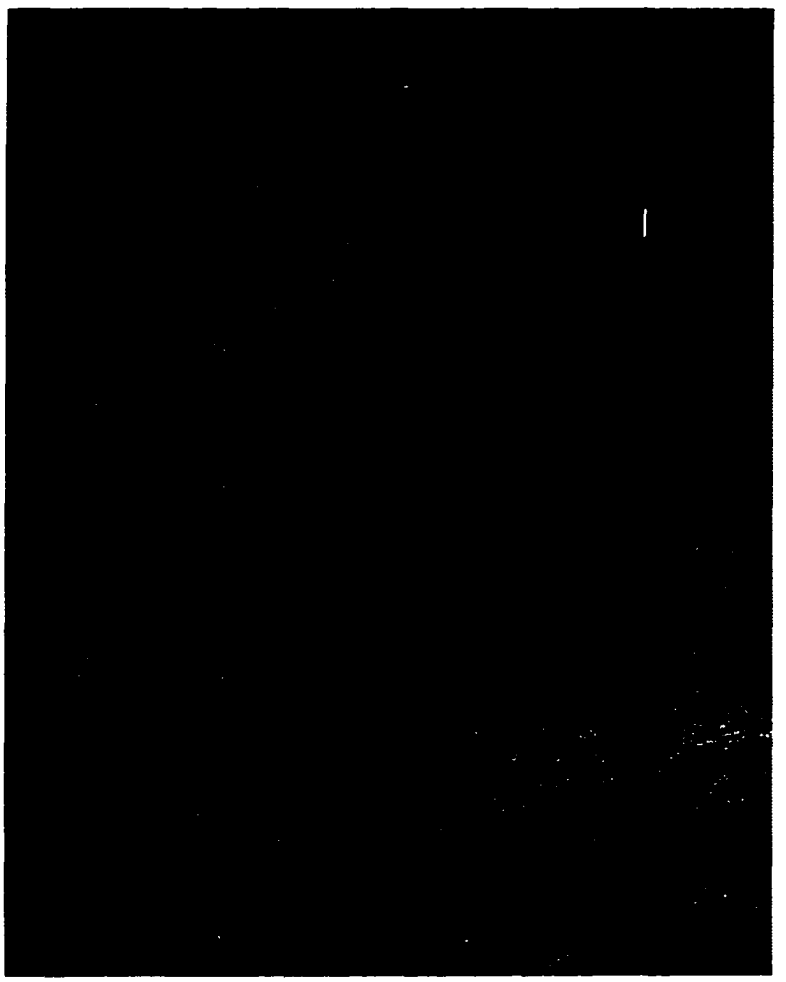

Mikhail Lomonosov (1711–1765) can be considered a founder of Russian Science. Scientist and a poet, who made substantial contributions to the natural sciences. At the age of 25 he went to Europe and for five years he had surveyed the main achievements of Western philosophy and science. Upon his return he reorganized the St. Petersburg Imperial Academy of Sciences, established in Moscow the university that today bears his name and created the first colored glass mosaics in Russia. He was a member of the Royal Swedish Academy of Sciences and of that of Bologna. His theories concerning heat and the constitution of matter were analyzed with interest in European scientific journals.

To my Mother

1. INTRODUCTION

1.1 Motivation

At high winds the surface layer of the ocean is one of the most active and violent environments on the surface of the earth (Figure 1.1). The wind work rate on the ocean depends approximately quadratically on wind speed so that the influence of a single severe storm can exceed the effects of extended periods of calmer weather.

The surface of the ocean and the layer beneath serve as an interface in mediating interaction between the atmosphere and the rest of the ocean. The near-surface physical processes govern the exchanges and determine distributions of heat, momentum, gases and pollutants [*Farmer*, 1998]. Therefore, detailed knowledge of these processes is important for a wide variety of studies including climate prediction, bioproductivity and fisheries, and waste control.

On average the ocean absorbs more than 2.5 times more incoming solar radiation (short wave) than does the atmosphere. On a global scale the ocean and the atmosphere behave as a coupled thermodynamical system, where the forcing by one leads to the

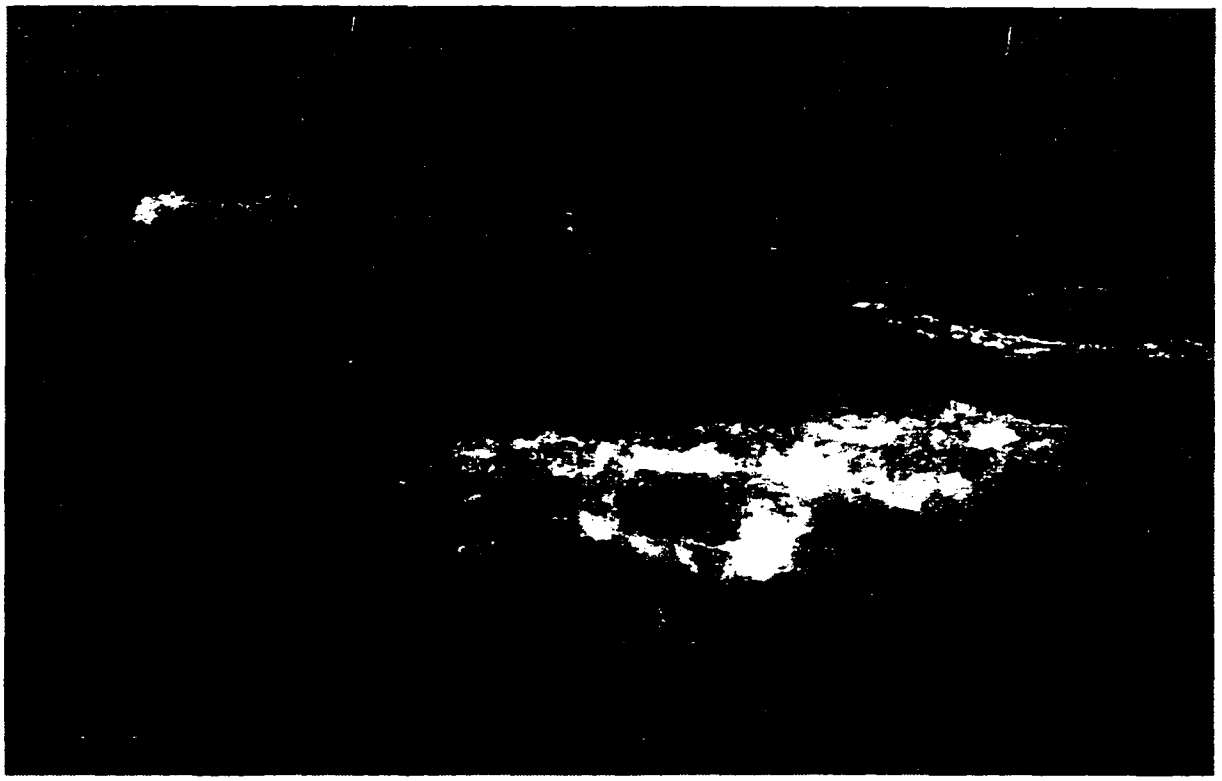

Figure 1.1: Surface of the ocean during the Marine Boundary Layer Experiment at winds in excess of 18 m/s, April 18, 1995.

response of the other. We are not concerned here with the general coupled ocean-atmosphere interaction, but rather with the specific air-sea interaction on scales of one to a few hundred metres.

The ocean at mid-latitudes usually exhibits a mixed surface layer, which has a thickness of a few to a hundred metres. The water adjacent to the sea surface is subjected to durinal heating, additional buoyancy fluxes due to precipitation and evaporation, and to turbulence generated by the wind stress and internal waves. Several small-scale processes, generated by surface fluxes of momentum and buoyancy, govern the structure of the ocean surface boundary layer. It is the presence of surface waves that distinguishes the oceanic and the atmospheric boundary layers. Wave breaking is a dominant source of turbulence near the surface and produces a greatly enhanced dissipation rate near the

surface [*Agrawal et al.*, 1992]. The interaction between the mean particle (Stokes) drift of surface waves and the wind-driven shear flow produces coherent structures, in the form of counterrotating helical vortices, known as Langmuir circulation [*Langmuir*, 1938]. Thermal convection can occur when the ocean surface is cooled. The shear stress instability generated by surface wind stress also contributes to mixing.

Turbulence in the mixed layer may be dominated by so-called "large eddies", in particular Langmuir circulation. These eddies can affect biological productivity by controlling the supply of nutrients [*Denman and Gargett*, 1995] and because the eddies advect phytoplankton in an exponentially varying light intensity with time scales comparable to those of light adaptation [*Marra*, 1978]. Numerical simulations of the global ocean using ocean global circulation models have shown that the thermohaline circulation greatly depends on the type of surface boundary forcing and on the strength of vertical diffusive mixing [*Bryan*, 1987; *Cummins et al.*, 1990]. Organic and inorganic matter is enriched in the surface films found on oceans and lakes so large eddies may cause concentration of nutrients and (or) contaminants and thus promote or inhibit the life cycle of various organisms.

Vertical downward motions produced by Langmuir circulation are coherent over several minutes and can carry near-surface bubbles, created by breaking waves, down to 7−12 m depths [*Vagle and Farmer*, 1992; *Thorpe*, 1986a, *Farmer et al.*, 1998a]. This bubble subduction provides an effective mechanism for the vertical gas transport which greatly enhances vertical gas fluxes [*Thorpe*, 1982, *Farmer et al.*, 1993].

Numerical models of climate, weather, ocean circulation, and bioproductivity generally represent fluxes at the air-water interface by bulk diffusion parameters, which are usually valid over some large time scales and areas and describe the transfer produced by smaller unresolved processes [*Thorpe*, 1995; *Garrett*, 1996]. The validity of applying an empirically determined transfer coefficient is not always certain and knowledge of physical processes is therefore important. Much work has gone into establishing

empirical variables representing air-sea drag, heat exchange and related properties. Laboratory studies have been useful in identifying the relevant physics, but scaling difficulties and other limitations emphasize the need for field measurements.

A comprehensive understanding of near-surface dynamics therefore requires measurement of small-scale processes close to the ocean surface. While the dynamics of the ocean surface layer have been studied rather extensively at lower wind speeds, the detailed physics at higher winds has remained largely inaccessible because of limited sea-going operations at high sea states and difficulty conducting *in situ* measurements during these violent conditions. This brings extra requirements to the instrumentation: the probes should be made robust enough to sustain violent forces and, at the same time, small enough not to interfere with measured phenomena. The observational task is daunting, not least because the sea surface itself can be in rapid motion (Figure 1.1)! One of the most challenging aspects is that there are several different physical processes that affect circulation, mixing, bubble distributions, etc. This requires measurement of different variables simultaneously including wind, waves, and buoyancy.

This has determined our approach: developing techniques that are comprehensive enough so that we can capture driving processes and detect the resulting circulation. In this thesis a novel instrumentation and new measurement techniques, based on acoustical remote sensing, are described. These new methods allow us to sample surface bubble layers, turbulence, thermal structure and circulation patterns, even in extreme conditions, and contribute to our understanding of small-scale structure and dynamics in the wind-driven surface layer. In contrast to *Dairiki's* [1997] work, which is concentrated more on the full depth of the mixed layer, the data and the analysis described in the thesis focus primarily on the near-surface aspects and structure of the circulation. By imaging the near-surface structure in full circles from a freely drifting instrument our measurements extend the work of *Smith* [1992] and, together with the recent results of *Smith* [1998],

provide the opportunity to observe the time evolution of the near surface in three dimensions, previously inaccessible.

1.2 Thesis Layout

The overall objective of this project is to improve our understanding of the physics of small-scale processes relevant to air-sea exchange primarily of heat, gases and momentum at high wind speeds, and in particular to build a framework which combines observations of the near-surface bubble distributions, velocity, temperature and wave fields to trace and interpret the near-surface dynamics.

The thesis is structured in the following way. Chapter 2 summarizes the relevant background; terminology is introduced and prior work is briefly reviewed. The basics of acoustical remote sensing techniques are given in Chapter 3. The Craik-Leibovich model (CL2), modified by the author, is described in Chapter 4 and used to explain generation of Langmuir circulation when wind and waves are not parallel. Chapter 5 contains the description of data collection and primary processing techniques. The analysis and interpretation of these data are given in Chapter 6, which is split into four major sections. The first deals with the vertical velocity measured in Langmuir circulation convergences. This includes a discussion of scaling, comparison with CL2 model predictions and with other measurements. The second part considers scattering depth evaluation. In the third part, the observations of Langmuir circulation surface structure, as manifested in the near-surface bubble distributions, are analyzed. Comparisons are drawn with the model described in Chapter 4. The last part demonstrates how synthesis of a broad variety of measurements, obtained in part by the author and partially by others, are brought together to describe the inhibition of Langmuir circulation by pre-existing stratification.

2. BACKGROUND

2.1 Surface Gravity Waves

When air flows above the water surface it produces pressure variations which displace near-surface water parcels from their equilibrium state. The restoring force of gravity tends to bring these parcels back but they "overshoot" their original state due to the inertia in the system, thus generating wave-like disturbances. Subsequently, the form drag exerted by the wind stress acts on the surface roughness elements "feeding" energy into the growing waves [*Miles*, 1957].

Neglecting the effects of surface tension, surface gravity waves can be categorized, depending on the water column depth compared to their wavelength, as shallow and deep water waves. Here, I shall focus mainly on deep water waves, which are of most importance in the open ocean. Waves are classified as deep water waves if the water depth is more than 28% of their wavelength [*Kundu*, 1990]. The phase speed c_p of a monochromatic wave in deep water can be expressed as [*Kinsman*, 1965]

$$c_p = \sqrt{\frac{g}{k}}, \tag{2.1}$$

giving the corresponding wave period $\mathcal{T}$

$$\mathcal{T} = \sqrt{\frac{2\pi\lambda}{g}}, \tag{2.2}$$

where g is the gravitational acceleration, λ is the wave length and $k = 2\pi/\lambda$ is the wavenumber. A dominant period of wind-generated surface waves in the ocean is usually between 9 and 11 s [*Mitsuyasu*, 1977; *Banner et al.*, 1989; *Trevorrow*, 1995], which corresponds to approximately 150-m long waves. Longer waves propagate faster (Eq. (2.1)): the phase speed of a 1.5-m wave is ~1.5 m/s while a 150-m wave moves with the speed of more than 15 m/s. A wave of amplitude A and frequency ω propagating in the x direction induces hydrostatic pressure perturbations, which decay exponentially with depth as [*Kinsman*, 1965]

$$p(\omega,z) = \rho_w g A e^{kz} \cos(\omega t + kx) \tag{2.3}$$

and is only 4% of the surface value at a depth of $\lambda/2$, therefore limiting the use of pressure gauges for wave height measurements.

2.1.1 Random Wave Field

Ocean wind waves are random in nature and wave spectra are used to characterize mean distributions of wave energy with respect to both spatial and temporal scales of variability. A directional wave height frequency spectrum $S(\omega,\theta)$ is often employed to describe the random wave field. It can be decomposed into the directional $\Phi(\omega,\theta)$ and the frequency $F(\omega)$ parts [*Phillips*, 1981]

$$S(\omega,\theta) = \Phi(\omega,\theta)\, F(\omega), \tag{2.4}$$

where ω is the frequency of the wave component propagating in a direction θ and

$$\int_{-\pi}^{\pi} \Phi(\omega,\theta)\, d\theta = 1. \tag{2.5}$$

Following development by *Kitaigorodskii* [1962], *Pierson and Moskowitz* [1964]

obtained an analytical form of the wave height frequency spectrum (hereafter referred to as the PM spectrum),

$$F(\omega) = 4.9\,\omega^{-5} \exp\left[-\frac{5}{4}\left(\frac{\omega}{\omega_p}\right)^{-4}\right], \tag{2.6}$$

where ω_p is the peak spectral frequency. The PM spectrum (2.6) serves as an approximation of the ocean wave field for fully developed seas when there is no temporal and spatial wave growth, in which case ω_p is a function of the wind speed U_{10} only,

$$\omega_p \approx g/U_{10} \tag{2.7}$$

and the corresponding phase speed is equal to U_{10}. *Hasselmann et al.* [1973], summarizing the results of the Joint North Sea Wave Project (JONSWAP), proposed a more general analytical spectrum, which includes a fetch dependence χ and the peak enhancement, described by a factor Γ,

$$F(\omega, U_{10}, \chi) = \alpha(U_{10}, \chi)\,\frac{g^2}{\omega^5}\,\Gamma(\omega, U_{10}, \chi) \exp\left[-\frac{5}{4}\left(\frac{\omega}{\omega_p(U_{10}, \chi)}\right)^{-4}\right], \tag{2.8}$$

where $\alpha(U_{10},\chi)$ is a spectral power parameter accounting for the fetch changes.

A useful empirical quantity, i.e. significant wave height $H_{1/3}$, is commonly used to describe the measured wave field. It represents an average amplitude of the ⅓ highest waves [*Kinsman*, 1965] and is related to the rms surface elevation as

$$H_{1/3} = 4\left[\frac{1}{N-1}\sum_{i}^{N}\left(\eta(t_i)\right)^2\right]^{1/2}, \tag{2.9}$$

where $\eta(t_i)$ is the surface elevation sampled at times t_i and N is the total number of samples.

Applying the ideas of *Mitsuyasu et al.* [1975] to the analysis of wave observations in Lake Ontario, *Donelan et al.* [1985] showed that the directional spreading satisfies

$$\Phi(\theta,\omega) = 0.5\,B(\omega)\,\mathrm{sech}^2[(\theta - \theta_{mean})B(\omega)],$$

$$B(\omega)=\begin{cases}2.61X^{1.3}, & 0.56<X<0.95;\\ 2.28X^{-1.3}, & 0.95\le X<1.6;\\ 1.24, \text{ otherwise}, & X=\dfrac{\omega}{\omega_p}.\end{cases} \tag{2.10}$$

The directional dependence (2.10) was later derived by *Banner* [1990] from an equilibrium range model. Spectra (2.6), (2.8), and (2.10) serve as useful references when interpreting observations and will be used later for comparisons.

2.1.2 Stokes Drift

Deep water waves cause water particles to move around in circles, with radii equal to the wave amplitude A at the surface, and decreasing with depth. For a single wave component, corresponding particle orbital velocities are

$$\begin{aligned} u(\omega,z) &= A\omega e^{kz}\cos(\omega t+kx),\\ w(\omega,z) &= A\omega e^{kz}\sin(\omega t+kx). \end{aligned} \tag{2.11}$$

This leads to a very important feature of the surface gravity waves: *the particle drift.* If one were to look at the motion of a float on the ocean surface, the observer would notice a drift in the mean direction of wave propagation with a much smaller speed, compared to that of the waves. It is a second order, or finite amplitude effect, and is caused partly by the depth dependence of the wave orbital velocity (2.11), which causes the particles at a wave crest move faster than at a trough resulting in the non-closed particle orbit and a drift $U_s t$ (Figure 2.1). *Stokes* [1847] was the first to investigate this phenomenon, which now bears his name. The mean drift velocity U_s of a single irrotational wave train in an inviscid fluid can be written as

$$U_s(z)=A^2\omega k e^{2kz}. \tag{2.12}$$

The Stokes drift decreases exponentially with depth which causes particles near the surface to move faster than at depth and produces a tilt of an originally vertical streamline

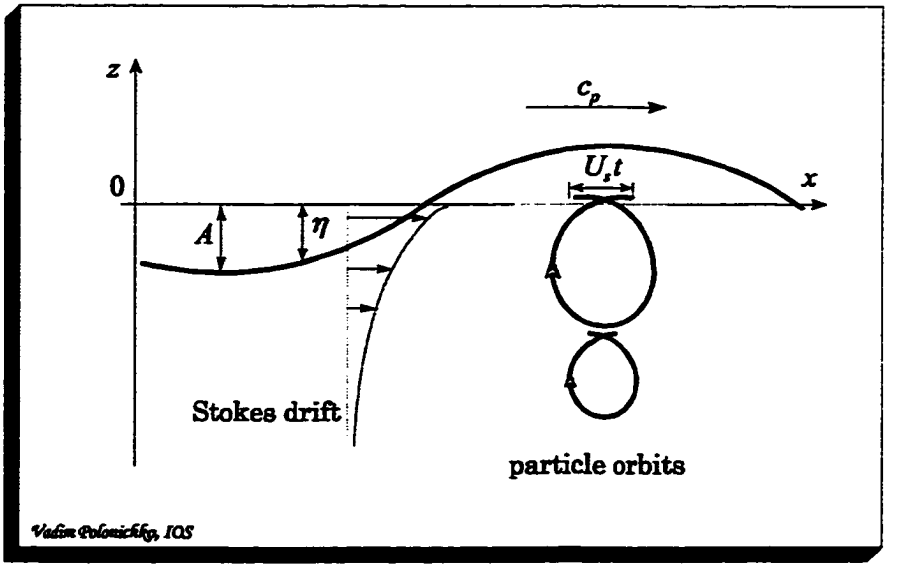

Figure 2.1: Surface gravity waves. The symbol A denotes the wave amplitude, η is the instantaneous surface elevation, c_p is the wave phase speed and U_s is the particle drift speed. The arrow marked $U_s t$ depicts a total drift over time t.

(Figure 2.1). This plays a crucial role in generation Langmuir circulation, as discussed in more detail in Section 2.3.

Kenyon [1969] and *Huang* [1971] derived general formulae for the Stokes drift due to a random gravity wave field. Assuming the deep water dispersion relation, directional Stokes drift $\mathbf{U}_s(z)$ can be calculated from a known directional wave frequency spectrum as

$$\mathbf{U}_s(z) = \frac{1}{\pi g}\iint [\cos\theta, \sin\theta]\omega^3 S(\omega,\theta)\exp\left(\frac{2\omega^2 z}{g}\right)d\theta\, d\omega. \qquad (2.13)$$

In (2.13) θ is the azimuthal direction and $S(\omega,\theta)$ can be either the measured or empirical spectrum. The effect of an angular spreading in the wave spectrum is to decrease the magnitude of the Stokes drift in the principal direction of wave propagation. For a spreading function described by (2.10) this reduction is approximately 14%.

2.1.3 Energy Input from Wind into Waves

Surface waves are primarily driven by the wind. The wind stress τ_a, supplying energy

to the surface waves, is usually related to the wind speed via parameterization:

$$\tau_a = C_D \rho_a U_{10}^2, \tag{2.14}$$

where U_{10} is the wind speed at 10 m height, ρ_a is the density of air, and C_D is the drag coefficient. The drag coefficient varies with surface roughness and stability of the air above the water and is estimated by comparison of direct measurements with bulk formulae (2.14) [*Smith*, 1981]. The momentum supplied by the wind goes almost entirely (97%) into the mean current [*Richman and Garrett*, 1977]. In fully developed seas most of the momentum transfer is done by breaking waves [*Melville*, 1994; *Thorpe*, 1993]. This creates a wave-enhanced layer within a few metres of the surface, where turbulent processes are greatly enhanced [*Drennan et al.*, 1992; *Agrawal et al.*, 1992; *Craig and Banner*, 1994; *Gemmrich*, 1997].

Stewart [1961] pointed out that while the rate of momentum input into the ocean must equal the wind stress in a steady state, the rate of the energy input equals the stress times a speed. This speed may be much greater than the mean surface drift current U if waves are generated. *Gemmrich et al.* [1994], hereafter referred to as GeMuPo, parameterized the energy acquisition by the waves using a concept of *effective* phase speed $\bar{c}_p$ and suggested that for fully developed seas the energy input into the waves E_{in} can be expressed as

$$E_{in} = \bar{c}_p \tau_w + U \tau_s, \tag{2.15}$$

where τ_w is the wave and τ_s is the skin friction components of the momentum flux respectively. For a fully rough flow ($U_{10} > 7.5$ m/s) all air-sea momentum transfer is supported by surface waves [*Kinsman*, 1965; *Donelan*, 1990]. Using recent measurements of enhanced dissipation levels near the surface, GeMuPo estimated that the effective wavelength of the energy-acquiring waves is between 0.2 and 0.4 m, almost independent of the wind speed. Accounting for the energy input underestimation due to neglect of buoyancy flux, divergence of the surface and internal wave energy fluxes and

the local change of wave energy, GeMuPo suggested that the maximum energy input occurs toward the high frequency end of the wave spectrum over a range from the capillary-gravity transition (17 mm) up to a length of 0.5 to 1 m, (approximately 1 to 5 Hz in frequency). This differs by up to two orders of magnitude from the length of dominant waves (about 60 m for unlimited fetch and 10 m/s wind speed). Comparisons with the estimates for the dissipation subrange [*Kitaigorodskii*, 1983; *Kitaigorodskii and Lumley*, 1983] indicate that in fully developed seas the energy input occurs at a slightly smaller scale than wave dissipation.

The findings of GeMuPo are important for the Stokes drift generation, especially in growing seas and seas responding to shifting winds. Although the magnitude of the Stokes drift decreases with frequency (Eqs. (2.6) and (2.12)), waves with frequencies above $3.5 \times \omega_p$ can contribute as much as 24% to the surface value of the total drift for fully developed seas. Considering that the energy input occurs at short waves, smaller waves can dominate the Stokes drift generation and facilitate faster directional adjustment of the Stokes drift to the changes in the wind direction.

2.2 Previous Studies of Langmuir Circulation

When wind blows over natural bodies of water numerous streaks of flotsam often appear. They are a visible surface manifestation of underlying motions, now commonly called Langmuir circulation, and are believed to consist of pairs of parallel counter-rotating helical vortices usually oriented downwind. These surface streaks, or windrows, were first adequately investigated and described by Irving Langmuir [1938]. He reported sightings of long lines of pelagic *Sargassum* in the Atlantic that were oriented in the direction of the wind and changed direction with a change in wind direction. He studied similar features, marked by leaves and foam, on the surface of Lake George, New York,

and confirmed experimentally his earlier deductions that the windrows are caused by water motions in the form of alternate left and right helical vortices, aligned within a few degrees of the wind direction, which appear within a few minutes of the wind onset. Langmuir believed that the energy of the vortical circulation is derived from the wind. He suggested that these circulations are largely responsible for the formation of the thermocline and for sustaining the mixed layer and concluded that the wind-driven vortices are the principal mechanism of mixing.

The commonly accepted structure of Langmuir circulation is presented schematically in Figure 2.2. Narrow convergence zones are separated by much wider divergences and maximal downward flows occur underneath convergences. The velocity in the convergence zones is believed to have a jet-like structure. The notation is as follows: u, v, w denote downwind, cross-wind, and vertical velocities, respectively; $\mathcal{L}$ and $\mathcal{D}$ are cell

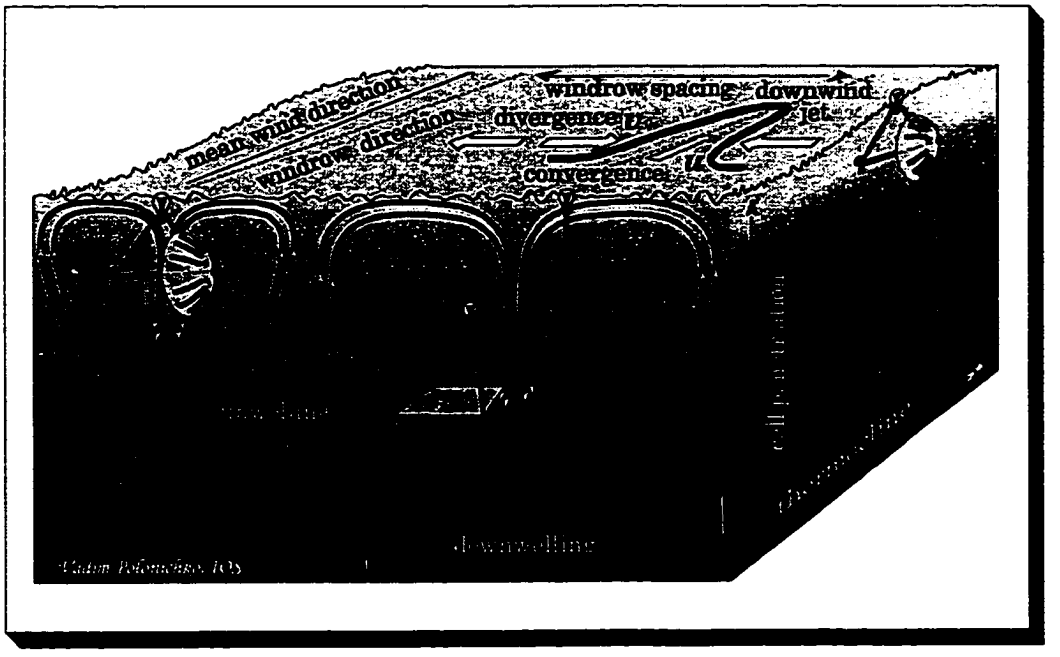

Figure 2.2: Schematic of Langmuir circulation and the pioneering studies of Irving Langmuir. Langmuir [1938] designed two types of Lagrangian floats to track motions associated with the circulation. An umbrella, balanced by a weight and attached to a light bulb, tracks horizontal motions. A float, consisting of a metal drogue screen and light bulbs, follows vertical motions.

spacing and penetration depth, respectively and α is the angle between the wind and cell direction. Cell penetration is limited by the depth of the thermocline.

2.2.1 Observations

Response to wind

Surface streaks (windrows) are usually reported to occur when wind exceeds some threshold value, most frequently placed at 3 to 4 m/s [*Pollard*, 1977, *Leibovich*, 1983]. Lake observations usually give a lower threshold of wind speed compared to the open ocean data: *Langmuir* [1938] observed the circulation when the wind speed exceeded 4 m/s. *Myer* [1969] observed windrows at even lower wind speeds, while *Thorpe and Hall* [1983] reported the appearance of organized bubble clouds on the lake surface in the lightest winds (about 3.5 m/s) and "numerous streaks" at wind speeds of 8.5 m/s. *Thorpe et al.* [1994] found that winds in excess of 3 m/s were sufficient to produce detectable bubble clouds and 8-m/s winds produced an abundance of streaks.

Observations of windrows in the ocean by *Faller and Woodcock* [1964] gave wind speeds between 4.5 and 7.5 m/s while *Faller* [1964] reported minimal wind speeds of 3 m/s. *Welander* [1963] observed no streaks at winds less than 4 m/s, and developed streaks at $U_{10} > 7$ m/s. More recent studies by *Thorpe and Hall* [1987] showed streak formation at winds of 5 m/s and multiple streaks at 11 m/s. However, *Weller and Price* [1988] reported a downwelling velocity signal, which they attributed to Langmuir circulation, at wind speeds as little as 1.5 m/s. Acoustical observations by *Zedel and Farmer* [1991] suggested a threshold wind speed in the vicinity of 7 m/s. *Smith* [1992] observed a rapid growth of Langmuir circulation in the open ocean within 15 min after the wind exceeded 8 m/s. Since visual detection of the streaks is subjective, the variability in the minimal wind speed is not surprising.

Time scales for formation of Langmuir circulation can be inferred from the time required for the windrows to re-orient themselves after a wind shift. It is usually observed that this is a rapid process with estimates ranging from 1 or 2 minutes [*Stommel*, 1951] to a tens of minutes [*Welander*, 1963; *Assaf et al.*, 1971; *Maratos*, 1971; *Ichiye et al.*, 1985].

Cell spacing

Windrow spacing has attracted much attention and it is, perhaps, the most frequently observed and well documented feature of Langmuir circulation. It is reported that the windrow spacing $\mathcal{L}$ varies from a metre or two up to hundreds of metres and a hierarchy of spacing is often observed.

Langmuir [1938] estimated windrow spacing in Lake George between 5 and 10 m with a shallow thermocline and light winds in May and June and 15 to 25 m in October and November with stronger winds. He judged that $\mathcal{L}$ is approximately proportional to the depth of the mixed layer. *Myer* [1969] reported spacing of windrows in Lake George of 1 to 15 m and the width of the windrows between 0.1 and 0.7 m. *Thorpe and Hall* [1982] gave $\mathcal{L}$ ranging from 3 to 24 m with a dominant spacing between 6 and 9 m.

Ocean observations revealed a wider range of spacing. *Langmuir* [1938] reported spacing of *Sargassum* between 100 and 200 m in the Atlantic, while *Faller and Woodcock* [1964] observed $\mathcal{L}$ between 26 and 50 m for a range of winds from 4 to 12 m/s and a statistically significant correlation between the two variables. *Assaf et al.* [1971], using aerial photographs, found the largest streak spacing to reach 280 m in the open ocean. *Ichiye et al.* [1985] observed rows of paper cards 2 to 23 m apart. *Zedel and Farmer* [1991] reported acoustical observations of cell spacing between 2 and 20 m, obtained with a side-looking sonar and *Thorpe et al.* [1994] gave a range of spacings from 9 to 22 m. Larger spacings were reported by *Smith et al.* [1987], who encountered dominant scales between 50 and 80 m with the maximum reaching 180 m. *Smith* [1992] observed

an increase of cell spacing from 15 to more than 60 m corresponding to the growth of Langmuir circulation and *Farmer and Li* [1995] estimated from their acoustical measurements values of $\mathcal{L}$ between 6 and 60 m, with dominant spacing between 15 and 20 m. *Plueddeman et al.* [1996] reported acoustical observations of near-surface bubbles and their cross-wind Doppler velocity measurements showed $\mathcal{L}$ between 20 and 200 m with a dominant spacing that increased from approximately 30 to 100 m as the circulation developed.

A few authors provided more quantitative descriptions and reported histograms of spacing [*Faller and Woodcock*, 1964; *Kenney* 1977; *Thorpe and Hall*, 1982; *Zedel and Farmer*, 1991; *Farmer and Li*, 1995]. Observations of *Zedel and Farmer* [1991] and *Plueddeman et al.* [1996] showed that Langmuir cells of different scales occur simultaneously with the dominant scale increasing with the wind. *Csanady* [1994] suggested that observed log-normal cell spacing distribution is associated with the chaotic nature of the cell origin.

Cell orientation

The windrows are usually observed to be nearly aligned with the wind direction (within 20°). Most of the lake observations show an almost perfect cell alignment with the wind [*Langmuir*, 1938; *Kenney*, 1977]. *Faller* [1964] conducted the first quantitative observations of windrow orientation. The data were obtained from small boats and aerial photographs for a range of wind speeds from 2.6 to 9 m/s. Paper cards (approximately 15,000 per experiment) were used to map the convergences and smoke plumes to map the wind direction. *Faller* [1964] found a systematic deviation of 13° (on average) for the windrows to the right of the wind direction. *Ichiye et al.* [1985] reported rows oriented between 0° and 12° to the right of the wind direction. *Farmer and Li* [1995] observed the dominant orientation of the cells at 17° to the right of the wind with a 16° spread.

Cell penetration depth and aspect ratio

Drogue observations (Figure 2.2) by *Langmuir* [1938] indicated sweeping motions at depths of 5 to 6 m below the surface streaks. More systematic inferences of the penetration depth $\mathcal{D}$ have been made by *Myer* [1969] from measurements of temperature anomalies near the surface. He found an isotherm displacement below surface streaks of up to 3.5 m under stable thermal conditions and larger displacements under unstable conditions. He estimated the depth of penetration between 2 and 7 m, although his measurements were limited to 7 m depth. Acoustical observations of the vertical structure of bubble clouds by *Thorpe* [1982] showed bubbles penetrating down to 4 m in fresh water and to 7 m in salt water. Based on similar observations, *Thorpe* [1986a] reported $\mathcal{D}$ between 4 and 14 m. *Weller and Price* [1988] gave an estimate of the cell vertical size between 25 and 35 m and *Zedel and Farmer* [1991] detected bubbles acoustically down to 10 m. *Dairiki* [1997] used neutrally buoyant Lagrangian floats [*D'Asaro and Dairiki,* 1996] to sample vertical motions within the ocean mixed layer. His data show floats reaching depths of 40 to 50 m, although there is no clear indication of the relative role of convection.

A range of aspect ratios $\mathcal{A}$ (*e.g.*, windrow spacing to the cell penetration) has also been reported. Using observed spacing and a mixed layer depth of 200 m, *Assaf et al.* [1971] inferred $\mathcal{A}$ to be approximately 1 while *Maratos* [1971] gave $\mathcal{A}$ between 1.4 and 1.7. Doppler sonar observations by *Smith et al.* [1987] from the Floating Instrument Platform (FLIP) during the Mixed Layer Dynamics Experiment (MILDEX) showed cell spacing to follow the mixed layer depth increase with a ratio close to 1.4. *Weller and Price* [1988] reported values of $\mathcal{A}$ between 1.3 and 1.7. Comparing cell spacing with mixed layer depth, *Smith* [1992] inferred the aspect ratio to be close to 1 while pointing out that there was no evidence of the mixed layer limiting the cell spacing. *Gemmrich* [1997] used three-dimensional tracks of the neutrally buoyant floats, mentioned above, in the open ocean and estimated $\mathcal{A}$ between 1 and 2 with a median value of 1.4.

Currents

Early measurements of the near-surface vertical velocities associated with Langmuir circulation revealed a generally similar pattern: more intensive downward currents below the streaks and more moderate upwelling in between. Measurements by *Sutcliffe et al.* [1963], using a float consisting of a circular plate and a calibrated shaft, showed downward currents of between 30 and 60 mm/s while *Rjanzin* [1980] and *Filatov et al.* [1981] observed descending motions of 20 to 30 mm/s and rising currents of 10 to 15 mm/s, using a similar device. *Myer* [1969] inferred downwelling of 30 mm/s for stable and 50 mm/s for unstable conditions by timing the isotherm displacement.

More recent observations using mechanical profiling current meters from FLIP by *Weller and Price* [1988] revealed very intensive downward motions exceeding 250 m/s with maxima located above mid-depth in the mixed layer. The maximal downwelling velocity showed a general increase with wind speed. They also observed downwind horizontal flows approaching 300 m/s, which are the largest observed currents due to Langmuir circulation. Simultaneously taken side-looking sonar observations indicated a typical surface convergence rate of ±30 mm/s and a cross-wind velocity variability of ±50 mm/s [*Smith et al.*, 1987]. *Smith* [1992] reported similar cross-wind current magnitudes (up to 60 mm/s), with a cross-wind velocity variance generally following the wind speed. *Zedel and Farmer* [1991] were the first to measure vertical currents beneath Langmuir convergences acoustically and obtained maximum downwelling values of 60 mm/s at 8 m depth using a conditional averaging scheme, where raw velocity estimates were sorted depending on the simultaneously measured bubble penetration depth. *Dairiki* [1997] used neutrally buoyant Lagrangian floats to sample vertical motions within the ocean mixed layer. His measurements revealed downward flows of 40 to 60 mm/s at depths between 10 and 25 m, extending at times down to 40 m; the corresponding upward flows were between 20 and 40 mm/s.

Thermal Structure

It has been observed that Langmuir circulation forms regardless of surface heating or cooling. However, surface cooling generally requires a lower threshold of wind speed. The original observations of the circulation in Lake George under various meteorological conditions by *Langmuir* [1938] hinted at the possible role of stratification. *Myer* [1969] conducted the first systematic field observations of the thermal structure of Langmuir circulation. He concluded that Langmuir circulation with surface cooling had a much greater vertical isotherm displacement compared with the distance between upwelling/downwelling than with surface heating. When the circulation was present *Myer* [1969] found that near-surface gradients were destroyed and the heat was transported downward creating a temperature difference of 100 mK beneath the streaks. He reported "As the surface vertical temperature gradients decreased the penetration became deeper and the downwelling motion appeared to be stopped only after penetrating into the water containing the vertical temperature gradient which was located at greater depth." His results also indicated an enhanced downward heat flux (by a factor of 5 to 20) during Langmuir circulation activity. *Thorpe and Hall* [1987] described measurements made with a towed spar equipped with thermistors and sonars. They found 10 to 20 mK temperature fluctuations coincident with bubble plumes although there was no systematic correlation between them. We should note that the absolute temperature deviations, cited above, depend on the air-sea heat flux as well as on the Langmuir circulation strength.

Weller and Price [1988] observed quite large near-surface temperature anomalies (~0.5 K) when Langmuir circulation was shallow and 15 mK for deeply penetrating cells. They also found that Langmuir circulation rapidly mixed away near surface stratification associated with diurnal heating, within ⅓ to ½ of the original mixed layer depth.

Recent measurements by *Gemmrich* [1997] showed near-surface temperature variability, consistent with the presence of Langmuir circulation. He found the magnitude

of temperature deviation to decrease with depth from approximately 17 mK at 0.2 m to 11 mK at 1.8 m, and the spacing of the thermal anomalies compared favorably with independent acoustical observations.

2.2.2 The Craik-Leibovich Theory

Conceptually, Langmuir circulation is described as consisting of pairs of nearly parallel counter-rotating vortices, usually oriented in the wind direction, as first suggested by *Langmuir* [1938]. Many mechanisms for Langmuir circulation have been proposed (see the review by *Leibovich* [1983]). Nowadays, the most commonly accepted theory of Langmuir circulation, termed CL2 [*Craik*, 1977; *Leibovich*, 1977, 1980] as it replaced an earlier theory [*Craik and Leibovich*, 1976], suggests that the circulation originates as a result of an instability arising from the interaction between the Stokes drift, produced by the irrotational surface waves, and wind-driven shear flow. This theory, as well as most of the previous and subsequent studies, assumes that the Stokes drift and wind are collinear and predicts the formation of Langmuir cells aligned with both wind and waves [*Leibovich*, 1983].

Scaling of the governing equations (see *Leibovich* [1977]) suggests that when wind and waves are aligned, the circulation can be characterized by one parameter, namely the Langmuir number La, which represents the ratio of viscous to inertial forces,

$$\mathrm{La} = \left(\frac{\beta \nu_e}{u_*}\right)^{3/2} \left(\frac{u_*}{S_0}\right)^{1/2} . \tag{2.16}$$

In (2.16) ν_e is the eddy viscosity, normally taken as a constant in this model, $2S_0 = U_s$ is the surface magnitude of the Stokes drift and $h_s = 1/(2\beta)$ is it's *e*-folding depth.

Subsequent model studies by *Leibovich and Paolucci* [1980, 1981] and *Li and Garrett* [1993, 1995] were able to reproduce some of the observed features of the circulation. Numerical simulations of Langmuir circulation by *Leibovich and Paolucci*

[1980] produced asymmetrical vertical velocity profiles with the maxima occurring closer to the surface at approximately ¼ to ⅓ of the cell depth. The magnitudes of the downward velocity were larger than the upwelling and the horizontal velocity had a jet-like structure. Results of *Leibovich and Paolucci* [1980] also showed that the strength of mixing by Langmuir circulation increased as the scales increased and indicated an energy cascade. *Leibovich and Paolucci* [1981] analyzed the instability of the ocean surface layer to Craik-Leibovich forcing and found that typical ocean conditions are highly unstable to the Langmuir circulation. They showed that when the Langmuir number is smaller than the critical threshold of 0.67, mechanical stirring exceeds viscous damping and generation of the circulation is possible.

Li and Garrett [1993] considered the cell merging process and its strength and structure. Their numerical tests showed asymmetrical upwelling and downwelling, with maximum downwelling velocities larger than upwelling. From boundary layer adjustment reasoning and numerical results they expressed the maximal downwelling velocity $\tilde{w}_{max}$ as

$$\tilde{w}_{max} = w_{max} u_* \left(\frac{S_0}{u_* \mathrm{La}} \right)^{1/3}, \qquad w_{max} = 0.72 , \tag{2.17}$$

where w_{max} is the dimensionless velocity. They further introduced the "pitch", the ratio of the jet strength to downwelling strength of the circulation,

$$\mathrm{Pt} = \frac{u_{con} - u_{div}}{w_{max}}, \tag{2.18}$$

where u_{con} is the surface downwind velocity component in the convergent zone, and u_{div} the corresponding value in the divergent zone. They found Pt to be proportional to $\mathrm{La}^{-1/3}$ and concluded that the CL2 model predicts a weaker surface jet than given by observations. Scaling analysis by *Li and Garrett* [1993] suggested that, at small La, friction is important in a thin, highly sheared surface layer, implying that the circulation is

generated mostly at the downwelling site and the thickness of downwelling regions should vary as $La^{1/2}$.

Li and Garrett [1995] added a buoyancy forcing term and the heat equation to the two dimensional model in order to derive the temperature field of Langmuir circulation. Studying the relative importance of the buoyancy forcing to the surface wave vortex forcing in driving the circulation they concluded that the wind-wave forcing usually dominates convection for wind speeds higher than 5 to 6 m/s and moderate (~200 W/m^2) heat flux indicating, however, that stratification induced by strong surface heating may suppress the CL2 instability. *Li and Garrett* [1995] expressed the ratio between hydrostatic forcing due to buoyancy and wave forcing in terms of the Hoenikker number

$$\mathrm{Ho} = \frac{B_0}{U_s h_s u_*^2}, \tag{2.19}$$

where B_0 is the surface buoyancy flux. For small La thermal forcing balances wave forcing when $\mathrm{Ho} \approx 3$. For $\mathrm{Ho} < 3$ the temperature field is dynamically inactive so that the heat can be regarded as a passive tracer.

Gnanadesikan and Weller [1995] investigated the instability of the Ekman spiral in the presence of surface waves and predicted the formation of Langmuir cells at 10° to 30° to the right of the wind direction depending on the scaled Coriolis parameter $\mathrm{Fc} = f_C/(A^2k^2\omega)$ and the Langmuir number. They concluded that, when La/Fc is large, the Eulerian shear is essentially parallel with the wind and waves and the cell axis is oriented along wind. As La/Fc decreases the cell orientation is expected to move off to the right of the wind. *Gnanadesikan and Weller* [1995] also addressed the effect of the misalignment between wind and waves on the generation of the Craik-Leibovich instability, which I will describe in detail in Chapter 4.

Recently *Li et al.* [1995], *Gnanadesikan* [1996], *Li and Garrett* [1997] considered the interaction of Langmuir circulation with pre-existing stratification and its effect on mixed layer deepening. *Li et al.* [1995] examined the response of the mixed layer to shear

instability and Langmuir circulation-driven stirring in the presence of a buoyancy flux. Analyzing surface mixed layer deepening by both mechanisms, *Li et al.* [1995] showed that for developed seas Langmuir circulation is more important if the velocity difference across the base of the mixed layer is no greater than 1% of the wind speed. They concluded that the presence of stratification can inhibit the circulation, resulting in a shallower mixed layer. Conversely, the presence of Langmuir circulation may delay restratification, limiting development of seasonal thermocline. *Li et al.* [1995] proposed a criterion, expressed in terms of a Froude-Langmuir number FL, which describes the balance between mixing by Langmuir circulation (kinetic energy) and inhibition by buoyancy (potential energy) as

$$\mathrm{FL} = \mathrm{RS}\frac{u_*^2}{h\Delta b} \tag{2.20}$$

where Δb is the buoyancy difference over depth h, and RS is the wave Reynolds-like number defined as

$$\mathrm{RS} = 0.72\frac{U_s h_s}{\nu_e}. \tag{2.21}$$

Deepening is expected when FL exceeds 1. *Li and Garrett* [1997] incorporated Langmuir circulation into the mixed layer model and estimated the deepening rate for cells of different geometry and concluded that deepening is determined by stratification rather than by being constrained by lateral boundaries of the box, used for modeling.

Gnanadesikan [1996] conducted numerical studies of mixing by vertically variable forcing. Comparing cell penetration depth with the rate of energy input from the Stokes drift, *Gnanadesikan* [1996] argued that "typical Stokes drift shear responsible for driving the cells occurs at about ⅓ the cell penetration depth". He also suggested that increasing heat flux may actually increase cell strength by suppressing the background turbulence, which is more important than the increase in stratification.

2.2.3 Three-Dimensional Aspects

Applications of the CL2 model have, in general, been limited to two-dimensional studies, where variability in the downwind direction is not allowed. Perhaps because of these simplifications, theoretical studies of Langmuir circulation have not shown the range of scales in wavelength and along-wind variations that appear in the measurements. Spatial variations of the velocity and surface convergence cannot be effectively examined without considering the full three-dimensional structure of the circulation.

In several recent studies three-dimensional issues were considered. *Thorpe* [1992] analyzed the instability of the circulation pattern, represented by an array of linear vortices and found a dominant mode of instability in the parameter range in which Langmuir circulation mostly exists. By permitting three-dimensional motions he was able to reproduce the breakup of Langmuir cells, their pairing and amalgamation.

Leibovich and Tandon [1993] considered a three-dimensional linear model of Langmuir circulation in a stratified layer and found cell branching and merging. They also concluded that in an unstratified flow steady two-dimensional rolls are preferred. Expanding on their previous findings, *Tandon and Leibovich* [1995] examined secondary instabilities of Langmuir circulation in stratified fluid. They found the pitch to be closer to the observations although they pointed out that it can be highly variable and not a robust feature of the circulation strength.

Analyzing acoustical images of the near-surface bubble clouds, *Farmer and Li* [1995] found that at higher wind speeds the dominant characteristic of the surface convergences is the formation of Y-junctions in which three linear bands of bubbles are joined together, with the stem pointing downwind. *Li and Farmer* [1998] presented a dynamical interpretation of the observed three-dimensional variability of Langmuir circulation surface features as a result of Crow instability, leading to vortex reconnection and formation of vortex rings. They suggested it as a possible mechanism for producing amalgamation and termination of bubble bands observed in acoustical images.

Recent observations of the near-surface dynamics at moderate and high wind speeds point to another significant shortcoming of many existing models: an idealized assumption of constant eddy viscosity. The two-dimensional numerical modeling of Langmuir circulation shows a sensitivity to eddy viscosity as well. Recent measurements of energy dissipation in the surface layer [*Drennan et al.*, 1992; *Agrawal et al.*, 1992; *Anis and Moum*, 1992; *Osborn et al.*, 1992] indicate enhanced turbulence levels close to the surface, attributed to wave breaking. This can imply a larger near-surface diffusivity, as predicted by *Craig and Banner* [1994], who modified a conventional one-dimensional turbulence closure model to incorporate a boundary layer of enhanced turbulence due to wave-breaking matched to a law-of-the-wall layer beneath.

A further complication, not included in existing models, arises from the unsteady nature of the kinetic energy generation mechanism. If breaking waves are a primary source, this is inherently intermittent. Enhanced turbulence near the surface will also add to the modification of the eddy viscosity. *Gemmrich* [1997] observed enhanced temperature anomalies near the surface at high winds which he reconciled with the heat flux, utilizing the observed breaking frequency and enhanced turbulent diffusivity in the top 2 m. The concept of eddy viscosity assumes that there is a spectral gap in the frequency space between smaller scale "background" turbulence, which is then parameterized by a prescribed turbulent transfer coefficient and "large eddies". So far, the validity of this approximation has not been unambiguously justified and the implications are not well understood.

To address these problems and extend the use of the CL2 model, three-dimensional large eddy simulations (LES) are used [*Skyllingstad and Denbo*, 1995; *McWilliams et al.*, 1997]. LES employ different parameterizations of the sub-grid physics without assuming a spectral gap, although it is not clear how breaking waves can be incorporated directly. *Skyllingstad and Denbo* [1995] performed numerical experiments of Langmuir circulation and thermal convection using a three-dimensional LES model. Results of

their experiment showed that the vortex force dominated thermal convection and the simulated vertical velocity fields displayed linear, small-scale, coherent structures near the surface that extend downwind. These structures resemble commonly observed surface patterns in the open ocean, although they are more randomly distributed than in past conceptual models.

McWilliams et al. [1997] examined the role of Langmuir cells in the planetary boundary layer using LES. They found that, under typical wind and wave conditions, Langmuir circulation significantly alters the mean velocity and momentum flux profiles and gives greater anisotropy, and enhanced turbulent velocity variance and skewness, compared to shear turbulence. Their characteristic flow structure somewhat resembled the classical solutions of Langmuir circulation. However, it exhibited a complex structure, scale expansion, and orientation change with increasing depth. The horizontal pattern had intermittent Y-junctions near the surface. They introduced the turbulent Langmuir number $La_{tur}=\sqrt{u_*/U_s}$, suggesting that it determines the nature of the wind-driven surface layer.

Despite Langmuir circulation having been studied rather extensively, there are still deficiencies in our knowledge of it. We still do not know the time scales over which the cells evolve or the effective viscosity relevant to cell generation. The effect of the misalignment between wind and waves on the generation of the Craik-Leibovich instability needs to be addressed in more detail, especially the role of the relevant dimensionless parameters. To date there are no observations which describe the dependence of the circulation mechanism on wind and wave directions.

Is believed that stratification limits vertical penetration of the cells and it has been observed that surface cooling coincides with deeper cells and larger temperature signals. At the same time, observational evidence of the effects of stratification on Langmuir circulation dynamics remain sparse and no comparisons with model predictions are available to date, with the exception of work by *Li et al.* [1995].

Even though LES modeling has shown promising results in describing upper ocean dynamics, it is limited to low Reynolds number flows and lacks key quantitative predictions of the circulation parameters and its results are rather difficult to interpret. Hence in spite of its limitations, the two-dimensional Craik-Leibovich model provides key parameterizations and useful references for comparisons with measurements. However, it should be regarded only as a step in gaining insight into the key physics, rather than as a complete description.

2.2.4 Summary

Summarizing the knowledge of Langmuir circulation,

- Surface features exist on multiple scales. The maximal cell size is limited, presumably, by the depth of the mixed layer with an aspect ratio of cell depth to cell width between 1 and 2.

- Velocity field: more intensive downward currents below the streaks (30 to 60 mm/s) and more moderate upwelling (15 to 30 mm/s) in between. Downwind jet velocities are not well known and cross-wind convergent currents are on the order of 50 mm/s. Exceptionally high vertical (up to 250 m/s) and horizontal (300 m/s) velocities were observed by *Weller and Price* [1988].

- Thermal structure: convergences accumulate heat and associated temperature anomalies are on the order of 10 to 25 mK.

- Langmuir circulation provides an efficient mechanism for downward transport of heat and gases and may cause deepening of the mixed layer.

- Three-dimensionality: Y-junctions with streak interruption and amalgamation are dominant features at high winds.

3. MEASUREMENT TECHNIQUES

The ocean surface at high wind speeds is a very hostile and complex environment (Figure 1.1) and it is not surprising that field observations, especially of the crucial dynamic variables associated with near-surface circulation, remain sparse. Instrument deployment from ships is not always possible during high sea states. An *in situ* sensor should be built robust enough to sustain forces exerted upon it by the atmosphere and ocean without interfering with the measured phenomena.

During the past decade the Acoustical Oceanography Research Group at the Institute of Ocean Sciences has developed a measurement approach which relies primarily on the use of self-contained acoustical instruments that drift freely with the surface layer [*Farmer et al.*, 1990; *Farmer*, 1993a; *Trevorrow and Teichrob*, 1994]. This choice is dictated by the difficulty of acquiring data from a ship in heavy seas, and by the desirability of minimizing advective effects which are particularly unwanted in vertical flux studies.

Acoustical probing combines flexibility and resolution for the effective sampling of processes near the ocean surface on scales from several metres up to a few hundred and is a nondestructive remote sensing method. Sonars have proved capable of providing both images of bubble clouds [*Thorpe*, 1982b, 1986a,b; *Zedel and Farmer*, 1991; *Vagle and*

Farmer, 1992] as well as Doppler velocity measurements [*Pinkel and Smith*, 1987; *Smith et al.*, 1987; *Smith*, 1989; *Zedel and Farmer*, 1991; *Smith*, 1992]. Acoustic Doppler sonars operate at a much broader scale of ranges (up to a kilometer for a 100-kHz operating frequency) and provide velocity information at more than one point compared to conventional current meters.

If the sonar points directly upward it can detect bubble concentrations as a function of depth, and can show the way in which bubble clouds penetrate downward. The sonar oriented sideways (the side-looking sonar) measures the bubble distribution as a function of range, providing a measure of the horizontal distribution of bubbles. This has proved especially fruitful in the investigation of persistent flows, such as Langmuir circulation.

Taking velocity measurements near the surface of the ocean, in particular residual motions associated with Langmuir circulation, is not an easy task. Indeed, trying to measure a non-uniform velocity signal of 0.1 m/s on a background of wave orbital "noise", which can be as large as 2.5 m/s, from a platform which itself is moving at about 0.25 m/s, presents a challenging problem.

3.1 Self-Contained Imaging Sonar

A self-contained imaging sonar platform SeaScan III was used for data acquisition described in this thesis. This instrument was designed to acoustically measure concentrations of air microbubbles in the top 20 m of the ocean surface layer and represents a refinement of earlier versions of the same instrument [*Farmer et al.*, 1990]. The instrument's electronics controlling the performance of the upward-looking sonars were tuned to operate efficiently in the presence of intense bubble clouds, i.e., the gains on the receiving circuitry were set such as not to cause saturation when dense bubble

injections occur near the surface. Therefore, the sonars do not measure fields effectively when bubble concentrations are low.

This instrument is equipped with both vertically and horizontally oriented sonars. The six conical beam upward-looking sonars (hereafter sonars) operate at frequencies ranging from 28 to 400 kHz and four side-looking sonars (hereafter sidescans) operate at 100 kHz. A summary of the sonar parameters is given in Table 3.1. The four horizontally oriented sonars are of the "fan-beam" type (3-dB beam width is 3° in the azimuthal and 65° in the vertical plane with elevation angle 15°) which can be independently oriented by stepping motors. Our mechanical scanning approach is supplementary to the SecScan device developed by *Pinkel et al.* [1995], where the sonar beam is electronically steered in many different directions for each transmission.

The sonar platform also carries SeaBird SBE-3 temperature and salinity sensors, a ParoScientific pressure gauge, an Acoustic Communication Receiving (ACR) unit, a

Table 3.1: Sonar frequencies, beam patterns and code summary. The symbol M denotes number of code repetitions, σ_V is the velocity uncertainty and V_{alias} is the aliasing velocity. The code is discussed in Section 3.3.

Freq. [kHz]	Beam width at half power	Footprint [m] at 25 m depth	Code	M	σ_V [m/s]	V_{alias} [m/s]
88	8.8°	3.8	11101	6	0.22	6.2
118	4.6°	2.0	11101	6	0.16	4.6
198	3.4°	1.5	11101	6	0.10	2.8
397	3.0°	1.3	11101	6	0.05	1.4
103 sidescan	3° horizontal 65° vertical		1110111	4.6	0.16	3.9

Lucas Accustar dual axis clinometer, a fluxgate compass and a solid state Lucas NovaSensor accelerometer, which allows us to estimate the vertical motion of the instrument and correct the measurements. During one of the experiments a recording thermistor (Richard Branker Research, Ltd, TR-1000, hereinafter referred to as TR-1000) was attached to a rubber cord above the instrument at 6.5 and/or 3.5 m depth. Specifications for each of the sensors is given in Table 3.2. Both thermistors were calibrated by the manufacturers. To improve the accuracy of the TR-1000 calibration the sensor was re-calibrated using the facilities at the Institute of Ocean Sciences. The accuracy of this method is estimated as 3 mK and the details of the calibration method are described by *Gemmrich* [1997].

The raw backscatter sonar signal is heterodyned down to 3.675 kHz (mixed with an appropriate reference frequency and low-pass filtered to remove the sum harmonic) and digitized at four samples per cycle (14.7 kHz) using a 16-bit A/D converter to yield quadrature sampled data with a Nyquist frequency of 3.675 kHz. The data are then stored on VHS tapes, using Pulse Code Modulation, which allowed us to cope with a data rate of 88,000 integer samples per second. The platform carries eight storing units and each

Table 3.2: Summary of the environmental sensor specifications. Asterisk denotes internal averaging period of 3 s.

Sensor	Range	Accuracy	Resolution	Sampling rate
Thermistor (SBE 3)	-5 to +35°C	2 mK	1 mK	1.67 Hz
Thermistor (TR 1000)	-5 to +35°C	3 mK	1 mK	1 Hz
Accelerometer	-2g to +2g	0.01g	0.002g	1.67 Hz
Clinometer	-20° to +20°	0.2°	0.2°	1.67 Hz
Compass	0° to 360°	5°	1°	1.67 Hz *

tape can last for 8 h of continuous recording, storing approximately 5 GB of data. The endurance of the instrument is on the order of 34 h (depending on transmission schedule) of continuous operation and is limited by battery power. The instrument has an internal CPU and can be programmed to operate at a prescribed schedule. In addition, the schedule can be altered remotely by sending acoustical coded pulses to the ACR unit during the deployment [*Trevorrow and Teichrob*,1994].

The SeaScan platform is usually deployed from a surface float at about 23 to 30 m depth (Figure 3.1) on an elastic cord in order to decouple it from the orbital motions of the surface buoy. The instrument samples the surrounding media every 0.6 s. The operating sequence is as follows: first, six vertical sonars transmit a "short" 0.4-ms pulse and then listen for sound reverberation for 60 ms, thus sampling a water column of about

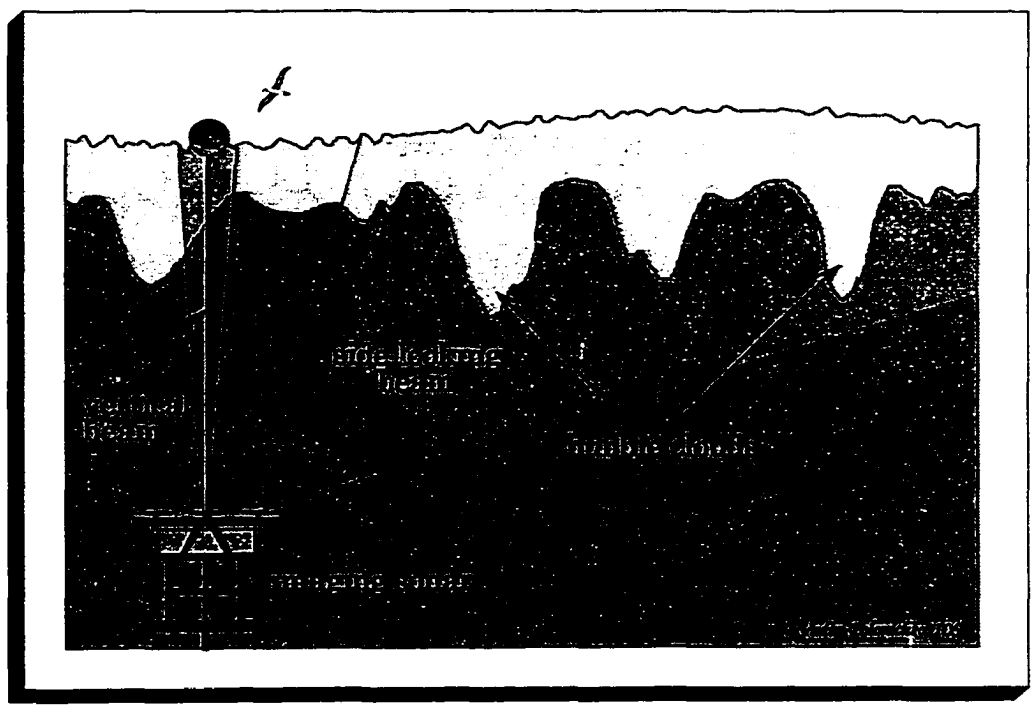

Figure 3.1: Typical deployment and transmission geometry of acoustical studies of the ocean mixed layer. A freely-drifting imaging sonar platform is suspended from a surface buoy on a rubber cord at about 30 m depth. The upward and the side-looking sonars sample vertical and horizontal distributions of the near-surface bubble clouds.

45 m depth with resolution of 0.30 m. Second, the two highest frequency sonars (200 and 400 kHz) and four sidescans transmit a "long" phase-modulated 4.08-ms (~3.2 m) pulse, and listen for 60 ms (sonars) and 390 ms (sidescans). For modulation, the Barker code is used which proved to be quite efficient for Doppler velocity measurements [*Pinkel and Smith*, 1992; *Trevorrow and Farmer*, 1992]. The codes are generated by reversing the phase of the carrier frequency by 180°; the code summary is presented in Table 3.1. The maximum useful range of sidescan measurements is limited mainly by the pulse repetition rate and the instrument depth between 270 and 285 m.

The upward-looking sonars provide measurements of vertical structure of the bubble clouds (Figure 3.1) as well as vertical velocity. As mentioned before, side-looking sonars can be independently oriented by stepping motors and two modes are used: (i) the fixed mode, when the sidescans are programmed to point in fixed geographical directions, compensating in real time for the small rotational motions of the platform, or (ii) the sweeping mode, where the four sidescans sweep in azimuth over 360° (each sidescan turns 50 times in 1.8° increments, covering a 90° sector), producing successive radar-like images of the surface backscatter every 30 s. The backscatter intensity is used to map the two-dimensional distributions of the near-surface bubble clouds, and Doppler velocity as a function of range is used to derive the directional wave field [*Pinkel and Smith*, 1987; *Smith*, 1989; *Trevorrow*, 1995].

3.2 Near-Surface Air Bubbles

Acoustical methods of remote sensing of the ocean surface rely on the presence of numerous microbubbles, which are injected into the water by breaking waves [*Thorpe*, 1982; *Crawford and Farmer*, 1987; *Farmer*, 1993b]. Ocean surface bubble clouds

include a broad bubble radius spectrum so that sonars operating from 10 kHz to several hundred kHz are able to readily detect bubble clouds. Bubbles themselves have been studied for quite some time using different approaches: *Kolovaev* [1976], *Johnson and Cooke* [1979], and *Walsh and Mulhearn* [1987] have used a photographic method; *Aleksandrov and Vaindruk* [1974], *Medwin* [1970, 1977a,b], *Thorpe* [1982, 1986b], *Akulichev et al.* [1986], *Crawford and Farmer* [1987] and *Vagle and Farmer* [1992] have relied on acoustical sampling. Although the results vary considerably, general conclusions are that the total number of bubbles decreases rapidly with depth, with an *e*-folding depth between 0.5 and 1.4 m; the penetration depth reaches 10 to 14 m; bubble concentration increases with wind speed, and the bubble size distribution has a peak around 50 μm (optical measurements) and 10 to 30 μm (acoustical measurements) (see review by *Farmer* [1993b]). The presence of bubbles results in changes of the sound velocity in the water which may affect the acoustical measurements themselves [*Navarini and Bruno*, 1982; *Farmer and Vagle*, 1989; *Bulanov and Polonichko*, 1990].

3.2.1 Sound Scattering from Bubbles

Our ability to detect bubbles acoustically in the ocean is based on the effect of acoustical resonance. Bubbles are effective scatterers of sound due mainly to large differences between air and water compressibility and the low efficiency of thermal conduction through the bubble surface during oscillations, which give bubbles a high "quality factor" at resonance. For example, a bubble of radius 0.5 mm at the sea surface resonates at a frequency of 6.5 kHz and has an acoustic cross-section of 4.2×10^{-3} m^2. That is approximately 4,500 times greater than the cross-section of a perfect reflector of the same size. When insonified by an acoustic field, bubbles reradiate (backscatter) acoustical energy back into the water. Each bubble has a natural frequency at which it resonates, depending primarily on its radius and ambient pressure. The efficiency of the

backscatter depends on the size of a bubble relative to the acoustical wavelength, reaching a maximum at resonance. The bubble resonance frequency $f_r(a)$ for a spherical adiabatic bubble of a radius a is defined as [*Minnaert*, 1933]

$$f_r(a) = \frac{1}{a}\sqrt{\frac{3\gamma P}{\rho_a}}, \tag{3.1}$$

where γ is the adiabatic constant of air, P is the hydrostatic pressure outside the bubble and ρ_a is the density of air. Radiation of sound by one isolated bubble is usually described by the bubble scattering cross-section $s(a,f)$ [*Urik*, 1983]

$$s(a,f) = \frac{4\pi^2 a^2}{\left[\left(f_r(a)/f\right)^2 - 1\right]^2 + \delta(a,f)^2}, \tag{3.2}$$

which can be interpreted as the geometrical cross-section of a perfect reflector producing a backscatter signal of the same amplitude. Here $\delta(a,f)$ is the bubble damping coefficient due to radiational, thermal and viscous losses [*Devin*, 1959]. The measure of how effectively bubbles radiate energy is the quality factor Q which is inversely proportional to the damping coefficient of a bubble and determines the width of the resonance curve [*Clay and Medwin*, 1977]. A resonant bubble cross-section is plotted in Figure 3.2 for four different insonifying frequencies. At higher frequencies resonant peaks are narrower, and the response of non-resonant bubbles increases with the bubble size.

The acoustical backscatter signal received by the sonar is proportional to the concentration of bubbles in the water. If bubbles are distributed by size, the shape of the resonance curve, together with the size distribution function, will define the total amount of received acoustical energy at a particular frequency. The integral scattering cross-section in that case is the sum of the contributions of the bubbles of different radii insonified by the sound wave of a frequency f,

$$S(f) = \int_{a_{min}}^{a_{max}} s(a,f)N(a)\,da. \tag{3.3}$$

Although formulation (3.3) is commonly used, it is only valid when bubble concentration is such that the distance between the neighboring bubbles is larger than the acoustical wavelength and multiple scattering effects are negligible [*Foldy*, 1945; *Prosperetti et al.* 1993; *Sarkar and Prosperetti*, 1993]. In practice, it translates to the bubble void fraction being smaller than 5×10^{-4} [*Polonichko*, 1992] which is normally the case, except for extremely intense bubble injections (Svein Vagle, IOS, personal communication).

If the concentration of bubbles varies with radius and the bubble resonance curve has a finite width (Figure 3.2), it is possible that acoustical backscatter received by the sonar may be dominated by the contribution from *non-resonant bubbles*. Therefore, it is necessary to estimate which part of the backscatter comes from the resonant bubbles and which part is due to the bubble "cross-talk". I use an empirical power law for the bubble size distribution [*Farmer et al.*, 1998b]

$$N(a) \propto a^n, \text{ where } n=\begin{cases} n1=2, & a<a_{peak}; \\ n2=-4, & a_{peak}\le a<100\,\mu m; \\ n3=-7, & 100\,\mu m\le a. \end{cases} \tag{3.4}$$

The slope $n2$ is normally between -3 and -5 and is taken equal to -4 [*Akulichev et al.*,

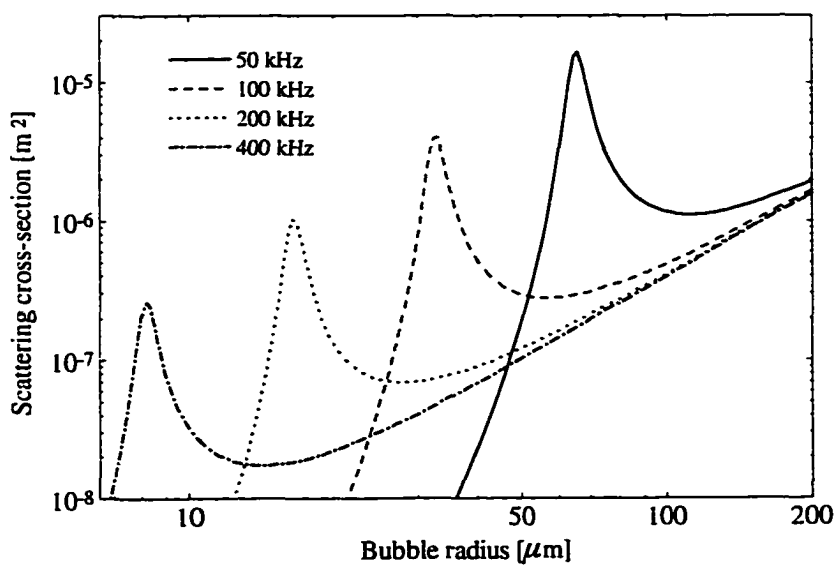

Figure 3.2: Bubble scattering cross-section at the sea surface for four sonar frequencies.

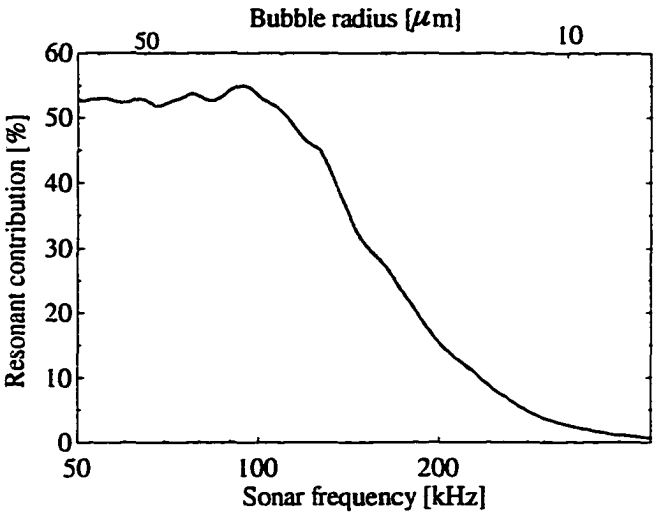

Figure 3.3: Resonant bubble backscatter for an empirical bubble size distribution.

1986; *Walsh and Mulhearn*, 1987] and the peak of the distribution is set at 30 μm [*Farmer*, 1993b; *Farmer and Vagle*, 1997]. For larger bubbles the distribution falls off more quickly with a slope of $n3=-7$ above approximately 100 μm [*Farmer et al.*, 1998b]. Using these empirical values, the ratio of the resonant contribution

$$S(f) = \int_{a_{min}}^{a_{max}} s[a_r(f), f]\, N[a_r(f)]\, da \tag{3.5}$$

to the total backscatter (3.3) is computed. The resonant contribution is maximal (~55%) at sonar frequencies between 80 and 120 kHz and rapidly drops down to 1% above 200 kHz (Figure 3.3). Therefore, at the two highest frequencies acoustical backscatter is dominated by non-resonant bubbles which are resonant at lower frequencies.

3.2.2 Bubble Rise Speed

Structure of the near-surface bubble clouds is determined by several physical processes occurring simultaneously. Bubbles, produced by breaking waves, are moved around by turbulent and organized flows, undergo diffusion and dissolution, and rise due

to the buoyancy force that depends on their radius. Effects of turbulence and wave breaking are most pronounced near the surface and occur on time scales that are smaller than that of Langmuir circulation. A rise speed of an air bubble through the water depends on its radius. At small bubble Reynolds numbers ($2aw_b/\nu < 0.33$ or $a < 80\,\mu$m) the terminal velocity an ideal spherical bubble (no slip condition) can be expressed as [*Lamb*, 1945]

$$w_b(a) = \frac{2}{9}\frac{a^2 g}{\nu}, \tag{3.6}$$

where ν is the molecular viscosity of the water. *Moore* [1963] considered enhanced drag on larger bubbles (larger Reynolds number) and showed that the rise speed of bubbles with $a > 80\,\mu$m can be approximated by

$$w_b(a) = \frac{1}{18}\frac{a^2 g}{\nu}\left[1 - \frac{2}{1+\sqrt{1+0.091a^3 g/\nu^2}}\right]^{-1}. \tag{3.7}$$

In the ocean bubbles are seldom clean due to the presence of surfactants near the surface which results in the smaller rise rates [*Thorpe*, 1982]. At small Reynolds numbers the rise speed of the dirty bubbles tends to a well-known Stokes solution for the flow past a sphere [*Kundu*, 1990].

The rise velocities of clean and dirty bubbles with radii between 6.5 and 540 μm are plotted in Figure 3.4. We see that the rise speed of the smaller bubbles ($a < 65\,\mu$m, which corresponds to an acoustical resonant frequency greater than 50 kHz) is less than 0.7 cm/s, which is more than two orders of magnitude smaller than the wave orbital velocity and an order of magnitude smaller than the maximal downwelling velocity of Langmuir circulation. Therefore, smaller bubbles with low rise speeds (0.2 cm/s for 33-μm radius bubbles which are primarily detected by a 100-kHz sonar) are essentially passive within the energetic surface layer and may be considered as quasi-passive tracers.

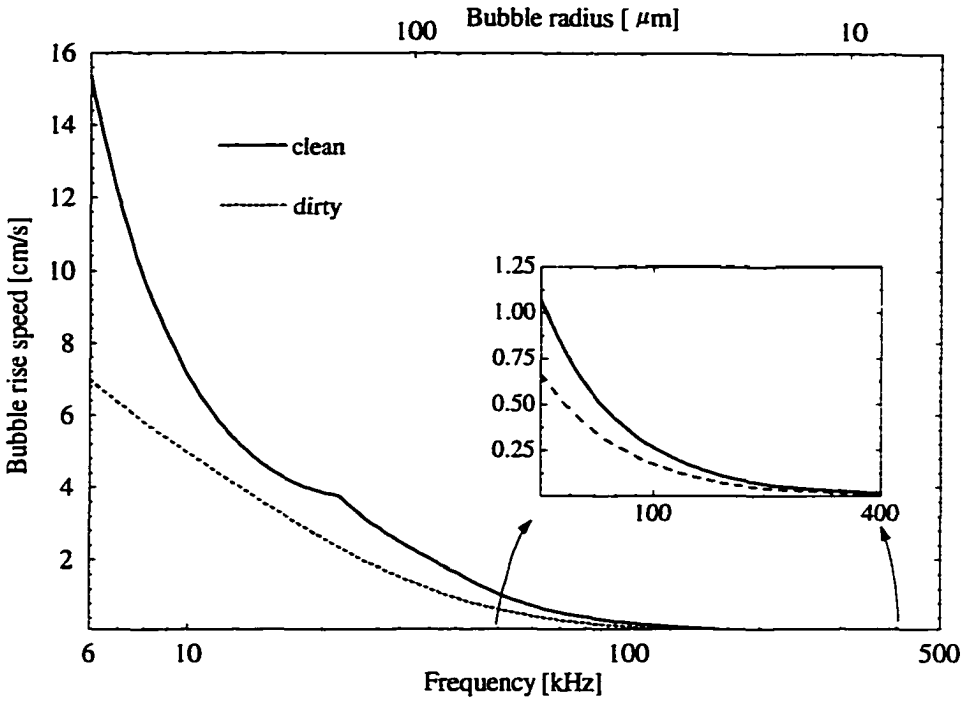

Figure 3.4: Bubble rise speed for clean and dirty bubbles. The rise speed for dirty bubbles is calculated using the formulae given in Thorpe [1982]; the rise speed for clean bubbles is calculated using (3.6) for $a < 80\ \mu m$ and (3.7) for $a > 150\ \mu m$ and is linearly interpolated between them.

When entrained at depth, the bubbles decrease in size due to hydrostatic pressure and molecular diffusion of gas through their surface and eventually dissolve. *Thorpe* [1982b] suggested a model which describes gas diffusion from the bubbles. He showed that the life time of a bubble is proportional to its radius and is of order 100 to 150 s for a range of radii between 20 and 80 μm.

3.3 Basics of Doppler Velocity Measurements

The signal recovered from the SeaScan storage units is a time series of acoustical backscatter which is referenced to range by time gating. To convert raw backscatter data

into a complex time series a quadrature exponential complex demodulation is used [*Skolnik*, 1980]. The amplitude of the signal is then proportional to the acoustical target strength and the phase changes reflect the motion of the targets. A standard time-domain complex covariance processing scheme [*Miller and Rochwarger*, 1972] is then applied to derive Doppler velocity estimates. The complex amplitude $Z(t)$ is divided into a set of bins with some overlap which we can vary depending on the required spatial resolution and the velocity variance of the data. Complex autocovariance $C_\tau(t)$ is computed for each bin at a time lag τ as

$$C_\tau(t) = \left\langle Z(t) * Z(t+\tau)' \right\rangle , \tag{3.8}$$

where the angular brackets, the symbol * and the prime denote ensemble averaging, convolution and complex conjugate operators, respectively. *Miller and Rochwarger* [1972] showed that the rate of change of phase of the autocovariance at small time lag τ is proportional to the mean velocity of the scatterers $V(t)$, which can be approximated as

$$V(t) = \frac{c}{4\pi f_0 \tau} \operatorname{atan}\left[\frac{\operatorname{Im} C_\tau(t)}{\operatorname{Re} C_\tau(t)}\right] \quad \text{at } \tau \to 0 , \tag{3.9}$$

where c is the speed of sound, f_0 is the sonar frequency a ' Re and Im denote real and imaginary parts.

The acoustical backscatter signal is composed of numerous echoes from individual targets occupying an insonified volume $\mathcal{V}$ (Figure 3.5a), which are moving with different velocities plus some ambient noise. Velocity, as defined in (3.9), is not an exact measure but an estimate with an inherent uncertainty. *Theriault* [1986] showed that the use of a finite bandwidth system leads to a velocity uncertainty of

$$\sigma_v = \frac{c}{4\pi f_0 T_p} , \tag{3.10}$$

where T_p is the pulse length. For systems consisting of a single transducer acting as transmitter and receiver, the spatial resolution of the system Δr is determined by the

length of the transmitted pulse

$$\Delta_r = 0.5cT_p . \tag{3.11}$$

The use of longer pulses reduces single transmission uncertainty (3.10). The trade-off is the loss of spatial resolution because a longer pulse insonifies a larger volume in the water column and the backscattered echo is an incoherent superposition of the individual scatterers located in this volume (Figure 3.5a).

To improve velocity accuracy without sacrificing the range resolution, a repeat-sequence coding technique is used [*Pinkel and Smith*, 1992; *Trevorrow and Farmer*, 1992]. Repeat-sequence codes are contemporary analogs of the simple "pulse-train" sequences developed in the early days of radar [*Skolnik*, 1980]. This is easy to implement and is a robust technique with respect to the scattering environment. Repeat-sequence

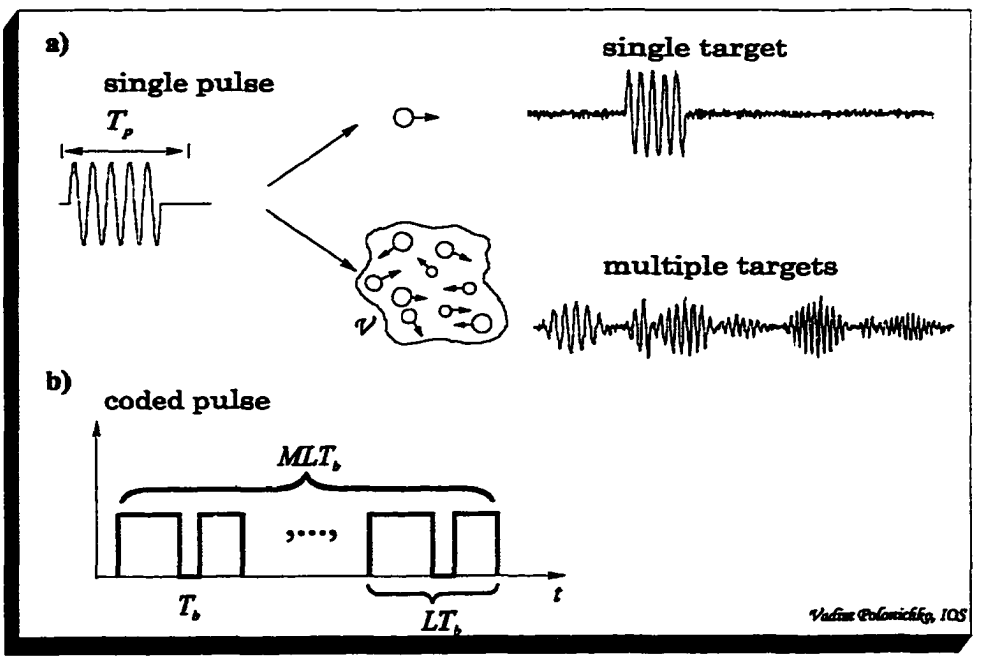

Figure 3.5: a) Effect of target motions on an acoustical backscatter signal. Multiple targets distributed in a volume $\mathcal{V}$ introduce different Doppler shifts which increase the variance of the velocity estimates, compared to a single target case. b) Broadband pulse structure: an optimal sub-code of length L (bits) is repeated M times to produce broadband pulse of length ML (bits).

codes are produced by taking a broadband "sub-code" and repeating it sequentially (Figure 3.5b). The sub-code is selected with the objective of having a minimal self-correlation except at zero lag. The use of coded pulses with subsequent time-domain complex autocovariance processing (3.8) reduces velocity uncertainty. *Pinkel and Smith* [1992] investigated the variance properties of repeat sequence codes and showed that optimal performance is reached when the time lag τ in (3.9) is equal to the sub-code length LT_b and the average is computed over $L(M-1)$ realizations, where L is the sub-code length in bits, M is the number of the sub-code repetitions and T_b is the code bit-length in seconds. The corresponding lower bound of a single transmission velocity variance is thus

$$\sigma_v^2 \geq \frac{3}{2}\left(\frac{c}{4\pi f_0}\right)^2 \frac{1}{T_b^2 L^3 M(M-1)}. \tag{3.12}$$

Another consideration for choosing the sub-code length is the velocity aliasing. When a long pulse scatters from moving targets, a cumulative phase difference over the code length can exceed 360° and the corresponding Doppler velocity is determined with an ambiguously. Aliasing velocity is smaller for higher frequencies and is defined as

$$V_{alias} = \pm c\frac{f_s}{4f_0 L}, \tag{3.13}$$

where f_s is the quadrature sampling frequency.

Taking into account these issues in combination with considerations of transmitted power, available sampling bandwidth, etc., Barker codes of length 5 for upward-looking sonars and 7 for sidescans, were implemented in the latest version of the imaging sonar platform SeaScan III. Velocity uncertainties and aliasing velocities for different sonars are listed in Table 3.1. In reality, velocity uncertainty is usually larger than the lower bound predicted by (3.12) due to oceanographic and electronic noise. *Brumley et al.* [1991] and *Pinkel and Smith* [1992] provide an estimate of the variance increase by

approximately 40 to 100%. As we see from Table 3.1 higher frequency sonars provide better velocity estimates: (0.05 m/s for 397-kHz sonar versus 0.22 m/s for 88-kHz sonar). However, higher frequency sonars have smaller aliasing velocities which may bias the measurements if the maximal ambient motions exceed V_{alias}. During our observations wave orbital velocity very seldom (< 0.5%) exceeded 2.8 m/s and the aliasing was not a problem for the 100- and 200-kHz sonars. It was corrected for the 400-kHz sonar using measured surface elevation, as described in Chapter 5.

4. MISALIGNMENT BETWEEN WIND AND WAVES: EFFECT ON LANGMUIR CIRCULATION

Most of the previous theoretical studies of Langmuir circulation assume that the Stokes drift and wind are parallel and predict the formation of Langmuir cells aligned with both wind and waves [*Leibovich*, 1983].

Analysis of the observed surface structure of Langmuir circulation (described in detail in Chapter 6, see also *Polonichko*, [1997]) under changing wind conditions indicates that the orientation of windrows is affected by the relative orientation of the surface Stokes drift and wind vectors. These observations motivate us to ask the following theoretical question: How does the relative orientation of the wind and the Stokes drift affect the orientation of Langmuir cells? *Leibovich* [1983] pointed out that such wind-wave misalignment might affect the generation and structure of Langmuir cells, but *Gnanadesikan and Weller* [1995] were the first to address this problem. They analyzed wave-current interaction within an Ekman layer of constant depth and concluded that one should expect cells to be generated in a direction, between the wind and the Stokes drift, "closer to the strongest shear." *Gnanadesikan and Weller* [1995] suggested that the

growth rate of the instabilities for a constant Eulerian mean shear decreases with the increase of the misalignment angle, that is, the angle between the wind and the Stokes drift, and when Eulerian mean shear and the Stokes drift shear are equal, they predicted maximum instability at half of the misalignment angle. They also considered various mechanisms which may play a role in the dynamics of the circulation and stressed the importance of the competition between cross-cell shear and along-cell wave forcing. *Mourad* [1998] focused on the competition between misaligned current and surface waves in providing the energy flux to Langmuir circulation. He considered different mean shear profiles and concluded that the presence of a nonlinear mean shear profile with a component across the surface waves may increase or decrease energy flux into the cells, as well as turn the orientation of Langmuir circulation away from the direction of the surface waves.

Although *Gnanadesikan and Weller* [1995] pointed out the importance of the magnitudes of Eulerian and Lagrangian shears for the direction of the maximal instability, a general study in terms of the main governing dimensionless parameters, which we suggest can be the shear ratio and the Stokes drift/friction velocity ratio, has not yet been provided. Also, description of *Gnanadesikan and Weller* [1995] is limited to a layer of constant depth. This chapter presents results of a detailed linear stability analysis in which the maximal growth rate and preferential direction of Langmuir cells are computed to elucidate their dependence on the misalignment angle, the shear ratio, and other dimensionless parameters that characterize the problem.

4.1 Governing Equations

We consider the instability generation process, in a way, similar to that described by *Leibovich* [1977], assuming that the motions in the surface layer are dominated by the

orbital motion of irrotational surface gravity waves. We assume that the surface Stokes drift arises from swell propagating in a different direction from local wind (Figure 4.1a) in infinitely deep homogeneous water.

We take the x axis parallel to the axis of an infinitesimal surface jet $u(y)$ that is parallel to neither wind nor waves (Figure 4.1a). Such a velocity field is equivalent to the existence of a pair of vertical vortices, depicted by circles in Figure 4.1a. Here, the dot and the cross represent the vortices pointing out of and into the x, y plane, respectively. The Stokes drift tilts vertical vortices ζ (Figure 4.1b) via nonlinear interaction, thus producing a horizontal component of vorticity Ω_H (Figure 4.1 c), which creates the inflow v' towards the center axis of the disturbance. As the water moves toward the x axis, it creates a convergence and must sink. The differences compared to the aligned case are that now the generated surface vorticity Ω_H is not in the x direction and the surface inflow $\mathbf{v}' = (u', v') = |\mathbf{v}'|(\sin\alpha, \cos\alpha)$, where α is the angle between the waves and the axis of the disturbance (see Figure 4.2), is not parallel to the y axis (Figure 4.1c,d). This results in a different surface flow structure: first, the "new" inflow v' in the y direction (Figure 4.1c) is now smaller by a factor of $\cos(\alpha)$, and second, an additional velocity component u' is generated in the x direction (Figure 4.1d). Note that the new flow u' is oriented in opposite directions on opposite sides of the initial disturbance $u(y)$ and will therefore tend to distort the initial shape of the flow (Figure 4.1d).

The second part of the instability is that the water parcel is accelerated by the x component of the wind as it approaches the convergence, thus reinforcing the jet $u(y)$. If the wind is not aligned with the jet, however, the cross-cell component of the wind generates a shear which distorts the cell, presumably reducing its growth rate.

The growth rate of the instability is reduced if the initial perturbation is misaligned with either waves or wind, with the reduction expected to be minimal for a cell axis somewhere between waves and wind. Determining the optimal angle, and the corresponding growth rate, requires mathematical analysis.

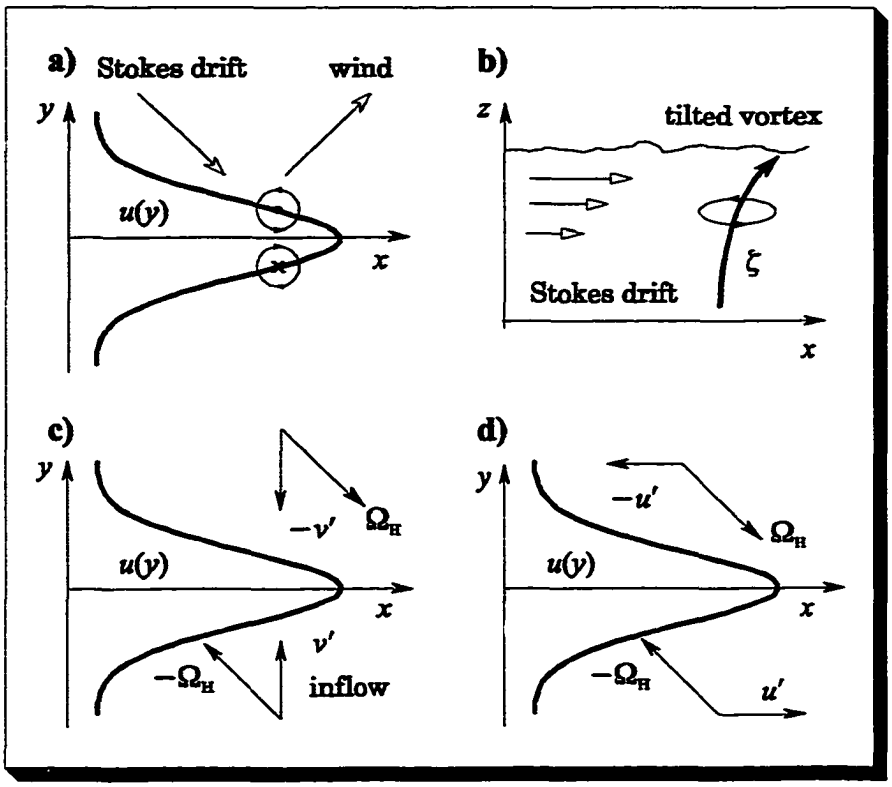

Figure 4.1: Schematic of the Craik-Leibovich mechanism of Langmuir circulation generation for non-aligned wind and Stokes drift. The velocity u(y) represents the initial disturbance in the mean flow; Ω_H and ζ are horizontal and vertical components of vorticity, respectively; u and v are the resulting advection and the inflow. a) Initial disturbance; b) vertical vortex; c) cross-cell inflow; d) along-cell advection.

The coordinate system (x, y, z) is chosen such that the x axis is aligned with the direction of the perturbation (Figure 4.2). The Stokes drift is at an angle α to the x axis, and the wind is at an angle $\theta + \alpha$, where θ is the angle between the Stokes drift and the wind. Thus α is likely to be negative for the fastest growing cells. The system of dimensional slow-time evolution equations for the x components of the velocity $\tilde{u}$ and vorticity $\tilde{\xi}$ is [*Leibovich*, 1977]

$$\frac{\partial \tilde{u}}{\partial \tilde{t}}+\frac{\partial \tilde{u}}{\partial \tilde{y}}(\tilde{v}+\tilde{V}_s)+\tilde{w}\frac{\partial \tilde{u}}{\partial \tilde{z}}=\nu_e \nabla^2 \tilde{u}\,, \tag{4.1}$$

$$\frac{\partial \tilde{\xi}}{\partial \tilde{t}}+\frac{\partial \tilde{\xi}}{\partial \tilde{y}}(\tilde{v}+\tilde{V}_s)+\tilde{w}\frac{\partial \tilde{\xi}}{\partial \tilde{z}}=\nu_e \nabla^2 \tilde{\xi}-\frac{\partial \tilde{u}}{\partial \tilde{y}}\frac{d\tilde{U}_s}{d\tilde{z}}. \tag{4.2}$$

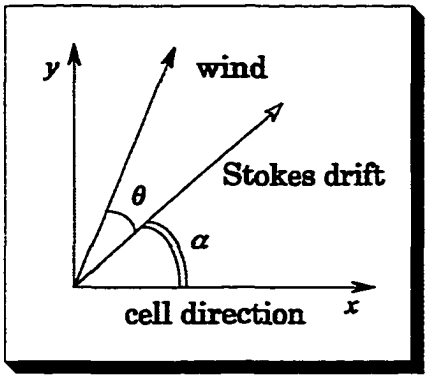

Figure 4.2: The coordinate system, where θ is the angle between the waves and the wind; α is the angle between the cell direction and the waves; the z axis is up.

where $(\tilde{U}_s,\tilde{V}_s)=|\tilde{\mathbf{U}}_s|(\cos\alpha,\sin\alpha)$ are the horizontal components of the Stokes drift, ν_e is the eddy viscosity and $\tilde{}$ denotes dimensional quantities.

We further assume that the horizontal flow $\tilde{\mathbf{u}}$ can be decomposed into a mean part and a perturbation

$$\begin{aligned}\tilde{\mathbf{u}}(\tilde{z},\tilde{y},\tilde{t})&=\tilde{\mathbf{U}}(\tilde{z},\tilde{t})+\tilde{\mathbf{u}}'(\tilde{y},\tilde{z},\tilde{t}),\\ \tilde{\mathbf{U}}(\tilde{z},\tilde{t})&=|\tilde{\mathbf{U}}(\tilde{z},\tilde{t})|\left[\cos(\theta+\alpha),\sin(\theta+\alpha)\right],\end{aligned} \tag{4.3}$$

where $|\tilde{\mathbf{U}}(\tilde{z},\tilde{t})|$ is the magnitude of the current and $\tilde{\mathbf{U}}(z,t)$ satisfies

$$\frac{\partial\tilde{\mathbf{U}}}{\partial\tilde{t}}=\nu_e\,\nabla^2\tilde{\mathbf{U}},\quad \tilde{\mathbf{U}}=(\tilde{U},\tilde{V}). \tag{4.4}$$

The boundary conditions are chosen as follows. At the surface, we require continuity of the stress $\tilde{\tau}_a$

$$\frac{\partial\tilde{\mathbf{u}}}{\partial\tilde{z}}=\tilde{\tau}_a,\ \tilde{\tau}_a=\frac{u_*^2}{\nu_e}\left[\cos(\theta+\alpha),\sin(\theta+\alpha)\right] \tag{4.5}$$

and zero vertical velocity which leads to the following boundary conditions on $\tilde{\mathbf{u}}'$, $\tilde{\mathbf{U}}$, and $\tilde{\xi}$ at $\tilde{z}=0$

$$\frac{\partial\tilde{\mathbf{U}}}{\partial\tilde{z}}=\tilde{\tau}_a,\ \frac{\partial\tilde{\mathbf{u}}'}{\partial\tilde{z}}=0,\ \ \tilde{\xi}=0. \tag{4.6}$$

where u_* is the friction velocity in the water. Thus u_*^2 is the kinematic wind stress on the water. Linearizing (4.1) and (4.2) and omitting the primes for clarity, we have

$$\frac{\partial \tilde{u}}{\partial \tilde{t}}+\frac{\partial \tilde{u}}{\partial \tilde{y}}(\tilde{V}+\tilde{V}_s)+\tilde{w}\frac{d\tilde{U}}{d\tilde{z}}=\nu_e\nabla^2\tilde{u}, \tag{4.7}$$

$$\frac{\partial \tilde{\xi}}{\partial \tilde{t}}+\frac{\partial \tilde{\xi}}{\partial \tilde{y}}(\tilde{V}+\tilde{V}_s)+\tilde{w}\frac{d^2\tilde{U}}{d\tilde{z}^2}=\nu_e\nabla^2\tilde{\xi}-\frac{\partial \tilde{u}}{\partial \tilde{y}}\frac{d\tilde{U}_s}{d\tilde{z}}. \tag{4.8}$$

Following *Leibovich* [1977], the following nondimensionalization of the perturbation quantities is applied

$$\tilde{u}=u\frac{u_*^2}{\nu_e\beta}, \tag{4.9}$$

$$(\tilde{v},\tilde{w})=(v,w)\,u_*\left(\frac{S_0}{\nu_e\beta}\right)^{1/2}, \tag{4.10}$$

$$\tilde{\xi}=\xi\,u_*\beta\left(\frac{S_0}{\nu_e\beta}\right)^{1/2}, \tag{4.11}$$

$$\tilde{t}=\frac{t}{u_*\beta}\left(\frac{\nu_e\beta}{S_0}\right)^{1/2}, \tag{4.12}$$

$$(\tilde{y},\tilde{z})=\frac{(y,z)}{\beta}. \tag{4.13}$$

Here $2S_0$ is the surface magnitude, and $\frac{1}{2}\beta^{-1}$ is the e-folding depth of the Stokes drift. Following *Li and Garrett* [1993], the Stokes drift profile corresponding to a monochromatic wave train is chosen. The current decays exponentially with depth and it is scaled with half of its surface value S_0:

$$|\tilde{\mathbf{U}}_s(\tilde{z})|=2S_0\exp(2\beta\tilde{z}),\quad |\mathbf{U}_s(z)|=2\exp(2z). \tag{4.14}$$

The mean current is scaled as

$$|\tilde{\mathbf{U}}(\tilde{z},\tilde{t})|=|\mathbf{U}(z,t)|\frac{u_*^2}{\nu_e\beta}. \tag{4.15}$$

Nondimensionalizing a set of linearized equations (4.7) and (4.8), we arrive at

$$\begin{aligned}\frac{\partial u}{\partial t}+\frac{\partial u}{\partial y}\left[\frac{2|\mathbf{U}|}{\sqrt{\mathrm{Sr}}}\sin(\theta+\alpha)+\frac{\sqrt{\mathrm{Sr}}}{2}|\mathbf{U}_s|\sin\alpha\right]\\ +\,w\frac{\partial|\mathbf{U}|}{\partial z}\cos(\theta+\alpha)=\mathrm{La}\,\nabla^2u,\end{aligned} \tag{4.16}$$

$$\frac{\partial \xi}{\partial t}+\frac{\partial \xi}{\partial y}\left[\frac{2|\mathbf{U}|}{\sqrt{\mathrm{Sr}}}\sin(\theta+\alpha)+\frac{\sqrt{\mathrm{Sr}}}{2}|\mathbf{U}_s|\sin\alpha\right] +w\frac{d^2|\mathbf{U}|}{dz^2}\sin(\theta+\alpha)=\mathrm{La}\nabla^2\xi-\frac{\partial u}{\partial y}\frac{d|\mathbf{U}_s|}{dz}\cos\alpha, \tag{4.17}$$

where Sr is the shear ratio, which is the ratio of the dimensional Stokes drift shear and mean shear magnitudes at the surface

$$\mathrm{Sr}=\left.\frac{d|\tilde{\mathbf{U}}_s|/d\tilde{z}}{d|\tilde{\mathbf{U}}|/d\tilde{z}}\right|_{\tilde{z}=0}=4\frac{\beta v_e S_0}{u_*^2}\,. \tag{4.18}$$

A streamfunction ψ is further introduced [*Leibovich,* 1977], and the problem (4.6), (4.16) and (4.17) reduces to a system with only two unknowns: $u(t, y, z)$ and $\psi(t, y, z)$.

The basic flow $\mathbf{U}(z, t)$ is generally nonsteady, which leads to the appearance of time-dependent terms in (4.16) and (4.17). To simplify the analysis, I choose a steady Couette flow with a linear depth profile as a mean current,

$$|\mathbf{U}(z)| = z\,. \tag{4.19}$$

Although this profile gives an infinitely large negative value for $z\to-\infty$, an exponentially decaying Stokes drift provides an effective forcing only within some fraction of the cell depth below the surface [*Gnanadesikan,* 1996]. This choice of the mean shear profile results in the disappearance of the forcing term containing the second derivative of $\mathbf{U}$ in (4.17), which is not true for a nonlinear profile (see *Mourad* [1998] for a discussion).

In the aligned case ($\theta = 0$) the only dimensional parameter describing the problem (4.16) and (4.17) is the Langmuir number La which represents the ratio of viscous to inertial forces (Eq. (2.16)). The velocity ratio

$$\mathrm{Su}=\frac{S_0}{u_*} \tag{4.20}$$

enters the scaling but drops out of the nondimensional equations [*Leibovich,* 1977]. This is not the case here. The ratio Su now enters the governing equations (4.16) and (4.17)

explicitly through the shear ratio Sr, which may be expressed in terms of Su and La as

$$\mathrm{Sr} = 4(\mathrm{La}\,\mathrm{Su}^2)^{2/3}. \tag{4.21}$$

The solution to the problem (4.16) and (4.17) may thus be discussed in terms of the misalignment angle θ and any two of La, Su, and Sr. We find that the shear-velocity ratio parameterization is better suited for analysis of the misalignment problem, as discussed below.

4.2 Stability Analysis

It is further assumed that the flow is periodic in the y direction and a standard normal mode expansion technique is applied

$$[u(y,z,t),\ \psi(y,z,t)] = [\bar{u}(z,t),\ \bar{\psi}(z,t)]\exp(ily). \tag{4.22}$$

In (4.22) l is the y component of the wavenumber. We then look for the most unstable mode in an infinitely deep layer. Exponential coordinate mapping $\chi = e^{z}$ so χ ranges from 0 to 1 [*Leibovich,* 1977] is further applied to simplify calculations.

To solve (4.16) and (4.17), the Galerkin expansion technique [*Canuto et al.*, 1986], which approximates the unknown functions $\bar{u}_i(\chi)$, $\bar{\psi}_i(\chi)$ as a linear combination of basis functions $\hat{u}_i(\chi)$, $\hat{\psi}_i(\chi)$, satisfying boundary conditions, is used

$$\bar{u}_N(\chi)=\sum_{i=1}^{N} a_i\,\hat{u}_i(\chi),\ \bar{\psi}_N(\chi)=\sum_{i=1}^{N} a_{N+i}\,\hat{\psi}_i(\chi). \tag{4.23}$$

Here a_i are constants which are chosen to satisfy (4.16) and (4.17). Since the Galerkin expansion is not an exact solution, it has an error which is described in terms of residual functions $\mathcal{R}_1(\chi)$, $\mathcal{R}_2(\chi)$. The residuals are required to be orthogonal to each of the basis functions [*Canuto et al.*, 1986]

$$\int_0^1 \mathcal{R}_1(\chi)\hat{u}_i(\chi)\,d\chi=0,$$
$$\int_0^1 \mathcal{R}_2(\chi)\hat{\psi}_i(\chi)\,d\chi=0,\ i=1...N. \tag{4.24}$$

This orthogonality condition leads to a system of $2N$ linear homogeneous first-order ordinary differential equations for **a**:

$$\mathbf{L}\frac{d\mathbf{a}}{dt}=\mathbf{M}\,\mathbf{a}, \tag{4.25}$$

where the elements of the matrices **L** and **M** are calculated from (4.24).

Stability analysis of the system (4.24) is based on the asymptotic stability approach developed by *Leibovich and Paolucci* [1981]. This approach consists of constructing a maximal instability (maximal growth rate) curve for the eigenvalues Λ_i of the matrix $\mathbf{a}\equiv\mathbf{L}^{-1}\mathbf{M}$, which are solutions of the characteristic equation. Since $\mathbf{A}\propto\exp(\Lambda_i t)$ [*Cesari*, 1969], a positive real part of the eigenvalue Λ_i would then result in an exponential growth of the solution, and the corresponding mode is therefore unstable. Polynomials, suggested by *Leibovich and Paolucci* [1981], which satisfy boundary conditions (4.6), are used as basis functions:

$$\hat{u}_i(\chi)=(\chi-0.5\chi^2)(1-\chi)^{2i-2},$$
$$\hat{\psi}_j(\chi)=(5\chi-3\chi^2)(1-\chi)^{2j-1}. \tag{4.26}$$

Eigenvalues Λ_i depend on the parameters La and Sr, which describe wave-current interaction, wavenumber l, cell direction α, and the misalignment angle θ giving

$$\Lambda_i=\Lambda(\mathrm{La},\mathrm{Sr},\,l,\alpha,\theta) \tag{4.27}$$

(Eqs. (4.16) and (4.17)). Langmuir number La and the shear ratio Sr both contain eddy viscosity ν_e as well as the surface value of the Stokes drift S_0 (Eqs. (2.16) and (4.18)). To separate the effects of viscosity and wave forcing on the instability growth, we need to choose the parameterization in terms of $\mathrm{Su}=S_0/u_*$, which is the function of the wind speed and surface Stokes drift only, and Sr, since all three numbers are related via (4.21). The subsequent analysis will show Sr to be the most important.

In order to calculate the maximal dimensionless growth rate and the corresponding direction (the preferential cell direction) for a particular Sr, Su, and θ, we find the pair (l,α) corresponding to the maximal $\mathrm{Re}(\Lambda)$, thus constructing $\Lambda_{max}(\mathrm{Sr},\mathrm{Su},\theta)$ and $\alpha_{max}(\mathrm{Sr},\mathrm{Su},\theta)$.

4.3 Model Results

I will now discuss the choice of the numerical values for the dimensionless parameters Sr and Su. *Li and Garrett* [1993] suggested that typical values of Su are between 4.6 and 6.9 for fully developed seas. Observations reported by *Plueddemann et al.* [1996] give estimates between 2 and 5. Directional wave measurements during the Marine Boundary Layer Experiment, April 1995 resulted in Su between 2.5 and 4.5 (Figure 6.15). Allowing for growing seas, or perhaps, swell and a weak wind, I use values of Su between 2 and 10. For open ocean eddy viscosity values [*Huang*, 1979], La falls between 0.001 and 0.05 [*Li and Garrett*, 1993]. *Farmer et al.* [1998a] reported observed maximal downwelling velocities in Langmuir circulation convergences between 4 and 9 cm/s which would imply a Langmuir number between 0.007 and 0.03, using scaling suggested by *Li and Garrett* [1993]. Therefore, La between 0.001 and 0.1 is chosen, which, in combination with the above values of Su, translates into Sr between 0.1 and 18.6. Recent dissipation observations near the ocean surface [*Agrawal et al.*, 1992] indicate the existence of enhanced dissipation in the top few metres of the ocean (compared to the law of the wall) caused by breaking waves, which implies a depth-dependent eddy viscosity. However, given the limitations of this model, the description is restricted to a fixed viscosity. Most of the subsequent calculations are done for the Stokes drift defined in (4.14), which corresponds to monochromatic waves. Effects of a realistic wave spectrum are also considered.

4.3.1 Monochromatic Waves

The maximal growth rate and its direction (preferential cell direction) depend on both Su and Sr. I first compute $\Lambda_{max}(\theta)$ and $\alpha_{max}(\theta)$ for a few velocity ratios, while keeping the shear ratio fixed (by adjusting La according to (4.21)) and then repeat these steps for a different Sr. The results for Sr = 0.1, 1.4, and 18.6 with Su = 2, 4.5, and 10 are presented in Figure 4.3. The middle values of Sr = 1.4 and Su = 4.5 are geometrical means of the corresponding limiting values.

Examining the maximal growth rate as a function of the misalignment angle θ (Figure 4.3a), we find that Λ_{max} is greatest overall when wind and waves are aligned ($\theta = 0$). As the misalignment angle increases, the maximal growth rate drops, which is due to decreasing wave forcing and increasing cross-cell advection ((4.16) and (4.17)). We also find that for a given velocity ratio (Figure 4.3a), the maximal growth rate is smaller for larger Sr which is not what one intuitively would expect, and will be explained later. When the shear ratio is small (Sr = 0.1) the growth rate is nearly independent of the other dimensionless parameter, namely, the velocity ratio Su (Figure 4.3a). For larger shear ratios (Sr = 1.4 and 18.6), larger Su (or equivalently larger wave forcing via S_0) corresponds to a larger growth rate (Figure 4.3a). As the misalignment angle approaches 180°, the maximal growth rate becomes negative, and the solutions become stable. Analyzing (4.16) and (4.17), we see that when θ = 180°, the cross-cell advection is minimal when $\alpha = 90°$. At the same time, when $\alpha = 90°$ and $\theta = 180°$ both forcing terms in (4.16) and (4.17) vanish and there are no instabilities since a linear mean shear profile does not give rise to shear instabilities [*Case*, 1960; *Gnanadesikan and Weller*, 1995;].

Analyzing the preferential cell direction for the same parameters (Figure 4.3b), we find that $\alpha_{max}(\theta)$ is in between the wind and the waves (α is negative, Figure 4.2). In Figure 4.3b, $\alpha = 0°$ corresponds to cells in the wave direction, and $\alpha = -\theta$ corresponds to cells aligned with the wind. Results in Figure 4.3b also show that the cell direction is strongly dependent on the shear ratio (families of curves with the same symbol) and is

nearly independent of the velocity ratio Su (different line styles). The preferential cell direction is closer to the wind ($|\alpha|$ increases) as Sr decreases and closer to the waves ($|\alpha|$ decreases) as Sr increases, as one might expect. While the preferential cell direction lies close to the wind for small Sr, it does not align with the waves for a reasonably large Sr.

These results are qualitatively consistent with that of *Gnanadesikan and Weller*

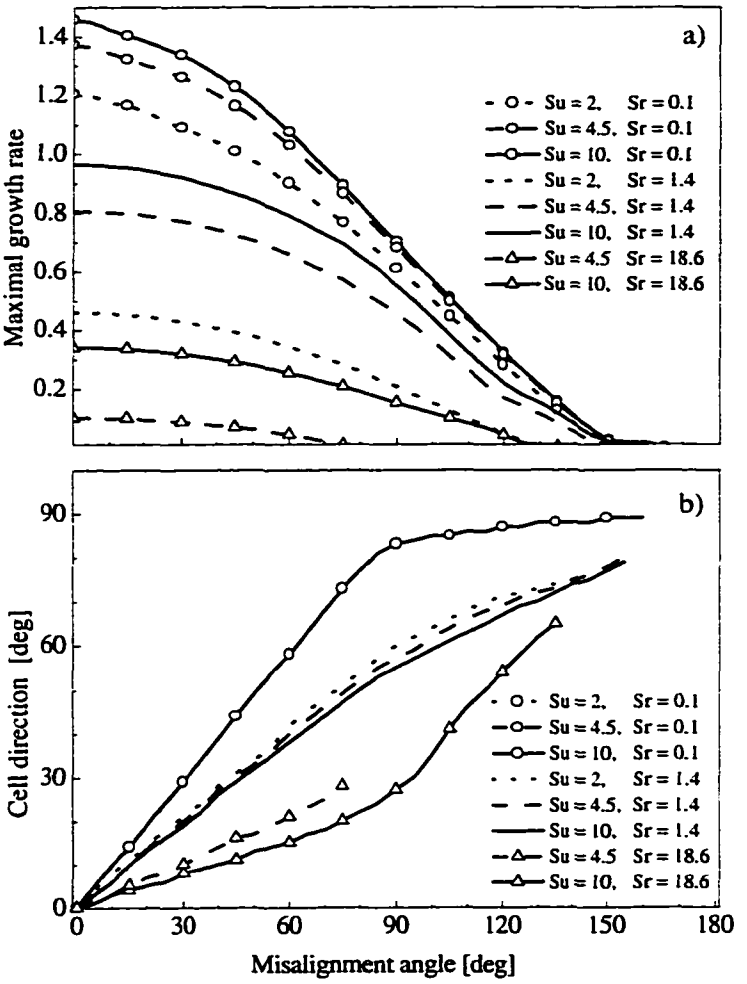

Figure 4.3: Dimensionless maximal growth rate and preferential cell direction ($-\alpha$) as a function of the misalignment angle θ for different values of the shear ratio: Sr = 0.1 (circles), Sr = 1.4 (lines without symbols), and Sr = 18.6 (triangles). Different line styles mark different values of Su. a) Maximal growth rate; b) preferential cell direction. The cell direction for Sr = 0.1 is independent of the velocity ratio (lines with the same Su overlap).

[1995] who find that as θ increases, the growth rate drops, as well as that "when the Eulerian shear and Stokes drift shear are equal ..." (that is, Sr = 1) "... the maximum instability occurs at ½ the separation angle." *Mourad* [1998] also reports that the angle of the fastest growing disturbances lies between the wind and the waves, although he parameterizes the growth rate in terms of across-wave to along-wave surface current ratio and a Rayleigh-like number.

Considering changes in the wavenumber l of the fastest growing cells, computed for the same shear ratios as in Figure 4.3 and Su = 4.5, we find (Figure 4.4) that for smaller shear ratios (Sr = 0.1 and 1.4), the wavenumber decreases (cell size increases) as the misalignment angle increases, which is consistent with the results of *Gnanadesikan and Weller* [1995]. However, the wavenumber drop rate is significantly smaller for the larger shear ratio and for Sr = 18.6, it becomes nearly independent of Sr.

To clarify the dependence of the cell size on the shear ratio, l(Sr) is computed (Figure 4.5). Results in Figure 4.5 show that when the shear ratio is small (La is small for a given Su), the fastest growing disturbances are ones with a larger wavenumber, which is consistent with the previous calculations of *Leibovich* [1980] and *Li and Garrett* [1993]. This means that the fastest growing cells are small, compared to the Stokes drift e-folding scale h_s. As the shear ratio increases, the cell penetration depth increases as well (the wavenumber decreases).

As stressed by *Gnanadesikan and Weller* [1995] the physical mechanism determining cell growth in the misaligned case is the trade-off between minimizing the cross-cell shear and maximizing wave-current interaction (wave forcing), which is not only a function of the mean shear and the Stokes drift shear but also of a size (depth) of the cells. While the along-cell component of the Stokes drift (4.17) provides the forcing for the circulation, the cross-cell projection of the mean shear causes cross-cell advection which tends to distort the circulation. This trade-off mechanism may explain why even for reasonably large Stokes drift shear, cells are not aligned with the waves.

The reason that the Stokes drift is less effective in aligning cells with it is that it decays with depth. When Sr is large, we have advection of deeper cells. Deeper cells are influenced less by the Stokes drift forcing compared to the shallower cells, while the mean shear forcing is the same in both cases, and therefore the effective shear ratio is

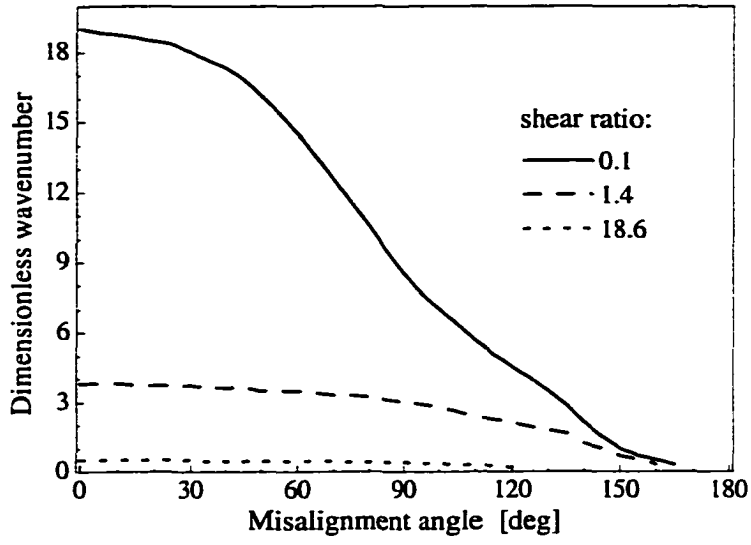

Figure 4.4: Dimensionless wavenumber of the fastest growing cells as a function of the misalignment angle for different values of the shear ratio; Su = 4.5.

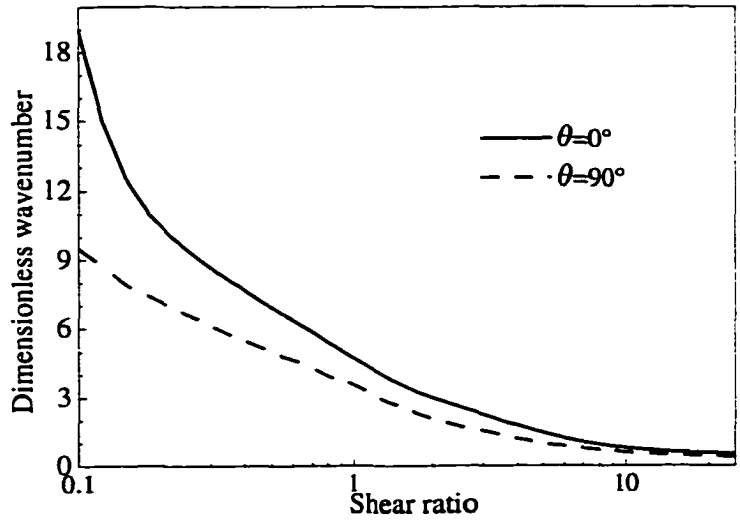

Figure 4.5: Dimensionless wavenumber of the fastest growing cells as a function of the shear ratio for different values of the misalignment angle, Su = 4.5.

reduced. Since the direction of the cells is determined from the competition between the forcing term in (4.17) $d|\mathbf{U}_s|/dz\cos(\alpha)$ and the advection term $|\mathbf{U}|\sin(\theta-\alpha)$, the cells are not necessarily aligned with the waves even when Sr is relatively large.

Exploring the dependence of the maximal growth rate on the shear ratio, we now compute $\Lambda_{max}(\theta)$ and $\alpha_{max}(\theta)$ for a few misalignment angles and Su = 4.5 (Figure 4.6). We see that Λ_{max} is smaller for larger θ (Figure 4.6a) which is consistent with the previous results. As Sr increases, the cross-cell component of the mean shear becomes larger which tends to dampen the growth of the cells and results in a decreasing growth rate (Figure 4.6a). Note that for a fixed Su, increasing shear ratio means increasing Langmuir number (Eq. (4.21)). When Sr becomes large enough so that the corresponding La exceeds the linear stability limit of 0.67 (as described by *Leibovich and Paolucci* [1981]) there is no circulation possible and the maximal growth rate is negative (Figure 4.6a).

Analyzing dependence of the cell orientation on the shear ratio for the same parameters as in Figure 4.6a we find that for smaller values of Sr, the direction of maximal growth lies close to the wind and as Sr increases, the direction of the cells gradually turns toward the direction of the waves (Figure 4.6b).

To understand the observed behavior of the growth rate, we apply dimensional arguments. The timescale $\mathcal{G}$ corresponding to the dimensionalization (4.10) is

$$\tilde{t} = t\mathcal{G}, \quad \mathcal{G} = \left(\frac{\nu_e}{S_0 \beta u_*^2}\right)^{1/2} = 4\left(\frac{d|\tilde{\mathbf{U}}_s|}{d\tilde{z}}\frac{d|\tilde{\mathbf{U}}|}{d\tilde{z}}\right)^{-1/2}, \tag{4.28}$$

where t is dimensionless and $\tilde{t}$ is dimensional time. The dimensional growth rate $\tilde{\Lambda}$ is therefore dependent on both Stokes drift shear and mean shear since

$$\tilde{\Lambda} = \Lambda/\mathcal{G}. \tag{4.29}$$

Calculations of the Stokes drift from the directional wave spectra show that the effective e-folding depth h_s does not change significantly for moderately or fully

developed seas (Figure 6.28b) and is assumed to be a constant for the present purpose. When S_0 and

u_* are fixed, increasing Sr implies increasing viscosity, which, according to (4.28) and (4.29), results in a decreasing growth rate which explains the results in Figure 4.6. When the wave forcing vanishes, the dimensional growth rate must go to zero since there is no other source of instability. As mentioned before, constant mean shear does not cause shear instabilities. Presented calculations show that for small Su (small S_0), the dimensionless maximal growth rate Λ does go to zero which means that the dimensional

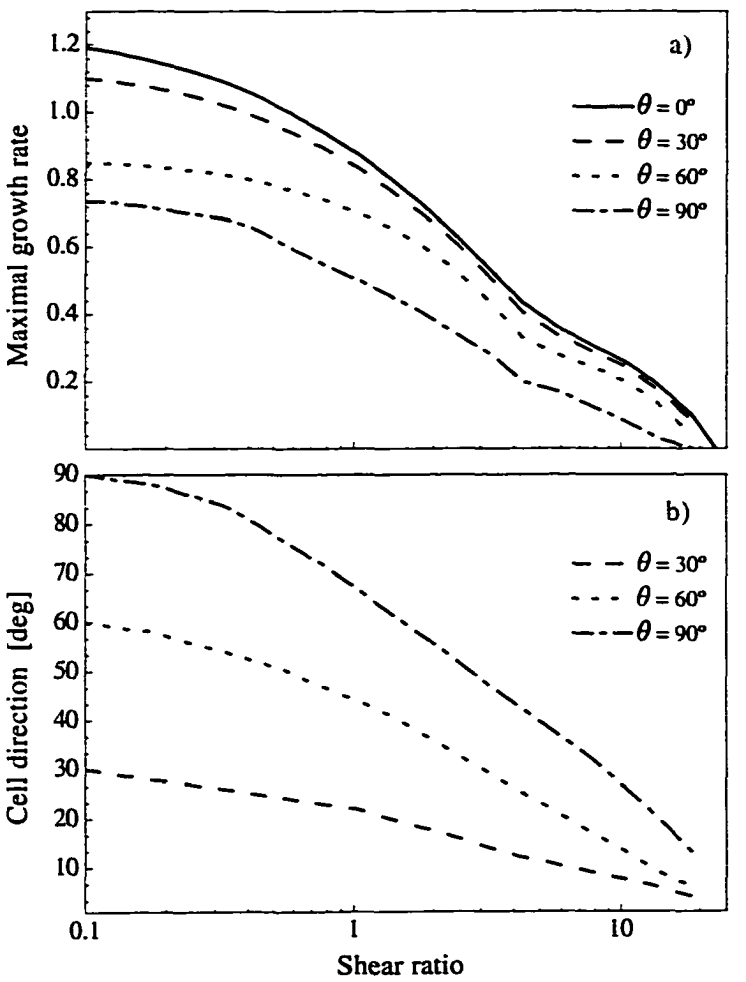

Figure 4.6: Dimensionless maximal growth rate and preferential cell direction ($-\alpha$) as a function of the shear ratio. Different lines mark different misalignment angles; Su = 4.5. (a) Maximal growth rate; (b) preferential cell direction.

growth rate $\tilde{\Lambda}$ is zero as well.

The role of the mean and the Stokes drift shears in the generation of Langmuir circulation is not similar: the Stokes drift shear tilts vertical vortex lines and generates longitudinal vorticity (Figure 4.1b), but the mean shear production of the longitudinal vorticity is canceled by the rotation of the transverse vorticity. On the other hand, the along-cell component of the wind-driven current accelerates the water parcel at it moves toward the convergence thus reinforcing the jet. Therefore, it is not surprising that the cell orientation is not symmetric with regard to the two shears.

If the mean shear and the Stokes drift shear are of the same order, the cells will tend to align in between so as to maximize the wave forcing and jet reinforcement and minimize the effects of the cross-cell shear. When the Stokes drift shear and mean shear components in the direction of the perturbation increase, the wave current forcing, as well as the growth rate (4.29), become larger. As we have seen, the maximal growth rate Λ_{max} drops faster with θ for larger values of the shear ratio (Figure 4.3a) due to increasing cross-cell advection ((4.16) and (4.17)). The cross-cell component of the mean shear tends to distort the circulation by "pushing" one cell on top of the other, thus destroying the circulation flow (Figure 4.7).

The above results suggest that the relative strength of the shears, which we describe by the shear ratio, is one of the key parameters determining the orientation and the growth rate of Langmuir cells in the misaligned case. The maximum growth rate occurs at an angle which maximizes the wave-current forcing of the perturbations, while minimizing the cross-component of the mean shear. For a constant misalignment angle θ and constant mean shear, the growth rate increases as the Stokes drift shear increases and the direction of the maximal growth rate becomes progressively more aligned with the waves. This can explain why our model shows the direction of maximal growth to lie in between the waves and the wind.

When wind and waves are not aligned, the cells drift sideways. We write an average

side drift velocity of the cells as

$$V_d = \frac{\mathrm{Im}(\Lambda)}{l}, \tag{4.30}$$

where l is the wavenumber and $\mathrm{Im}(\Lambda)$ is an imaginary part of the growth rate. Comparing this velocity with the cross-cell component of the mean current V at different depths, we find that they become equal at a depth of approximately $(0.6-0.8)\times D$ (Sr = 0.1, Su=4.5, θ=90°), where $D = l^{-1}$ is a measure of the cell depth. The magnitude of the drift increases as the misalignment angle increases, and is larger for larger values of the shear ratio because of the increasing cross-cell mean shear component. For a surface current of 0.1 m/s and a typical cell depth between 15 and 30 m this drift is of order 0.05 m/s.

Although the influence of the mean current profile on the instability growth is beyond the scope of this study, there is an important point to make. A linear mean shear profile results in the disappearance of the forcing term in (4.17) containing $d^2|U|/dz^2$, which is not the case for nonlinear profiles. *Mourad* [1998] discusses the competition between different instability mechanisms which flux energy between the background state and the perturbations. He suggests that there are circumstances when the cross-cell mean shear

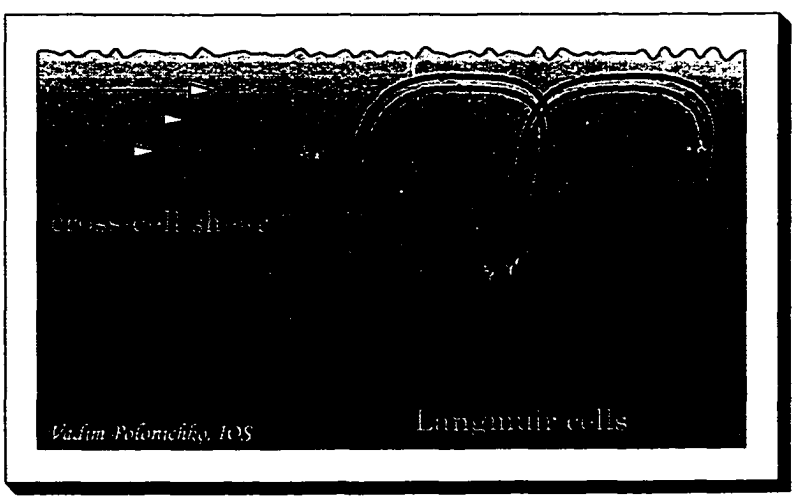

Figure 4.7: Schematic illustrating the effect of cross-cell shear Langmuir circulation. The dotted lines depict circulation streamlines in the absence of the cross-cell flow; the solid lines show distorted flow pattern.

can actually decrease the flux of energy even when there is an increase in the bulk Eulerian shear, and suggests that the presence of the cross-cell mean shear may suppress or enhance the growth of the perturbations depending upon the structure of the mean current.

4.3.2 Effects of the Wave Spectrum

In the previous calculations, an exponential profile for the Stokes drift corresponding to monochromatic waves was used. A realistic ocean surface wave field produces a different Stokes drift profile. Fully developed seas can be described using the Pierson-Moskowitz (PM) spectrum and the Stokes drift shear at the surface as

$$\left.\frac{d|\mathbf{U}_s|(z)}{dz}\right|_{z=0} \propto \int_0^{f_c} \exp(-f^4)df, \tag{4.31}$$

where f_c is a cutoff frequency, usually corresponding to capillary waves. This profile produces much stronger forcing at the surface. *Li and Garrett* [1993] showed that profile (2.6) drops more quickly close to the surface but decreases more gradually at greater depth and can be reasonably approximated as a sum of two exponents

$$|\mathbf{U}_s|(z) = E\, e^{0.8z} + (2-E)\, e^{8z}, \quad E \approx 1.07. \tag{4.32}$$

The maximal growth rate is now computed using the Stokes drift defined by (4.32). Note that the shear ratio at the surface is no longer as defined in (4.21). In order to make a comparison with the previous calculations, we need to rescale (4.32) by a corresponding factor. Comparison of the maximal growth rate, computed for two different Stokes drift profiles, indicates the reduction of maximal growth rate for the PM Stokes drift by about 35 to 45% (Figure 4.8), compared to the profile due to monochromatic waves. This is, perhaps, due to a weaker vorticity forcing at middle depths of the cells which results in a smaller integral forcing over the whole depth. Changes in the direction of the maximal growth rate are, however, small (2 to 3°).

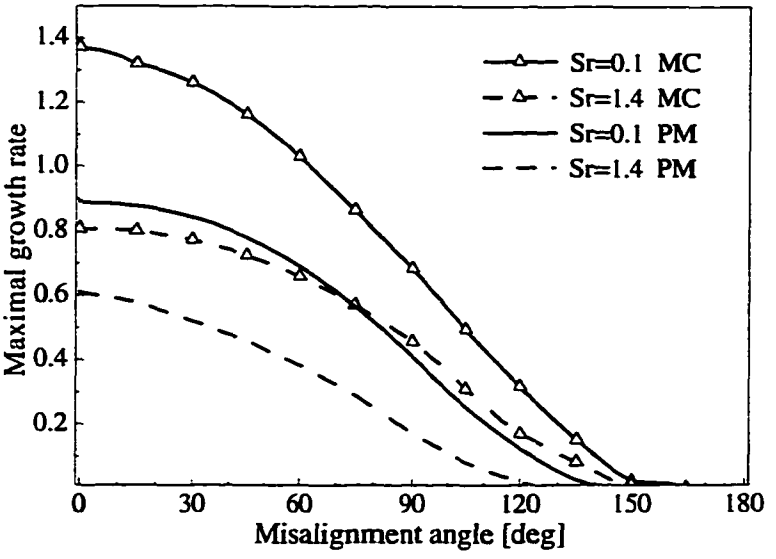

Figure 4.8: Maximal growth rate for monochromatic (marked by triangles) and Pierson-Moskowitz Stokes drift profiles as a function of the misalignment angle. MC refers to the exponential profile, and the lines are marked by triangles; PM refers to the Pierson-Moskowitz profile. Different line styles correspond to different shear ratios; Su= 4.5.

This result is, on the face of it, contradictory to *Gnanadesikan* [1996] who starts with a given wave height and a peak period and distributes it over a PM spectrum. The PM spectrum has a larger Sr and Su, which results in a larger growth rate. Here, I start with Su and adjust the significant wave height and period accordingly. This increases the Stokes drift shear, but only near the surface, while decreasing it at depth. Comparison of the PM and monochromatic growth rates without rescaling (which is equivalent to a larger shear ratio) shows the increase for the PM case, consistent with *Gnanadesikan* [1996].

4.3.3 Effect of Rotation

As a result of continuous wind forcing for an extended period, an Ekman current develops [*Pedlosky*, 1979]. *Leibovich and Lele* [1985] and *Gnanadesikan and Weller* [1995] considered the interaction between an Ekman spiral with the waves and suggested

that it may affect generation of Langmuir circulation as well. Taking into account effects due to the Earth's rotation, the nondimensional equations (4.1) and (4.2) will now contain extra terms on the right hand side, $f_C(\tilde{v}+\tilde{V}_s)$ and $f_C\partial(\tilde{u}+\tilde{U}_s)/\partial z$, respectively, where f_C is the Coriolis frequency. The corresponding nondimensional linearized equations (4.16) and (4.17) now become

$$\frac{\partial u}{\partial t}+\frac{\partial u}{\partial y}\left[\frac{2|\mathbf{U}|}{\sqrt{\mathrm{Sr}}}\sin(\theta+\alpha)+\frac{\sqrt{\mathrm{Sr}}}{2}|\mathbf{U}_s|\sin\alpha\right] + w\frac{\partial|\mathbf{U}|}{\partial z}\cos(\theta+\alpha)=\mathrm{La}\nabla^2 u+\mathrm{Ek}\,v, \tag{4.33}$$

$$\frac{\partial \xi}{\partial t}+\frac{\partial \xi}{\partial y}\left[\frac{2|\mathbf{U}|}{\sqrt{\mathrm{Sr}}}\sin(\theta+\alpha)+\frac{\sqrt{\mathrm{Sr}}}{2}|\mathbf{U}_s|\sin\alpha\right] + w\frac{d^2|\mathbf{U}|}{dz^2}\sin(\theta+\alpha)=\mathrm{La}\nabla^2\xi-\frac{d|\mathbf{U}_s|}{dz}\frac{\partial u}{\partial y}\cos\alpha+4\frac{\mathrm{Ek}}{\mathrm{Sr}}\frac{\partial u}{\partial z}. \tag{4.34}$$

Equations (4.33) and (4.34) contain an additional dimensionless parameter, the Ekman number Ek

$$\mathrm{Ek}=\frac{f_C\nu_e}{u_*^2}. \tag{4.35}$$

Since the Ekman number cannot be expressed as a combination of La, Sr and Su, an assumption needs to be made about eddy viscosity values. A discussion of the appropriate choice for the turbulent transfer parameters is given in Section 6.1.

Gnanadesikan and Weller [1995] suggested that an angle at which the cells are oriented depends on the current profile, which is a function of the Ekman number. When Ek is small the Eulerian shear is basically parallel with the wind and waves and the cells are formed in the same direction. They found the cells progressively moving to the right of the wind and waves (from ~9 to ~30°) as the Ek increased from 0.001 to 0.1.

To compare with their results, examples of the growth rate as a function of the cell wavenumber and orientation are given in Figure 4.9 for two choices of the Ekman number Ek=0.005 and Ek=0.1. The shear ratio Sr=3, Su=4 and equivalent Langmuir

number is equal to 0.04. In both cases the wind and waves are aligned and the Stokes drift profile for monochromatic waves is used. The first case (Ek=0.005) corresponds to a typical open ocean conditions (as discussed in Section 6.3), while Ek=0.1 represents an exaggeration for comparison purpose. The growth rate is calculated using formulation (4.27) and modified set of equations (4.33) and (4.34). Our results show that for small Ek the growth rate is symmetric with respect to the cell orientation (Figure 4.9a). When Ek is large the direction of the maximal growth moving slightly to the right from wind and waves (Figure 4.9b). These findings are in accord with *Gnanadesikan and Weller* [1995].

To summarize, our results and work by *Gnanadesikan and Weller* [1995] suggest that for typical open ocean conditions (in terms of the relevant dimensionless parameters) the inclusion of rotation does not significantly affect the orientation of Langmuir cells. However, there may be the circumstances when rotational effects become important.

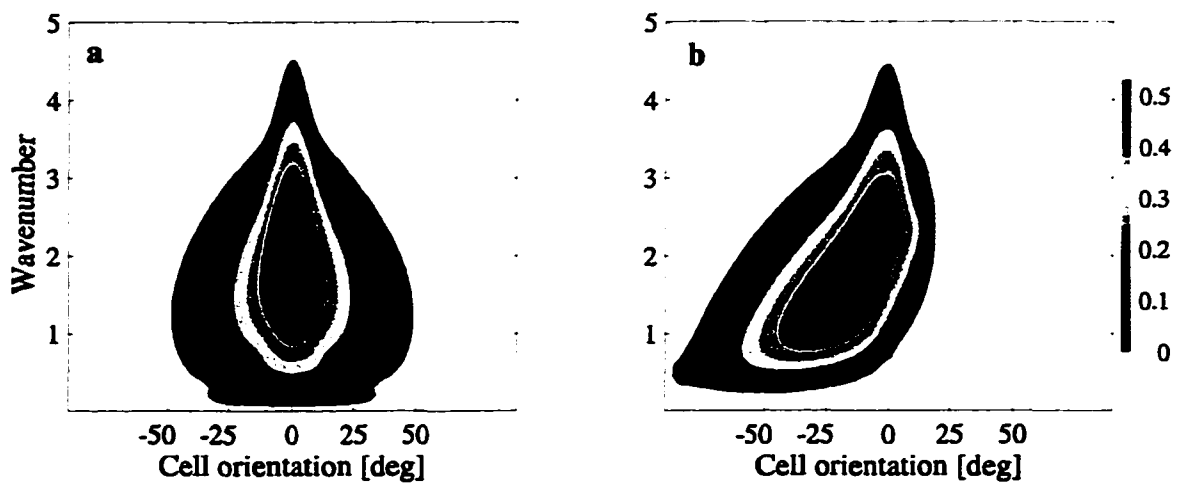

Figure 4.9: Effect of rotation on the cell maximum growth rate when wind and waves are aligned. Maximal growth rate (color bitmap) as a function of the cell wavenumber and orientation for two cases: a) Ek=0.005 and b) Ek=0.1. Sr=3, Su=4 and wind and waves are aligned.

5. OBSERVATIONS

5.1 Field Experiments

The data discussed in this thesis were collected during two open ocean experiments. The first took place between 11 and 31 of January 1995 between latitudes 47° and 49°N and longitudes 126°30′ and 128°30′W off the west coast of Vancouver Island (Figure 5.1) on board the *R/V Wecoma* (Oregon State University) jointly with the Applied Physics Laboratory (APL), University of Washington. The second experiment was conducted as a part of the Marine Boundary Layer (MBL) program together with the Woods Hole Oceanographic Institution (WHOI), University of Victoria (UVic) and the Scripps Institution of Oceanography (SIO). It took place in April to May 1995 at 36°N, 122°30′W, off Monterey, California on board the *R/V Wecoma*. Analysis and interpretation of these observations is given in Chapter 6.

5.1.1 Wecoma I Experiment, January 1995

During the Wecoma I experiment we collected observations of the near-surface bubbles and velocity field using the instrument platform SeaScan III described in

Chapter 3. Three deployments during strong wind and wave forcing are of interest here (Figure 5.2). The instrument recording schedule on January 15 was such that the fixed-orientation sidescan measurements were taken between 09:00 and 12:00 (PST) and the rotating sidescans mode was used for the rest of deployment 1. During deployments 2 and 3 the imaging sonars were set to record for one hour each in fixed and sweeping modes with 4-h breaks in between.

Interpretation of the near-surface velocity data require a knowledge of forcing, i.e., wind stress, wave field and the air-sea heat flux. Standard meteorological observations were available, including wind speed and direction, air and sea-surface temperature. Wind stress was subsequently calculated using bulk coefficients [*Smith*, 1981].

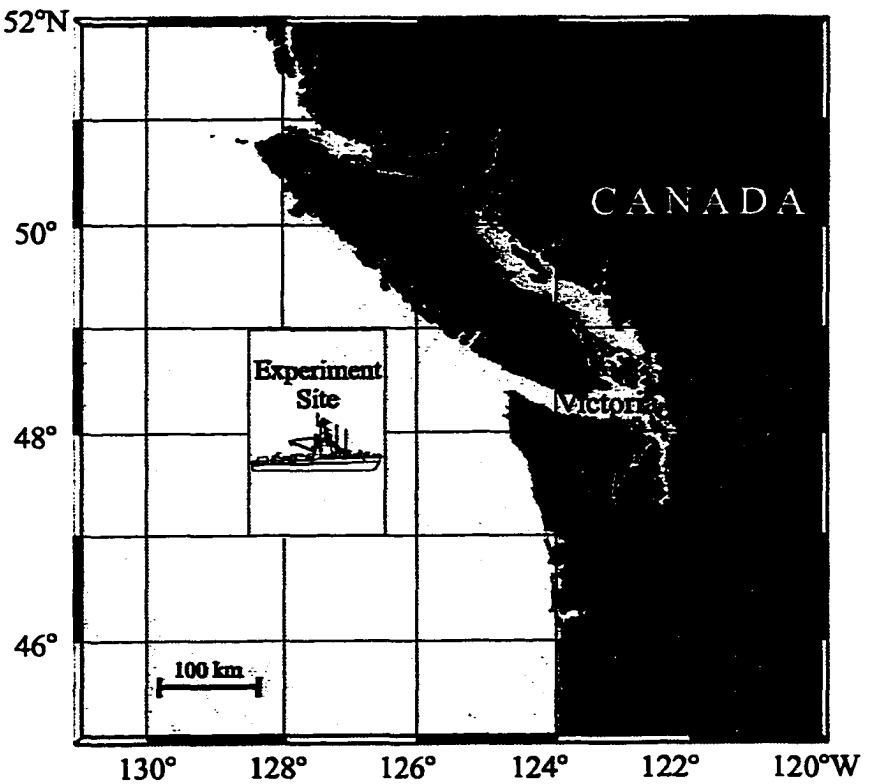

Figure 5.1: Wecoma I experimental site.

During the experiment we encountered several moderate wind events (U_{10} up to 14 m/s) between January 15 and 19 and one storm on January 27. The corresponding wind direction was variable for deployments 1 and 2 and was almost constant for deployment 3. Note that at winds below 5 m/s the wind direction behaves rather erratically (Figure 5.2a), which is, perhaps, caused by the shadowing of the anemometers by the ship

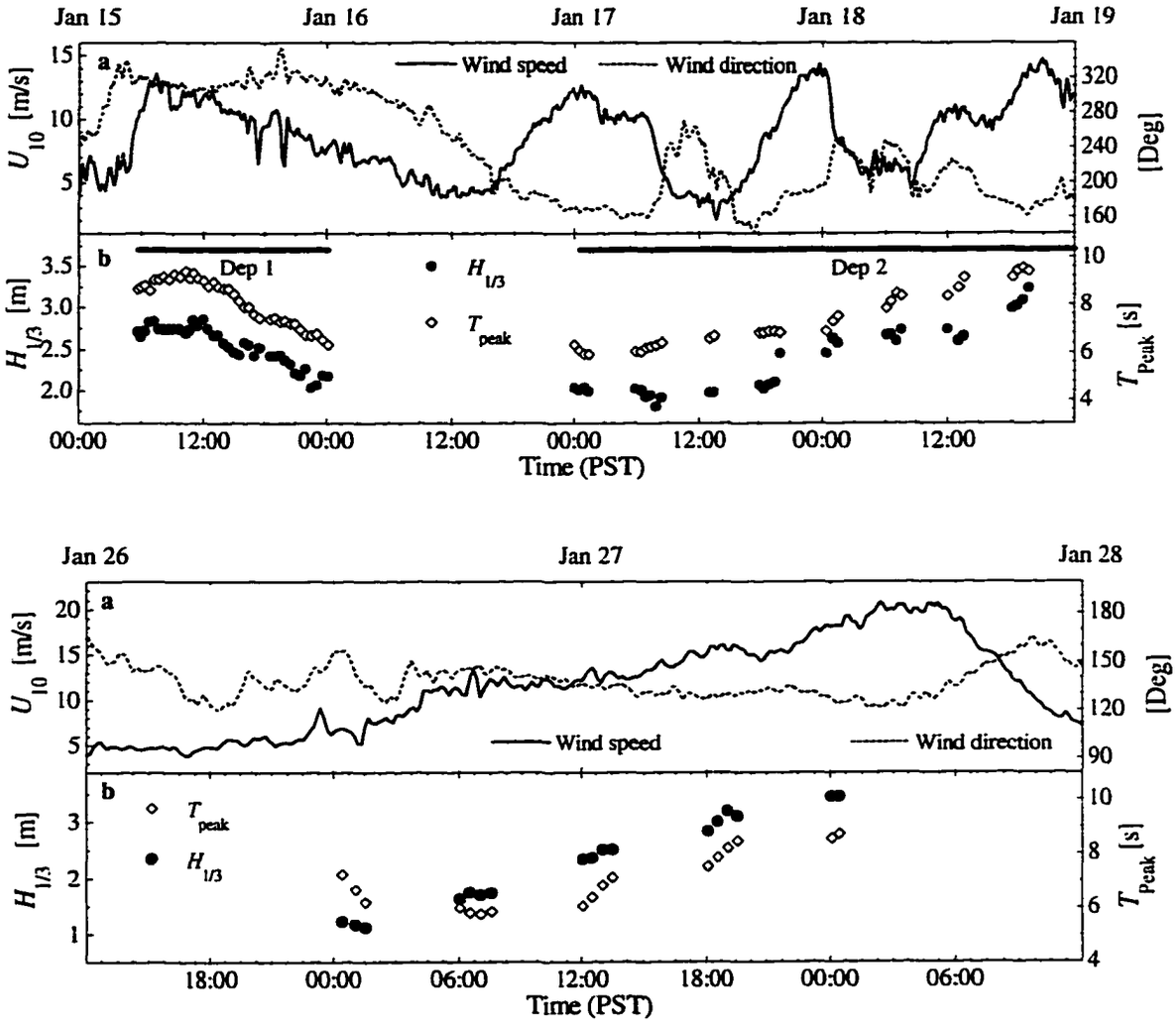

Figure 5.2: Meteorological and oceanographic parameters for Wecoma I for January 15-19 and 27, 1995. Deployments 1 and 2 are shown on the top figure and deployment 3 is on the bottom figure. a) Wind speed and direction corrected to 10 m height; b) significant wave height $H_{1/3}$ and period of the dominant waves T_{peak} calculated from upward-looking sonar measurements. Original meteorological data were provided by J. Dairiki, APL, U. Washington.

structure. However, the main focus here is on the periods when winds are in excess of 10 m/s, when wind direction is more reliable.

Wave observations, described below, displayed a developing wave field on January 17−19 and January 27 and relaxing waves on January 15 (Figure 5.2b). Significant wave height was between 1 and 3.5 m and the period of the dominant waves was between 6 and 9.5 s.

5.1.2 Marine Boundary Layer Experiment, April 1995

The major focus of the Marine Boundary Layer Experiment (MBL) was small-scale air-sea interaction, and dynamics of the wave enhanced near-surface layer. Several instruments were deployed. The same imaging sonar instrument was used for all acoustical observations with one important addition: a recording temperature sensor was attached to the rubber cord above the platform at approximately 3.5 and 6.5 m below the surface for the first deployment and at 3.5 m for the rest of the experiment. Simultaneous observations of the near-surface temperature structure were also acquired with a separate drifting surface float, FLEX (described in detail by *Gemmrich* [1997]), which was deployed in close proximity to the acoustical platform. Temperature measurements and bubble distributions at several depths were also obtained with a spar float Drifting Acoustical Resonator and Sound Speed Instrument (DARSI) [*Farmer and Vagle*, 1997]. FLEX temperature time series were provided by Dr. J. Gemmrich and bubble size distributions by Dr. S. Vagle. A simplified layout of our measurements during the MBL Experiment is given in Figure 5.3.

Near-surface turbulence measurements were taken with a Towed Microstructure Instrument, TOMI [*Wolk and Lueck*, 1997] at the same time by Dr. R. Lueck, Turbulence Laboratory, UVic. Acoustical current Doppler velocity measurements were taken on board the *R/V Wecoma* during the Experiment. Three components of raw velocity data

were supplied by S. Holgate, Turbulence Laboratory, UVic. An extensive set of meteorological observations, including wind speed and direction, wind stress, air-sea heat flux was provided by Dr. J. Edson (WHOI).

During the deployments, the imaging sonar recorded every even hour, alternating between the fixed and sweeping sidescan modes. Therefore, the directional wave field and the surface bubble cloud images were made available every 4 hours with a 2-h offset and the upward-looking sonar data were available every 2 hours. The upward-looking observations consisted of both 200- and 400-kHz sonar data while only 400 kHz sonar was available during Wecoma I.

Of interest here are two deployments: the 32-h period (between 20:00, April 17 and 04:00, April 19 PDT), during which a strong storm passed over the experimental site

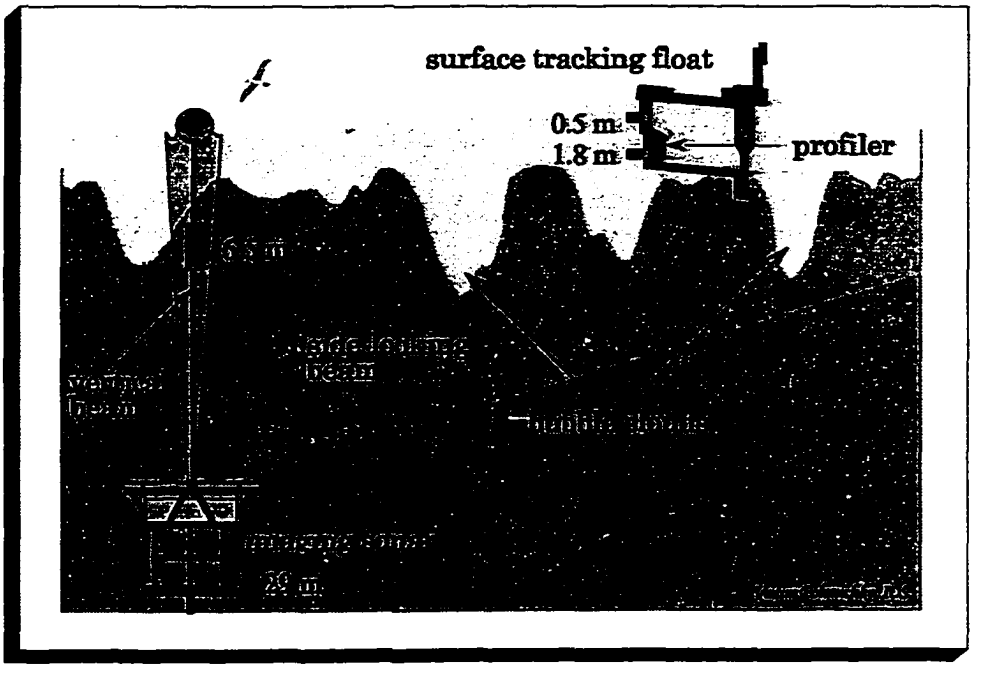

Figure 5.3: Observations of the near-surface processes during the Marine Boundary Layer Experiment. The imaging sonar platform freely drifts at ~29 m below the sea surface with the upward- and side-looking sonars measuring vertical and horizontal near-surface bubble clouds. Additional temperature sensors are placed at 6.5 and 29 m depths. A separate surface tracking float equipped with fixed and profiling thermistors provides high resolution temperature distributions in the top 1.8 m.

(Figure 5.4, top). After the wind increased from less than 2 m/s to approximately 13 m/s

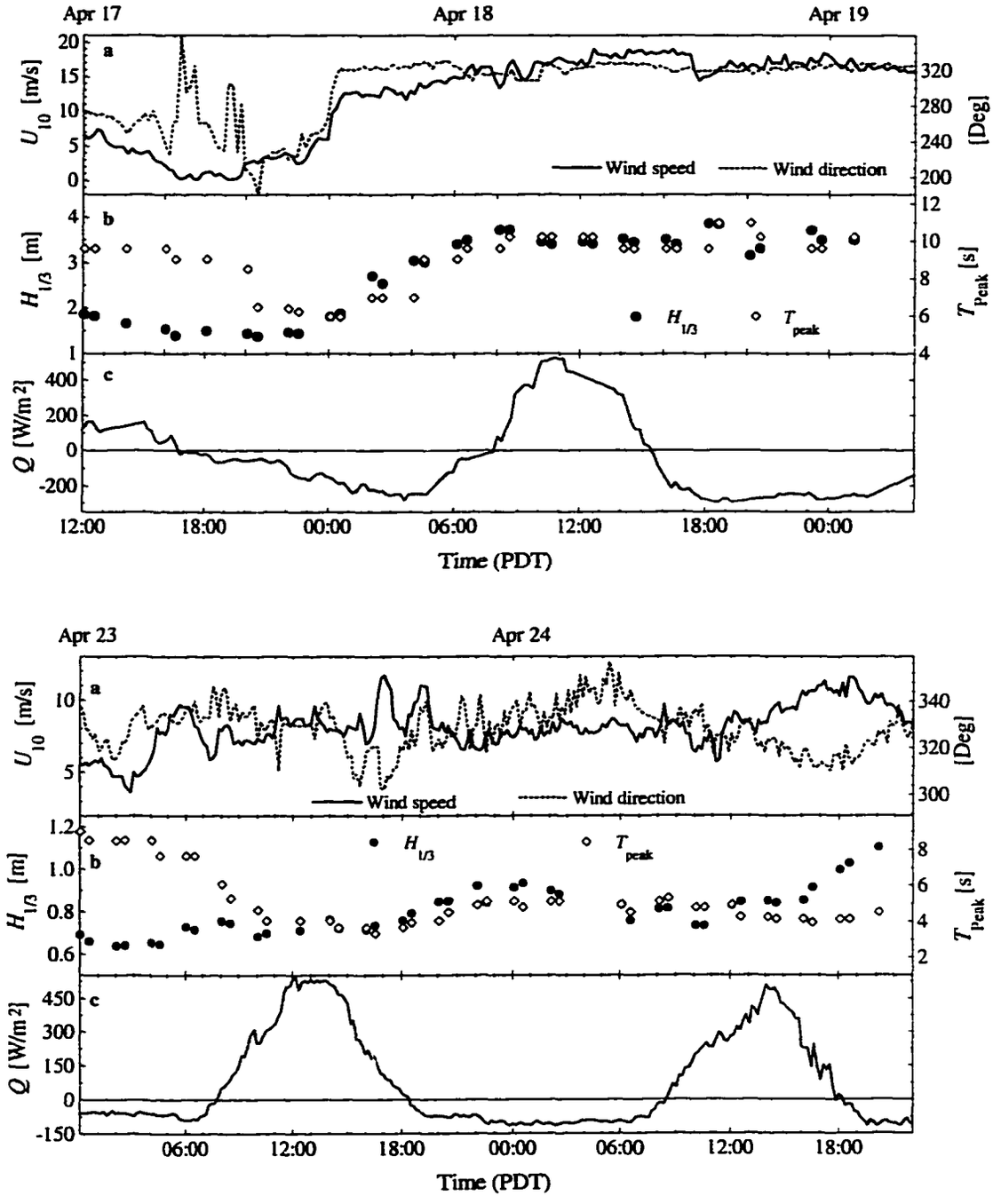

Figure 5.4: Environmental conditions during the MBL Experiment during high winds (top diagram) and moderate winds (bottom diagram). a) Wind speed and direction corrected to 10 m height; b) significant wave height $H_{1/3}$ and period of the dominant waves T_{peak} calculated from upward-looking sonar measurements; c) air-sea heat flux. Positive flux corresponds to the ocean acquiring heat.

at 02:00, April 18, the wind direction was fairly constant. Wave measurements showed a transition from gradually decaying seas prior to 22:00, April 17 to a moderately developed wave field after 11:00, April 18. A different period of moderate winds on April 23 to 24 is shown in Figure 5.4, bottom. Here, the winds changed quickly, seldom exceeding 10 m/s, resulting in a fairly weak wave field ($H_{1/3} < 1.5$ m).

5.2 Wave Field Measurements

5.2.1 Wave Spectra

During a storm the near-surface layer of the ocean is a very energetic environment (Figure 1.1). Figure 5.5 provides an example of the surface and instrument motions during one of the deployments showing 7-s waves with maximal amplitude of 2.2 m and corresponding orbital velocity of more than 2 m/s (Figure 5.5b). Maximal instrument displacement was, however, much smaller (±0.2 m) and vertical velocity amplitude < 0.25 m/s (Figure 5.5a). As the instrument platform drifted beneath the surface, it pitched and rolled in response to the ambient forces. Dynamic rms tilts (referenced to the instrument's "North") were 0.5° for the x component and 0.7° for the y component with mean values of 0.7° and 2.9°, respectively (Figure 5.5d). The larger mean y tilt was due to the pull exerted by the surface buoy on the platform. The maximal observed tilt magnitude never exceeded 4°.

The compass record (Figure 5.5c) indicated that the instrument was rotating at an average rate of 0.4°/s. Spectral analysis of the compass time series showed that the oscillatory rotational motion of the instrument has an average period between 50 and 60 s. The mean rotation rate was between 0.3 and 0.5°/s with a maximal spin of 2.5°/s. The compass used on SeaScan III had a time response of 3 s and a resolution of 1°. A rapid

rotation introduced an error in apparent heading, which had to be corrected for. The details of the compass correction procedure are given in Appendix A.

Surface elevation time series were used to estimate parameters of the wave field. It is derived using backscatter intensity measured with the upward-looking sonars. The position of the surface corresponds to the sudden rise in the backscatter intensity (of order 12 dB, Figure 5.6) and the distance from the platform to the surface R_s is proportional to the acoustical travel time delay Δt

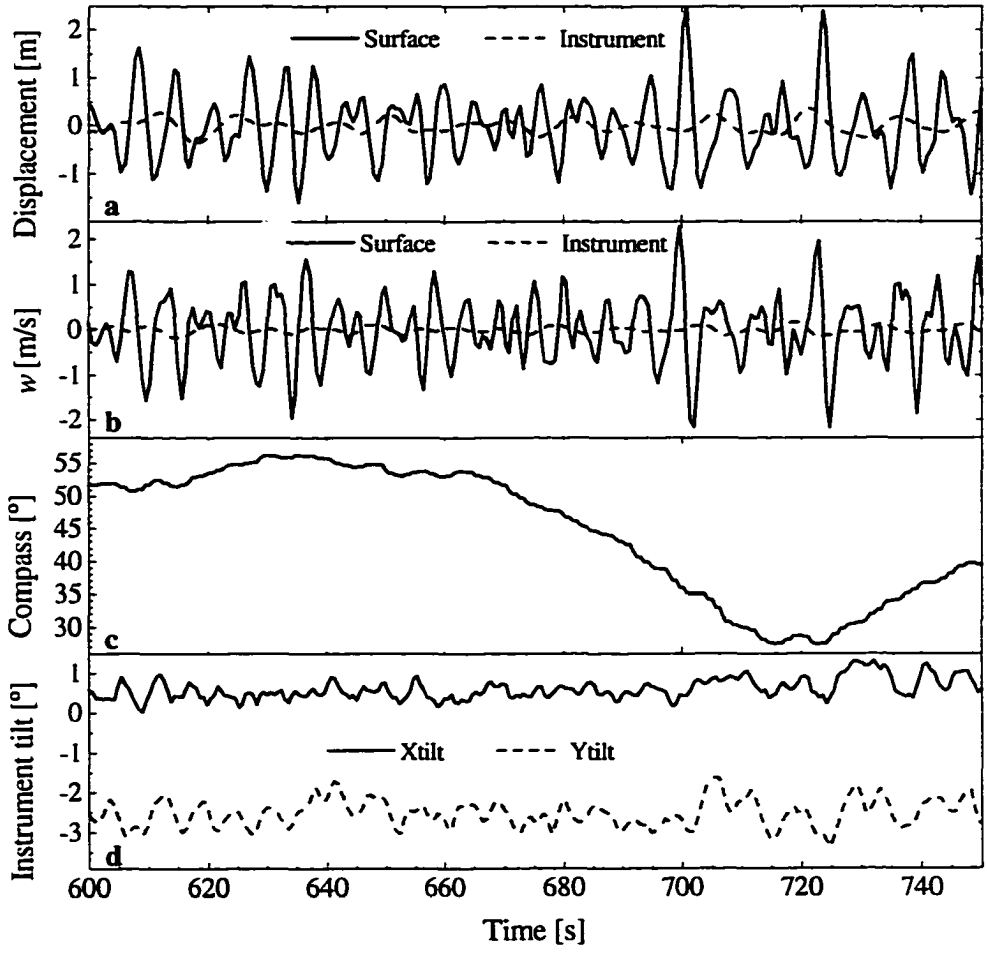

Figure 5.5: An example of the instrument and surface motions during the MBL Experiment, April 18, 1995. a) Instrument and surface displacement; b) instrument and surface wave motion; c) instrument rotation; d) instrument tilt. The platform depth was 29 m, and mean wind speed was 13 m/s.

$$R_s = c\Delta t/2 \tag{5.1}$$

where c is the speed of sound in the water.

Two methods were tested for the time delay calculations. For the "short" non-coded pulse transmissions the maximum slope technique described by *Zedel* [1994] was used. This technique detects surface return as the place where the time derivative of the backscatter amplitude vs. range has a maximum. Unfortunately, this method is not very robust when phase-modulated pulses are transmitted, in order to reduce velocity variance as discussed above, due to multiple peaks in the return signal (Figure 5.6).

Instead, an adaptive filtering (decoding) scheme was implemented which is based on computing a cross-correlation between the received signal and a transmitted template. In addition, a pressure sensor record was used to locate approximately the position of the surface and the decoding was further applied to within a ±3.5-m range from the recorded instantaneous depth. Wave-induced pressure decays exponentially with depth (2.3) and therefore is not well suited for wave measurements above approximately 0.17 Hz. The resolution of both techniques is limited by the distance between two successive samples, which, in our case, was 0.1 m. To improve this estimate a second degree polynomial was fitted near the peak. An example of the raw backscatter amplitude measured with an upward-looking sonar and its decoded envelope is given in Figure 5.6. Adaptive filtering removed higher frequency variability from the raw backscatter and provided a more robust estimate of the peak location.

Wave orbital motion is calculated from the surface elevation and uncertainties in the latter will result in uncertainties in the estimates of the former. A major factor contributing to the uncertainties in measurements of the surface elevations is the error produced in the determination of the surface location (travel time), which comes from the finite size of the sonar surface footprint [*Zedel*, 1993]. Because of the conical spreading, the sonar beam insonified some finite surface area immediately above it (Figure 5.7) and was not able to resolve horizontal scales smaller than a footprint size, which is different

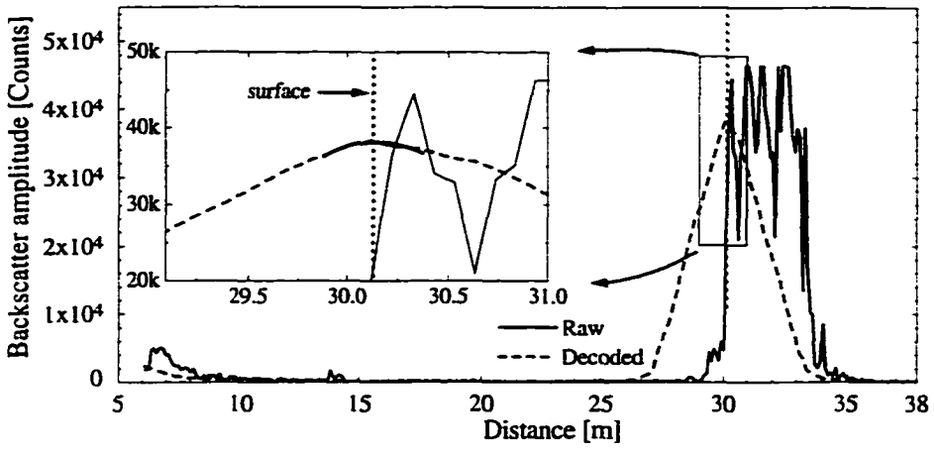

Figure 5.6: Raw sonar backscatter amplitude (solid line) and its decoded envelope (dashed line). The position of the surface return is at the maximum of the envelope. To improve accuracy, a second order polynomial (thick line in the insert) is fitted near the envelope peak.

for the different sonars (Table 3.1). The footprint-related error will result in the *underestimation* of the surface elevation η primarily at the wave crests (Figure 5.7). The upper limit of this error is calculated assuming maximal possible wave steepness of $1/7$ for a fully developed wave [*Longuet-Higgins*, 1963] and the maximal uncertainty in the surface height is estimated between 0.22 and 0.30 m for the two highest frequency sonars. However, it will be significantly smaller for developing seas.

During our deployments, we observed wave slopes to within 0.03 to 0.07 which correspond to smaller uncertainties of 0.11 and 0.15 m, respectively. To correct for the footprint-induced error using velocity continuity, a significantly higher pulse repetition rate is necessary. The footprint-related underestimation of the surface height subsequently produced a smaller surface velocity at the peak and trough of the wave by 0.25 to 0.35 m/s. In addition, a "mis-positioning" of the surface return in the backscatter time series would also affect Doppler measurements due to the inclusion into the surface bin (surface scattering) of part of the bubble scatter (volumes scattering), which is of much lower amplitude. It can be shown that the resultant error was of order 3% for the

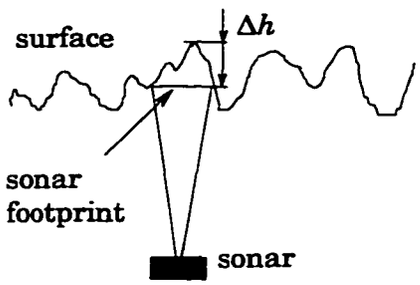

Figure 5.7: Sonar footprint geometry. Vertical scale of the surface elevation is exaggerated. The measured wave height is underestimated by Δh.

surface-bubble backscatter signal ratio of 12 dB. The instrument displacement was usually 8 to 10 times smaller than the wave motion and its effect on the accuracy of the surface height measurements is smaller compared to the footprint geometry.

The measured range from the instrument to the surface $H_s(t)$ is a linear superposition of the instrument motion and the true surface elevation. The displacement of the instrument $h_p(t)$ was calculated by double integration of the measured vertical acceleration $a(t)$ which, prior to that, was high-pass filtered to remove the low frequency bias, associated with the integration. The filtering was done in the frequency domain via

$$h_p(t) = \mathcal{F}^{-1}\left\{\frac{H(\omega)\mathcal{F}[a(t)]}{\omega^2}\right\} \tag{5.2}$$

using an equivalent of a fourth-order high-pass Butterworth filter with the stop frequency centered at 0.045 Hz. No wave motion was usually present below 0.05 Hz so this procedure was sufficient to remove low-frequency "noise" due to the instrument's inertial motion. The maximal magnitude of this low-frequency motion was estimated from the depth record and is less than 8 mm/s. The true surface elevation was then calculated as

$$\eta(t) = H_s(t) + h_p(t) - H_0, \tag{5.3}$$

where H_0 was an averaged (over an hour or so) depth of the instrument. The acceleration of the platform was measured by a floating cantilever beam accelerometer and was therefore affected by the instrument pitch and roll. The maximal combined tilt-introduced error was fairly small: 95% of the time it is less than 0.25% with a maximum

of 1% and we therefore expected the accelerometer to measure true instrument motion.

The wave height spectrum was estimated using Welch's method of averaged modified periodograms [*De Fatta et al.*, 1988] with a 256-bin window length and 128-bin overlap. Uncertainties related to a finite sonar footprint limited the length of the resolvable shortest waves. The raw surface height spectra were therefore truncated above 0.6 Hz, which approximately corresponds to the wavelength of twice the footprint diameter.

Two examples of measured spectra are shown in Figure 5.8 for moderately developed seas (a) winds over 8 m/s for more than 8 h) and very young seas (b) winds over 8 m/s for less than 2 h). The model JONSWAP and Pierson-Moskowitz spectra (Eqs. (2.7) and (2.5), respectively) are given for reference. Model spectra were calculated using U_{10} and fetch χcorresponding to the observed peak frequency f_p [*Donelan et al.*, 1985]

$$f_p(U_{10},\chi) = 3.5\frac{g}{U_{10}}\left(\chi\frac{g}{U_{10}^2}\right)^{-0.33}. \tag{5.4}$$

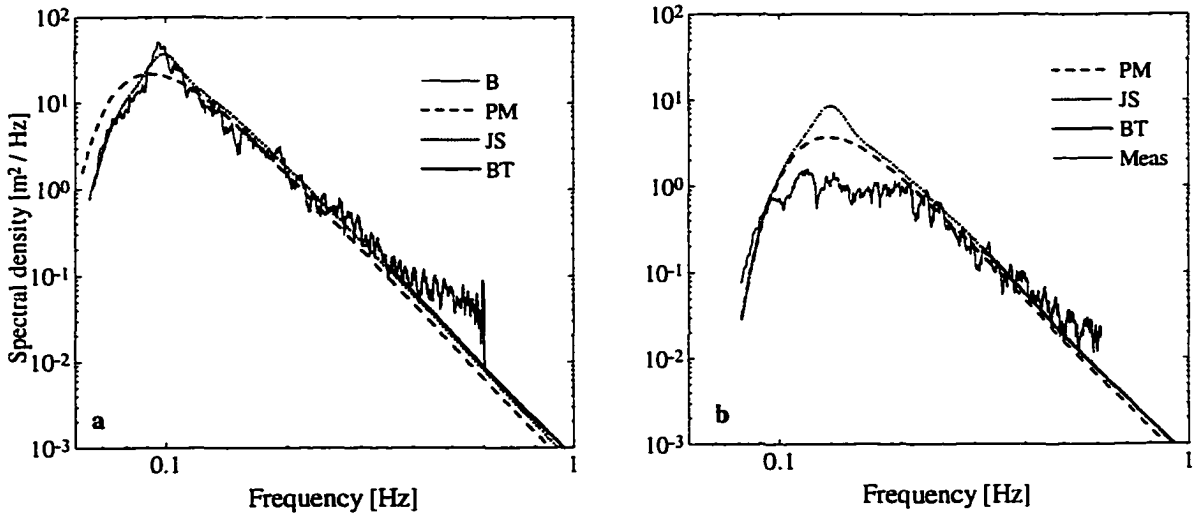

Figure 5.8: Comparison of modeled and measured wave height spectra for a) moderately developed seas and b) very young seas. The thin solid line is measured, and the lines marked PM and JS denote Pierson-Moskowitz and JONSWAP spectra, respectively. Line marked BT represents the "banner-tail" augment to the measured spectrum above 3.5 f_p. Environmental conditions are a): U_{10} = 17.1 m/s, h_s = 3.9 m, 12:30, April 18, 1995; b): U_{10} = 12.2 m/s, h_s = 1.9 m, 02:30, April 18, 1995.

For moderately developed seas the PM model approximates the observations fairly well above the peak frequency while underestimating the wave power in the neighborhood of the peak (Figure 5.8a). The JONSWAP model, taking into account the peak enhancement, agrees very well with the observations. An example of very young seas (Figure 5.8b) shows that both JONSWAP and PM models greatly overestimate wave power below 0.2 Hz. This results in the overestimation of the Stokes drift.

A noticeable increase in the power level is observed above ~0.4 Hz (Figure 5.8). This corresponds to a wave height of order 0.15 m which is close to the vertical resolution limitation of the sonar system due to the footprint effect. To avoid contamination of wave field parameters estimations, I parameterize the contribution of the unresolved waves using the approach first suggested by *Banner* [1990]. Considering an equilibrium spectral behavior of ocean gravity and combining model results with the wave spectra observations, *Banner* [1990] demonstrated that the wave energy decays as f^{-5} at high frequencies and a high frequency "tail" can be appended to the measured spectra above $3.5 \times f_p$ (lines marked BT in Figure 5.8).

In calculations of wave parameters for the open ocean, a linear dispersion relation for deep water waves is commonly used. It is valid when the wave slope is small. We estimate the slope from both the measured wave height using a zero-crossing technique [*Thorpe*, 1996], which gives a wave period as a time between two zero crossings in the surface elevation time series, and the wave spectrum. The wave slope is defined as A/λ, where $A^2 \sim f F(f)$, $\lambda = g/(2\pi f^2)$ and the slope, therefore, is

$$\frac{A}{\lambda} = \frac{2\pi}{g}\sqrt{f^5 F(f)}, \tag{5.5}$$

where the wave spectral density $F(f)$ is defined by (2.6). Calculations for the same deployment as the examples in Figure 5.8 give 95% of the values of the slope less than 0.1 with a median of 0.03. This shows that the surface slope is small, which justifies the use of the linear dispersion relation in the subsequent calculations of the wave orbital

motion. The above examples demonstrate that our wave measurements compare well with the model predictions for moderately developed seas (Figure 5.8a) and that the unresolved part of the wave spectrum can be adequately parameterized using the high frequency tail. However, models significantly underestimate wave power near the peak for very young seas (Figure 5.8a). A unidirectional spectral spreading was assumed for comparisons for the model spectra.

Although potentially (5.5) has a white spectrum integration within finite limits produces a finite slope. By varying the upper limit of the integration I find that waves with the frequencies above 1.5 Hz do not contribute significantly to the Stokes drift: frequency increase from 1.5 to 3 Hz results in the velocity increase of 7% increase, while integration only to 1 Hz produces smaller drift by 20%.

The Doppler velocity calculated from the acoustical backscatter contains information about the motion of the bubbles, which, in the near-surface region, are primarily driven by the orbital motion of the surface waves. Radial Doppler velocity measured along four sidescan beams, separated by 45° in the azimuth, as a function of range, together with the wave height derived from the upward-looking sonars is used to resolve the directional wave power distribution. Time series of horizontal wave velocity at 16 range points along each of two beams are used in a maximum-likelihood array processing scheme to estimate the directional spreading function $\Phi(\omega,\theta)$ [*Trevorrow*, 1995]. Combined with a surface height $F(\omega)$ spectrum, derived from the measured surface elevation $\eta(t)$, this gives rise to the in directional wave height frequency spectrum $S(\omega,\theta)$.

The normalized directional spreading function is given in Figure 5.9 at two frequencies: (a) 0.1 Hz and (b) 0.25 Hz for the MBL Experiment on April 18, 1995. Model spreading (Figure 5.9, thick dotted lines) is calculated using the formulation of *Donelan et al.* [1985]. The wave direction is referenced to the local wind direction with positive angles corresponding to the waves traveling to the right from the wind. At approximately midnight, April 18 the wind changed direction from 270° to 320° (Figure

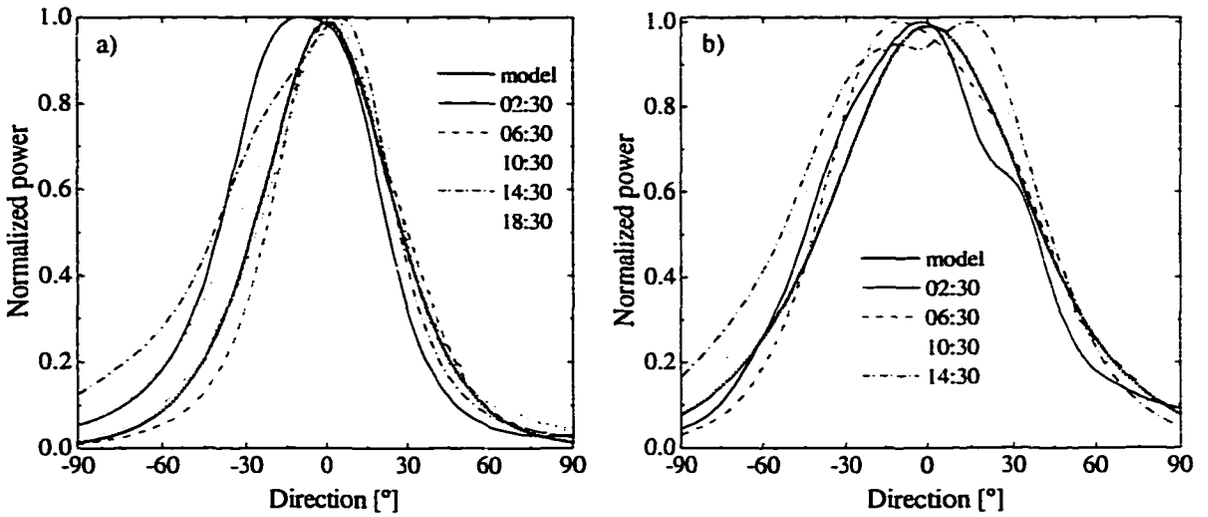

Figure 5.9: Normalized directional spreading at a) the peak frequency and b) 2 f_p during the MBL Experiment, April 18, 1995 together with the model prediction of Donelan et al. [1985]. The wave direction is given relative to the wind direction.

5.4). Measured spreading near the peak frequency shows that waves have not completely adjusted to the wind shift and propagate to the left from the wind at the beginning of the storm (02:30) and adjust to the changes afterwards (Figure 5.9a). Directional spreading calculated at 0.25 Hz generally agrees with the model, except for the set at 14:30, when a 15° deviation to the right from the wind is observed (Figure 5.9b).

Wave forcing has an important role in the generation of Langmuir circulation. Within the CL2 model it is parameterized in terms of the surface Stokes drift U_s and its e-folding depth h_s. The directional Stokes drift, used for subsequent analysis, is calculated from the measured directional wave spectrum using Eq. (2.12). During the MBL Experiment, the directional wave field is measured every 4 h and is interpolated in between, considering that the wind direction does not vary significantly (Figure 5.2a).

Examples of the Stokes drift profiles, calculated for the same set of spectra as in Figure 5.8, are given in Figure 5.10. A unidirectional wave field is assumed here for comparison purposes. In a moderately developed case (Figure 5.10a) both PM and JONSWAP (JS) models agree with the wave height based observations fairly well: the surface Stokes drift for JS is within 5% and for PM is within 10% of measurements. The

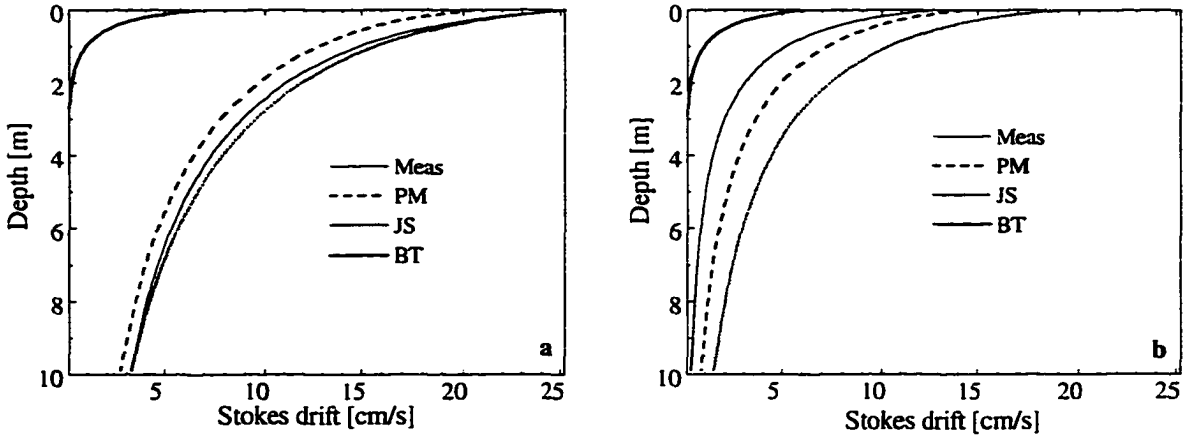

Figure 5.10: Stokes drift profiles calculated using wave height spectra shown in Figure 5.8, assuming unidirectional waves. The thin solid line is measured and the lines marked PM and JS denote Pierson Moskowitz and JONSWAP spectra, respectively. The line marked BT corresponds to the high frequency "tail" contribution. Measurements were taken at a) 12:30, April 18, 1995 and b) 2:30, April 18, 1995.

relative contribution of the short waves (BT) is approximately ⅓ at the surface and vanishes below 2 m. The case of very young seas is quite different (Figure 5.10b) where the surface values for JS and PM exceed the measurements by 50% and 15%.

It is also interesting that the short waves now contribute almost half of the surface Stokes drift. This implies that short waves are equally important for Langmuir circulation generation as dominant waves and Langmuir circulation may respond preferably to the forcing by the "younger" short waves when the wind changes direction. The resulting Stokes drift then has a direction that differs from the local wind. The consequences of this effect are considered in Chapter 6.

5.3 Vertical Velocity Measurements

The upward-looking sonars image bubble clouds as they drift past the instrument (Figure 5.11). Vertical Doppler velocity is calculated from the raw acoustical backscatter

signal using the complex covariance approach described in Chapter 3. Binned velocity estimates are computed using a lag equal to the sub-code length L with $L(M-1)$ points averaging (Eq. 3.12), where M is the number of sub-code repetitions. For the upward-looking sonars, $L=5$ and $M=6$. The dynamic range of the receivers' electronics is tuned to operate efficiently in the presence of bubble clouds and we are unable measure fields effectively elsewhere. Thus the velocity measurements are confined to the areas of high bubble concentrations.

5.3.1 Velocity Decomposition

Computed velocity represents a projection of a true velocity on to the direction of the sonar beam and is a measure of the *relative* motion between the source/receiver (instrument platform) and the targets (bubbles and water surface). The changes in the instrument position over the transmission cycle are negligible. The largest velocity signal

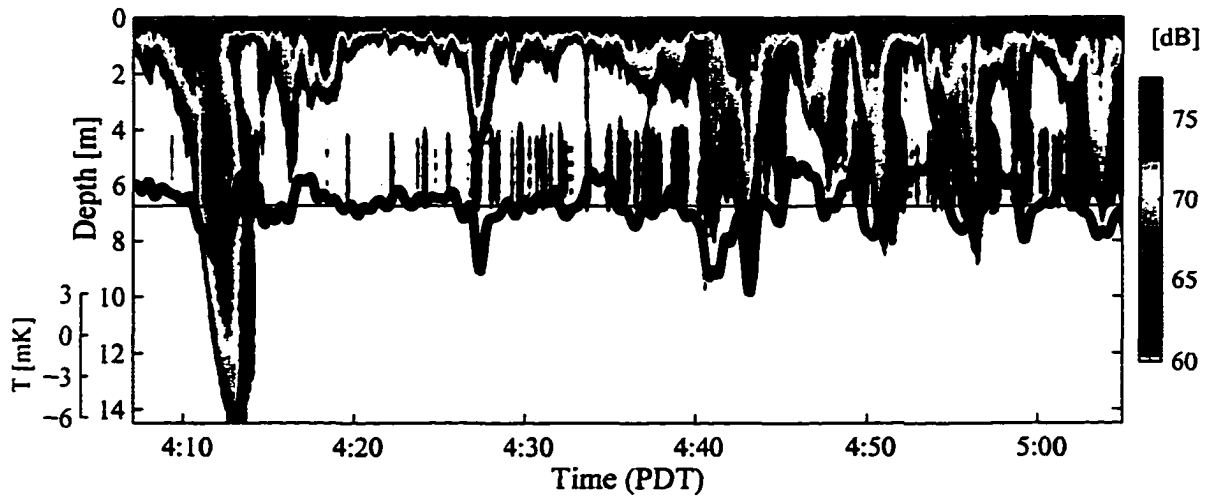

Figure 5.11: Backscatter intensity detected with an upward-looking 200-kHz sonar during the MBL Experiment, April 18, 1995. Average wind speed is 14.8 m/s, and the average heat flux shows cooling at a rate of 308 W/m^2. Also shown is a time series of the temperature deviation at 6.5 m depth (thick line on the top plot). A band centered at approximately 6 m represents contamination due to temperature sensor.

is due to the wave orbital motion which can be an order of magnitude larger than the expected velocities associated with Langmuir circulation (Figure 5.5). Therefore, much effort has been devoted to the accurate estimation and subsequent removal of the wave orbital motion.

We derive surface velocity from the corrected surface height (5.3) using a differentiator, based on a third order Finite Impulse Response (FIR) filter with a cut-off frequency at 0.35 Hz. This is a quite efficient technique which assures a linear frequency response in a broader frequency band compared to a conventional pair-difference and does not introduce a phase lag [*De Fatta et al.*, 1988].

The spectral component of vertical velocity $W_{orb}(z,k)$ induced by a monochromatic linear wave with wavenumber k decays with depth z as

$$W_{orb}(z,k) = W(0,k)e^{-kz}, \tag{5.6}$$

where $W(0,k)$ is the velocity at the surface. Using a linear dispersion relation for deep water surface gravity waves ($\omega^2 = gk$) and a Fourier transform of the surface elevation $\eta(t)$, the vertical velocity profile $W_{orb}(z,\omega)$ is recovered as

$$\begin{aligned} &W_{orb}(z,\omega)=W_{surf}(\omega)e^{-\omega^2 z/g}, \\ &W_{surf}(\omega)=-i\omega F(\omega),\ F(\omega)=\mathcal{F}\{\eta(t)\}, \end{aligned} \tag{5.7}$$

where the symbol $\mathcal{F}$ denotes the Fourier transform and ω is the angular frequency.

As mentioned in Chapter 3, the Doppler method has an inherent limitation, namely, the velocity ambiguity. Limiting values for the 200- and 400-kHz upward looking-sonars are 2.8 and 1.4 m/s, respectively (Table 3.1), and the ambiguity effects may contaminate velocity estimates close to the surface. The surface elevation-derived velocity is used as a reference to recover the true velocity values. I construct a difference $|w_{orb} - w_{meas}|$ and unwrap the points where it exceeds $(v_{alias} - \sigma_V)$, where σ_V is the velocity uncertainty.

To validate acoustical Doppler velocity measurements, a comparison is made between vertical velocities calculated using both Doppler processing and the surface elevation

time series. Comparing velocity time series at different depths (Figure 5.13), we observe a generally good agreement between the two estimates when the signal-to-noise ratio (SNR) is sufficiently large. On several occasions at the wave peaks, the Doppler estimate exceeds the orbital component, which can be due to the footprint effects previously described. At lower SNR the Doppler method is biased towards zero [*Plueddeman and Pinkel*, 1991] and gives a smaller estimate. An additional source of error, contributing to the Doppler measurements and found after more detailed analysis, is the saturation of the surface return which may result in a 10% uncertainty in the Doppler velocity measurements, depending on the level of saturation. It is not possible to correct for the saturation and recover the true surface Doppler velocities. However, the bubble return from just beneath the surface almost never saturated and therefore saturation should not affect the fluid velocity measurements in the water column.

Comparison of the vertical velocity profiles shows that both methods agree within the errors (Figure 5.12) and we therefore conclude that the Doppler method gives a good estimate of the surface velocity within the uncertainties of the measurements. A spectral decomposition is further applied to removed wave and instrument motions from the measured velocities and thus gives rise to the residual fluid motion $w_c(t,z)$ as

$$w_c(z,t) = \mathcal{F}^{-1}[W(z,\omega) - W_{orb}(z,\omega) + W_{plat}(\omega)] \,. \tag{5.8}$$

The resultant velocity estimates have a theoretical single transmission velocity uncertainty (Table 3.1) which is comparable to or exceeds the expected Langmuir circulation component. In reality, a low SNR [*Brumley et al.*, 1991] and oceanic turbulence contribute additional variance. Successive raw velocity estimates are accumulated into a two-dimensional array $w(z,t)$ which is then low-pass filtered, using a fourth order elliptic filter with a cut-off frequency corresponding to 30 s. The use of this filter assures sharp roll-off and minimizes spectral energy leakage.

An example of the residual vertical velocity distribution, corresponding to the

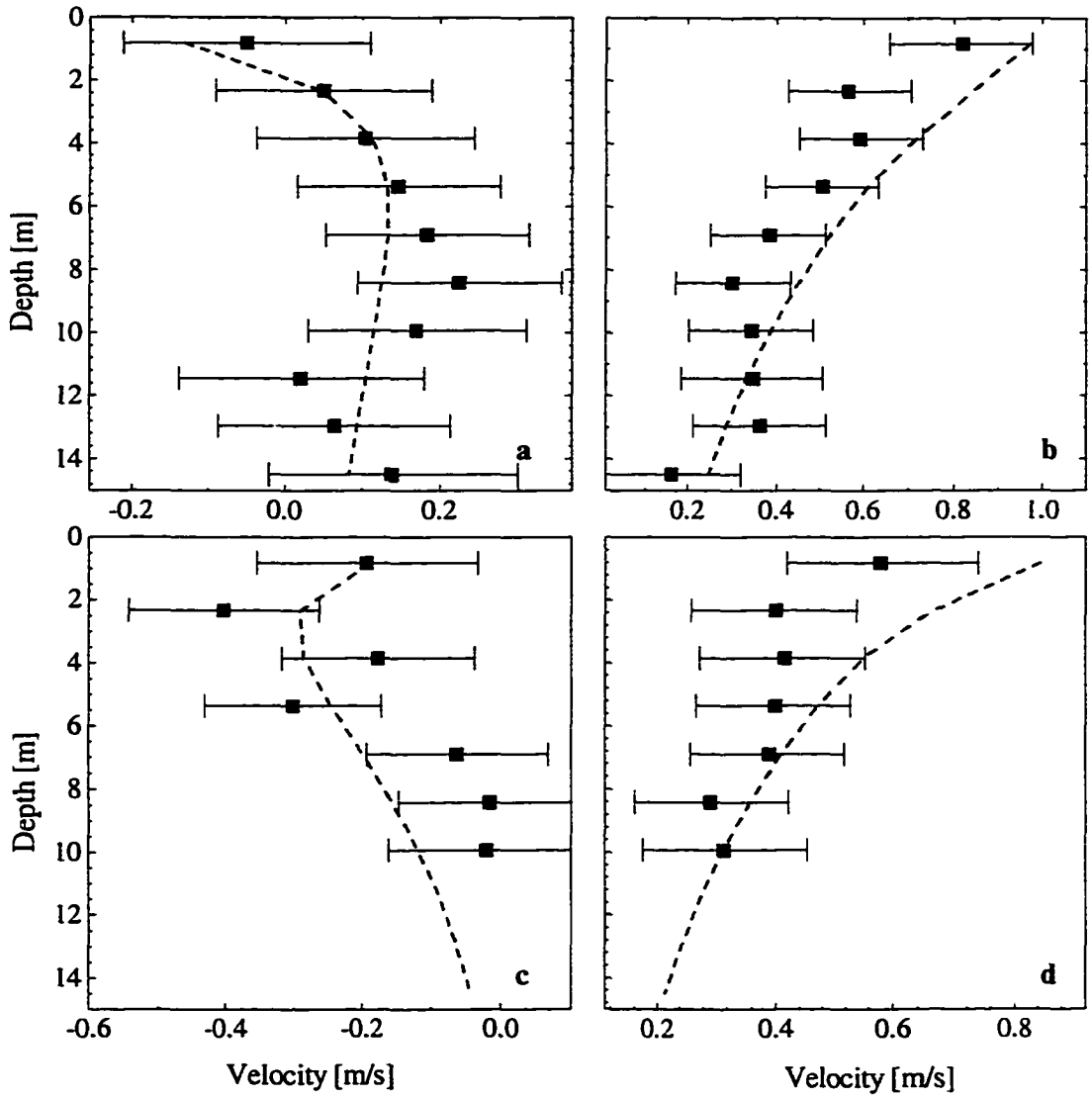

Figure 5.12: Examples of instantaneous vertical velocity profiles. The dashed line indicates velocity taken from the surface elevation; the solid line is the velocity, using Doppler measurements. Error bars denote one standard deviation, as described below. a)—d) correspond to individual profiles taken between 04:07 and 04:37, April 18, 1995.

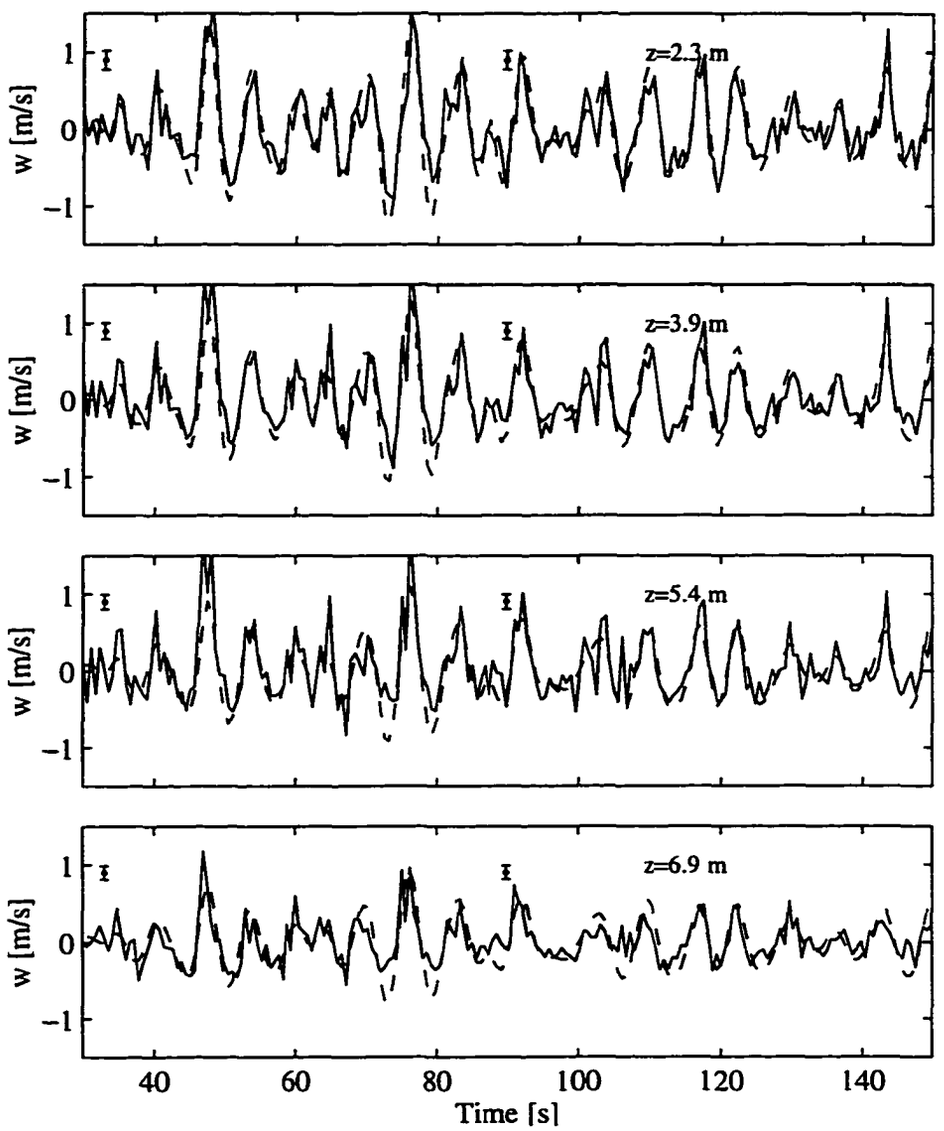

Figure 5.13: Measured vertical velocity time series at different depths. The dashed line marks the velocity derived from the surface elevation; the solid line is the velocity from the Doppler measurements. Velocity error is given as one standard deviation.

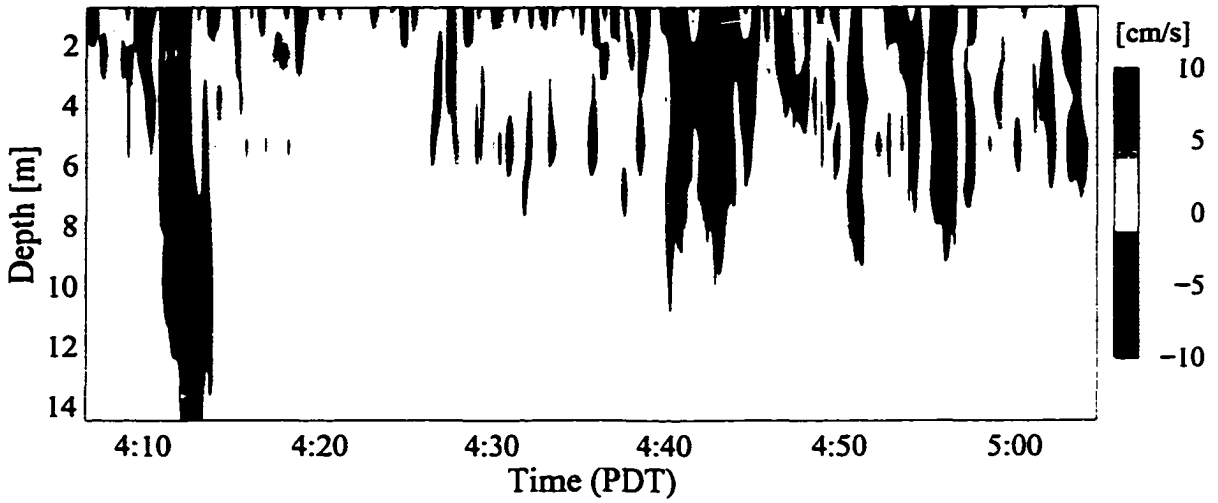

Figure 5.14: Residual vertical velocity component detected with an upward-looking 200-kHz sonar during the MBL Experiment, April 18, 1995. Velocity estimates are limited to the areas of high backscatter and positive velocity is upwards.

intensity image in Figure 5.11, is presented in Figure 5.14. Temperature sensors contaminated the acoustical signal during the MBL Experiment (Figure 5.11) resulting in unreliable velocity measurements in the top 6.5 m except for a few very dense clouds such as the one observed at 04:13. Residual vertical velocity distribution in Figure 5.14 reveals downward flows between 80 and 90 mm/s within the deeply penetrating plumes in the backscatter intensity image (Figure 5.11) which correspond to the convergences.

5.3.2 Velocity Error Estimation

As mentioned before, we can reliably measure vertical velocities only where there are bubbles (Figure 5.11). In the absence of bubbles at low SNR the instrument measures background noise. To estimate the velocity uncertainties, the following scheme is used.

First, a noise threshold for the acoustical intensity is determined so the velocity data, when the backscatter signal is below the threshold, are considered as noise. Examples illustrating threshold estimation, corresponding to the data in Figure 5.11, are given in

Figure 5.15. The analysis of the backscatter intensity distribution (Figure 5.15a) shows two peaks due to "noise" and "signal" separated by an 8-dB gap. This gives a threshold level between 52 and 58 dB. To improve this estimate another sample is constructed using backscatter intensity below 7 m (to avoid the temperature sensor interference). I assume that this new sample is dominated by the noise, although it would still contain some of the deeply penetrating clouds. A threshold is set at two standard deviations above the peak of the distribution in order to include 95% of the noise. This estimate gives values between 55 and 57 dB. Intensity threshold on this range is also consistent with the correlation coefficient of 0.75, computed from complex covariance (3.8) [*Brumley et al.*, 1992].

Second, a velocity noise sample is constructed by applying a binary mask (based on the intensity threshold) to the unfiltered residual velocity and the variance of this sample is computed at each depth. Low-pass filtering acts effectively as an averaging process and reduces the variance. The reduction, however, is smaller compared to a box averaging and is proportional to the filter's pass-band/Nyquist frequency ratio. The raw velocity variance, scaled with the normalized filter bandwidth, gives an *upper bound* velocity uncertainty for the Doppler measurements. For the example discussed above, the values are 31, 19, 18 and 28 mm/s at 4.7, 7.7, 10.7 and 13.7 m depth, respectively. To

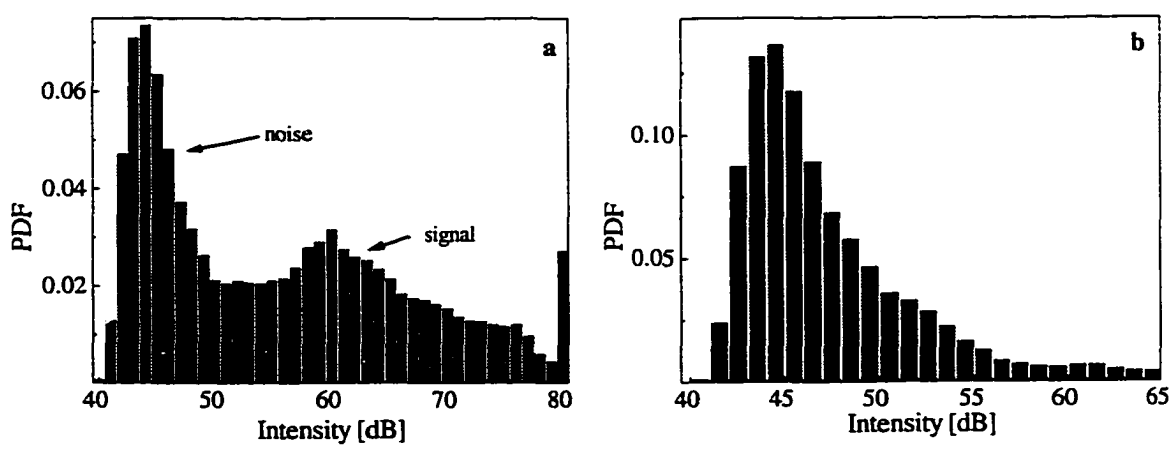

Figure 5.15: Acoustical backscatter noise threshold estimates. a) Total intensity distribution; b) intensity distribution below 7 m dominated by noise.

check if any wave information still remains in the filtered signal, the orbital velocity time series are fed through the filter. The variance of the output signal is significantly below (0.1 mm/s) the uncertainties calculated above. A sensitivity test shows that velocity variance estimates do not change significantly (a few percent) when the threshold changes from 54 to 58 dB.

5.4 Horizontal Velocity Extraction

Similar to the upward-looking sonars, the fixed-orientation side-looking sonars (ALS) provide measurements of the near-surface horizontal velocity component. The raw Doppler velocity is estimated from the backscatter intensity using lag 7 and 25-point averaging (Eq. 3.12) which corresponds to a 3.2-m range resolution.

The dominant velocity signal arises from the resolved orbital component of the surface waves (Figure 5.16) from which the directional wave spectrum is recovered, using

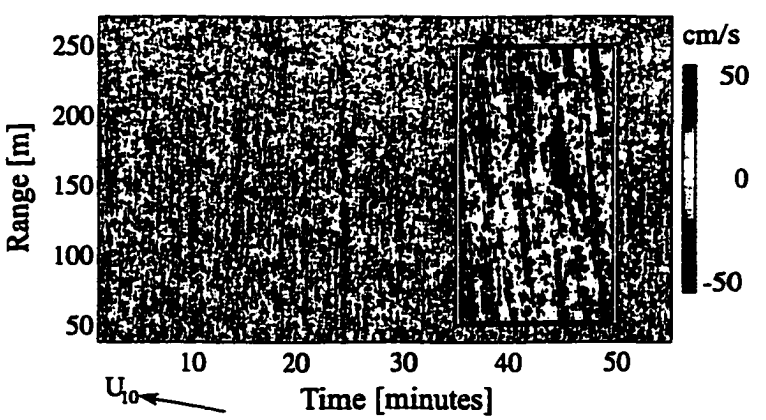

Figure 5.16 Horizontal velocity field observed with the side-looking sonar. Raw velocity is dominated by the wave orbital motion (insert). The close-up covers a 5-min period. Positive velocity is away from the sonar and the arrow marked U_{10} depicts wind direction. The sidescan beam is pointing up.

the maximum likelihood technique and the software developed by Dr. M. Trevorrow, IOS. A more challenging task is to separate the weak and more slowly changing velocity field induced by Langmuir cells from the wave motion.

Time series of the horizontal Doppler velocity, as a function of range, are modified at close ranges by changes in the beam elevation (the slant range effect), which is corrected by interpolation from a slant range r_s to horizontal range $r=\sqrt{r_s^2-d^2}$, where d is the instrument's mean depth. The presence of the spectral gap between the wave and the residual coherent components allows signal separation. A two-dimensional Fourier transform is applied to this corrected time-range velocity field and the resulting signal is expressed in terms of wave number (from the range dependence) and frequency (from the time dependence). Retaining only the portion near the origin (Figure 5.17) and inverting the transform, this then serves as a convenient 2-d spectral filter which isolates the residual low-frequency motions regardless of the mutual orientation of the waves and

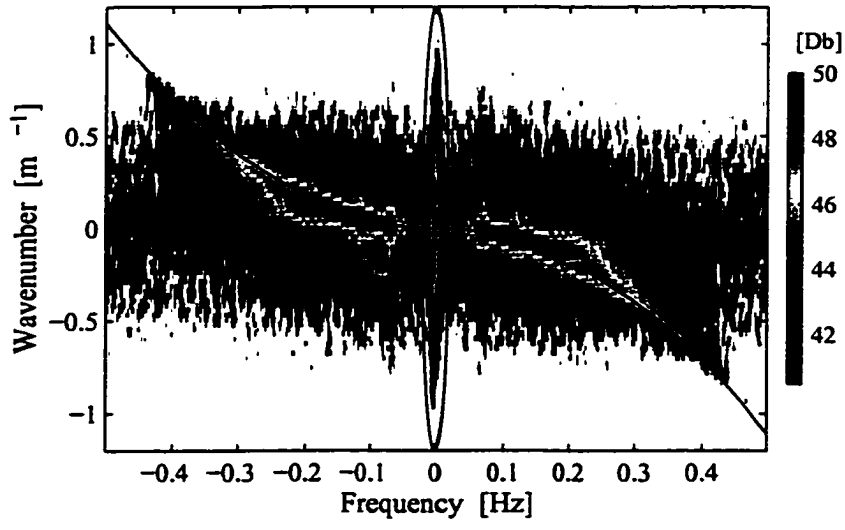

Figure 5.17: Two-dimensional raw velocity spectrum shows both quasi-steady velocities (within the ellipse) and a wave group. The wave energy has been fitted with a directionally resolved dispersion relationship (continuous curve). The ellipse shows the contour of the low-pass Fourier domain filter (5.9) which is applied to the raw velocity spectrum in order to remove the wave signal.

surface structure, namely the presence of surface jets where water is moving downwind. However, occasional patches of slower moving fluid (the flow actually seems to be moving more slowly than the drifting buoy) are thought to be due to more deeply penetrating clouds.

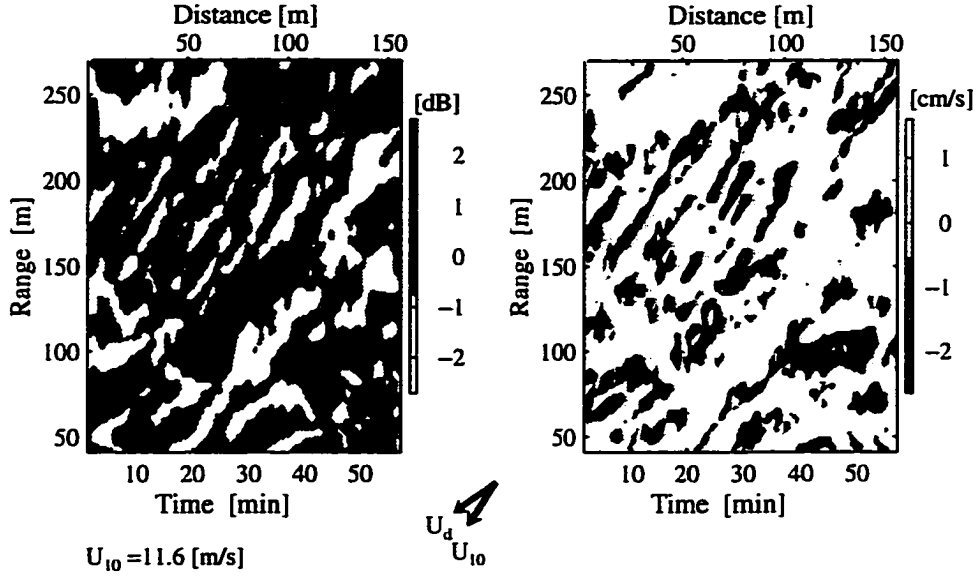

Figure 5.18: Filtered backscatter intensity (left) as a function of range and time when the sonar is pointing in a fixed orientation as the bubble clouds drift by. The arrows (lower center) marked U_d and U_{10} identify the direction of surface drift relative to the instrument and the wind direction, respectively. The sonar heading is upward. Filtered Doppler velocity measurements (right) for the same period, corresponding to the areas of strong bubble scatter. Positive speed is away from the sonar. (Observed at 02:00 PST, January 17, 1995).

6. Response of the Upper Ocean to Wind, Wave and Buoyancy Forcing

6.1 Vertical Velocity in the Convergences

The upward-looking Doppler sonars provide measurements of the vertical structure of bubble clouds well as the vertical velocity of the bubbles. The side-looking sonars measure the two-dimensional horizontal distribution of the near-surface bubble clouds. The residual intensity variations reveal bubble distributions, both vertically as the sonar passes beneath bubble injections (Figure 5.11), and horizontally along the scanning path near the sea surface. The left plate in Figure 5.18 shows the fixed orientation sidescan backscatter variations along a fixed path, where the dark corresponds to higher and the white to lower backscatter. Easily identifiable bands of higher bubble concentrations correspond to the clouds of bubbles collected in Langmuir circulation convergences.

Simultaneous observations of the vertical bubble cloud structure and vertical velocity with an upward-looking sonar at high winds reveal downwelling jets within vertical bubble plumes (Figure 5.11 and Figure 5.14). In addition to imaging bubbles we measure

the temperature signal produced by the heat anomalies collected in the convergences (line in Figure 5.11). The example in this figure shows colder water being brought down within the convergences when there is net surface cooling. We usually observe good correlation between the intensity and the temperature deviations when the magnitude of the surface heat flux exceeds ~100 W/m^2. The data in Figure 5.11 and Figure 5.14 display several dense clouds penetrating down to 7−10 m and on one occasion to more than 16 m, with vertical velocities reaching 90 to 98 mm/s at high winds and sea state (U_{10} up to 15 m/s and $H_{1/3}$ of 3.8 m). This is usually the signature of a well developed circulation. This interpretation is also supported by the imaging sonar data.

We note that bubble concentration not necessarily correlated with the instantaneous vertical velocity $w(t)$. Bubble population at a depth z is a cumulative effect due to the velocity field acting through the water column above that depth over some time. Taking an average downward flow of 50 to 70 mm/s, the time required to bring bubbles down to a depth of 6 to 10 m is of order between 85 and 200 s, which is comparable with the life time of a bubble [*Thorpe*, 1982]. Assuming that the bubble is a Lagrangian particle, its Lagrangian velocity u_L is then

$$w_L = \frac{\partial z}{\partial t}. \tag{6.1}$$

The position of the bubble is found by integrating (6.1)

$$z(t, z_0) = z_0 + \int_0^t w_L(t', z_0)\, dt'. \tag{6.2}$$

At time t, the Eulerian velocity at a point z equals the Lagrangian velocity of the particle at the same time $w(t,z)=w_L(t,z_0)$. Therefore, we might expect bubble concentration N to be better correlated with the time integral of velocity at a particular location

$$N \propto \int_0^t w(t', z)\, dt'. \tag{6.3}$$

Although our observations are limited to the measurements of an instantaneous Eulerian velocity and, therefore, we cannot test relation (6.3), the subsequent analysis does not rely

quantitatively on the bubble concentration-vertical velocity correlation.

Observations taken in different conditions, at more moderate winds, show that the vertical motions are not so strong (60 to 73 mm/s, Figure 6.1), and bubble clouds do not penetrate as deep as in the example in Figure 5.11. An approach to systematize observations of residual vertical velocity is proposed in the next section.

Scaling of the governing equations of Langmuir circulation (see *Leibovich* [1977]) suggests that the circulation can be characterized by one parameter, namely the Langmuir number La, which represents the ratio of viscous damping to inertial forcing (Eq. 2.15). When La is smaller than the critical threshold of 0.67 [*Leibovich and Paolucci*, 1980], mechanical stirring exceeds viscous damping and generation of the circulation is possible. Although the prescription of a depth-independent eddy viscosity is an artificial and generally unfounded assumption, the majority of available theoretical predictions of Langmuir circulation dynamics are based on it. We will therefore employ this parameterization to make comparisons of the observations and model predictions, and discuss possible implications of this assumption. A plume-like structure of the near-surface bubbles indicates that the background turbulence is acting on different time scales

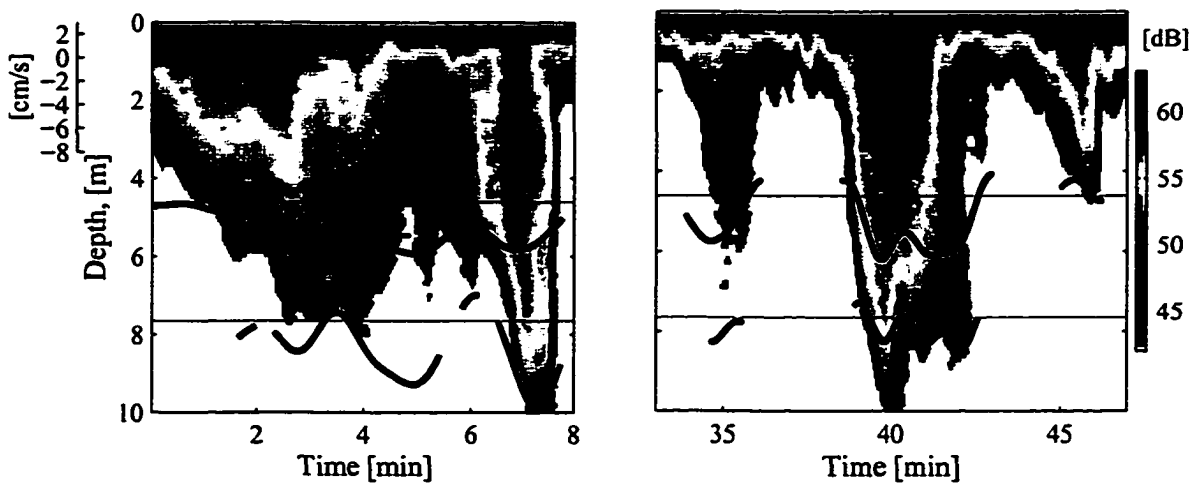

Figure 6.1: Examples of vertical bubble clouds and residual vertical velocity (thick lines) observed with 400-kHz upward looking sonar during the Wecoma I experiment, January 17, 1995. Velocity variance is estimated between 14 and 11 mm/s.

compared to Langmuir circulation and serves as an experimental justification of the spectral gap hypothesis, which is assumed in the CL2 model.

As emphasized before, our Doppler vertical velocity measurements are restricted to areas of high backscatter which occur primarily within the bubble clouds (Figure 5.11). We can reliably detect bubbles to depths of approximately 14 to 16 m, and hence, the question arises whether the measured maximal velocities are biased by the depth limitations of our measurements. Mean cell penetration depth is evaluated from the cell spacing, measured with the side-looking sonars, between 6.5 and 18 m (shown in Figure 6.22), and the cell aspect ratio γ. This ratio between cell depth and cell width has been evaluated from observations previously. *Smith et al.* [1987] found an aspect ratio of 1.5 for quasi-steady conditions, and *Smith* [1992] reported sonar measurements which yield aspect ratios close to 1. Analyzing mixed layer float tracks, *Gemmrich* [1997] estimated γ ranging from 0.8 up to 3.5 with a median value of 1.4. Hence, I use an aspect ratio of 1.4 which, combined with the measured cell spacing, gives a bound on the median cell penetration depth of 16 to 24 m. Numerical studies [*Leibovich and Paolucci*, 1980] show a vertical cell asymmetry with the maximal downwelling velocity occurring at a depth of roughly 30% of the cell penetration. This implies that we are able to resolve maximal downwelling velocities within the convergences.

6.1.1 Parameterization of Turbulent Transfer

We now use observed downwelling velocity data to test the validity of the existing model predictions. *Li and Garrett* [1993] suggested the following parameterization for the maximal downwelling velocity within Langmuir convergences, from which the implied eddy viscosity can be inferred,

$$w_{\max} = \tilde{w}_{\max} u_* \left(\frac{U_s}{2u_* \mathrm{La}} \right)^{1/3} = \tilde{w}_{\max} u_* \sqrt{\frac{U_s h_s}{\nu_e}}, \tag{6.4}$$

where $\tilde{w}$ and w are dimensionless and dimensional downwelling velocities, respectively. *Li and Garrett's* [1993] numerical results give a maximum nondimensional velocity of 0.72. The Stokes drift profile is calculated from the measured directional wave spectrum [*Huang*, 1979] and hence, U_s and h_s are evaluated. The measured frequency spectra are extended using a high-frequency tail as described in the Section 5.2. The arbitrary component of (6.4) is the eddy viscosity ν_e, which is usually taken as a constant within the Craik-Leibovich model framework. It therefore represents a vertically and horizontally averaged property parameterizing the turbulence in a layer. In spite of its limitations, this two-dimensional model provides useful references for comparisons with measurements. Using velocity measurements within the convergences, we infer depth-averaged eddy viscosities from (6.4).

An alternative approach is to compute eddy viscosity from turbulence models. In the classical flow along a solid wall, viscosity increases linearly with depth as $\nu_e = \kappa u_* z$, with von Karman constant $\kappa = 0.4$. Recent measurements of energy dissipation in the surface layer [*Drennan et al.*, 1992; *Agrawal et al.*, 1992; *Anis and Moum*, 1992; *Osborn et al.*, 1992] indicate enhanced turbulence levels close to the surface, attributed to wave breaking [*Drennan et al.*, 1992], which imply larger near-surface viscosity. This is also predicted in a model of the wave-stirred surface layer by *Craig and Banner* [1994] who modified a conventional one-dimensional mixing length type turbulence model. Prescribing a surface flux of the turbulent kinetic energy associated with wave breaking and a surface roughness length, they predict a boundary layer of wave-breaking enhanced turbulence matched to a law-of-the-wall layer beneath.

Based on measurements of the fine-scale temperature structure, obtained with the surface tracking drifter for the same period which is of interest here, *Gemmrich* [1997] linked the diffusivity profile given in the Craig and Banner model to the advective field of Langmuir circulation and evaluated the free model parameters. He found that diffusion in the wave-enhanced surface layer is well represented by their model, with the surface flux

of the turbulent kinetic energy specified by the energy flux from wind into waves [*Gemmrich et al.*, 1994] and a roughness length $z_0 = 0.2$ m, which is consistent with the variability in the observed temperature profiles.

Due to an exponential decay of the Stokes drift with depth, we expect that most of the Craik-Leibovich torque [*Leibovich*, 1983] occurs near the surface over a few *e*-folding depths of the Stokes drift. I use the near-surface diffusivity profile calculated by *Gemmrich* [1997] from the measured vertical temperature distributions and the *Craig and Banner* model, which takes into account enhancement due to waves. Assuming a turbulent Prandtl number Pr=1 [*Gemmrich*, 1997] this gives the turbulent viscosity $\nu(z)$ profile. An effectively averaged viscosity (Craig-Banner-Gemmrich, CBG) is further computed as the mean value within a surface layer of thickness h

$$\nu(h)=\frac{1}{h}\int_0^h \nu(z)dz \ . \tag{6.5}$$

Then, the matching depth h_m is calculated, where the mean values of the turbulent

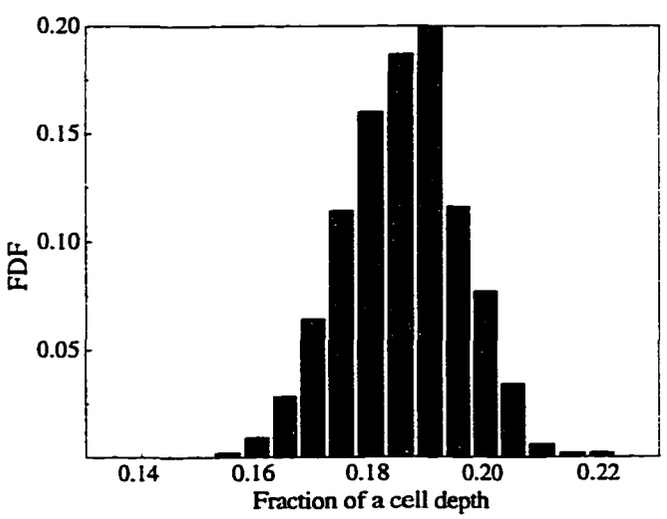

Figure 6.2: Distribution of the normalized matching depth, where a depth-averaged CBG viscosity (6.5) from the Craig-Banner-Gemmrich model and observed temperature variability matches the values inferred from the measured downwelling velocity in the Langmuir circulation convergences. The matching depth values are scaled with the cell penetration depth.

transfer coefficient (6.5), inferred from the temperature measurements, match the effective turbulent viscosities inverted from the velocity measurements in Langmuir convergences (6.4). The distribution of this matched depth, normalized with the Stokes drift *e*-folding depth h_s, gives a mean value of 1.9. The cell depth is obtained from the mean cell spacing, derived from the side-looking sonar measurements (discussed in the Section 6.3.4, Figure 6.22) and an average aspect ratio of 1.4 [*Gemmrich*, 1997]. Comparing h_m with the cell depth, we find that the Craik-Leibovich forcing acts over the top 18% ± 6% of the depth (Figure 6.2), which is slightly less than recent numerical results of ⅓ obtained by *Gnanadesikan* [1996].

Comparison of the temperature-inferred effective viscosities at $H = h_s$, $1.9h_s$ and $3h_s$ with the values inferred from the vertical velocity measurements, is given in Figure 6.3.

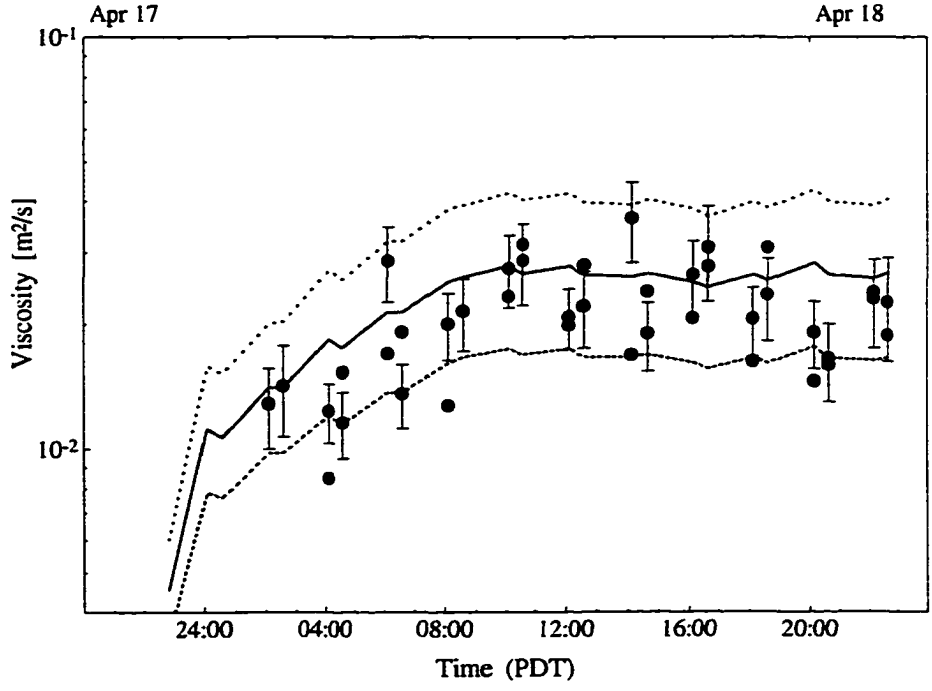

Figure 6.3: Comparison between velocity- (symbols) and temperature-inferred (curves) eddy viscosity estimates. Dashed, solid and dotted lines represent the effective wave-enhanced viscosity calculated at 1 (the lower bound), 1.9(best fit) and 3 (the upper bound) h_s respectively. Error bars are shown for every other point for clarity. Temperature-inferred eddy diffusivity profiles is courtesy of Dr. J. Gemmrich, IOS.

The mean model viscosity at $1.9h_s$ compares favorably with the velocity-inferred values and is used later for stability calculations in Section 6.4. We note in Figure 6.3 that the viscosity above one *e*-folding depth $\nu(h_s)$ is a lower bound and $\nu(3h_s)$ gives an upper bound for the velocity-inferred viscosities; these bounding values are used for a sensitivity study. Given that the scaling (Eq. (6.4)) comes from a two-dimensional model, containing significant simplifications, the agreement between the data in Figure 6.3 is remarkable!

Comparing the relative viscosity increase due to wave enhancement (CBG viscosity of (6.5)) relative to a wall-layer scaling (WL) at different depths, we find that the increase is the greatest (~33%) at a depth equal to h_s, (which is what one would expect). This increase becomes much smaller, 12% and 6% at $2h_s$ and $3h_s$, respectively. Therefore, within approximately 12% accuracy limits, wall-layer scaling can be used to estimate the depth-averaged viscosity for the Wecoma I experiment data when thermal observations were not available.

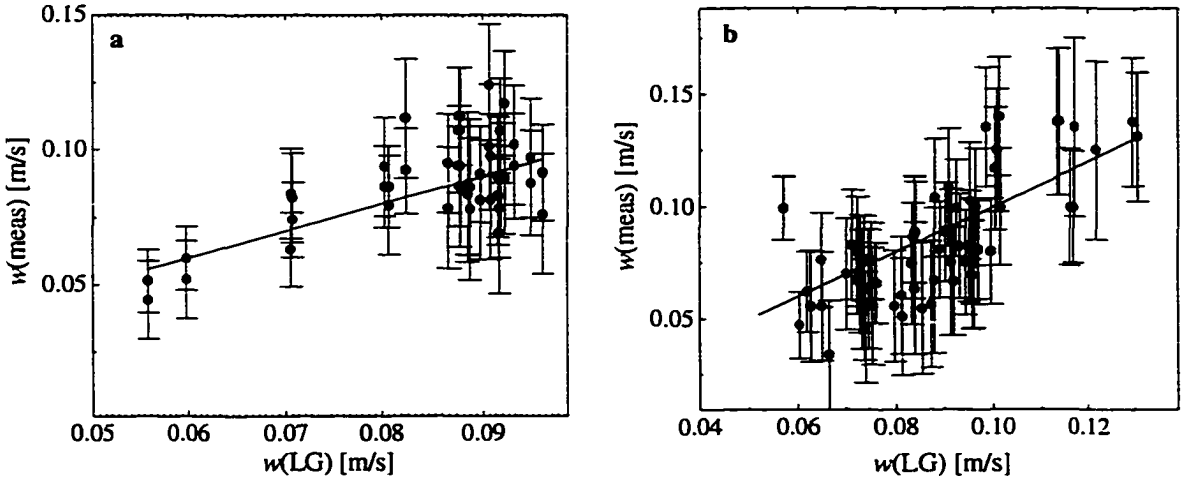

Figure 6.4: Measured maximal downwelling velocity within the convergences versus Li and Garrett [1995] (LG) parameterization for a) the MBL and b) Wecoma I experiments. MBL observations consist of both 200- and 400-kHz sonar data while only 400-kHz sonar data were available during Wecoma I. The error bars are calculated using the velocity error estimation described above.

Combining CBG viscosity values at $2h_s$ for MBL data and WL for Wecoma I datasets with the measured wave field parameters, I compute expected vertical velocity values using (2.17). Comparing *Li and Garrett's* [1995] (LG) parameterization against the observed values, we find that although there is a noticeable scatter in the data, both estimates display a similar tendency. MBL observations are limited to one storm event and consequently provide sparser coverage in the parameter space, compared to Wecoma I data. The correlation coefficient between measured and scaled velocities in (Figure 6.4) is 0.7 for the MBL data and 0.76 for the Wecoma I data.

Using the effective viscosity calculated at different depth using (6.5) and the observed Stokes drift and friction velocity, we estimate the Langmuir number from (2.16). Calculations for the MBL Experiment (Figure 6.5) using the lower (h_s) and the upper ($3h_s$) viscosity bounds give La between 0.015 and 0.1. Similar computations for the Wecoma I data give the lower bound for La from 0.011 to 0.015 and the upper bound between 0.048 and 0.077. Numerical simulations by *Li and Garrett* [1993] give steady

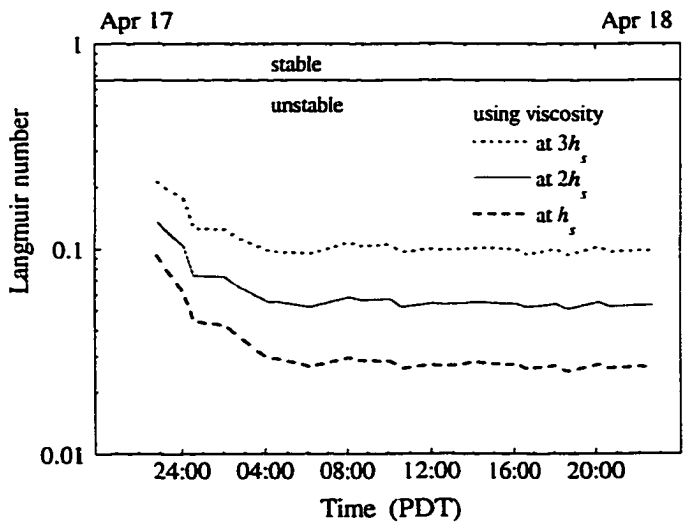

Figure 6.5: Langmuir number estimated during a storm between April 17 and 19, 1995 for different viscosity values. The dashed and the dotted lines correspond to the lower and the upper viscosity bounds, respectively (at h_s and $3h_s$, Figure 6.3). Values below the critical value of 0.67 indicate unstable conditions, favorable for generation of Langmuir circulation [Leibovich and Paolucci, 1981].

state solution for La in the range of 0.01 to 0.1. Simulations using smaller La give rise to cell regeneration (Keir Colbo, UVic, personal communication).

Our lower limit estimate of La between 0.01 and 0.02 falls in the range used by *Li and Garrett* [1995]. However, our "best-fit" estimate gives larger La: between 0.02 and 0.05. This coincides with the well developed, time-evolving cells observed in the sidescan sonar images (discussed in detail in Section 6.3). *Li and Garrett* [1998] pointed out that LES simulations reproduce features broadly similar to those found in two-dimensional direct numerical simulations at a larger value of La (by up to an order of magnitude), suggesting that small eddies resolved in the LES model produce higher levels of turbulence. These can imply that higher viscosity values (larger La) than have been previously assumed in the models may be relevant for Langmuir circulation dynamics in the open ocean. This interpretation is also supported by the recent observations of the enhanced near-surface dissipation rates [*Anis and Moum* 1992; *Agrawal et al.* 1992] and turbulent diffusivity [*Gemmrich*, 1997] due to breaking waves.

McWilliams et al. [1997] suggested that the turbulent Langmuir number $La_{tur} = \sqrt{u_* / U_s}$ determines the nature of the wind-driven surface layer. Their numerical simulations produce quasi-steady cells for La_{tur} = 0.3. That is consistent with our observations of an almost constant cell spacing and penetration (described in Section 6.3).

6.2 Estimation of Scattering Depth

Side-looking sonars have been successfully used for more than a decade for imaging bubble clouds near the ocean surface [*Thorpe and Hall*, 1983; *Smith et al.*, 1987; *Smith*, 1992; *Farmer and Li*, 1995] and surface wave measurements [*Pinkel and Smith*, 1987; *Trevorrow*, 1995]. They also have proved especially useful in the investigation of persistent coherent flows [*Smith et al.*, 1987; *Smith*, 1992; *Farmer et al.*, 1998a]. These

sonars usually have a narrow beam in the azimuthal direction and a fairly wide beam in the vertical. In most applications the sidescan sonars transmit sideways and the time-gating method is used to assign a particular range to each point in the raw backscatter time series. Usually it is assumed that the backscatter signal is dominated by the scatter from the near-surface bubbles while the Bragg-scatter from the surface contributes only occasionally [*Smith*, 1992]. Therefore, a fundamental question must be answered: scatter at what depth dominates the signal measured with a side-looking sonar? To date, this issue has not been addressed.

The upward-looking sonar measurements show that although bubbles created by breaking waves usually produce the signal, which is several dB lower than the surface return (Figure 5.6), there are occasions when shadowing occurs (e.g., at around 04:14, Figure 5.11). The side-looking sonar insonifies a finite nearly-vertical volume (Figure 6.6). The echo signal is then an incoherent sum of the individual target returns, which are distributed over some depth with an unknown depth weighting. During strong winds bubbles form an almost continuous strata, sometimes 2 to 3 m deep, and they penetrate down to 10 to 15 m in the convergent regions (i.e. 04:14 in Figure 5.11).

In the open ocean bubble distributions decay rapidly with depth with an *e*-folding scale of 1 to 1.5 m [*Thorpe*, 1982; *Farmer and Vagle*, 1997], which gives larger near-surface weights in the backscatter intensity signal. However, the orbital velocity field decays with depth over much greater scales: e.g. 20-m waves have an *e*-folding scale of 3 m and 100-m waves have a scale of 16 m, which produces a different velocity weighting. Although we expect the scatter to be dominated by the near-surface contribution, a detailed analysis is necessary to get a quantitative answer.

Here, a method combining the wave height measured with vertical sonar and the wave field measured with a side-looking sonar is proposed. It is based on the coherent nature of the wave orbital motion at different depths. We measure wave height above the instrument $\eta(t, r_0)$ and wave vertical orbital velocity is derived as

$$w_{meas}(r_0,t) = \frac{d\eta(r_0,t)}{dt}. \tag{6.6}$$

Velocity v_{meas} measured with a side-looking sonar is a projection of the wave orbital velocity v_{orb} onto the sonar beam (Figure 6.6b),

$$v_{meas} = v_{orb}\cos\theta. \tag{6.7}$$

where θ is the direction of wave propagation. The wave with a wavenumber $\mathbf{k}$ sampled with a side-looking sonar at a point $\mathbf{r}$ has a different phase compared to the same wave sampled with the vertical sonar at a point $\mathbf{r}_0$ by

$$\Delta\phi = \mathbf{k}\cdot(\mathbf{r}-\mathbf{r}_0) = k(r-r_0)\cos\theta. \tag{6.8}$$

We know θ from directional wave measurements and therefore, can estimate $\Delta\phi$ for each wavenumber for each range bin.

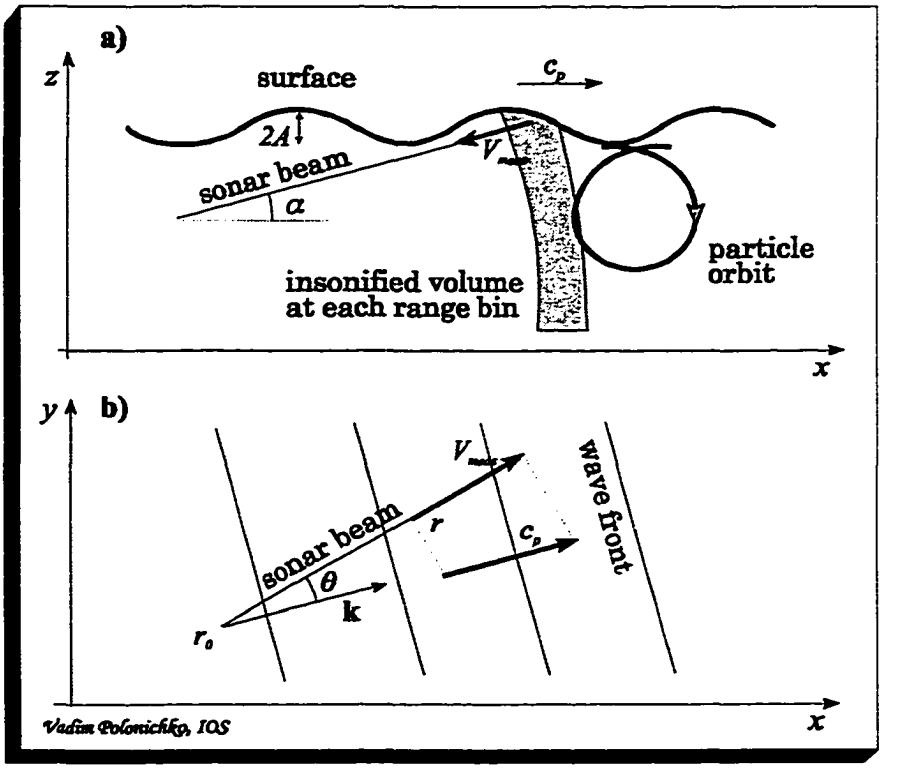

Figure 6.6 Diagram of radial velocity measurements taken with a side-looking sonar. The sonar beam at a particular range insonifies a volume proportional to the pulse length (gray area in a)). Measured velocity is a projection of the water velocity onto the sonar beam direction. a) Side view; b) top view.

The orbital velocity V of a particular wave component at range $\mathbf{r}$ and depth z can be expressed as

$$V(k,z)=V(k,0)\,e^{kz}, \quad V(k,0)=A\omega[\cos(\mathbf{k}\cdot\mathbf{r})+i\sin(\mathbf{k}\cdot\mathbf{r})], \tag{6.9}$$

where ω and k are related via the dispersion relation. The velocity magnitude $|V|$ of a wave spectral component V is thus

$$|V(k,z)|^2=V(k,0)V'(k,0)\,e^{2kz}, \tag{6.10}$$

where the prime denotes a complex conjugate. At the same time velocity magnitude for each wave spectral component can be estimated using a Fourier transform of the orbital velocity time series as

$$V(\omega,r)=\mathcal{F}\{v_{orb}(t,r)\}. \tag{6.11}$$

We now construct a new parameter, the velocity difference δV, describing an absolute difference between measured vertical and horizontal spectral velocity magnitudes

$$\begin{aligned}\delta V(\omega,r,z)&=\left|\left\langle V(\omega,r)V'(\omega,r)-W(\omega,r)W'(\omega,r)e^{2kz}\right\rangle\right|,\\ V(\omega,r)&=\mathcal{F}\left\{\frac{v_{meas}(t,r)}{\cos\theta}\right\}, \quad W(\omega,r)=\mathcal{F}\{w_{meas}(t,r_0)\}e^{i\Delta\varphi},\end{aligned} \tag{6.12}$$

where the angular brackets denote time averaging. This averaging is possible because the particles at different depths, move in phase under the wave action. By calculating the velocity difference (6.12) at different depths we can estimate an effective scattering depth z_s, defined as the depth where the velocity difference is minimal. The averaging time is chosen to be 30 min and the depth range is between 0 and 10 m with a 0.1-m resolution.

The suggested approach has several limitations. Because the transmitted pulse has a finite length (3.2 m), it acts as a spatial filter reducing the velocity signal (Figure 6.6a). This reduction is larger for shorter waves: 16% for 10-m waves, but only 1.5% for 100-m waves. Another possible source of bias can be masking of the wave crests. It occurs when the sonar beam elevation angle (Figure 6.6) is smaller than the wave slope. To minimize the bias due to possible masking of the waves, the sidescan velocity data are

considered at horizontal ranges between 50 and 150 m. For a platform deployed at 30 m depth the beam elevation is then between 0.6 and 0.2, which is larger that the observed wave slope: maximal slope of order 0.1 and a median value of 0.03. Although short waves might be affected by the masking, a 100-m wave would not. Waves of different frequency (different wavelength) propagate at different angles due to directional spreading which results in a smaller resolved velocity component for a given beam, compared with unidirectional waves. The velocity reduction is less for longer waves due to smaller directional spreading and is of order 0.91 (calculated at 0.1 Hz).

Taking into account the above considerations, we compute the estimator (6.12) for waves near the peak of the spectrum (0.11 Hz) using sidescan velocity measurements between 50 and 150 m ranges with 3-m increments. The effective scattering depth, estimated for the MBL Experiment is given in Figure 6.7 along with the significant wave height and bubble cloud penetration depth. The maximal penetration depth is inferred

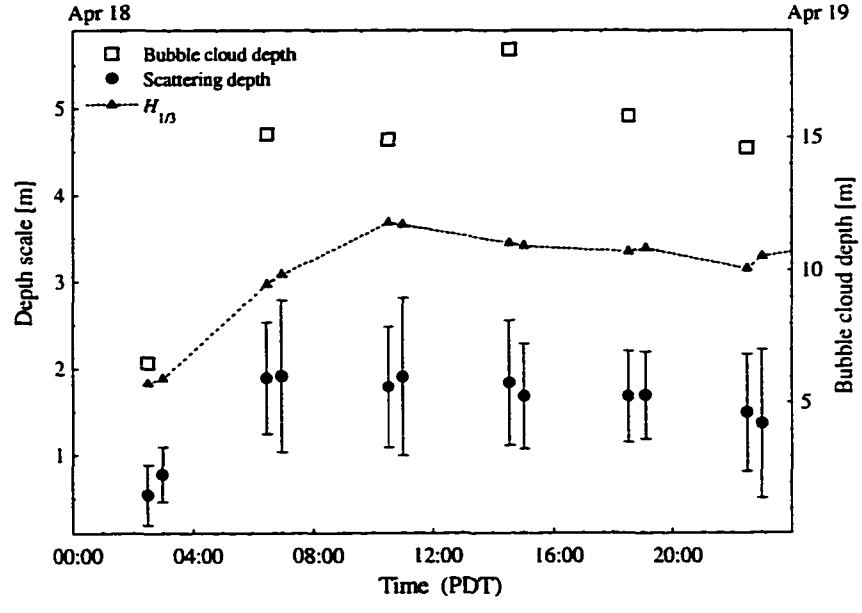

Figure 6.7: Scattering depth (solid circles) estimated from horizontal and vertical Doppler velocity measurements for the MBL Experiment. Triangles mark significant wave height and squares mark bubble penetration depth. Bubble cloud penetration depth is inferred from a 100-kHz upward-looking sonar.

from the upward-looking sonar backscatter using a threshold derived from the backscatter distribution in a way similar to that described in Section 5.3.2. The results in Figure 6.7 show that the scattering depth is between 0.7 and 2 m and is correlated with both significant wave height and the bubble penetration depth. The correlation coefficients between z_s and significant wave height is $C_{zH} = 0.84$ and between z_s and the bubble penetration depth D_b it is $C_{zD} = 0.75$.

The fact that the scattering depth is not equal to zero means that wave velocity measured with a side-looking sonar is reduced. The velocity reduction factor depends not only on the effective scattering depth but also on the wave length e^{kz}. Longer waves are less affected by deeper scatter: the velocity reduction for a 150-m wave is between 2 and 8%, for the data in Figure 6.7. However, contributions to the wave motion due to shorter waves decrease dramatically: 20−45 and 28−70% reduction for 20- and 10-m waves, respectively. The total velocity reduction integrated over a range of wavelengths between 150 and 10 m, assuming the Pierson-Moskowitz spectral shape, is given in Figure 6.8. We see that velocity reduction is almost negligible at the beginning of the deployment,

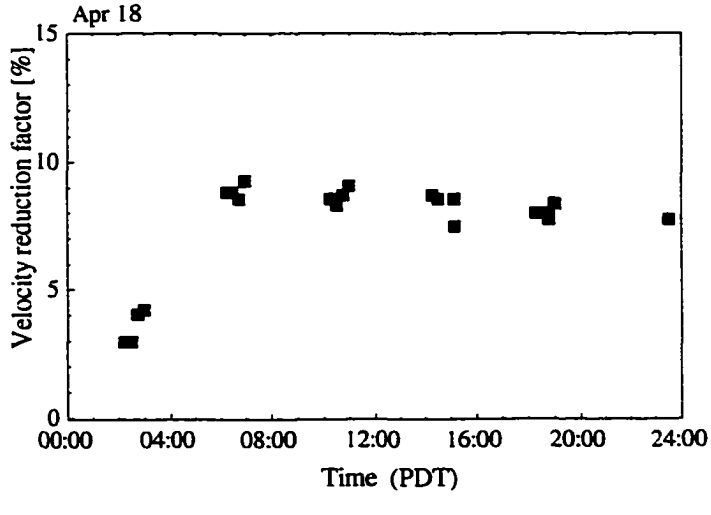

Figure 6.8: Total reduction factor (%) of the wave orbital velocity calculated, taking into account wave decay with depth, using estimates of the scattering depth (Figure 6.7) and Pierson Moskowitz spectral slope.

when bubble clouds are not well developed and it is of order 10% after 04:00.

To summarize, the analysis presented in this section shows that at high wind and wave states the backscatter measured with a side-looking sonar occurs not right at the surface but at 0.7 to 2 m depth. Consequently, the observed velocity due to wave orbital motion is reduced by 3 to 9 % and an appropriate correction is necessary to recover the corrected wave velocity magnitude.

6.3 Observed Surface Structure of Langmuir Circulation

The analysis presented in Chapter 4 along with the work by *Gnanadesikan and Weller* [1995] provides a theoretical framework for studying the generation of Langmuir circulation when wind and waves are not aligned. In spite of existing model studies, there are hardly any field measurements for comparison. *Farmer and Li* [1995] analyzed a limited set of Langmuir circulation surface pattern observations and reported that on one occasion the dominant cell direction was 17° off the wind direction, which might be due to wind-wave misalignment. In this section, I shall present the analysis, where, for the first time, observations of the two-dimensional surface structure of Langmuir cells and directional wave measurements, obtained in the open ocean, are combined in order to make comparisons with a model which takes into account wind-wave misalignment.

The data discussed here were collected during the Wecoma I experiment (January 15 and 19, 1995) and the MBL Experiment (April 18, 1995). Acoustical observations included images of the vertical and horizontal bubble cloud structure and measurements of the directional wave field. During the MBL Experiment and for most of the Wecoma I experiment, the imaging sonars were recording for one hour every other hour, alternating between the two horizontal scanning modes.

In the sweeping mode each of the four sidescans rotates in 1.8° increments (a total of 50) such that the whole 360° disk is sampled in 30 s. The data from different sonars (mapping four different quadrants) are then joined together, while making corrections for the rotation of the platform, producing *B*-scan (azimuth versus range) images [*Ulaby et al.* 1981]. Typically, the raw acoustical backscatter intensity varies by three orders of magnitude over the range of interest. Hence, to enhance the signature of the bubble clouds in the image, the effects of attenuation and spherical spreading are removed so that the processed signal then represents deviations from the mean level (Figure 6.9). A correction is further made to compensate for the geometrical distortion at close ranges when converting from a slant range to surface range [*Trevorrow*, 1995]. A DC offset (if any) is then removed and the data from each transmission is normalized with the signal variance in the image. Next, the *B*-scan data are converted into Cartesian coordinates using a bilinear interpolation in the x-y plane. The residual intensity variations reveal two-dimensional near-surface bubble distributions (Figure 6.9).

Provided that the overall surface pattern does not change significantly over the 30-s period [*Farmer and Li*, 1995], one can think of the sweeping sidescan image as an instantaneous acoustical "snapshot" of the ocean surface. Successive images of this kind provide information on Langmuir circulation spatial and temporal variability. Another consideration for the study of the time evolving patterns of the surface convergences is that the structures are not advected beyond the sampled area between successive "sweeps". The deployment scheme we use allows the imaging sonar platform to drift almost freely with the surface layer, thus significantly reducing the effects of advection. An average instrument drift, relative to the surface, is estimated to be between 40 and 80 mm/s which makes advection effects negligible.

A typical backscatter intensity image acquired at high wind speed and waves (significant wave height of more that 3.5 m) reveals a rich and complex surface structure (Figure 6.9). The scan was taken approximately 17 h after the onset of the storm. We

note large dominant horizontal scales: the thickness of the individual streaks, the length and the spacing. However, not all of the features are aligned with the wind and Y-junctions are easily identifiable. These features were first analyzed by *Farmer and Li* [1995] who suggested that, at higher wind speeds, the dominant characteristics of the surface convergences is the formation of Y-junctions, in which two linear bands of bubbles are joined together.

Although the bubble clouds can be coherent over at least some hundreds of metres, they also display considerable variability: there is an observable difference in the surface structure when looking in along- and cross-wind directions (Figure 6.9). When the sonar points cross-wind it is sampling the side of the Langmuir convergence; along-cell fluctuations of the bubble density are much smaller compared to the cross-cell variability.

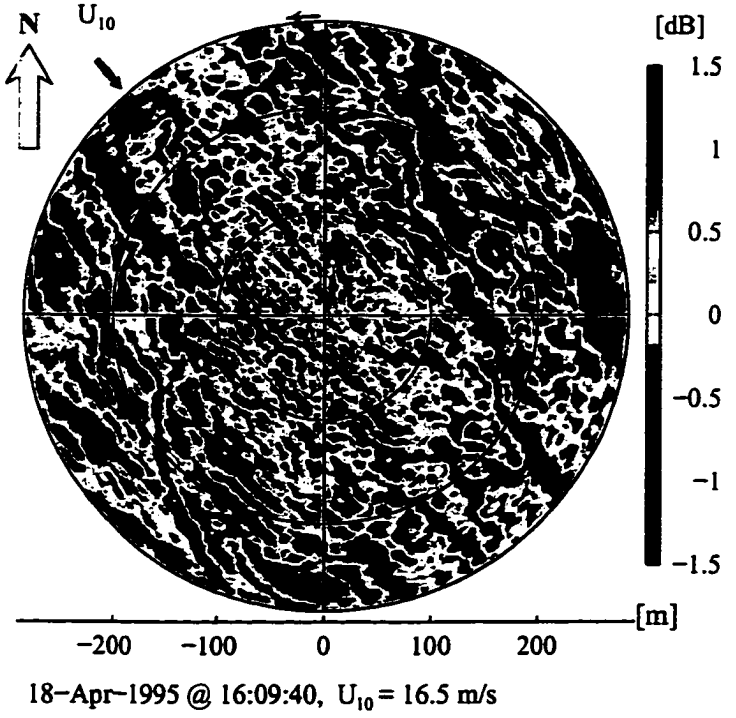

Figure 6.9: Scanning sonar image showing near-surface backscatter patterns in the middle of a storm on April 18, 1995. An arrow marked U_{10} depicts the local wind direction and the wind speed is 16.2 m/s. Range rings are drawn at 100 m apart. High backscatter regions (red color) are bubble clouds organized by Langmuir circulation.

When the sonar beam is pointing upwind or downwind, the elongated structures are not always observed due to irregularity in bubble penetration depth in the cross-wind direction. Particularly deep and dense bubble clouds can also cast shadows, which appear as swaths of dark blue in the image.

The side-looking sonars produce images, like the one presented in Figure 6.9, every 30 s, which result in a fairly large quantity of data. By putting the consecutive images from each hour into a movie, we can get a visual picture of the time evolution of the surface structure of the convergences.

6.3.1 Radon Transform Analysis of the Surface Backscatter Structure

To acquire a quantitative measure of the circulation response to the wind and wave forcing, we employ the Radon transform to analyze near-surface backscatter intensity distributions and to calculate preferential direction, directional spreading and the time evolution of Langmuir circulation dominant scales. The Radon transform, often used as a basis of computer tomography, is a projection of the two-dimensional measured intensity $I(x,y)$ onto a particular direction θ and is defined as [*Lim*, 1990]

$$p(\theta,r)=\int I(x,y)\Big|_{x=r\cos\theta-u\sin\theta,\ y=r\sin\theta+u\cos\theta}\,du\,. \tag{6.13}$$

According to the projection-slice theorem, the Fourier transform of the Radon transform $\mathcal{P}(\theta,k)$ is related to the Fourier transform of the original signal via

$$\mathcal{P}(\theta,k)=A(k_1,k_2)\Big|_{k_1=k\cos\theta,\ k_2=k\sin\theta}=A(k\cos\theta,k\sin\theta)\,, \tag{6.14}$$

where $A(k_1,k_2)$ is the two-dimensional Fourier transform of the original backscatter intensity $I(x,y)$ interpolated onto a new coordinate grid defined by (k_1, k_2). The formulation (6.14) significantly simplifies computations which are basically reduced to interpolating the Fourier transform of the original intensity image in the Fourier space.

The complete Radon transform $p(\theta,r)$ is a two-dimensional matrix (angle versus range) containing information about the directionality in the data at various ranges. It will be used later in this section to estimate the dominant spacing of Langmuir cells. To estimate a mean sense of direction (or spatial coherence) in the image we compute an average directional intensity factor $\bar{p}(\theta)$, which is a measure of the directional energy distribution in the original backscatter image. First the two-dimensional intensity image $I(x,y)$ is transformed into wavenumber space and the interpolation (6.15) is applied. The resulting matrix $\mathcal{P}(\theta, k)$ containing directional information at different wave numbers is then averaged over all wave numbers and normalized as

$$p(\theta)=\frac{1}{N}\sum_{n=1}^{N}\mathcal{P}(\theta,k_n), \quad \bar{p}(\theta)=\frac{p(\theta)}{\sigma_p}, \tag{6.16}$$

where σ_p^2 is the variance of $p(\theta)$ and N in the number of the wavenumber bins. Since bubbles, organized into streaks by Langmuir cells, are the primary source of the backscatter, the normalized directional intensity factor $\bar{p}(\theta)$ provides a measure of the preferential cell direction for each image.

This technique was applied to analyze a series of images from the Wecoma I and the MBL experiments. A representative image of the surface bubble cloud structure during a period of steady, moderate winds on January 15 (Wecoma I experiment) is given in Figure 6.10. We observe cells, aligned preferentially in the wind direction, although there is a considerable variability in the along-wind direction. A signal degradation at close ranges, within 50 m from the instrument, is caused by the sonar directional beam pattern.

A summary of the directional analysis for a deployment on January 15 is presented in Figure 6.11. Here, $\bar{p}(\theta)$ is shown as a color bitmap with red and blue corresponding to the high and low values, respectively. A hollow line in the center marks local wind direction and the wind speed is shown in the lower part of Figure 6.11. Each rectangular section in Figure 6.11 corresponds approximately to a 2-h period. No simultaneous directional wave data are available. High directional intensity (yellow-red areas around

the wind direction) corresponds to closely aligned bubble streaks and is interpreted as a measure of the preferential cell direction. The instantaneous magnitude of the directional intensity depends not only on the cell alignment but also on other factors, like the area covered by the bubbles and their concentration, and it displays significant variability throughout the record. From the distribution of $\bar{p}(\theta)$ for the whole deployment we find that $\bar{p}(\theta)$ larger than 1 corresponds to significant cell alignment.

We see high levels of directional intensity centered at the wind direction (within a 15° sector) during the first 2-h period (Figure 6.11, top) when both wind speed and direction held steady. This is consistent with the bubble streaks aligned in the wind direction (Figure 6.10). However, the alignment is not always perfect: the cell direction deviates from the wind shortly after 15:00 and just before 16:00. We also notice periodical intensity variations with approximately 25-min period occurring throughout the record. Similar intensity "vacillations" with a period of 30 min have been recently reported by

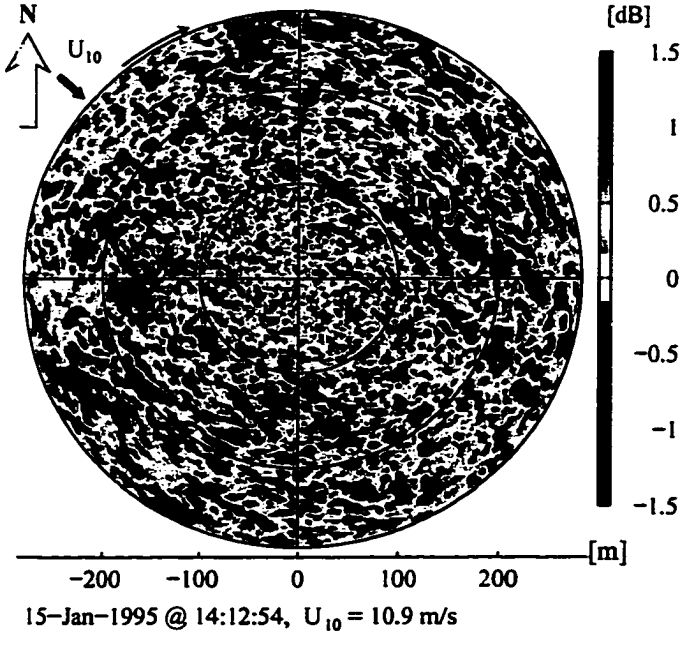

Figure 6.10: Near-surface backscatter distribution during January15, 1995, Wecoma I experiment. Note significantly smaller horizontal scales and less coherent patterns compared to the data in Figure 6.9, collected at higher wind and wave states.

Smith [1998]. Although the source of these variations is not yet established (they seem to be uncorrelated with the variability in the forcing or the mixed layer depth) one possible mechanism could be variability in the supply of the bubbles, which depends on the wave breaking. Fresh bubble injections in the vicinity of the convergences will be more likely dragged to depths by the converging currents and produce stronger backscatter signal. *Smith* [1998] reported that the velocity field (which is not a function of bubble concentration), observed simultaneously, did not reveal "vacillations" which supports the "bubble supply" explanation of the intensity variations.

We observe cells adjusting to the changes in the wind direction within approximately 20 to 25 min at around 16:30 and within 15 min just before 20:00. A brief disappearance of the cells after 17:20 is apparently due to the wind speed dropping below 8 m/s, although they reappeared rather quickly (within 10 min) after the wind picked up again.

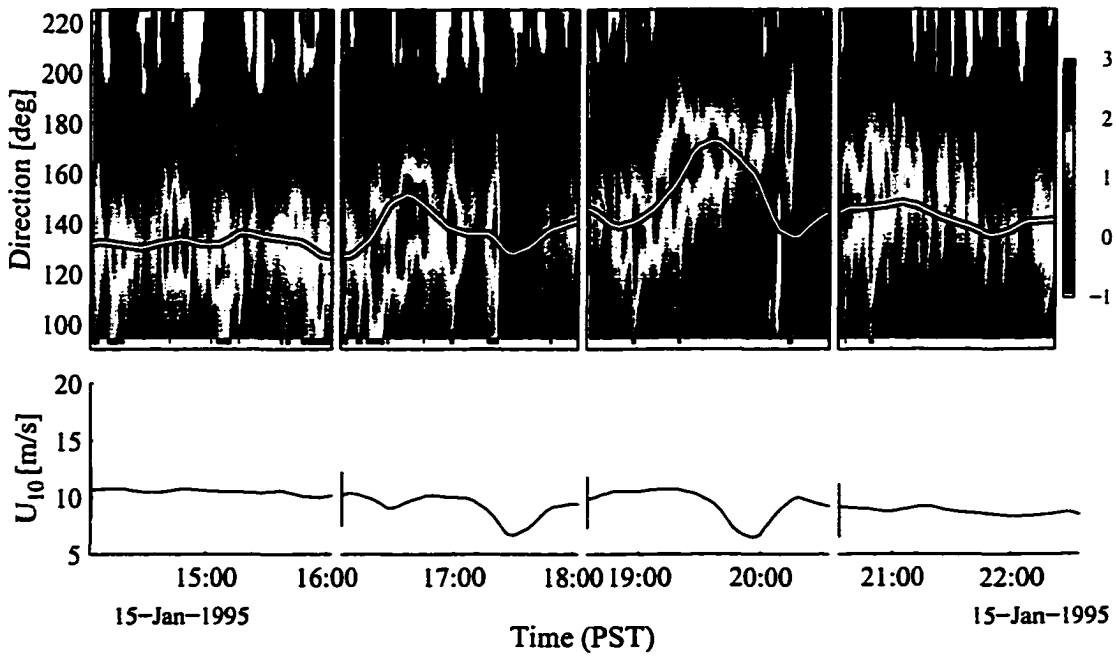

Figure 6.11: Normalized directional intensity factor, local wind direction (top) and the corresponding wind speed (bottom) for the deployment on January 15, 1995. Wecoma I displays cells adjusting to the changes in the wind direction within approximately 15-25 min. No simultaneous directional wave data are available. The wind direction is in the direction of the air flow.

Again, shortly after 20:00 cells disappear and reappear following wind speed decrease and increase. A peculiar elongated feature observed at 20:15 corresponds to patches of backscatter, apparently owing to breaking waves. Finally, between 20:30 and 22:30 the cells are seen following the direction of the slowly changing winds.

To summarize, the time evolution of the averaged directional intensity index presented in Figure 6.11 suggests that the orientation of Langmuir cells is a strong function of the wind direction and the adjustment time for the circulation is of order 20 min. It also suggests that when the wind speed drops below 8 m/s, even for a short period, the cell surface pattern becomes less organized. Unfortunately no simultaneous directional wave measurements were available for that period to draw comparisons with model predictions described in Chapter 4. To address this issue the data from January 19 and April 18, 1995 are used, when the sidescans were alternating between sweeping and fixed modes.

6.3.2 Directional Wave Field

Directional wave energy distributions (log), obtained with the fixed side-looking sonars, averaged over 32 min are presented in Figure 6.12 for the deployment on April 18, 1995. Because of the instrument recording schedule, we do not have wave measurements simultaneously with the backscatter observations, but rather 2 h before and later. The plot in Figure 6.12a corresponds to a developing wave field shortly after the beginning of the storm while Figure 6.12b displays moderately developed seas in the middle of the storm. The spectrum in Figure 6.12a shows "old" waves propagating towards 120° and "new" waves developing in the 130−160° sector. The local wind has changed direction shortly before midnight on April 18 (Figure 5.4) and the Stokes drift, which is an integral over the whole spectrum, is strongly affected by the "old" wave contribution and is 12° to the left of the local wind direction. The spectrum in Figure

6.12b, taken 8 h later, shows a moderately developed wave field with the dominant waves propagating mainly towards 150° and having a spread of about 40°. The wave field has now adjusted to the wind shift and surface Stokes drift is aligned with the wind.

The directional dependence of the surface Stokes drift is shown in Figure 6.13 for the period between 02:30 and 22:30 (PDT) on April 18, 1997. Initially (at 02:30 and 06:30) the peak of the Stokes drift is to the left of the wind direction (curves marked with squares and circles) with a smaller peak developing at about 30° to the right at 06:30. Later (10:30 to 18:30) this new peak dominates, although there is a significant current in the wind direction (Figure 6.13).

Two examples of the wave field for the Wecoma I experiment are given in Figure 6.14. Originally, the waves and the Stokes drift are in alignment (left plot) although the wave field directional spread is significant, possibly due to veering winds prior to that. Later, at 13:00, the wind shifts about 40° to the left from it's previous direction and the

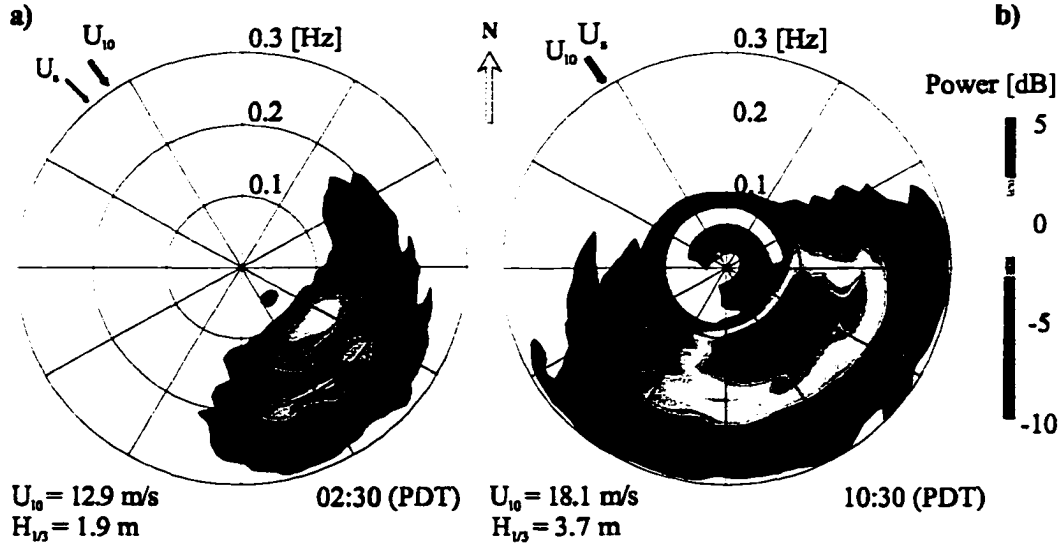

Figure 6.12: Directional wave spectra for the April 18, 1995, MBL Experiment shown for a) developing wave field at 02:30 and b) moderately developed waves at 10:30. Note the significant difference in the power (color scales) between the spectra. Wind speed (U_{10}) and significant wave height ($H_{1/3}$) are given as well. Small arrows marked U_{10} and U_s depict the wind and the surface Stokes drift directions, respectively.

Stokes drift remains in the "old" direction (right plot). Thus there is a noticeable wind-wave misalignment; the implications are discussed below.

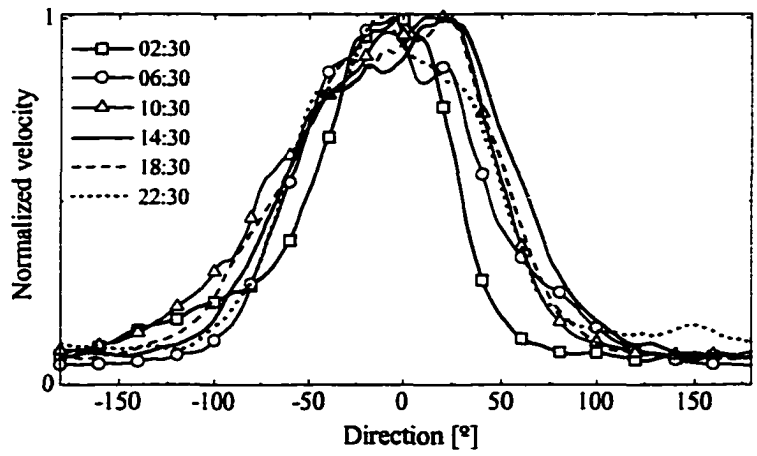

Figure 6.13: Directional dependence of the surface Stokes drift on April 18, 1995. The Stokes drift is calculated from the directional wave field, and is normalized with the maximal value. Direction is given relative to the wind direction with positive angles corresponding to the waves propagating to the right of the wind direction.

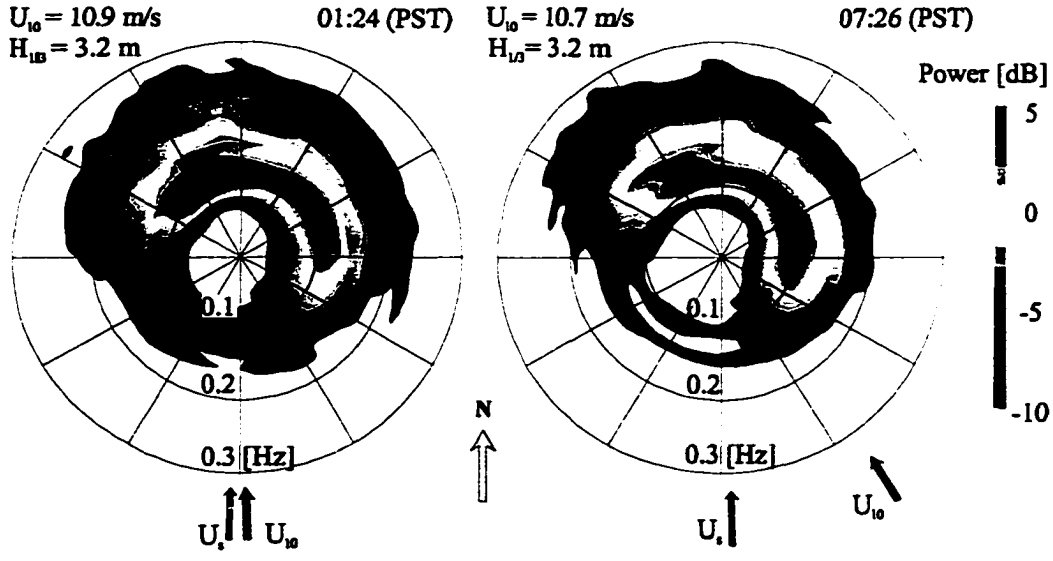

Figure 6.14: Directional wave spectra on January 19, 1995 for the Wecoma I experiment. Left and right plots show the wave field prior to and after the wind direction change, respectively. The averaged wind speed is 10.9 and 10.7 m/s and significant wave height is 3.4 and 3.2 m, respectively.

6.3.3 Comparisons with Model Predictions

Model predictions for the preferential cell direction when wind and waves are not aligned are made in terms of the misalignment angle between wind and waves and a pair of the dimensionless parameters, the shear ratio Sr and the velocity ratio Su, defined by (4.18) and (4.20). Assuming a linear mean shear profile and an exponential Stokes drift profile, the two dimensionless numbers and the Langmuir number are related via (4.21). Utilizing directional wave measurements, we can estimate wave forcing parameters for the Craik-Leibovich model, i.e. the surface magnitude and direction of the Stokes drift (Eq. 2.14). Using maximum downwelling velocity parameterization described in Section 6.1, the eddy viscosity is inferred from (6.4) and Sr is subsequently evaluated. Together with Su, this gives the necessary dimensionless parameters for calculating the preferential cell direction using the linear stability approach described in Chapter 4.

The shear ratio, calculated using viscosity at $2h_s$, and the velocity ratio are shown in Figure 6.15 for the deployment on April 18, 1995. Both Sr and Su rapidly increase during the first 3 h from approximately 1 to 4 (Sr) and 1 to 3.5 (Su) (Figure 6.15) and remain at these levels after 03:00, April 18, 1995. Corresponding La, evaluated at 2 h_s, is initially of order 0.15 and decreases later to 0.05 (Figure 6.5).

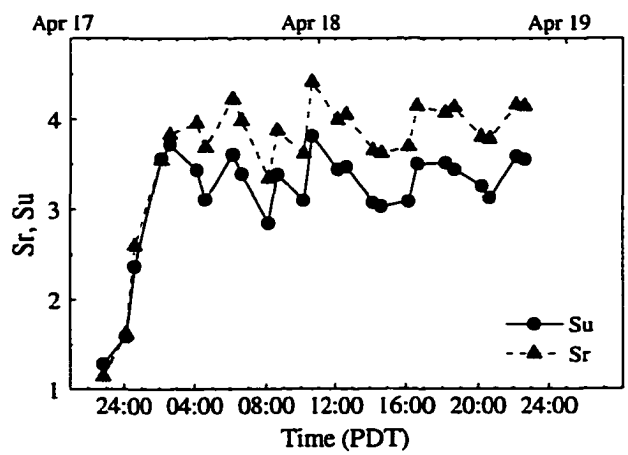

Figure 6.15: Shear ratio Sr and Stokes drift/friction velocity ratio Su during the storm on April 18, 1995, MBL Experiment. Initial rapid increase is followed by a period of an almost constant level. The shear ratio is calculated using viscosity at $2h_s$ (Section 6.1).

Directional intensity analysis was applied to the series of images from the MBL Experiment on April 18, 1995 and from the Wecoma I experiment on January 19, 1995 when a noticeable wind-wave misalignment was observed. Summary plots for both deployments are given in Figure 6.16 and Figure 6.18. The color bitmaps show $\overline{p}(\theta)$, thick hollow lines show local wind direction and the corresponding wind speed is shown in the lower plots. The three thin green lines in each figure mark the theoretically predicted direction of the maximal (center line) growth rate of the Langmuir cell and it's half level (two bounding lines). Black lines mark Stokes drift direction. Wind direction is given in the direction of the air flow (i.e. 120° means wind blowing towards 120°). Each framed part in the top plot in Figure 6.16 corresponds to approximately 1-h periods separated by 4 h. The maximal growth rate is computed using hourly averaged values of

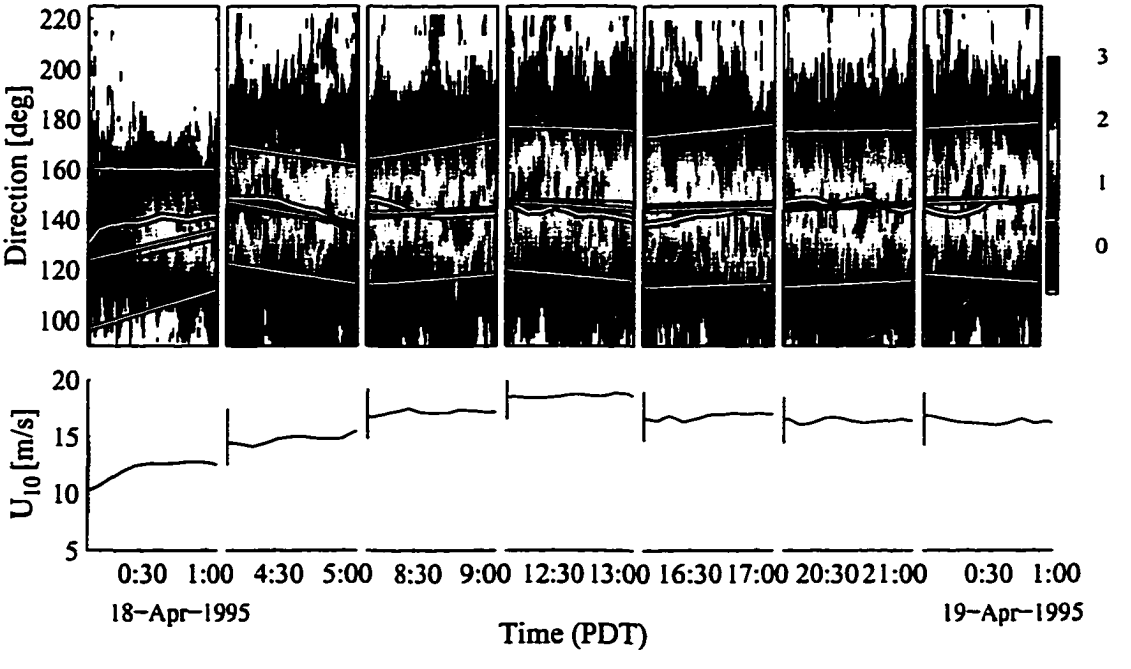

Figure 6.16: Normalized directional intensity (top plot) for the MBL deployment on April 18, 1995 and the corresponding wind speed (bottom plot). Thick hollow line shows local wind direction and the three thin green lines mark the maximal (center line) and a half level of the maximal growth rate (two bounding lines) and black lines mark the Stokes drift direction. The maximal growth rate is calculated using Sr = 4, Su = 3.5 and Ek = 0.01.

Sr and Su and directional surface Stokes drift. The results for each direction are combined using linear superposition so that each wave directional component is accounted for.

Analyzing the time evolution of the directional intensity for the MBL Experiment (Figure 6.16, first subset), we see that $\overline{p}(\theta)$ is very small at the beginning but increases rapidly after 00:30 while being centered to the left of the wind direction. This corresponds to the transition from an almost randomly distributed bubble field to the coherent structures which mark the onset of Langmuir circulation following an increase in wind speed. This conclusion is also supported by other measurements described below. The next subsets show $\overline{p}(\theta)$ centered at approximately the wind direction, although deviations occur with a 30° to 40° spread. The winds for that part exceed 16 m/s and are almost steady. Comparison of the observed cell direction with the maximal growth rate with the calculations shows a generally good agreement. The inclusion of the Ekman spiral does not affect the preferential direction for this range of dimensionless parameters.

As mentioned above, deviations of the observed cell direction ($\overline{p}(\theta)$) relative to the maximal growth rate occur during the record in Figure 6.16. A close analysis of the surface backscatter images provides additional insight on the evolution of Langmuir circulation surface structure during this period. We focus on one such event between 12:00 and 12:35, when the peak of the directional intensity factor gradually shifts 20° to the right from the predicted direction of the maximal growth rate. Sweeping images, corresponding to this period are shown in Figure 6.17A−D. Between 12:08 and 12:27 we observe larger-scale features oriented slightly to the right from the local wind direction (Figure 6.17A,B). Several Y-junctions contribute to the directional variations of the intensity. A prominent Y-junction is formed in the upper right quadrant and can be traced for 13 min between 12:08 and 12:21 (Figure 6.17A−C). Smaller structures of this kind, however, are less persistent and can be traced only for short periods. After 12:27 the smaller surface structures prevail and the cells become more aligned with wind and waves

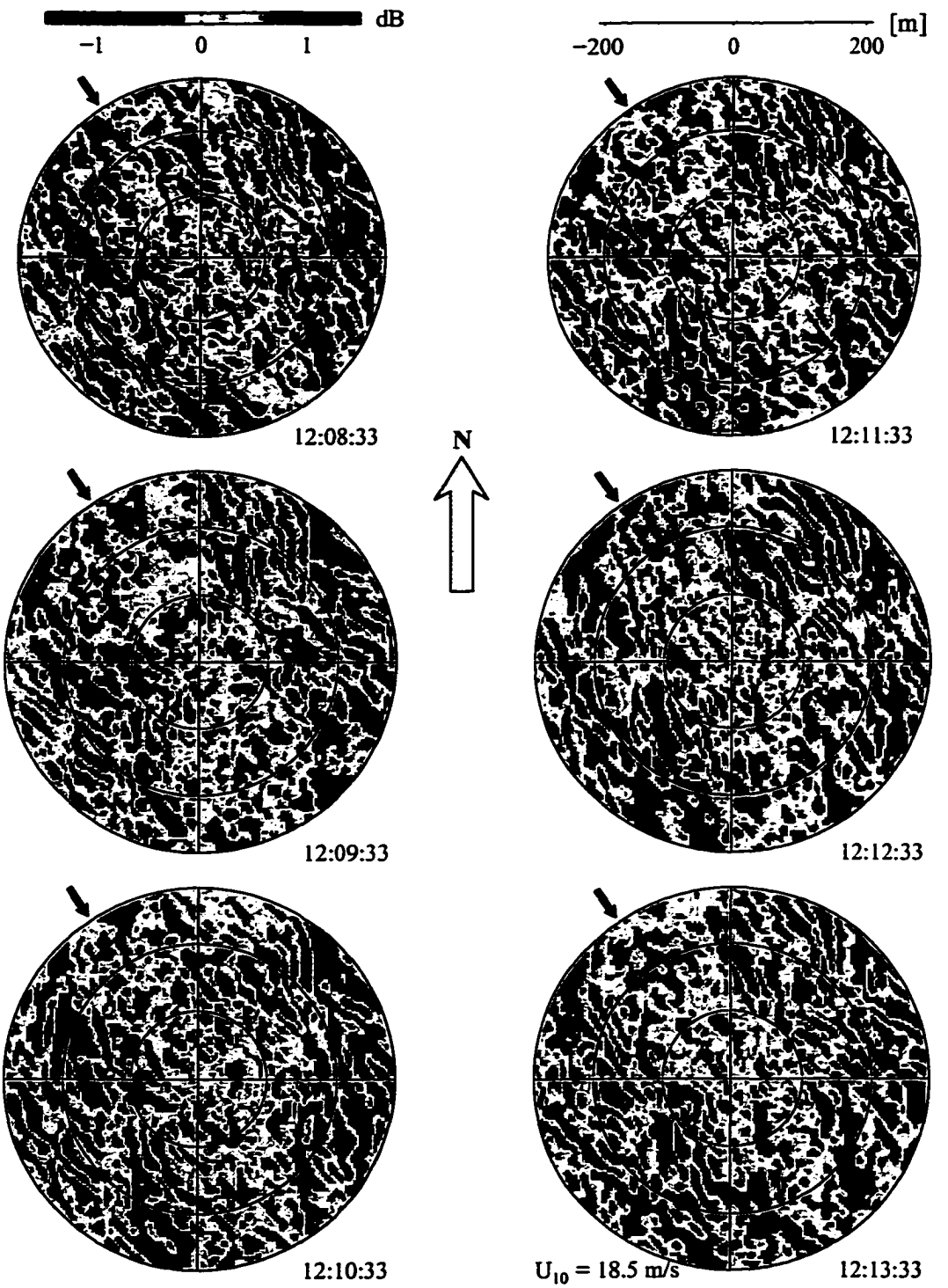

Figure 6.17A: Succession of sweeping images corresponding to a period during a storm between 12:08 and 12:31 on 18 April 1997. Every second image is shown. Blue unmarked arrow depicts the wind direction.

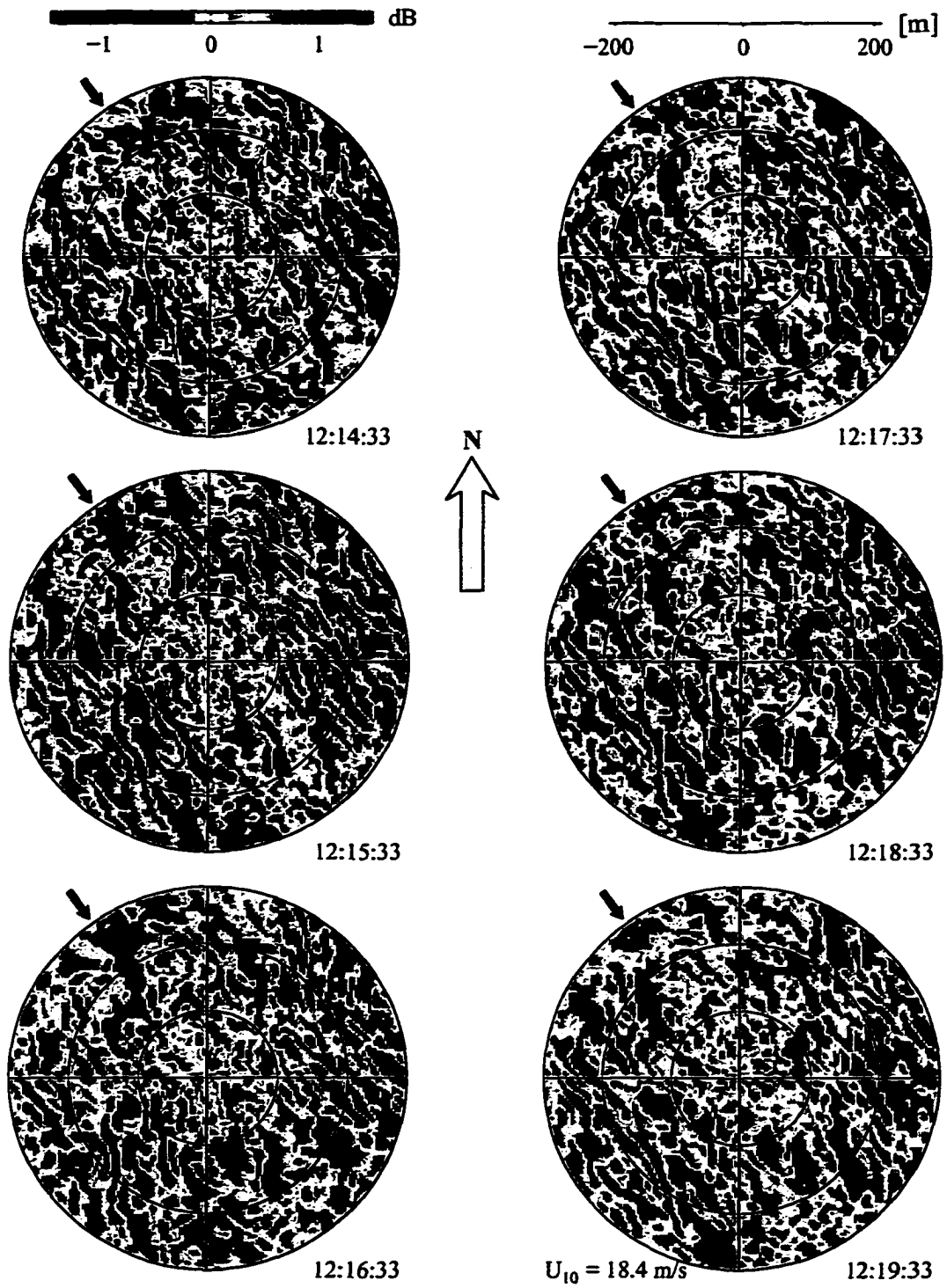
dB
−1
0
1
[m]
−200
0
200
12:14:33
12:17:33
N
12:15:33
12:18:33
12:16:33
U_{10} = 18.4 m/s
12:19:33

Figure 6.17B.

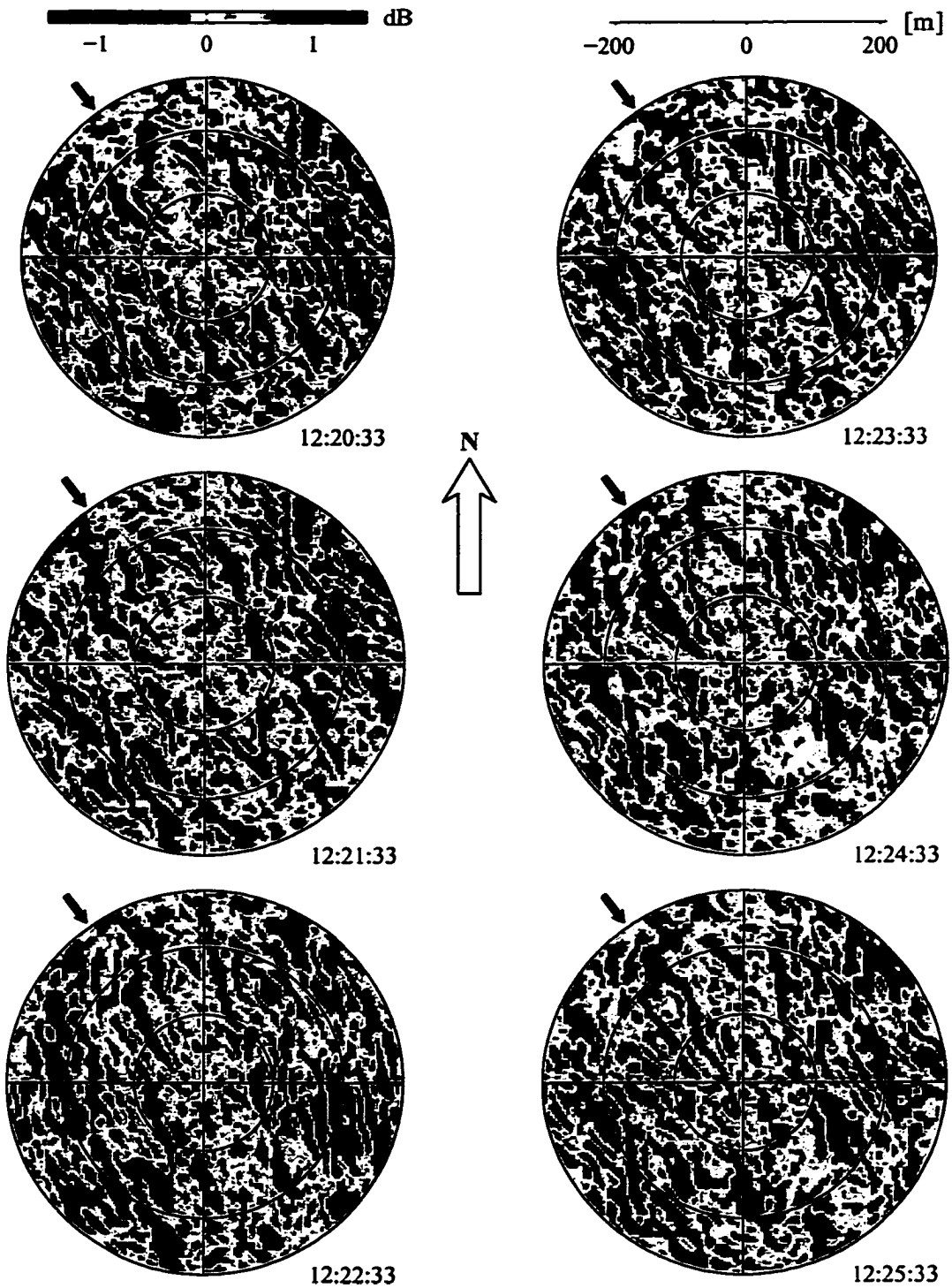
dB
−1
0
1
[m]
−200
0
200
12:20:33
12:23:33
N
12:21:33
12:24:33
12:22:33
12:25:33

Figure 6.17C.

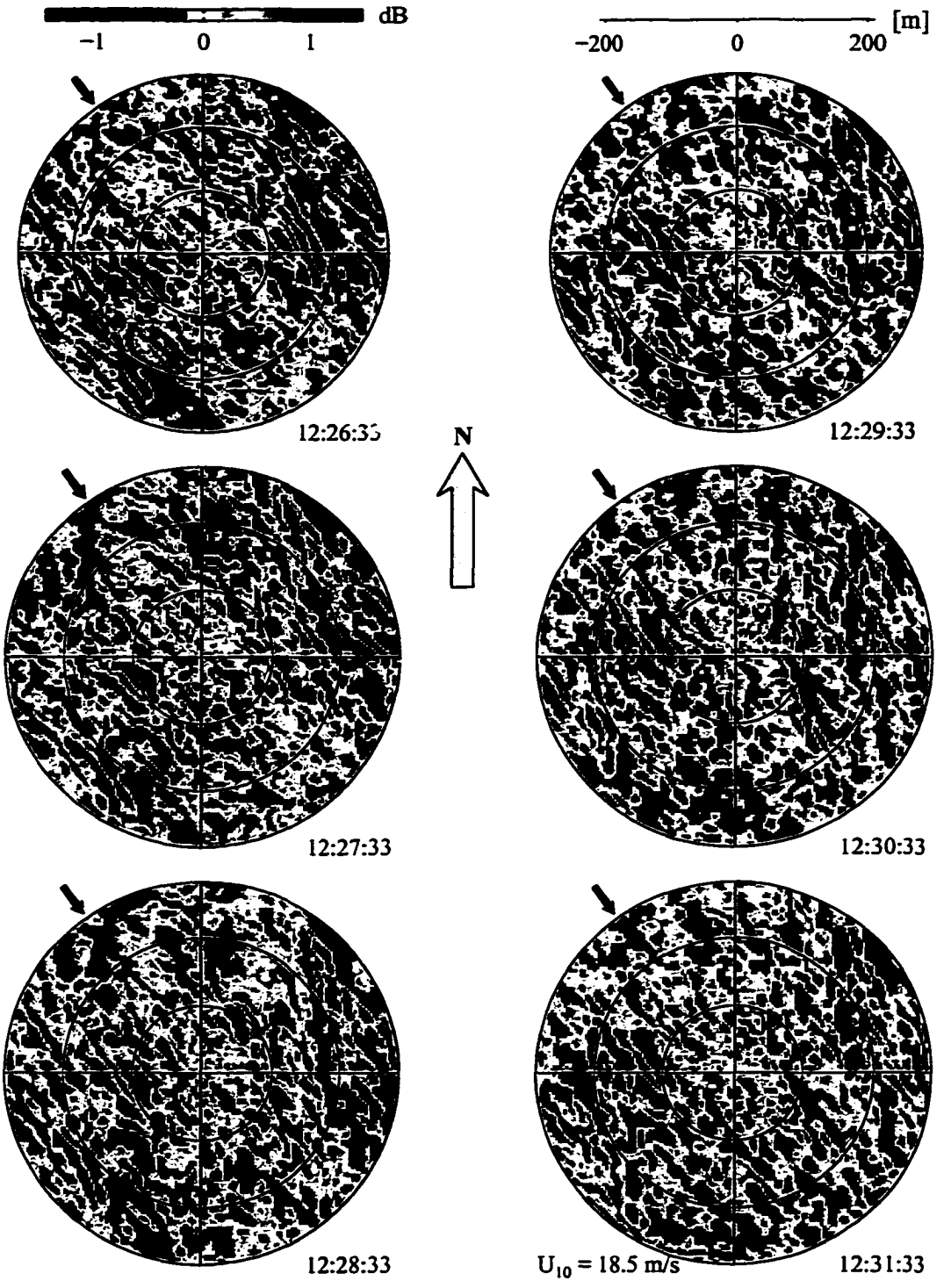
dB
−1
0
1
[m]
−200
0
200
12:26:33
12:29:33
N
12:27:33
12:30:33
12:28:33
U_{10} = 18.5 m/s
12:31:33

Figure 6.17D.

The directional intensity factor calculated on January 19, 1995 (Figure 6.18) is originally maximal in a rather narrow band, aligned with wind and waves (the first section). After 06:00 the wind shifts from 0° to 330° with the waves lagging behind and Langmuir cells formed in between (second plot). Later, waves adjust to the changes in the wind direction and after 12:00 the cells become progressively aligned with both wind and waves (the third and the fourth sections). The wind speed is almost constant for the first 2 h and increases slightly towards the end of the deployment, at which point the cells become more spread apart and intensity variations increase. The difference between these observations and the data collected on April 18 is stronger wave forcing on January 19, which is reflected in fairly large values of Sr and Su (Figure 6.19). Perhaps we have here a case of "overdeveloped seas" when winds have decayed but waves have not yet adjusted: winds on the order of 10 to 11 m/s coincide with a significant wave height of more than 3 m.

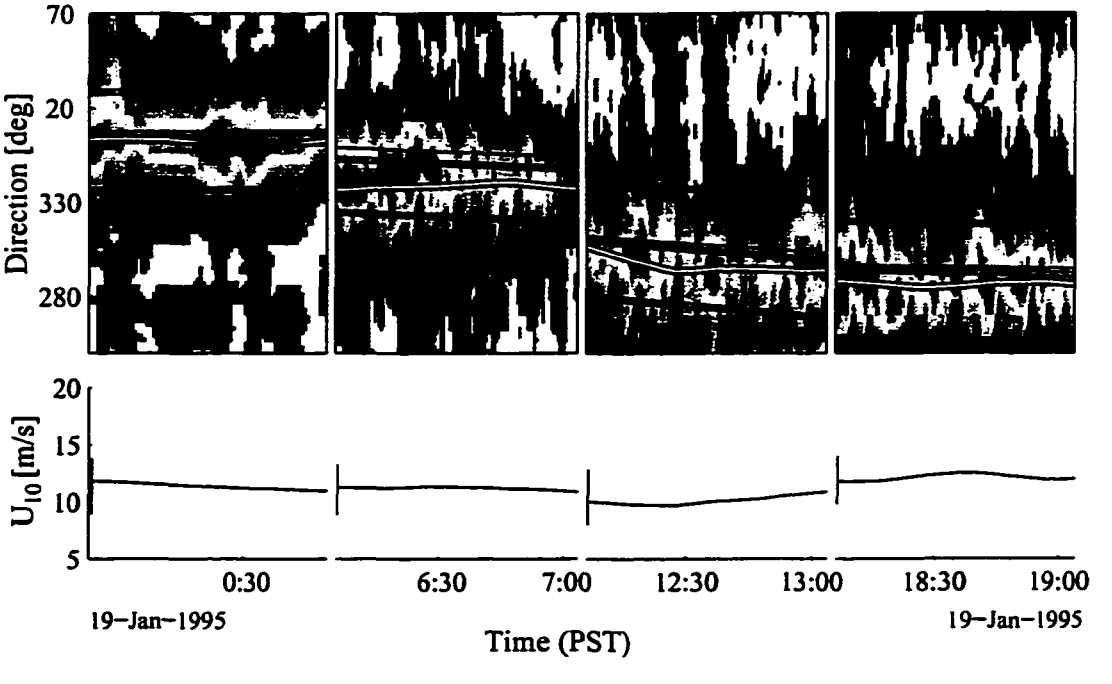

Figure 6.18: Normalized directional intensity factor (top plot) and the corresponding wind speed (bottom plot) for the Wecoma I deployment on January 19, 1995. Marking is the same as in Figure 6.16.

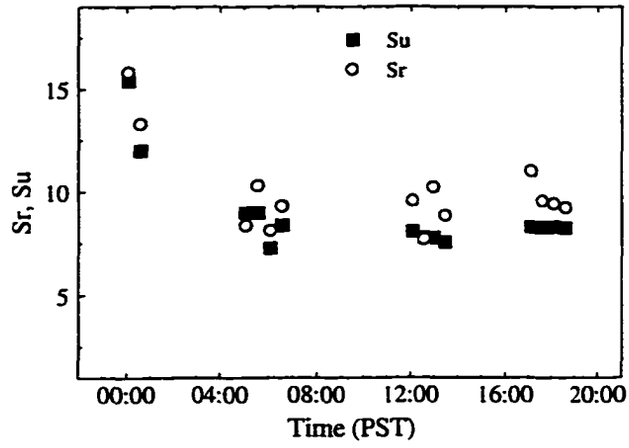

Figure 6.19: Shear ratio and the Stokes ratio during January 19, 1995.

The results of the directional intensity analysis displayed in Figure 6.11, Figure 6.16 and Figure 6.18 show that for our open ocean observations, the orientation of Langmuir cells is a strong function of the wind direction. Large Sr and Su, corresponding to the Wecoma I data, suggest that the cells there are more influenced by the wave forcing, compared to the MBL data, and tend to form closer to the wave rather than the wind direction, although not totally aligned with the waves. This is consistent with the model results, showing that while cells form close to the wind for small Sr, they do not align with the waves for reasonably large Sr. Extended observations taken over almost 24 h on April, 18 also suggest that the inclusion of the Coriolis force does not affect cell orientation.

6.3.4 Time Evolution of the Surface Patterns

Analysis of vertical and horizontal backscatter distributions provides several other useful parameters, such as cell spacing, penetration depth, and surface bubble coverage which can be used to describe the development of Langmuir circulation. Analyzing successive series of sweeping images in Figure 6.17A–D, we gain some insights on the temporal persistence of the surface convergences, as described above.

Cell spacing is estimated using horizontal backscatter images like the one shown in Figure 6.9. This approach differs from a related technique developed by *Thorpe and Cure* [1995] for "skeletonizing" fixed orientation (range versus time) sidescan images, but is similar to the approach used by *Farmer and Li* [1995]. To remove the effect of changes of relative cell orientation each backscatter matrix $I(x,y)$ is first counter-rotated by an angle corresponding to the preferential direction in the image inferred using (6.16). This procedure ensures that most of the bubble streaks align with the x axis. Although there appear to be some streaks which are oriented within $15-20°$ from the x axis (Figure 6.20), the associated error does not exceed 5%. A "peak search" algorithm in the cross-cell direction is then applied to these images to detect the points of local intensity maxima which are above a threshold noise value. The threshold level is estimated from the total backscatter distribution from the image and varies between 0.2 and 0.4 dB, depending on the wind, waves and ambient noise conditions. Afterwards, a dilation routine is used which connects broken lines within a radius of 5 m. The resulting skeletonized diagram (Figure 6.20) provides a measure of the locations of Langmuir convergences. Further, by using a range derivative, a spacing between consecutive convergences is estimated for each image and the result is averaged over ½ hour (approximately 60 images) to compute spacing distribution.

Spacing distributions for April 18, 1995 (4Figure 6.21) show that all distributions have a similar structure with a peak at around 15 to 19 m and a tail extending to 100 m. The distributions can be approximated by a log-normal dependence, which agrees with the previous observations of *Farmer and Li* [1995]. This suggests that generation of surface convergences is a multiplicative random process. If a new windrow is generated at a random location it breaks up the pre-existing spacing in a random proportion. This is in accord with the conclusions of *Csanady* [1994] based on the analysis of historical data.

Mean cell spacing for the April 18 to 19 period is between 18 and 27 m (Figure 6.22) and follows the wind record approximately. The average cell width, derived from the cell

spacing (Figure 6.22) ranges from 12 m up to 17 m. Assuming an aspect ratio of 1.4 this translates into the mean cell depth between 16 and 25 m. The corresponding maximal bubble penetration depth, inferred from 100-kHz upward-looking sonar data, is smaller than 6.5 m at the beginning of the storm and is between 12 and 18 m. Although bubbles are apparently unable to penetrate to the bottom of the cells, they do penetrate deep enough to provide an adequate sampling of the maximal downwelling.

Another method to determine spacing of Langmuir cells is based on the complete Radon transform $\mathcal{R}(\theta, k)$ of the sweeping intensity images. As discussed above, $\mathcal{R}(\theta, k)$ is derived by converting the backscatter intensity map $I(x,y)$ into a wavenumber space and subsequently interpolating the result onto the angle-wavenumber grid using Eq. (6.14). The resulting image $\mathcal{R}(\theta, k)$ then contains information about the directionality of the image at different spatial scales. We average data points over the angles within $\pm 30°$ from the preferential direction in the image in order to include Y-junctions and other features not completely aligned with the wind. This average quantity then, in a way

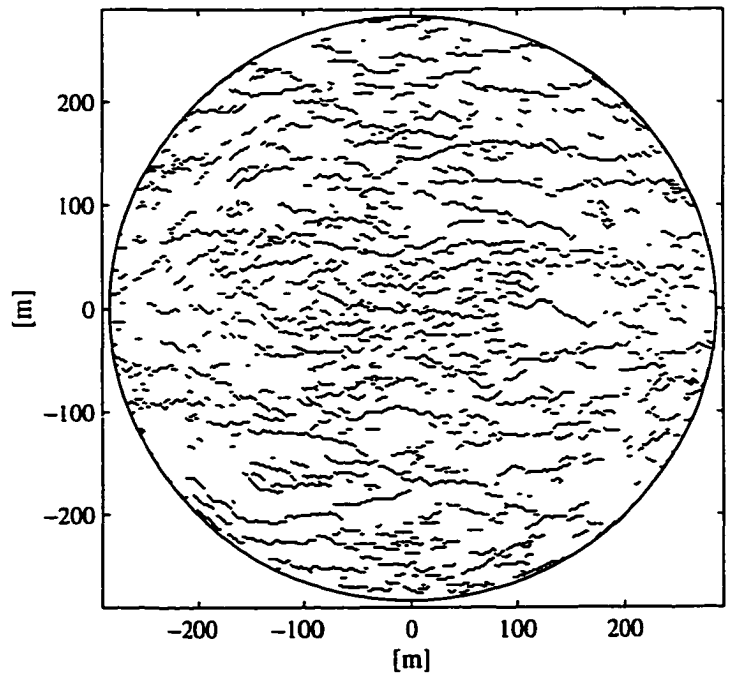

Figure 6.20: Skeletonized backscatter image at 12:14, April 18, 1995.

similar to a wavenumber spectrum, describes the scales contributing to the intensity distribution at angles close to the preferential direction.

The principal difference between this method and the "skeletonizing" technique is different weighting: the "skeletonizing" weights all cells equally, while the transform weights cells according to their cross-cell extent and intensity. Therefore, the transform method provides an estimate of the spacing of the dominant cells. To reduce the effect of the intensity variations between different bubble streaks a binary intensity slicing was applied [*Lim*, 1990] to the data, which sets all points above the noise threshold to 1.

Cell spacing, calculated using the transform method for the same period as in Figure 6.22, is given in Figure 6.23. We notice that at the beginning of the storm this method does not detect preferential scales. Afterwards, it gives the wavenumber of the dominant

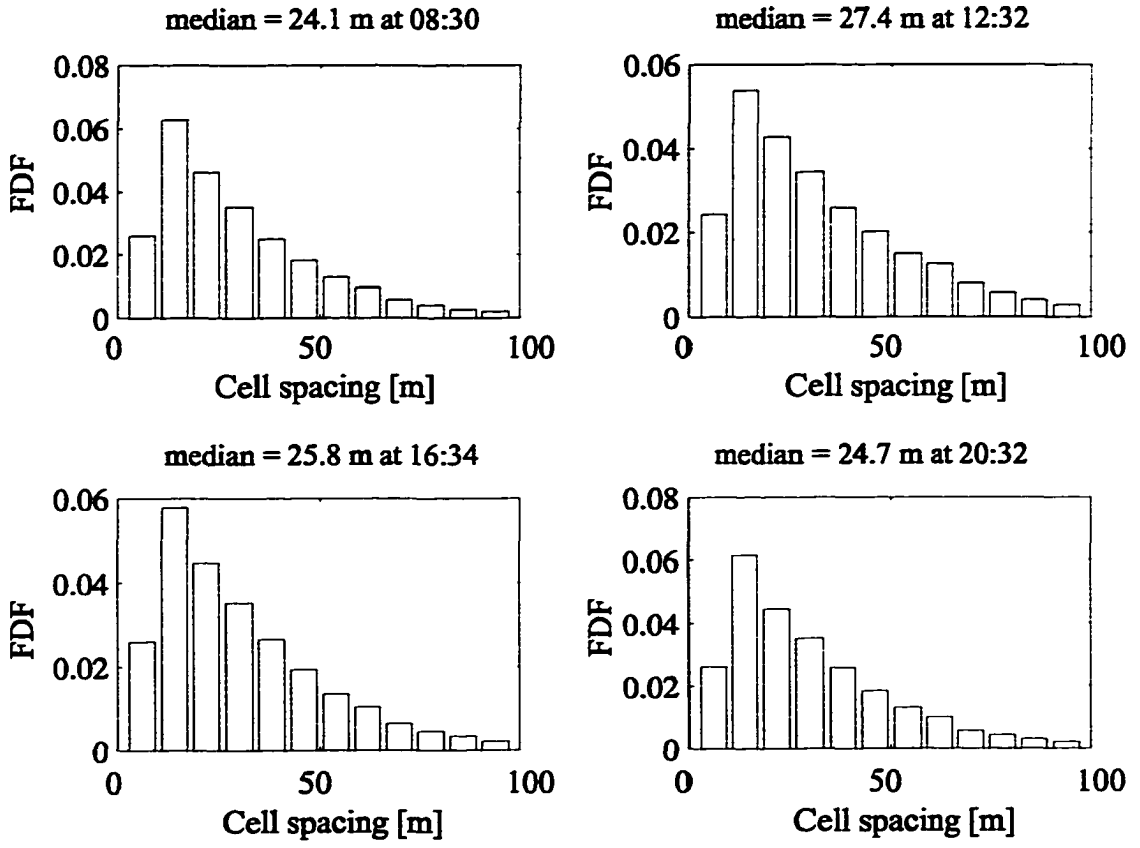

Figure 6.21: Frequency distributions of cell spacing obtained from the "skeletonized" two-dimensional near-surface backscatter patterns. April 18, 1995, MBL Experiment.

cells distributed between 0.14 and 0.25 m^{-1}, corresponding to the dominant spacing between 25 and 44 m, which is larger than the mean spacing estimated with the skeletonizing technique. Langmuir circulation is believed to penetrate through the whole depth of the actively mixing layer. Assuming an aspect ratio of 1.4 [*Gemmrich*, 1997], the maximal cell size is of order 25 m for a 35-m deep mixed layer. This estimate is close to the spacing of the dominant cells observed in Figure 6.23.

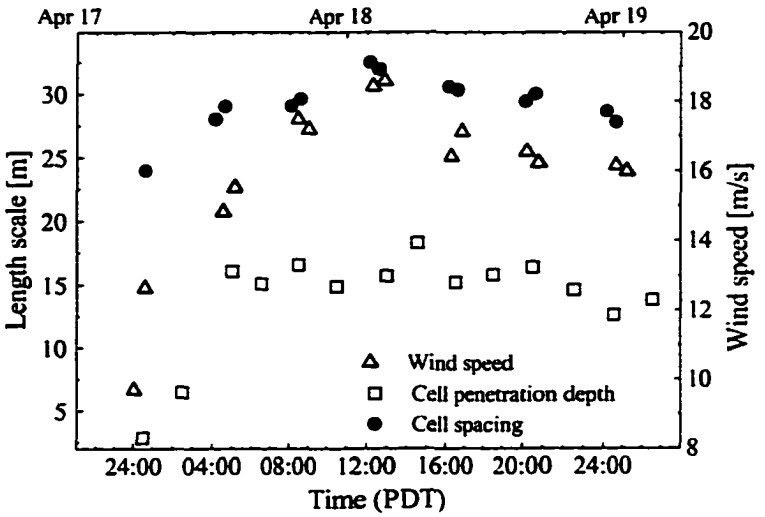

Figure 6.22: Mean cell spacing and maximal penetration depth on April 18 to 19, 1995. The cell spacing is evaluated from the two-dimensional backscatter intensity distributions measured with rotating side-looking sonars. The penetration depth is inferred from the upward-looking sonar backscatter (100 kHz, short pulse).

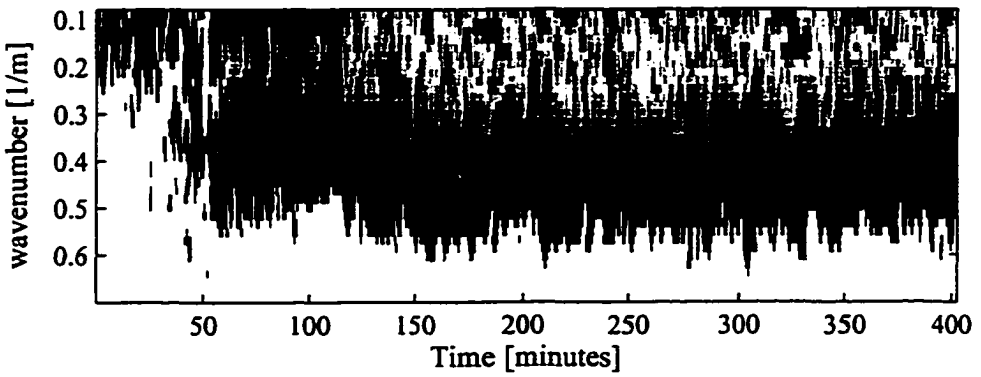

Figure 6.23: Dominant cell spacing, estimated using the transform method. April 18, 1995, MBL Experiment. The x axis runs consecutively with the gaps removed.

Applying an intensity slicing technique to the sweeping images, we can also estimate the surface bubble cloud coverage. Areas of high backscatter in an image like Figure 6.9 are signatures of the near-surface bubble clouds. Although the backscatter does not come from the surface itself but rather from the area approximately 1 to 2 m beneath (Figure 6.7), it may serve as a reasonable proxy for the surface bubble coverage.

Estimated surface coverage for April 18, 1995 (Figure 6.24) displays a similar tendency as the cell spacing and penetration depth, i.e. it follows the wind speed, and is between 10 and 12% at winds stronger than 12 m/s. Note that our acoustic coverage is larger than the white-cap coverage, usually observed using optical methods: less than 5% for the same range of wind speeds [*Monahan and Lu*, 1990], apparently due to the difference in observation techniques. Nevertheless, the absolute magnitude is not what we are seeking here. It is the wind speed dependence that is of interest. *Monahan and Lu* [1990] suggested a wind speed-cubed parameterization for the bubble coverage, based on the arguments that the rate of energy input by the wind into the ocean is proportional to the friction velocity cubed u_*^3

$$BC=[5.21\times10^{-4}(X-75.9)]^3,\quad X=U_{10}(g\nu)^{-1/3}, \tag{6.17}$$

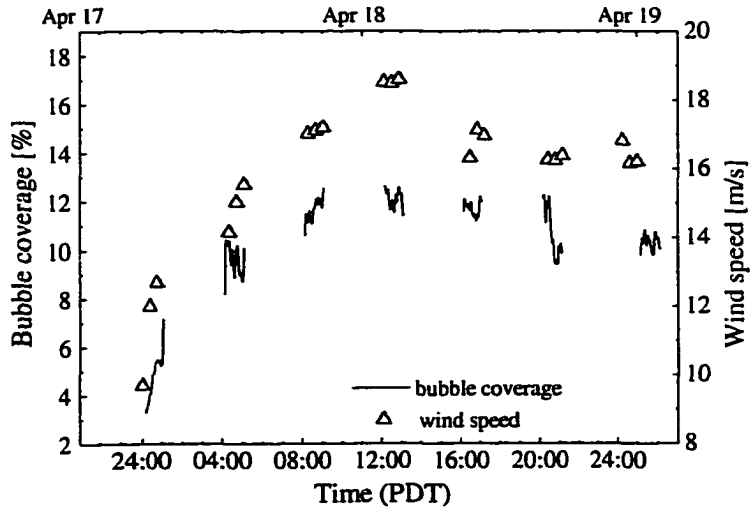

Figure 6.24: Relative surface bubble coverage calculated from acoustical backscatter intensity distributions measured with the side-looking sonars on April 18, 1995.

where ν is the kinematic viscosity of sea water. We note here that the results of GeMuPo, based on the energy input into the waves by the wind, suggest a u_*^2 energy dependence.

Comparison between our acoustical observations and *Monahan and Lu's* [1990] (ML) parameterization shows that the latter gives significantly lower values (Figure 6.25). The ML parameterization, adjusted to match acoustical bubble coverage prior to onset of Langmuir circulation (line marked (ML+2.5%), still produces significantly lower coverage afterwards. This is not surprising since ML parameterize only contributions of primarily surface bubbles. We, however, measure bubbles distributed in the top 0.5 to 2 m. In addition the u_*^3 parameterization does not incorporate Langmuir circulation, which draws bubbles to greater depths resulting in higher acoustical bubble coverage. Therefore, a caution should be used when interpreting photographically observed bubble coverage.

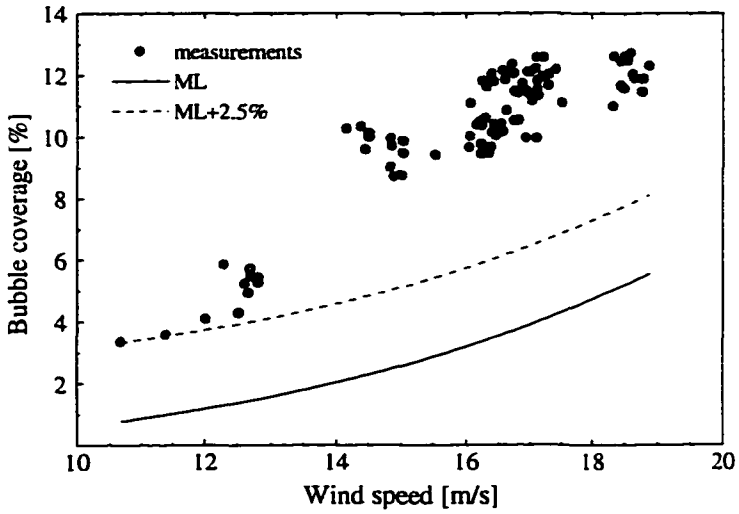

Figure 6.25: Comparison of the acoustically measured bubble coverage with parameterization of Monahan and Lu [1990] (line marked ML). Line marked ML + 2.5% represents ML parameterization adjusted to match acoustical bubble coverage prior to onset of Langmuir circulation.

6.4 Observed Thermal Inhibition of Langmuir Circulation

Previous observations suggest a minimum wind speed for the onset of the circulation ranging from 3 to 8 m/s (see Section 2.3). In this section I will discuss simultaneous observations of Langmuir circulation horizontal and vertical structure, temperature, velocity and wave fields taken during a storm. Based on these observations we examine the role of stratification in the inhibition of Langmuir circulation and the conditions required for its initiation. The data motivate a Froude number stability analysis which allows evaluation of the influence of pre-existing stratification on the generation of Langmuir circulation. Previously available measurements of Langmuir circulation have not allowed a direct test of the role of stratification in circulation dynamics.

6.4.1 Environmental Conditions

Data discussed here were obtained in the MBL Experiment, in the vicinity of 36°N, 122°30'W, off Monterey, California. Of interest here are two periods: the 32-h period between 20:00, April 17 and 04:00, April 19, 1995 (PDT), during which a strong storm passed through the experimental site (Figure 6.26), and an 8-h period on April 24, 1995.

The experiment was conducted in California coastal waters where a complex sea surface temperature structure is commonly observed. Satellite surface temperature imagery shows that eddies, multiple jets and cold filaments extending several kilometers offshore are commonly observed south of 39°N [*Bernstein et al.*, 1977; *Strub et al.*, 1991]. *Ramp et al.* [1991] report cold (12−13.5°C) and intense filaments 10 to 15 km wide surrounded by broader and warmer (13.5−16°C) oceanic water structures. The sea

surface temperature structure over the area of the experiment is visible in the satellite-based Advanced Very High Resolution Radiometer (AVHRR) thermal image taken on April 21 (Figure 6.26). Warmer Pacific waters and the filaments of colder coastal upwelling are easily identifiable, with horizontal temperature gradients of approximately 0.5 K/km in the offshore direction.

The data set includes acoustical observations of the vertical and horizontal structure and velocities of Langmuir circulation, measurements of the fine-scale temperature structure in the upper 2 m, temperature time series at 6.5 and 29 m, directional wave spectra derived from the acoustical wave measurements, ship-mounted Acoustical Doppler Current Profiler (ADCP) data and meteorological observations.

A simplified layout of relevant measurements during the MBL Experiment is sketched in Figure 5.3. Acoustical observations of the Langmuir circulation surface

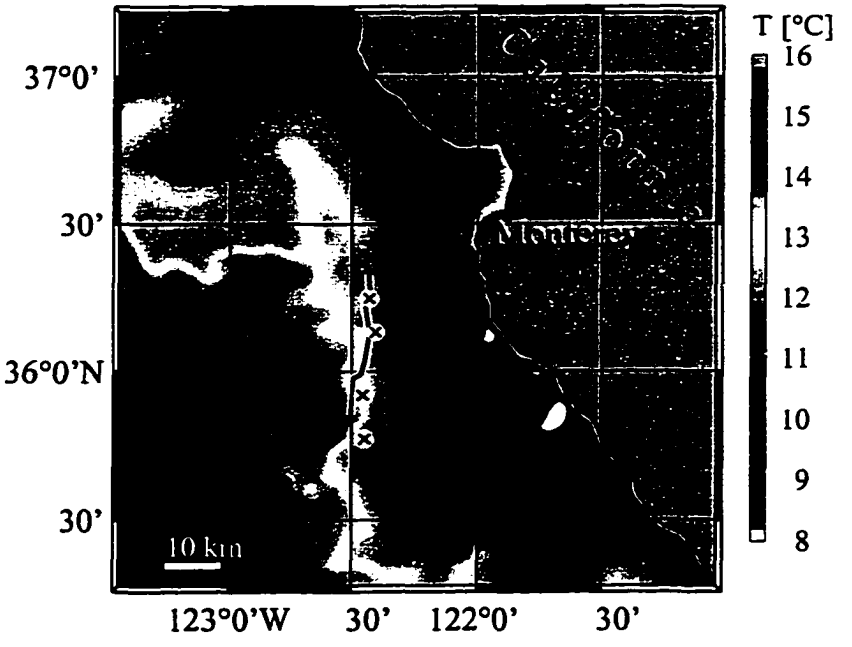

Figure 6.26: Satellite image of the sea surface temperature over the experiment area taken at 21:38 (PDT) April 21. Drift tracks of the imaging sonar (line) and the surface drifter FLEX (crosses) show that both instruments are drifting almost directly south, starting at 12:33, April 17 and ending at 04:26, April 19. Original AVHRR satellite data provided by Dr. J. Gower, IOS.

structure, vertical bubble cloud penetration and velocity in Langmuir convergences were obtained with the imaging sonar platform SeaScan III. Temperature measurements were taken using a SeaBird SBE-3 thermistor on board the platform at an average depth of 29 m and an additional recording thermistor TR-1000 was attached to the rubber cord above SeaScan at approximately 6.5 m or 3.5 below the surface. Specifications for both temperature sensors can be found in Table 3.2. Observations of the near-surface temperature structure were also acquired with a separate surface tracking float FLEX (Figure 5.3) which drifted in close proximity to the imaging sonar (Figure 6.26). FLEX temperature measurements were provided by Dr. J. Gemmrich and the calibration is described in *Gemmrich* [1997].

Because of the severe sea conditions, hydrographic measurements were limited to CTD casts before and after the storm. Temperature and salinity profiles at 07:45, April 17 (solid lines in Figure 6.27) show a fairly well mixed 35-m deep layer. After the storm (at 09:45, April 19) the layer had deepened to 45 m and the water cooled by 0.15 K. Note that near the surface CTD data are contaminated by the ship-induced mixing.

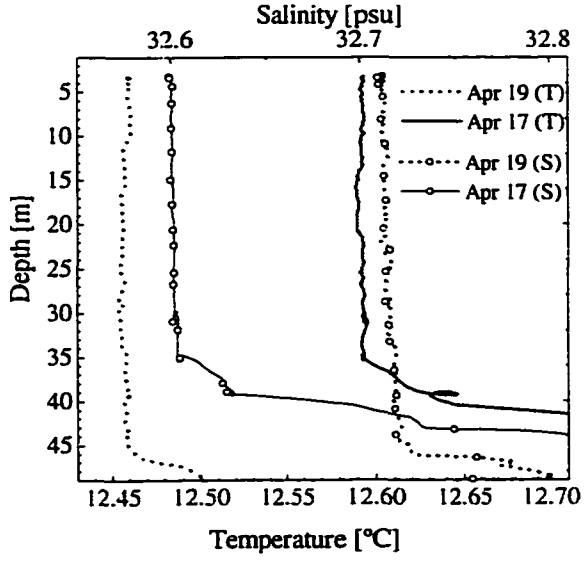

Figure 6.27: Temperature (thick lines) and salinity(lines with circles) profiles taken from R/V Wecoma before (solid lines) and after the storm (dotted lines).

Meteorological and oceanographic parameters for the period before and during the storm are presented in Figure 6.28. Observations prior to midnight on April 17 show winds gradually decaying to 1−3 m/s (Figure 6.28a). A slight increase in the wind speed to 5 m/s occurs at 20:00. However, between 23:00 and 24:00, April 17, the winds

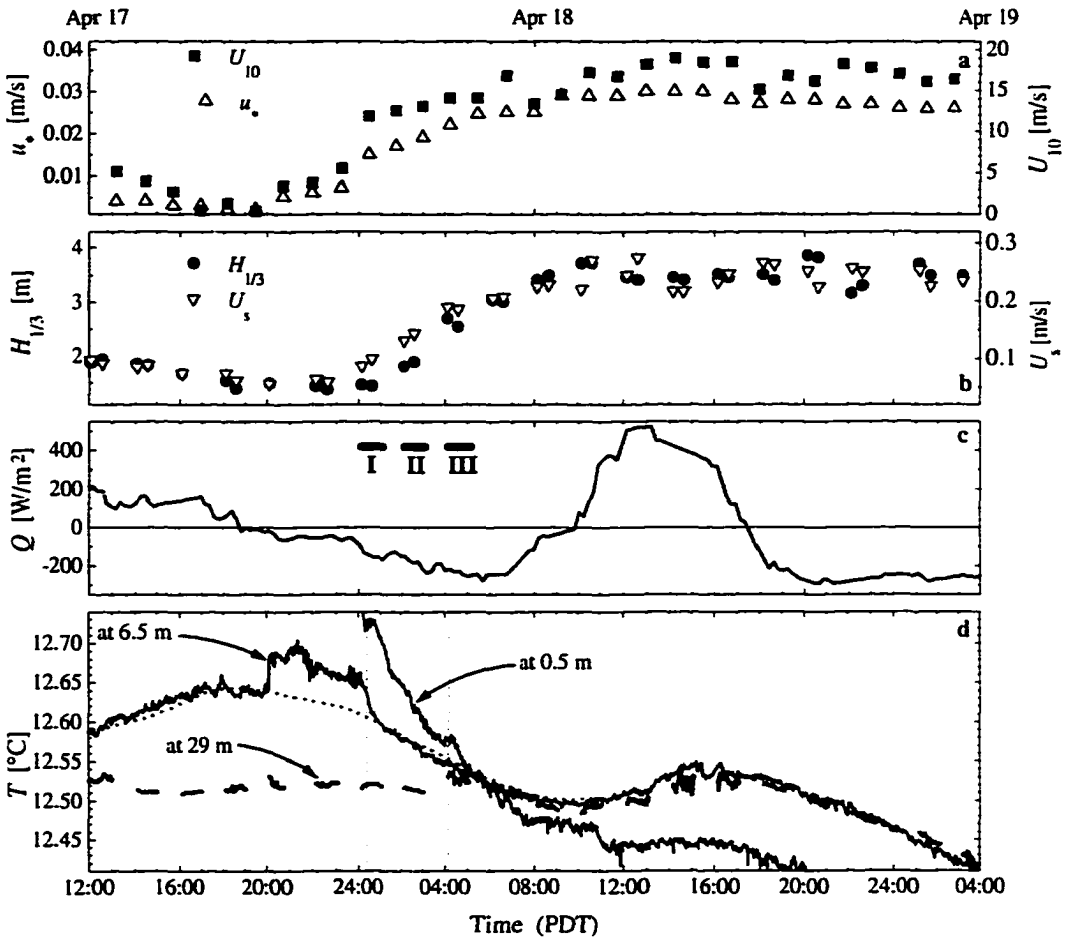

Figure 6.28: Environmental data covering the period before and during the storm on April 17 to 19, 1995. a) Wind speed (solid squares) and friction velocity in water (open triangles), b) significant wave height (solid circles) and the surface Stokes drift U_s (open triangles), c) heat flux, and d) temperature time series at different depths. The thick dashed line in d) shows cooling, consistent with the measured heat flux. Two vertical dashed lines in d) mark time when the circular images in Figure 6.29 were taken. In c) gray horizontal bars, marked I, II, and III, depict time intervals for which vertical sonar data are shown in Figure 6.31. Calculations of the cooling rate and temperature measurements at 0.5 m provided by Dr. J. Gemmrich, IOS and meteorological data by Dr. J. Edson, WHOI.

increase rapidly to 10 m/s, and a maximum value of 18 m/s is reached in the afternoon on April 18. Prior to the onset of the storm, wave measurements reveal a decaying moderate swell, with significant wave height decreasing from about 2 to 1.4 m and a surface Stokes drift of less than 0.1 m/s (Figure 6.28b). Following the onset of the storm, the surface Stokes drift increases to 0.28 m/s, and the significant wave height grows from less than 1.5 m to almost 4 m (Figure 6.28b). Simultaneous directional wave measurements show waves propagating predominantly in the wind direction. Measurements of the heat flux (Figure 6.28c) show periods of strong heating, peaking at more that 500 W/m^2, between 10:00 and 17:00, and strong cooling (down to $-300 W/m^2$) at night.

At the beginning of the storm the temperature measurements near the surface reveal stratification with the surface water at 0.5 m depth being roughly 0.25 K warmer than water at the depth of the acoustical platform (29 m) (Figure 6.28d). This is not visible in the CTD data, apparently because of the mixing of the water in the 3-m column by the ship propellers. By midnight on April 18, however, the auxiliary near-surface sensors indicate almost homogeneous water in the top 1.8 m while the temperature difference between 6.5 and 29 m depth is approximately 0.1 K. Prior to the storm little variability of our deepest (29 m) temperature record was observed, whereas the temperature at 6.5 m approximately follows the cycle of the air-sea heat flux. However, a rapid cooling of 0.28 K is observed at 0.5 m depth during the first 8 h of the deployment. Approximately 6 h after the onset of the storm, the entire water column above 29 m becomes well mixed, showing a uniform temperature at all three sensor depths after 06:00, April 18 (Figure 6.28d).

The temperature record at 6.5 m depth displays a sudden temperature increase of more than 70 mK at 20:00 on April 17 (Figure 6.28d), which cannot be explained in terms of the air-sea heat flux. Temperature, consistent with the air-sea heat flux, is modeled from

$$\frac{dT}{dt} = \frac{Q(t)}{h\rho_w c_p}. \tag{6.18}$$

In (6.18) h represents the depth of the actively mixing surface layer, where temperature changes are depth independent. The modeled temperature time series is matched to the observed record for $h = 11$ m prior to 20:00 and $h = 18$ m after 01:00, April 18. It demonstrates the presence of anomalous warm surface water between 20:00 and 24:00. We, therefore, attribute the above feature to the instrument drifting into a horizontally inhomogeneous temperature field. Sharp boundaries of this kind have been previously described by *Soloviev et al.* [1988].

This interpretation is supported by a complex sea surface temperature structure which is commonly observed in California coastal waters. The imaging sonar platform, supporting thermistors at 6.5 and 29 m depth, drifts with a mean speed of 0.4 m/s relative to the ground, which might result in rapid temperature changes similar to the observed anomalous surface temperature seen in Figure 6.28d. A further temperature change, most likely associated with the instrument drifting into different water masses, occurs at 11:00, April 18, at the shallowest temperature record. The horizontal separation between the surface drifter supporting the thermistor at 0.5 m depth and the deeper temperature sensors is on the order of 1 km at 18:30, April 17 and 2 km at 19:30, April 18.

To get a more detailed picture of the near-surface dynamics during this period of rapid evolution we employ acoustical data. Two examples of the acoustical images of the near surface are given in Figure 6.29 where the bubble clouds appear red. The image on the left, taken at 00:15 when the wind was above 8 m/s for about 30 min before exceeding 10 m/s, shows a highly irregular surface patterns, with no signs of organized cells. Considering that previous observations of near-surface bubble clouds indicate Langmuir circulation evolving within a few minutes after the onset of the wind [*Thorpe*, 1986a; *Smith*, 1992], we would expect to see signs of the circulation in this image. The right image in Figure 6.29 was taken approximately 4 h later and reveals a strikingly different picture: well organized, narrow, elongated structures approximately aligned with the wind. However, these are not uniform parallel convergence lines, as observed at lower

winds. Normalized directional intensity, discussed in the previous section, is small at beginning of the storm and rapidly increases at around 00:30 (Figure 6.16).

Successive sweeping images taken during this period provide an additional insight to the time evolution of the near-surface bubble clouds (Figure 6.30A–D). The first set in Figure 6.30A displays an almost random pattern similar to that in Figure 6.29 (left). However, the second set (Figure 6.30B) shows a gradual transformation from unorganized structures at 00:28 to somewhat more aligned features at 00:32 and 00:33. These features become progressively more coherent during next 20-min period and Figure 6.30C–D displays small-scale bubble streaks preferentially aligned with the wind. Images in Figure 6.30 capture the transition from an almost randomly distributed bubble field to organized structures, which suggests the onset of Langmuir circulation. This is consistent with the rapid increase of the spatial coherence during that time (Figure 6.16).

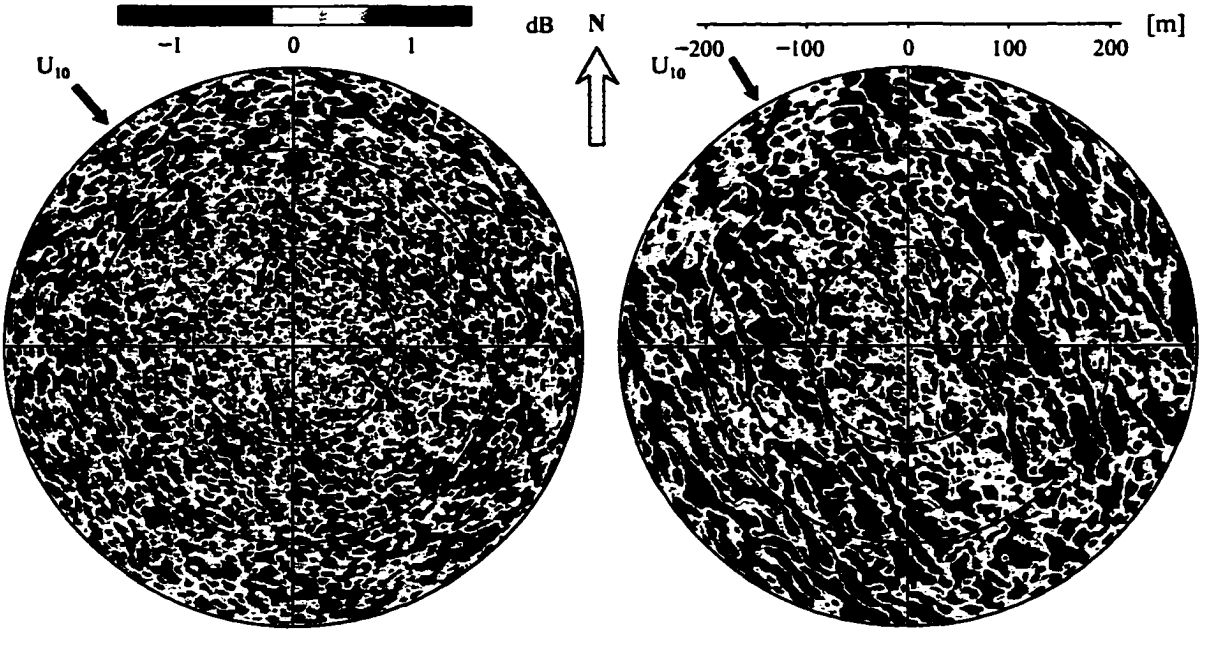

Figure 6.29: Distribution of the near-surface acoustical backscatter intensity measured with rotating side-looking sonars. Left image, taken at 00:15, April 18, (U_{10} = 10.3 m/s) shows a highly irregular surface pattern. The image on the right (U_{10} = 14.7 m/s), taken approximately 4 hours later (at 04:07), reveals clouds of bubbles organized into streaks by Langmuir circulation.

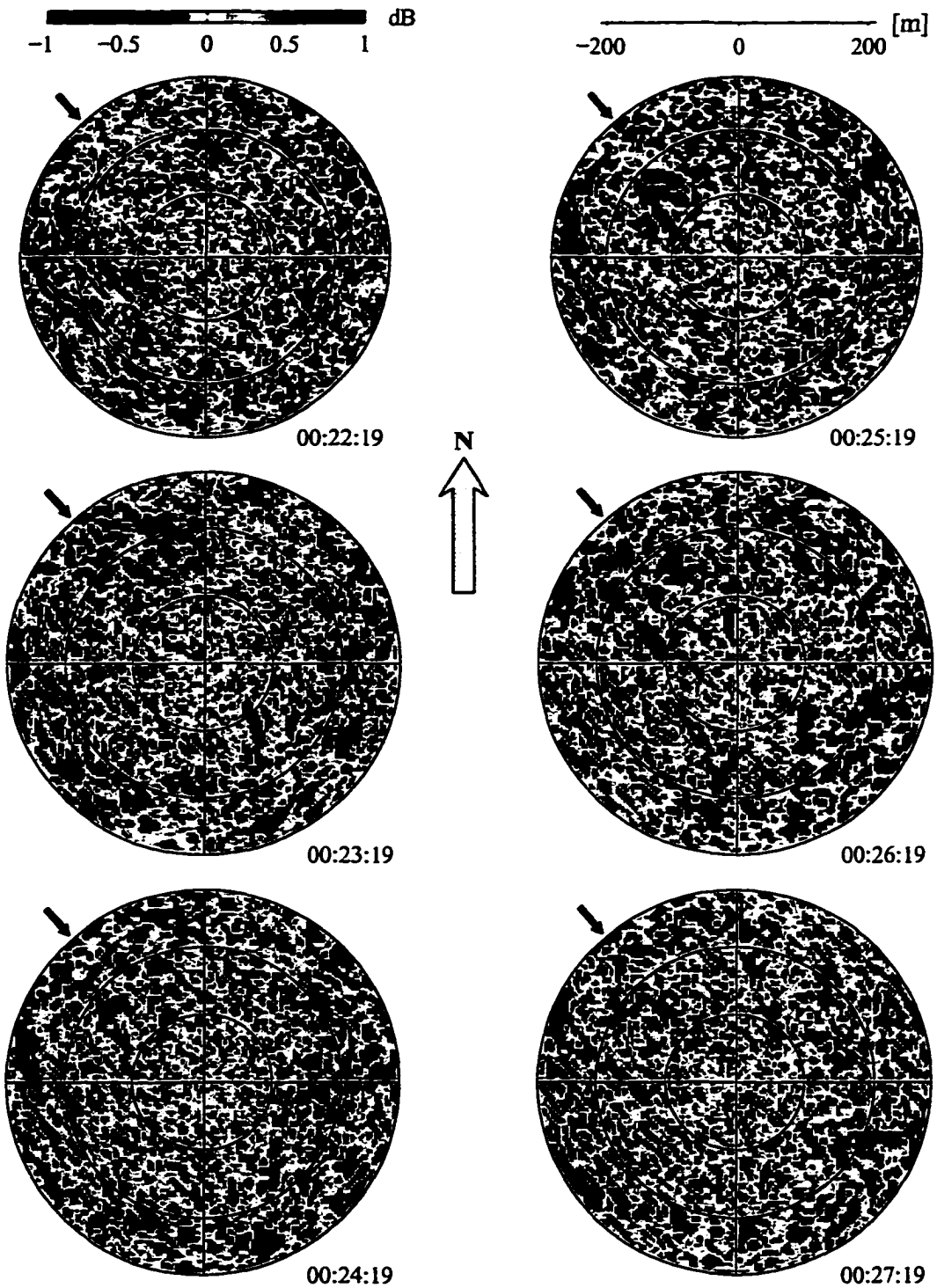

Figure 6.30A: Successive sweeping images showing a transition from an almost randomly distributed bubble field to organized structures during a storm between 00:22 and 00:51, April 18, 1997.

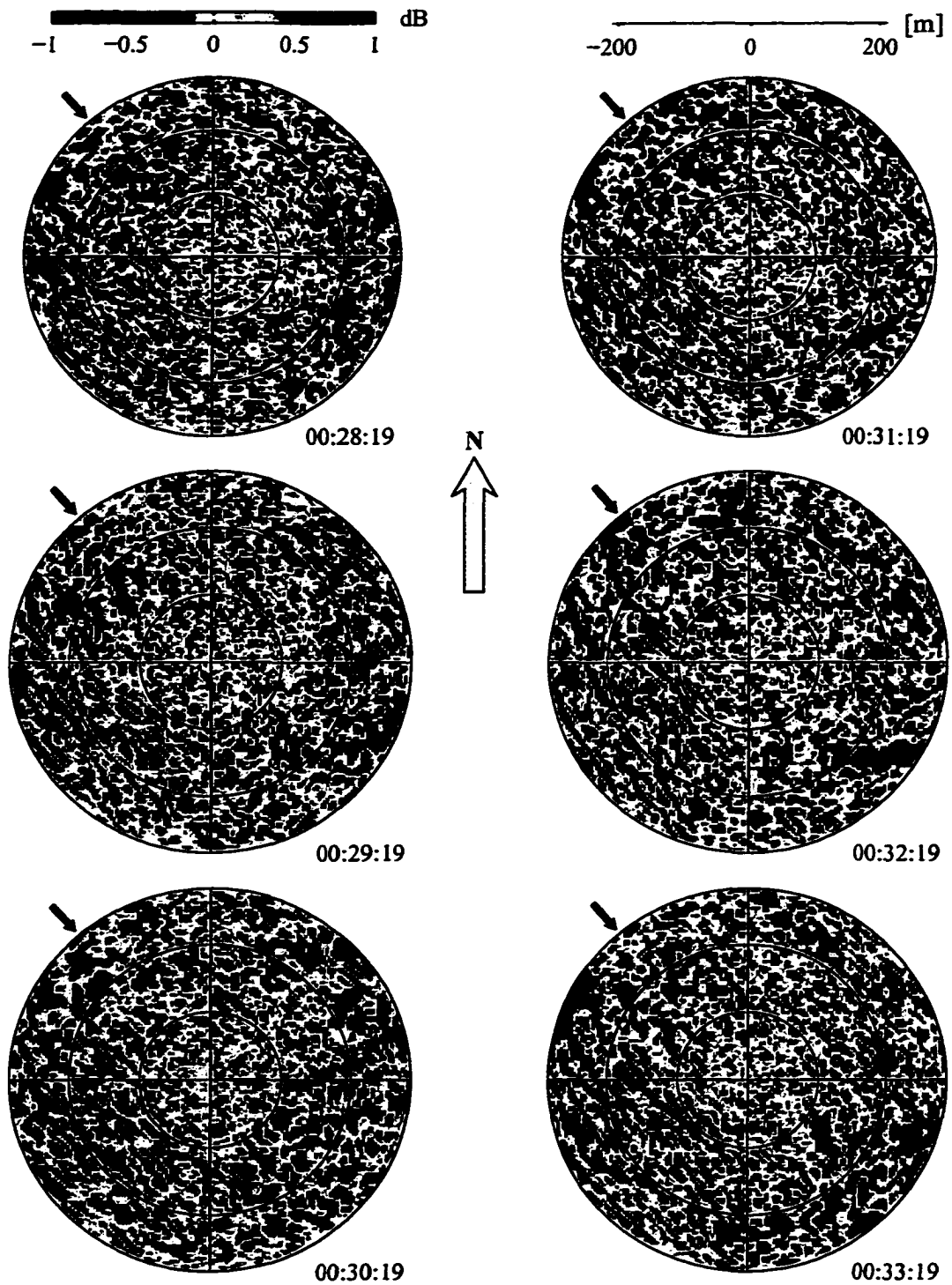
dB
−1
−0.5
0
0.5
1
[m]
−200
0
200
N
00:28:19
00:31:19
00:29:19
00:32:19
00:30:19
00:33:19

Figure 6 30B

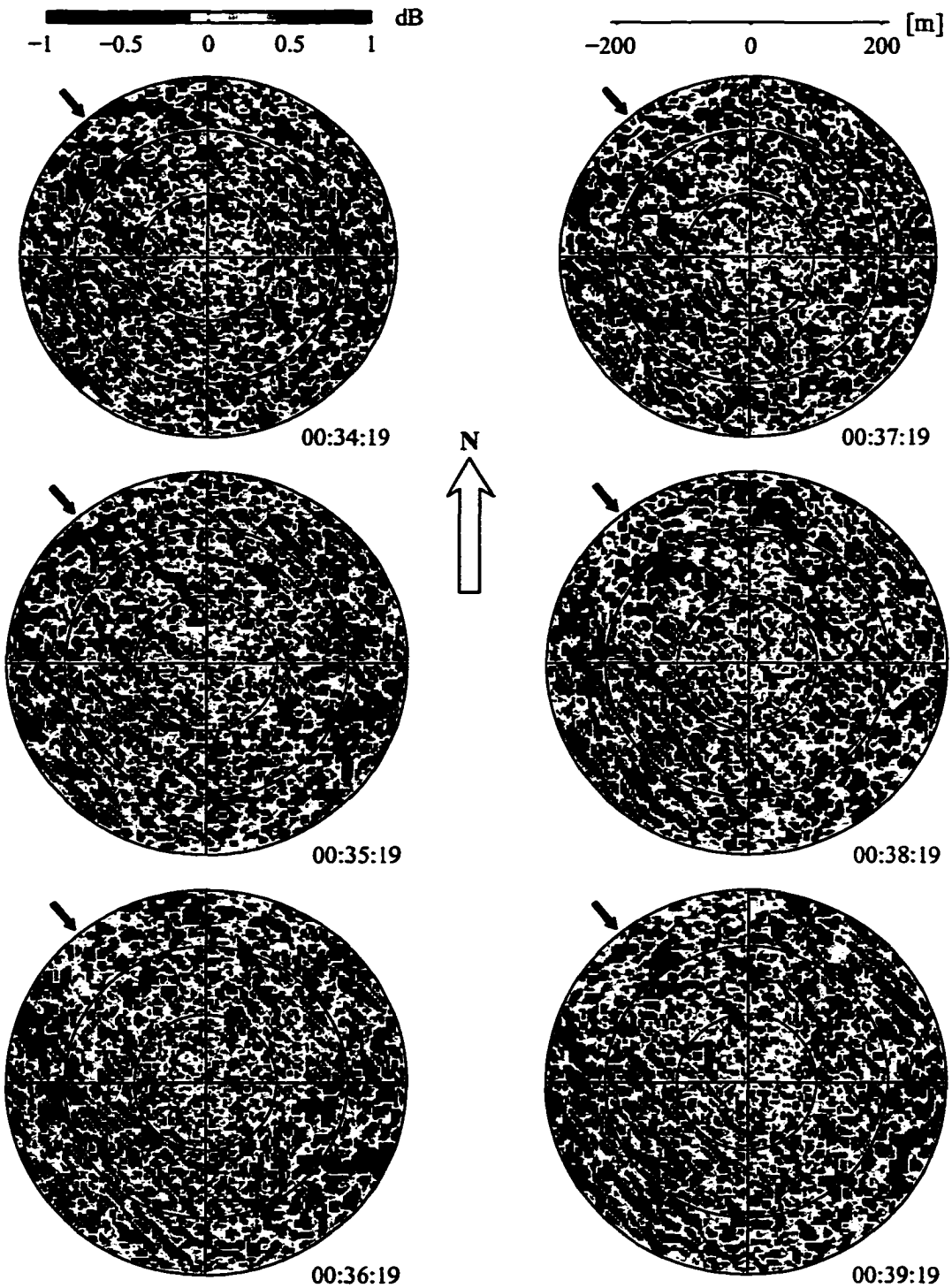
dB
−1
−0.5
0
0.5
1
[m]
−200
0
200
00:34:19
00:37:19
N
00:35:19
00:38:19
00:36:19
00:39:19

Figure 6.30C

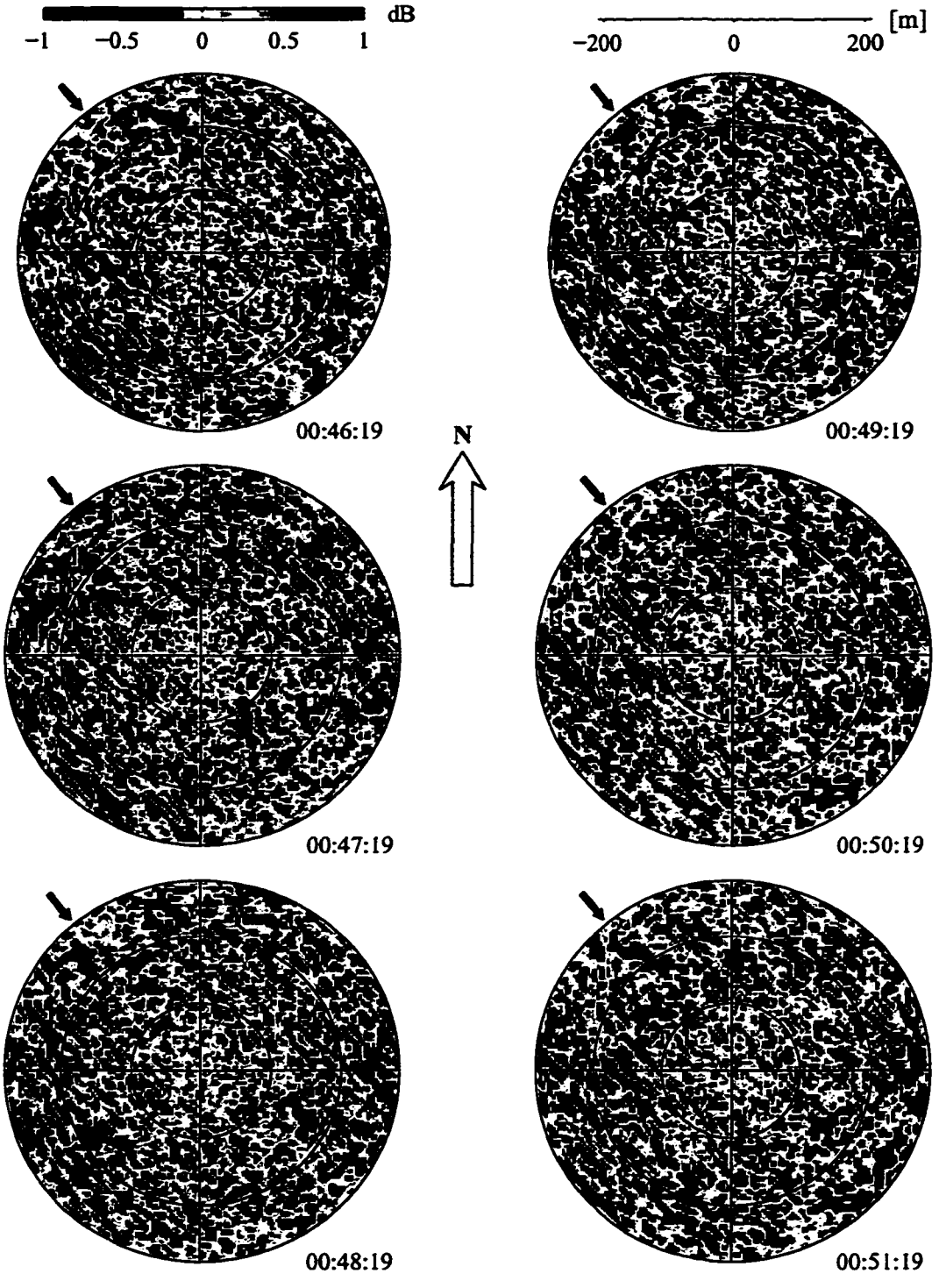
dB
−1
−0.5
0
0.5
1
[m]
−200
0
200
00:46:19
00:49:19
N
00:47:19
00:50:19
00:48:19
00:51:19

Figure 6.30D.

In addition to the horizontal backscatter structure, the vertical bubble cloud structure is observed with upward-looking sonars, shown in Figure 6.31 for three 1-h periods at the beginning of the storm. Due to the recording schedule the upward-looking sonars recorded every even hour). In the absence of bubbles, the recording thermistor, attached to the cord above the instrument, is visible as a band of color between 5 and 7 m but dense bubble plumes, extending below 6 m, easily overcome this interference. The data in Figure 6.31 (panel I) covering the period from 00:06 to 01:07, do not show significant bubble cloud penetration. Observations taken between 02:06 and 03:07 (panel II) show more intense and deeper clouds, although they fail to penetrate below 6−7 m. Residual vertical velocities indicate downwelling between 21 and 38 mm/s. The data in the segment III from 04:07 to 05:07 display several much denser clouds penetrating down to 7−10 m and, on one occasion, to more than 15 m. Residual vertical velocities corresponding to this period, given in Figure 5.14, show downward flows in the convergences with vertical velocities reaching 90−98 mm/s. This is indicative of a well developed circulation, and is in agreement with the imaging sonar data (Figure 6.29,

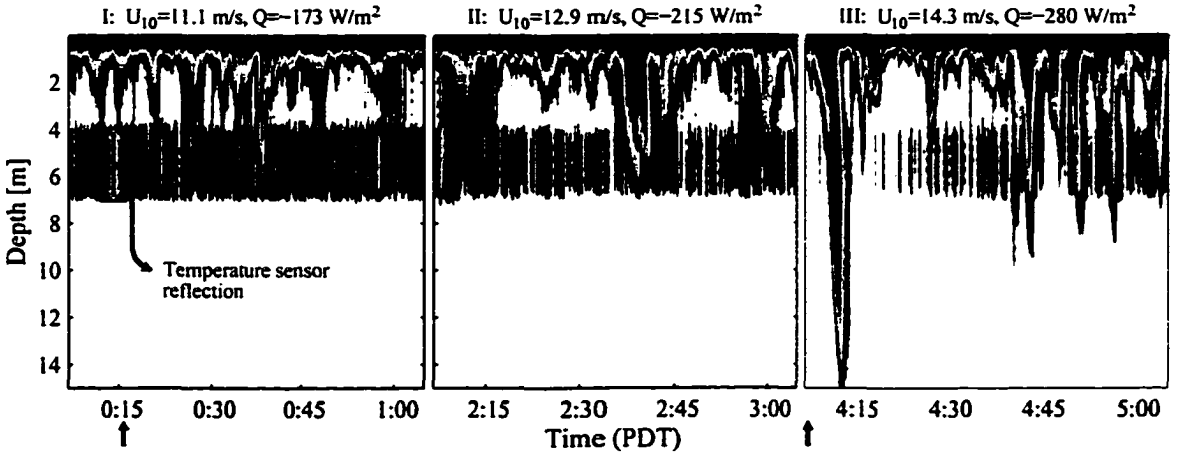

Figure 6.31: Vertical bubble clouds during the first part of the storm on April 18, 1995 measured with the upward-looking 200-kHz sonar. Horizontal band of color centered around 5.5 m corresponds to the acoustical reflection from the temperature sensor. Vertical arrows mark times when the images in Figure 6.29 were taken. Sections labeled I, II, and III correspond to the same markings in Figure 6.28.

right).

Hence both observations of horizontal and vertical bubble structure consistently show no circulation at the beginning of the storm, weak cells confined near the surface during the second hour (02:06 to 03:07) and signatures of a well developed deeply penetrating circulation during the last hour (04:07 to 05:07). These coincide with the subcritical Langmuir number (Figure 6.5), favorable for generation of Langmuir cells. Therefore, the question arises as to what caused inhibition and delay of the onset of circulation.

6.4.2 Stability Criterion

Besides the wind-wave forcing, Langmuir circulation can be affected by the buoyancy. *Li and Garrett* [1995] showed that for a typical wind speed of 5 m/s and surface cooling of 200 W/m^2, wind-wave forcing dominates thermal forcing in generating Langmuir circulation, but strong surface heating may suppress the circulation. For the data of interest here, which were collected during strong cooling ($Q \sim -250$ W/m^2) and wind speeds exceeding 10 m/s, the maximum value of the Hoenikker number Ho, representing the ratio of thermal to wave forcing [*Li and Garrett*, 1995] is 0.01, and hence thermal forcing is not an important factor.

Bubble buoyancy may also contribute to the near-surface stratification. We observe a mean 0.15-K temperature difference between 0.5 and 6.5 m depth (Figure 6.28d) which is equivalent to a mean air void fraction on the order of 2×10^{-6} over this depth. Although the instantaneous bubble void fraction may reach 5×10^{-5} at 0.7 m depth inside the breaking wave injections [*Farmer et al.*, 1998b], these are very intermittent events. At 9 to 15 m/s wind speed, the mean void fraction in the top 1 m is usually between 5×10^{-7} and 1×10^{-6} and decreases exponentially with depth to 6×10^{-9} and 5×10^{-8} at 5 m (*e*-folding depth of 1 to 1.2 m) [*Farmer and Vagle*, 1997]. This is equivalent to temperature anomalies of 2.5 to 10 mK and 0.25 mK, respectively. Together with a rapid decay of the

bubble concentrations with depth, this makes the integral bubble contribution to the stratification small compared to the thermal effects over a 5- to 6-m depth. In addition, the wave forcing decay depth is larger than that of bubble concentration ($h_s \sim 2$ to 2.5 m) and we therefore, can neglect the bubble inhibition effects, especially at moderate winds at the beginning of the storm. However, there may be circumstances when intense bubble clouds contribute significantly to the buoyancy at the upper 1 m of the surface layer and may play a significant role in Langmuir circulation inhibition.

Li et al. [1995] proposed a framework for interpreting the suppression of Langmuir circulation in the presence of stratification. They examined the response of the mixed layer to shear instability and Langmuir circulation, in the presence of a pre-existing stratification, and established a criterion describing the balance between buoyancy and mechanical forcing. This criterion is expressed in terms of the Froude-Langmuir number FL, which describes the competition between erosion of the mixing layer due to Langmuir circulation and restratification due to buoyancy

$$\mathrm{FL} = \mathrm{Rs}\frac{u_*^2}{h\,\Delta b}, \tag{6.19}$$

where Δb is the buoyancy difference over a depth h and Rs is the wave Reynolds-like number associated with the Stokes drift and is defined as [*Li et al.*, 1995]

$$\mathrm{Rs} = 0.72\frac{U_s h_s}{\nu_e}, \tag{6.20}$$

where a coefficient 0.72 arises from numerical simulations. Note that the stability index FL describes the balance between mechanical mixing and the *pre-existing stratification* but not the heat flux Q effect, which is parameterized in terms of Ho [*Li and Garrett*, 1995]. Although stratification may depend on the surface heat flux, Q is not the only parameter that determines it.

Deepening of the mixing layer is expected for FL > 1, i.e. when the stirring by Langmuir circulation overcomes the inhibition due to stable stratification. *Li et al.* [1995]

use Rs = 50 for fully developed seas, while pointing out that it could be smaller for developing seas. Considering that the data we analyze here correspond to a rapid growth of the wave field (the surface Stokes drift increased from 0.05 to 0.12 m/s and the significant wave height from 1.4 to 2.8 m in the first 4 hours of the storm (Figure 6.28a,b), it is necessary to estimate Rs directly.

Based on the results discussed in Section 6.1, we take the effective viscosity at a depth of $1.9h_s$, obtained from the measured vertical temperature field using the Craig-Banner model, as an approximation of the depth-averaged viscosity affecting Langmuir circulation dynamics. This allows direct evaluation of Rs via (6.20) and hence, the Langmuir circulation stability parameter FL using (6.19). Calculations of Rs reveal a rapid increase from 4 to 12 during the development stage between 23:00 and 06:00, April 17 to 18 and give values between 12 and 14 afterwards. Our mean value of $Rs \approx 13$ for a developed stage is smaller than that used by *Li et al.* [1995], due mainly to larger effective turbulent viscosity. This is consistent with recent reports of enhanced near-surface turbulence [*Craig and Banner*, 1994; *Gemmrich*, 1997] (caused by breaking surface waves) which affects Langmuir circulation as reported by *Farmer et al.*, [1998a].

The index FL can be evaluated for different pairs of thermistors: 0.5−6.5 m and 0.5−29 m (hereinafter referred to as $FL_{6.5}$ and FL_{29}, respectively) using (6.19) while approximating changes in the buoyancy by the temperature difference ΔT,

$$\Delta b = \alpha g \Delta T, \tag{6.21}$$

where α is the coefficient of thermal expansion. In calculating the buoyancy jump, I take into account that we have almost homogeneous water in the top 1.8 m and a layer with a gradually decreasing temperature beneath. The depth of the layer is taken as the difference between the depths of the corresponding thermistors. Because $FL_{6.5}$ describes the balance in the top 6.5-m deep layer and FL_{29} throughout the upper 29 m, we expect $FL_{6.5}$ to become supercritical first.

The time evolution of the Langmuir circulation stability parameters for different depths is given in Figure 6.32. The best least squares linear fit for the development stage is also presented. The parameter FL for the top part of the mixing layer (marked by triangles) is subcritical for the first 1.5 h, becoming supercritical near 00:15, April 18. Observations of the surface backscatter, taken shortly after, demonstrate a gradual organization of the surface structures which became progressively more aligned (Figure 6.29). The stability index for the whole layer (circles) becomes supercritical at approximately 03:00, April 18 and we observe deeply penetrating cells afterwards (Figure 6.31, III).

The time evolution of the stability index for the middle pair (Figure 6.32, diamonds) shows a rapid growth in the first 7 h, corresponding to the erosion of the buoyant lid near

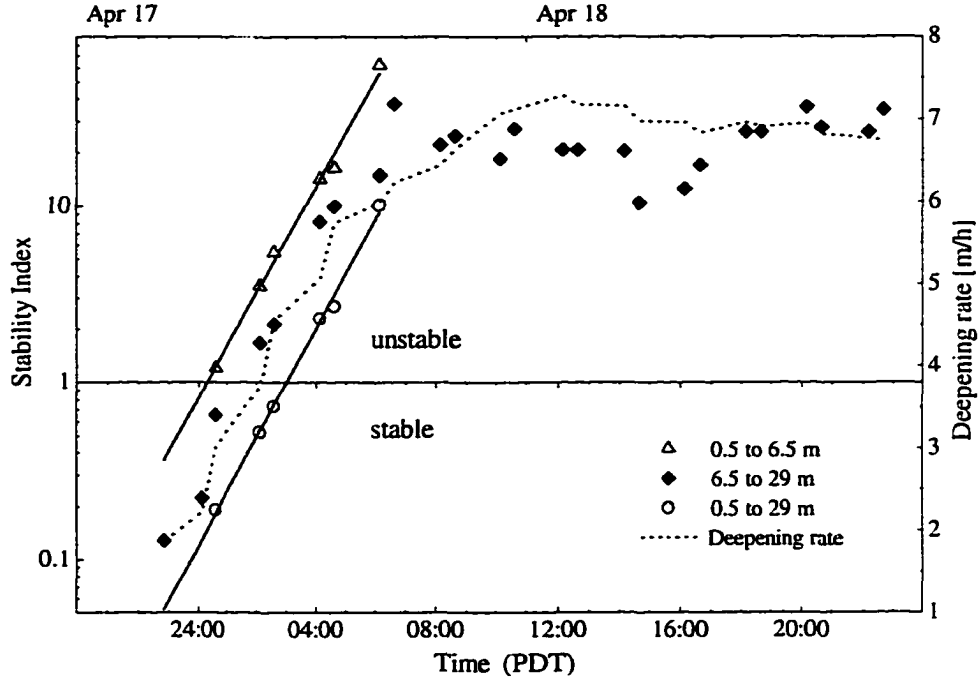

Figure 6.32: Time evolution of the Langmuir circulation stability parameter during the storm, April 17–18, 1995. Different symbols represent FL calculated for three different pairs of temperature sensors. Solid lines show the best fit for the developing period. Dotted line shows the effective deepening rate estimated using (6.23) and numerical results of Li and Garrett [1997].

the surface. At around 06:00 it levels out (Figure 6.32) at which point all three thermistors show the same temperature, meaning that the water column is well mixed at least down to 29 m (Figure 6.33b). Analyzing temperature records in (Figure 6.33b) we notice that temperature at 6.5 m originally follows the cooling rate, consistent with the measured heat flux (Figure 6.33a) between 00:30 and 02:00, April 18 and drops below it afterwards. In addition, we observe a temperature increase of ~20 mK at 29 m depth after 04:00. These can be interpreted as follows: originally the circulation is weak and does not penetrate to 6.5 m depth prior to 02:00. Afterwards, the circulation penetrates deeper, mixing warmer surface water with colder water from below, thus causing the signal observed in Figure 6.33b.

Conducting a sensitivity study, we repeat the calculations of the stability index for the mean wave-enhanced viscosity over depth h_s (the lower bound) and $3h_s$ (the upper bound). The results for the lower bound of the viscosity give larger values of FL which delay predicted instability by an extra ½ hour. The upper bound computations give a smaller FL and the conditions become unstable a ½ h earlier.

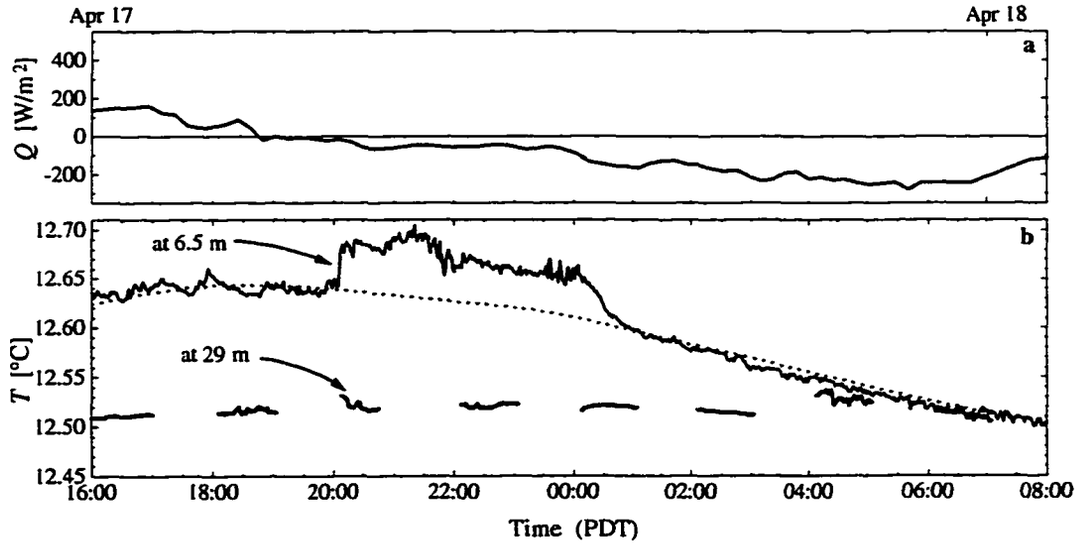

Figure 6.33: Thermal structure of the surface layer during April 17–18, 1995. a) surface heat flux; b) temperature time series at different depths. Dashed line marks cooling, consistent with the measured heat flux.

To elucidate the importance of the shear-induced mixing on the erosion of stratification in the top 6.5-m layer we compute the inverse bulk Richardson number using mean horizontal velocity measurements at different depths obtained with a ship-mounted ADCP as

$$\mathrm{Rb}^{-1} = \frac{|\Delta U|^2}{0.65 h \Delta b}, \tag{6.22}$$

where ΔU is the velocity difference over a depth h. The ADCP velocity data between 04:00, April 18 and 23:00, April 19 are available below 5.5 m and display an almost uniform shear down to the base of the mixed layer (35 m, which is consistent with the CDT measurements shown in Figure 6.27). Using a mean shear between 5.5 and 35 m and the temperature difference between 0.5 and 6.5 m, we evaluate Rb for the top 6.5-m layer during the first 6 h from the onset of the wind. When $\mathrm{Rb} > 1$ mixing layer deepening is expected [*Price et al.* 1986]. During the initial stage of the storm between 00:30 and 04:00 on April 18, 1995 the Richardson number is marginally stable (Figure 6.34) and we conclude that the direct wind-driven shear mixing did not cause the erosion

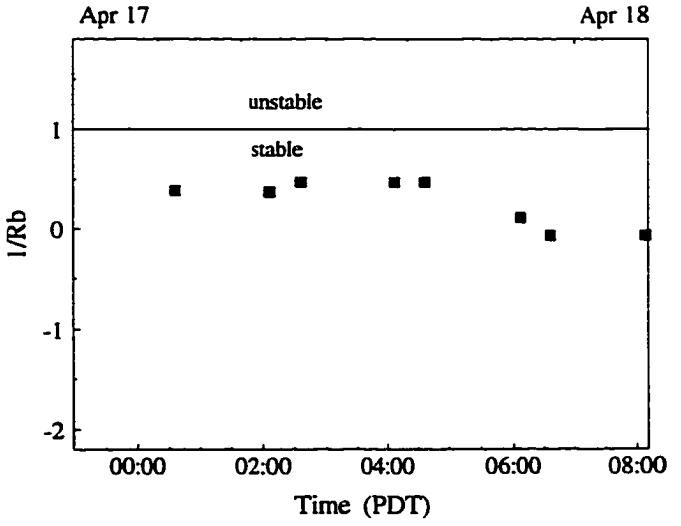

Figure 6.34: The inverse bulk Richardson number during the first part of the storm from April 17 to 18, 1995. Values below a critical threshold of 1 [Price et al, 1986] correspond to the suppression of the shear-driven mixing by stratification.

of the stratification during this period. Note that Rb changes sign after 06:00, when the buoyancy difference becomes negative.

The observed disappearance of the buoyant lid can be due to both mixing by Langmuir circulation and by advection. The average drift speed of the imaging sonar platform relative to the water varied between 10 and 20 mm/s during the first few hours of the storm amounting to a total drift of 100 to 200 m. Horizontal extensions of a meander in a front, separating the warm Pacific water from the coastal water are typically O(1 km) [*Strub et al.*, 1991; *Ramp et al.*, 1991]. We therefore take erosion of the buoyant lid by mixing as the most likely cause for the observed homogenization of the water column. However, our main interest here is the effect of the pre-existing stratification on Langmuir circulation, rather than the source for the warm anomaly.

Li and Garrett [1997] conducted a numerical examination of the ocean mixing layer deepening rate induced by Langmuir circulation and found that the layer reached a depth of $4.6h_s$ in approximately $130/\sigma$, where σ is the growth rate of the Craik-Leibovich instability in a quasi-steady state. This growth rate is proportional to the square root of the geometrical mean of the Stokes drift shear and mean Eulerian shears and can be expressed as (4.28)

$$\sigma = \left(\frac{u_*^2 U_s}{4 \nu_e h_s} \right)^{1/2} . \tag{6.23}$$

Substituting numerical values of the parameters we find that the *effective* deepening rate is quite small (less than 2 m/h) at the initial stages of the storm (Figure 6.32). However, σ increases rapidly, reaching 6 m/h at approximately 06:00, April 18 (Figure 6.32). An average deepening rate between 01:00 and 06:00 is thus of the order of 5.2 m/h. This result is consistent with the bulk estimate of 5.8 m/h that we derive from the temperature records (Figure 6.33b) and the stability index evolution (Figure 6.32). After 06:00 the deepening rate remains almost constant (Figure 6.32) which is an indication of the arrested development of the circulation. As the cells penetrate deeper into the mixed

layer, viscous damping increases due to increasing turbulent viscosity [*Gemmrich*, 1997]. At the same time, the wave component of the forcing decays exponentially with depth and the balance between the wind-wave forcing and viscous dissipation prevents cells from further growth. This interpretation is also supported by an almost constant La for that period (Figure 6.5).

Another example of Langmuir circulation thermal inhibition, apparently associated with strong heating, was observed during the second deployment in the afternoon of April

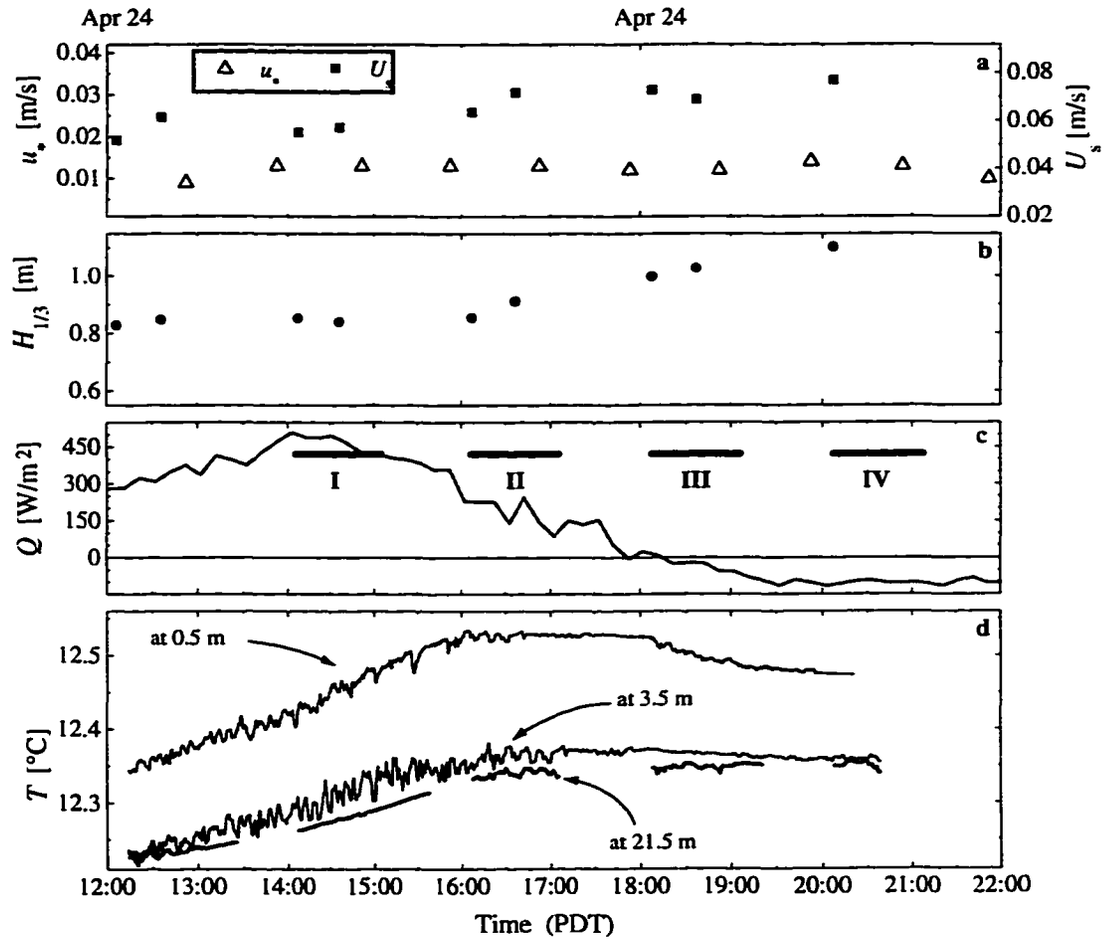

Figure 6.35: Environmental conditions during deployment 2 of the MBL Experiment, April 24, 1995. a) Friction velocity in water (open triangles) and the Stokes drift (solid squares); b) significant wave height (solid circles); c) heat flux. Black horizontal bars mark intervals for which the vertical sonar data are shown in Figure 6.36; d) temperature time series at different depths.

24, 1995. Temperature observations reveal much warmer (by almost 0.18 K) water close to the surface (Figure 6.35d) coinciding with strong heating. In combination with a moderate wind-wave forcing (Figure 6.35a,b), these conditions inhibit bubble penetration below 4 m depth prior to 16:30 on April 24 (Figure 6.36,I). The temperature difference between 0.5 and 3.5 m decreases slightly after 18:00, April 24, which coincides with deeper bubble penetration below 6 m (Figure 6.36,III-IV), and down to 8−9 m (Figure 6.36,III-IV).

Calculations for the 3.5-m layer give F_L close to 1 (marginally stable) and the best fit line indicates that the top 3.5-m layer becomes unstable to the Langmuir circulation at around 16:00, April 24 (Figure 6.37). However, the 21.5-m layer remains stable for the whole deployment. These are consistent with the vertical cell penetration observed in Figure 6.36. The Langmuir number for the same period is always subcritical which means that the wave-current mechanical forcing is sufficient for the generation of the circulation. However, these rather high values of La ~ 0.15 indicate the regime that gives quasi-steady rather than time-dependent cells [*Li and Garrett*, 1993].

Our results thus appear generally consistent with an interpretation based on the

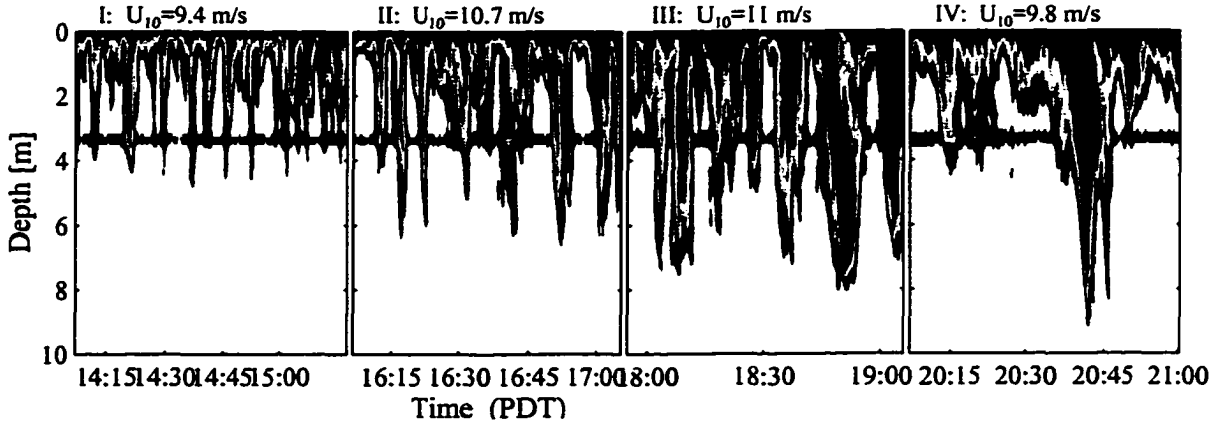

Figure 6.36: Vertical bubble clouds observed with a 200 kHz upward-looking sonar during deployment 2 of the MBL Experiment, April 24, 1995. Average heat flux from I to IV is 460, 210, −20 and −100 W/m², respectively.

stability criterion expressing the competition between mixing layer erosion by Langmuir circulation and buoyant resistance. On April 18, in the first hour of the storm, the pre-existing stratification inhibited the generation of Langmuir circulation, despite strong wave-wind forcing: U_s ~ 0.2 m/s, H_s on the order of 2 m and inferred subcritical La between 0.09 and 0.025 (Figure 6.5), and delayed cell deep penetration by more than 3 h. On April 24, large near-surface thermal gradients resulted in a 4-h delay of the circulation onset and inhibited its deep penetration altogether. This interpretation agrees with the observed near-surface signatures of Langmuir circulation, derived from acoustical imaging (Figure 6.29, Figure 6.31 and Figure 6.36) and is also in accord with the predictions of *Li et al.* [1995] and *Gnanadesikan* [1996], who suggest that the presence of pre-existing stratification may delay or inhibit Langmuir circulation.

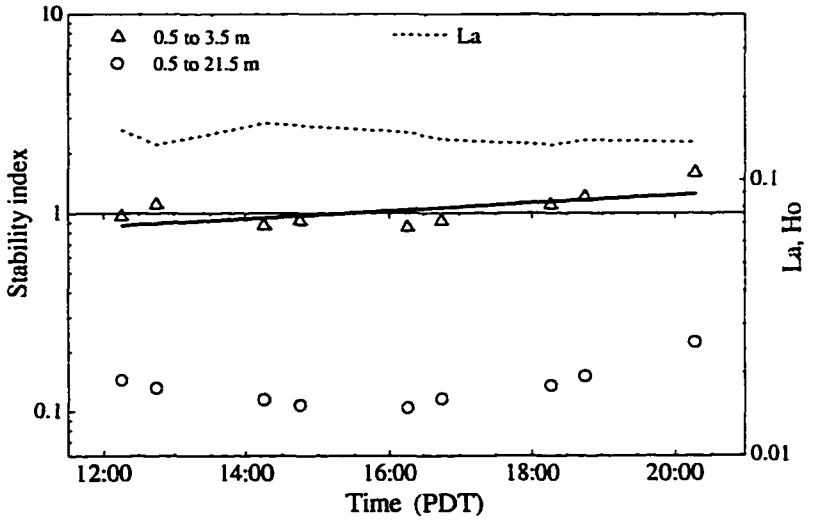

Figure 6.37: Stability index for the deployment 2 of the MBL Experiment, April 24, 1995. Different symbols represent FL calculated for two layers and the sloping line marks the best fit. The Langmuir number (dotted line) is estimated using wall layer viscosity at $2h_s$ and is always subcritical (La < 0.67), indicating unstable conditions.

7. SUMMARY AND CONCLUSIONS

This work describes the response of the near-surface circulation to wind, wave and thermal forcing in the open ocean, particularly during strong winds. Although there have been previous observations of the circulation dependence on the individual forcing components: *Thorpe and Hall* [1983] investigated thermal structure, *Zedel and Farmer* [1991] applied a conditional sampling to extract vertical velocity in the convergent regions and *Smith* [1992, 1998] reported observations of cell spacing and horizontal velocity, this work provides the first description which combines simultaneous observations of the directional wave field, the surface structure of Langmuir circulation, vertical velocity, cell penetration and the near-surface thermal field in order to reconcile dynamics of Langmuir circulation, particularly, its spatial structure and temporal suppression by buoyancy.

Here we employ a freely drifting imaging sonar platform, which allows us to follow time-evolving features for an extended period. The imaging sonar extends the acoustical approach beyond fixed orientation sonars [*Thorpe and Hall*, 1983; *Zedel and Farmer*, 1991; *Smith*, 1992] and covers a full 360° on the surface, although without the simultaneous angular resolution of the phased array approach [*Pinkel et al.*, 1995; *Smith*, 1998]. This full circle capability turns out to be a key addition to the measurements: for the first time it is allowing quantitative evaluation of the directional properties of

Langmuir circulation and comparisons with models. By adding measurements of the near-surface temperature field we are able to confirm experimentally the inhibition of Langmuir circulation by buoyancy.

A modified Craik-Leibovich model was developed to describe the generation of Langmuir circulation when wind and waves are not aligned. Results of linear stability analysis, with the appropriate choice of the dimensionless parameters, suggest that the growth rate is maximal overall when wind and waves are aligned. For a given angle between the Stokes drift and the wind (the misalignment angle) the direction of the cell axis for maximal growth lies between the Stokes drift and the wind and is mainly determined by (i) the misalignment angle and (ii) the shear ratio, defined as the ratio of the Stokes drift shear to the mean Eulerian shear. For a fixed value of the latter, the orientation of the fastest growing cells (the cell direction) is nearly independent of the one other dimensionless parameter which could be the Stokes drift/friction velocity ratio or the Langmuir number.

The most important conclusion, however, is that the shear ratio Sr is the key parameter defining the maximal growth rate and the direction of the cells. The preferential cell direction becomes more aligned with the wave direction as the Stokes drift shear increases relative to the mean shear, and vice versa. When $Sr \geq 0.5$, the preferential cell direction becomes dependent on the other dimensionless parameter Su. We find that while the preferential cell direction lies close to the wind for small Sr, it does not align with the waves for a reasonably large Sr. The maximal growth rate computed for a realistic wave spectrum shows a significant growth rate reduction, compared to a simple exponential Stokes drift profile for the same Sr and Su. When the waves and the wind are oriented in the opposite directions there is no source of the instability and the cells are damped. These results are consistent with the findings of *Gnanadesikan and Weller* [1995] and *Mourad* [1998] but go beyond them in the dimensional analysis. Certainly the model presented here is not complete, but rather a

first step in studying a complex physical phenomenon; it possesses several limitations. This is a linear, two-dimensional model which allows us to get only the preferential direction of the fastest growing cells. It does not provide information about the finite amplitude behavior and velocity structure of the cells. The model also does not include any transient effects associated with the wave field and wind current generation. For mathematical simplicity a steady linear mean current profile is assumed, but the model can be extended to a different mean current as well as more realistic eddy viscosity.

Analysis of the backscatter data, obtained with the upward-looking sonars brings out an important point. Analyzing Figure 5.11 and Figure 6.31 we observe rather narrow vertical bubble plumes, extending down to 10−16 m, coexisting with an almost continuous bubble stratum the top 2 to 3 m, which means that the background turbulence is acting on different time scales than Langmuir circulation. This serves as a indication for the existence of a spectral gap, which is usually assumed in two-dimensional models but has not been experimentally justified before.

We address an issue of scattering depth in order to understand the limitations of the measurement approach. We find, that at high wind and wave states the backscatter measured with a side-looking sonar occurs not right at the surface but at 0.7 to 2 m depth. Consequently, the observed velocity is reduced by 3 to 9 % and the appropriate correction is necessary to recover true velocity magnitude.

Observations of the orientation of surface bubble clouds, the near-surface velocity field and the directional wave field during several deployments provide an opportunity for comparison of the directional properties of Langmuir circulation with the model that takes into account effects associated with the misalignment of the Stokes drift and wind forcing. Our open ocean observations show that Langmuir cells respond to changes in winds direction within 15 to 20 min. On two occasions, when the wind changed direction and the waves lagged behind, the cells were observed to form in an intermediate orientation (between wind and waves), consistent with model predictions. Our

observations also suggest that for the observed range of the forcing parameters the inclusion of the Coriolis force does not affect cell orientation. Although observed cell orientation is generally consistent with the observed wind and waves, there is a significant (40−50°) spreading and directional deviations occur. Variations in the cell strength with a period of 20 to 25 min are also observed.

Vertical velocity measurements, although limited only to the convergent regions, provide a measure of the circulation strength. Comparisons of the measured vertical velocity with the scaling proposed by *Li and Garrett* [1993] show a general consistency, although the measurements were taken over a narrow parameter range. Using velocity measurements and the scaling we infer the effective viscosity relevant to cell generation. Matching the velocity- and temperature-inferred turbulent viscosities, we estimate the depth scale over which the wind-wave forcing is of most importance. The mean model viscosity at $1.9h_s$ compares favorably with the velocity-inferred values. The matching depth is found to be 18% ± 6% of the cell depth which is slightly less than recent numerical results of ⅓ obtained by *Gnanadesikan* [1996]. Given that *Li and Garrett's* [1993] scaling comes from a two-dimensional model, containing significant simplifications, the agreement between the data and the model is remarkable!

Combining effective viscosity calculated at different depths with the observed Stokes drift and friction velocity, we estimate the Langmuir number La to be between 0.015 and 0.1. Numerical simulations by *Li and Garrett* [1993] give steady-state solutions for La in the range from 0.01 to 0.1. Simulations using smaller La give rise to Langmuir turbulence (Keir Colbo, UVic, personal communication). The lower limit estimate of La between 0.01 and 0.02 falls in the range used by *Li and Garrett*, [1995]. However, our "best-fit" estimate gives larger La: between 0.02 and 0.05. This coincides with the well developed, quasi-steady cells with an approximately constant spacing. *Li and Garrett* [1998] pointed out that LES simulations reproduce features broadly similar to those found in two-dimensional direct numerical simulations at a larger value of La (by up to an order

of magnitude), suggesting that small eddies resolved in the LES model produce higher levels of turbulence. These results imply that higher viscosity values (larger La) than have been previously assumed in the models may be relevant for Langmuir circulation dynamics in the open ocean. This interpretation is also supported by the recent observations of the enhanced near-surface dissipation rates [*Anis and Moum*, 1992; and *Agrawal et al.*, 1992] and turbulent diffusivity [*Gemmrich*, 1997] due to breaking waves.

Simultaneous measurements of Langmuir circulation, temperature, velocity and wave fields during the deployment on April 17 to 19, 1995 in the MBL Experiment allowed a direct test of the role of stratification in circulation dynamics, which was not previously available. Based on these observations and previous work by *Li et al.* [1995], we are able to examine the role of stratification in the inhibition of Langmuir circulation and the conditions required for its initiation. The data motivate a Froude number stability analysis which allows evaluation of the influence of pre-existing stratification on the generation of Langmuir circulation. Our results of the analysis appear generally consistent with an interpretation based on the stability criterion expressing the competition between mixing layer erosion by Langmuir circulation and buoyant resistance. Stability index calculations show that in the first 1.5 h of the storm on April 18, during the MBL Experiment, the pre-existing stratification inhibited deep penetration of Langmuir circulation, despite strong wave-wind forcing. These results agree with the observed signatures of Langmuir circulation, derived from acoustical imaging.

The approach presented here suggests a basis for evaluating the importance of pre-existing stratification on the initiation of Langmuir circulation. The stability index of Langmuir circulation depends on several parameters, including stratification, wind and wave forcing. The stratification and wind stress are readily determined but the turbulent transfer rates, which in their simplest form are described by an eddy viscosity ν_e, can only be inferred from models, which are inevitably idealized. Estimation of the wave forcing generally requires measurements of the wave field, which can be difficult to obtain in

stormy conditions. The Stokes drift can be also calculated using the JONSWAP or Pierson-Moskowitz spectra. For moderately developed seas both model predictions agree with the observations within 10%, while significantly overestimating U_s for growing seas.

The viscosity evaluation employed in the analysis of the MBL Experiment data involves the use of a turbulence closure model based on measured vertical temperature profiles [*Gemmrich*, 1997]. The viscosity enhancement by the waves is greatest close to the surface and rapidly decreases with depth. Comparisons of the wave-enhanced viscosities with the wall-layer values show a 35% and 13% increase at h_s and $2h_s$, respectively, and therefore, to a first approximation, one can use wall-layer viscosity scaling. All remaining parameters required for stability calculations can be readily evaluated using measurements of wind speed and temperature at two depths.

The analysis presented in this thesis is not intended to provide a precise timing, but rather provides insights on the competition between the stratification and mixing by Langmuir circulation. The Froude-Langmuir index FL is a necessary but not a sufficient criterion for determining Langmuir circulation penetration: wind-wave forcing (described by La) is required for Langmuir circulation to develop.

The observed thermal inhibition of Langmuir circulation can affect the mixing layer deepening parameterizations that rely primarily on the wind speed. Observations of the vertical bubble cloud penetration on January 17, 1995, during the Wecoma I experiment show clouds of bubbles extending down to 10 m and associated downwelling velocities in the convergences reaching 73 mm/s at wind speeds between 11 and 12 m/s and a significant wave height between 1.9 and 2.1 m (Figure 6.1). Here, in the presence of warm surface water the circulation was confined to the top 5 to 6 m at even higher wind and wave states. Considering that the daytime heating is stronger in the summer and the storms are weaker and shorter, these may lead to a *seasonal asymmetry* in the coefficients parameterizing mixing layer deepening due to Langmuir circulation. Failure to take into account the pre-existing stratification may lead to a significant *overprediction* of the

mixing layer depth if seasonally independent parameters, which depend only on the wind-wave forcing, are used. For example, consider mixing by Langmuir circulation during a storm of the same strength and duration in winter and spring conditions. The stratification-related inhibition in the spring may delay the onset of Langmuir circulation long enough to produce a shallower mixed layer than would be predicted from a parameterization based solely on the wind speed. The mixed layer depth overprediction, in turn, could affect studies of bioproductivity and exchange of gases between the atmosphere and the oceans and is particularly important in the North Pacific and the North Atlantic oceans where the average monthly wind speeds are 12 m/s in January and 8 m/s in July, as taken from the Comprehensive Ocean Atmosphere Data Set (COADS).

We relied primarily on the predictions derived from a two-dimensional Craik-Leibovich model to interpret the measurements. The comparison between model and our observations demonstrates a reasonably good agreement and the interpretation provides new insights into the dynamics of the circulation. However, there still remain questions about the validity of model limitations which we need to discuss. Recent reports by *Skyllingstad and Denbo* [1995] and *McWilliams et al.* [1997] point to the limiting nature of the two-dimensional approach to Langmuir circulation studies. Although our observations show some three-dimensional dependence of the circulation we also see that variability in the cross-cell direction exceeds the variability in the along cell direction and, for the most part, the cells can be considered as two-dimensional. While the three-dimensionality in Langmuir circulation structure will undoubtedly increase the variance of the observed variables, we suggest that the most important limitation of CL2 model is the use of a constant turbulent transfer parameterization. This has not been removed in the Large Eddy Simulations. Although there are experimental indications pointing to the existence of a spectral gap, studies based on the three-dimensional LES, incorporating a more realistic parameterization of turbulence, will be capable of providing guidelines similar to ones presently available within the CL2 model framework.

BIBLIOGRAPHY

AGRAWAL, Y. C., E. A. TERRAY, M. A. DONELAN, P. A. HWANG, A. J. WILLIAMS III, W. M. DRENNAN, K. K. KAHMA, AND S. A. KITAIGORODSKII, 1992: Enhanced dissipation of kinetic energy beneath surface waves. *Nature*, **359**, 219–220.

AKULICHEV, V. A., V. A. BULANOV, AND S. V. KLENIN, 1986: Acoustic sensing of gas bubbles in the ocean medium. *Soviet Physical Acoustics*, **32**, 177–180.

ALEKSANDROV, A. P., AND E. S. VAINDRUK, 1974: *A study of the variability of the physical fields in the ocean.* In: R. Ozmidov (Ed.), Nauka Publishing Office, 122–128.

ANIS, A., AND J. N. MOUM, 1992: The superadiabatic surface layer of the ocean during convection. *Journal of Physical Oceanography*, **22**, 1221–1227.

ASSAF, G., R. GERARD, AND A. L. GORDON, 1971: Some mechanisms of oceanic mixing revealed in aerial photographs. *Journal of Geophysical Research*, **76**, 6550–6572.

BANNER, M. L., 1990: Equilibrium spectra of wind waves. *Journal of Physical Oceanography*, **20**, 966–984.

BANNER, M. L., I. S. F. JONES, AND J. C. TRINDER, 1989: Wavenumber spectra of short gravity waves. *Journal of Fluid Mechanics*, **198**, 321–344.

BERNSTEIN, R. L., L. BREAKER, AND R. WHRITNER, 1977: California current eddy formation: Ship air and satellite results. *Science*, **195**, 353–359.

BRUMLEY, B. H., R. G. CABRERA, K. L. DEINES, AND E. A. TERRAY, 1991: Performance of a broadband Doppler current profiler. *IEEE Journal of Oceanic Engineering*, **16**, 402–407.

BRYAN, F., 1987: On the parameter sensitivity of primitive equation ocean general circulation model. *Journal of Physical Oceanography*, **17**, 970–985.

BULANOV, V. A., AND POLONICHKO, V., 1990: Effect of dispersion due to bubbles on parametric acoustic array formation in the ocean subsurface layer, *Black Sea, 90*, Varna, Bulgaria, 71–80.

CANUTO C., M. Y. HUSSAINI, A. C. QUARTERONI, AND T. A. ZANG, 1986: *Spectral Methods in Fluid Dynamics.* Springer Verlag, 567 pp.

CASE, L., 1960: Stability of inviscid plane Couette flow. *Physics of Fluids*, **3**, 143–148.

CESARI, L., 1969: *Asymptotic Behavior and Stability Problems in Ordinary Differential Equations.* Third edition, Springer Verlag, 210 pp.

CLAY C., AND H. MEDWIN, 1977: *Acoustical Oceanography: Principles and Applications.* Wiley Interscience, 544 pp.

CRAIG, P. D., AND M. L. BANNER, 1994: Modeling wave-enhanced turbulence in the ocean surface layer. *Journal of Physical Oceanography*, **24**, 2546–2559.

CRAIK, A. D. D., 1977: The generation of Langmuir circulations by an instability mechanism. *Journal of Fluid Mechanics,* **81**, 209–223.

CRAIK, A. D. D., AND S. LEIBOVICH, 1976: A rational model for Langmuir circulations. *Journal of Fluid Mechanics*, **73**, 401–426.

CRAWFORD, G., AND D. M. FARMER, 1987: On the spatial distribution of ocean bubbles. *Journal of Geophysical Research*, **92** (C8), 8231–8243.

CSANADY, G. T., 1994: Vortex pair models of Langmuir circulation. *Journal of Marine Research*, **52**, 559–581.

CUMMINS, P. F., G. HOLLOWAY, AND A. E. GARGETT, 1990: Sensitivity of the GFDL ocean general circulation model to a parameterization of vertical diffusion. *Journal of Physical Oceanography*, **20**, 817–830.

D'ASARO, E. A., AND G. T. DAIRIKI, 1996: Turbulence measurements in a wind driven mixed layer. *Journal of Physical Oceanography*, submitted.

DE FATTA, D., J., J. G. LUCAS, AND W. S. HODGKISS, 1988: *Digital Signal Processing.* John Wiley & Sons, 661pp.

DENMAN, K. L., AND A. E. GARGETT, 1995: Biological-physical interactions in the upper ocean: The role of vertical and small-scale processes. *Annual Review of Fluid Mechanics*, **27**, 225–255.

DEVIN, C., 1959: Survey of thermal, radiation and viscous damping of pulsating air bubbles in water. *Journal of the Acoustical Society of America*, **31**, 1654–1667.

DONELAN, M., 1990: Air-sea interaction. In: B. LeMehaute, and D. M. Hanes (Eds.), *The Sea: Ocean Engineering Sciences*, **9A**, 239–292.

DONELAN, M. A., J. HAMILTON, AND W. H. HUI, 1985: Directional spectra of wind generated waves. *Philosophical Transactions of the Royal Society of London, Series A*, **315**, 509–562.

DRENNAN, W. M., K. K. KAHMA, E. A. TERRAY, M. A. DONELAN, AND S. A. KITAIGORODSKII, 1992: Observations of the enhanced of the kinetic energy dissipation beneath breaking wind waves. In: M. L. Banner and R. H J. Grimshaw (Eds.), *Breaking Waves IUTAM Symposium*, Sydney, Australia, 1991, Springer Verlag.

FALLER, A. J., 1964: The angle of windrows in the ocean. *Tellus*, **3**, 363–370.

FALLER, A. J., AND A. H. WOODCOCK, 1964: The spacing of windrows of *Sargassum* in the ocean. *Journal of Marine Research*, **22**, 22–29.

FARMER, D. M., 1993A: Acoustical studies of air–sea interaction and ocean climate. *Physics in Canada*, **9**, 253.

FARMER, D. M., 1993B: Properties of bubble distributions relevant to surface reverberation. In: D. D. Ellis, J. R. Preston, and H. G. Urban (Eds.), *Ocean Reverberation*. Kluwer Academic Publishers, 403 pp.

FARMER, D., 1998: Observations of small-scale structure in the wind-driven surface layer. *Oceanography* (in press).

FARMER, D. M., AND S. VAGLE, 1989: Wave guide propagation of ambient sound in the ocean surface bubble layer. *The Journal of the Acoustical Society of America*, **86**, 1897–1908.

FARMER, D., AND M. LI, 1995: Patterns of bubble clouds organized by Langmuir circulation. *Journal of Physical Oceanography*, **25**, 1426–1440.

FARMER, D., AND V. POLONICHKO, 1995: Observations of velocity and spatial structure of Langmuir circulation. Paper presented at IUTAM Symposium on Physical Limnology, International Union of Theoretical and Applied Mechanics, Broome, Australia.

FARMER D. M., AND S. VAGLE, 1997: Bubble measurements using a resonator. In: T. G. Leighton (Ed.): *Natural Physical Processes Associated with Sea Surface Sound.* Southampton, 155–162.

FARMER, D. M., R. C. TEICHROB, C. J. ELDER, AND D. G. SIEBERG, 1990: Novel acoustical

instrumentation for the study of ocean surface processes, *IEEE-OCEANS '90, Journal of Atmospheric and Oceanic Technology,* **12**(3), 603–616.

FARMER, D. M., C. L. MCNEIL, AND B. D. JOHNSON, 1993: Evidence for the importance of bubbles in increasing air-sea gas flux. *Nature,* **361**, 620–623.

FARMER, D., J. R. GEMMRICH, AND V. POLONICHKO, 1997A: Velocity, temperature and spatial structure of Langmuir circulation. In: J. Imberger (Ed.), *Physical Processes in Lakes and Oceans.* AGU Press, (in press).

FARMER, D. M., S. VAGLE, AND A. D. BOOTH, 1997B: A free flooding acoustical resonator for measurement of bubble size distributions. *Journal of Atmospheric and Oceanic Technology,* (in press).

FILATOV, N. N., S. V. RJANZIN, AND L. V. ZAITSEV, 1981: Investigation of turbulence and Langmuir circulation in Lake Ladoga. *Journal of Great Lakes Research,* **7**, 1–6.

FOLDY, L., 1945: The multiple scattering of waves. *Physical review,* **67**, 107–119.

GARRETT, C., 1996: Processes in the surface mixed layer of the ocean. *Dynamics of Atmosphere and Oceans.* **23**, 19–26.

GEMMRICH, J. R., 1997: A study of turbulence and fine scale temperature variability of the ocean thermal boundary layer under breaking surface waves. Ph.D. dissertation, University of Victoria, Victoria, B. C., 209 pp.

GEMMRICH, J. R., T. D. MUDGE, AND V. D. POLONICHKO, 1994: On the energy input from wind to surface waves. *Journal of Physical Oceanography,* **24**, 2413–2417.

GNANADESIKAN, A., 1996: Mixing driven by vertically variable forcing: An application to the case of Langmuir circulation. *Journal of Fluid Mechanics,* **322**, 81–107.

GNANADESIKAN A., AND R. A. WELLER, 1995: Structure and instability of the Ekman spiral in the presence of surface gravity waves. *Journal of Physical Oceanography,* **25**, 3148–3171.

HASSELMANN, K., T. P. BARNETT, E. BOUWS, H. CARLSON, D. E. CARTWRIGHT, *et. al.*, 1973: Measurements of wind-wave growth and decay during the Joint North Sea Wave Project (JONSWAP), *Deutsche Hydrographische Zeitung, Supplement A,* **8**(12).

HUANG, N. E., 1971: Derivation of the surface Stokes drift for a deep-water random gravity wave field. *Deep-Sea Research,* **18**, 255–259.

HUANG, N. E., 1979: On surface drift currents in the ocean. *Journal of Fluid Mechanics*, **91**, 191–208.

ICHIYE, T., J. R. MCGRATH, AND M. HOWARD, 1985: Some dynamic features of Langmuir circulation. In: Y. Toba and H. Mitsuyasu (Eds.), *The Ocean Surface*. D. Reidel Publishing, 479–486.

JOHNSON B. D., AND R. C. COOKE, 1979: Bubble population and spectra in coastal water; A photographic approach. *Journal of Geophysical Research*, **84**, 3761–3766.

KENNEY, B. C., 1977: An experimental investigation of the fluctuating currents responsible for the generation of the windrows. Ph.D. dissertation, University of Waterloo, Ont., 163 pp.

KENYON, K. E., 1969: Stokes drift for random gravity waves. *Journal of Geophysical Research*, **74**, 6991–6994.

KINSMAN, B., 1965: *Wind Waves*. Prentice-Hall, 676 pp.

KITAIGORODSKII, S. A., 1962: Applications of similarity theory to the analysis of wind-generated wave motion as a stochastic process. *Bulletin of the Academy of Sciences of USSR, Geophysical Series*, **1**, 105–117 (in Russian).

KITAIGORODSKII, S. A., 1983: On the theory of the equilibrium range in the spectrum of wind-generated gravity waves. *Journal of Physical Oceanography*, **13**, 816–827.

KITAIGORODSKII, S. A., AND J. L. LUMLEY, 1983: Wave turbulence interaction in the upper ocean. Part I: The energy balance of the interacting fields of the surface wind waves and wind-induced three dimensional turbulence. *Journal of Physical Oceanography*, **13**, 1977–1983.

KOLOVAEV, D. A., 1976: Investigation of the concentration and statistical size distribution of wind-produced bubbles in the near-surface ocean. *Oceanology*, **15**, 659–661 (English translation).

KUNDU, P. K., 1990: *Fluid Mechanics*. Academic Press, 638 pp.

LAMB, H. 1945. *Hydrodynamics*. Dover Publications, New York, 687 pp.

LANGMUIR , I., 1938: Surface motion of water induced by wind. *Science*, **87**, 119–123.

LEIBOVICH, S., 1977: On the evolution of the system of wind drift currents and Langmuir circulations in the ocean. Part 1. Theory and averaged current. *Journal of Fluid Mechanics*,

79, 715–743.

LEIBOVICH, S., 1980: On wave-current interaction theories of Langmuir circulation. *Journal of Fluid Mechanics*, **99**, 715–724.

LEIBOVICH, S., 1983: The form and dynamics of Langmuir circulations. *Annual Review of Fluid Mechanics*, **15**, 391–427.

LEIBOVICH, S., AND S. K. LELE, 1985: The influence of the horizontal component of Earth's angular velocity on the instability of the Ekman layer. *Journal of Fluid Mechanics*, **150**, 41–87.

LEIBOVICH, S., AND S. PAOLUCCI, 1980: The Langmuir circulation instability as a mixing mechanism of the upper ocean. *Journal of Physical Oceanography*, **10**, 186–207.

LEIBOVICH, S., AND S. PAOLUCCI, 1981: The instability of the ocean to Langmuir circulation. *Journal of Fluid Mechanics*, **102**, 141–167.

LEIBOVICH, S., AND A. TANDON, 1993: Three-dimensional Langmuir circulation instability in a stratified layer. *Journal of Geophysical Research*, **98**, 16501–16507.

LI, M., AND D. M. FARMER, 1998: Crow instability and vortex reconnection in an array of Langmuir vortices. *Journal of Physical Oceanography* (in press).

LI, M., AND C. GARRETT, 1993: Cell merging and jet/downwelling ratio in Langmuir circulation. *Journal of Marine Research*, **51**, 737–769.

LI, M., AND C. GARRETT, 1995: Is Langmuir circulation driven by surface waves or surface cooling. *Journal of Physical Oceanography*, **25**, 64–75.

LI, M., AND C. GARRETT, 1997: Mixed layer deepening due to Langmuir circulation. *Journal of Physical Oceanography*, **27**, 121–132.

LI, M., AND C. GARRETT, 1998: Large eddies in the surface mixed layer and their effect on mixing, dispersion and biological cycling. In: J. Imberger (Ed.): *Physical Processes in Lakes and Oceans*. AGU Press, (in press).

LI, M., K. ZAHARIEV, AND C. GARRETT, 1995: The role of Langmuir circulation in the deepening of the ocean surface mixed layer. *Science*, **270**, 1955–1957.

LIM, J. S., 1990: *Two Dimensional Signal and Image Processing*. Prentice Hall, 694 pp.

LONGUET-HIGGINS, M. S., 1963: The generation of capillary waves by steep gravity waves. *Journal of Fluid Mechanics*, **16**, 138–159.

MARATOS, A., 1971: Study of near shore surface characteristics of windrows and Langmuir circulation in Monterey Bay. M. Sc. thesis, U.S. Naval Postgraduate School, Monterey, Ca.

MARRA, J., 1978: Phytoplankton photosynthesis response to wind vertical movement in a mixed layer. *Journal of Marine Biology*, **46**, 203–208.

MCWILLIAMS, J. C., P. P. SULLIVAN, AND C. H. MOENG, 1997: Langmuir turbulence in the ocean. *Journal of Fluid Mechanics*, **334**, 1–30.

MEDWIN, H., 1970: In situ acoustic measurements of bubble populations in coastal waters. *Journal of Geophysical Research*, **75**, 599–611.

MEDWIN, H., 1977A: Acoustical determination of bubble-size spectra. *The Journal of the Acoustical Society of America*, **62**, 1041–1044.

MEDWIN, H., 1977B: In situ acoustic measurements of microbubbles at sea. *Journal of Geophysical Research*, **82**, 971–976.

MELVILLE, W. K., 1994: Energy dissipation by breaking waves. *Journal of Physical Oceanography*, **24**, 2041–2049.

MILES, J. W., 1957: On the generation of surface waves by shear flows. *Journal of Fluid Mechanics*, **3**, 185–204.

MILLER, K., AND M. ROCHWARGER, 1972: A covariance approach to spectral moment estimation. *IEEE Transactions of Information Theory*, **IT-18**, 588–596.

MINNAERT, M., 1933: On musical air bubbles and the sounds of running water. *Philosophical Magazine*, **16**, 235–248.

MITSUYASU, H., 1977: Measurements of the high frequency spectrum of ocean surface waves. *Journal of Physical Oceanography*, **7**, 882–891.

MITSUYASU, H., F. TASAI, T. SUHARA, S. MIZUNO, M. OKUSO, T. HONDA, AND K. RIKIISHI, 1975: Observations of the directional spectrum of ocean waves using a cloverleaf buoy. *Journal of Physical Oceanography*, **5**, 750–760.

MONAHAN, E. C, AND M. LU, 1990: Acoustically relevant bubble assemblages and their dependence on meteorological parameters. *IEEE Journal of Ocean Engineering*, **15**, 340–

349

MOORE, D. W., 1963: The boundary layer of a spherical gas bubble. *Journal of Fluid Mechanics*, **16**, 161–176.

MOURAD, P. D., 1998: The effects of competition between lateral currents and surface waves on the flux of energy to Langmuir circulation. *Journal of Physical Oceanography* (in press).

MYER, G. E., 1969: A field study of Langmuir circulations. Proceedings of the *12th Conference on Great Lakes Research*, University of Michigan, 1969, International Association for Great Lakes Research, 652–663.

NAVARINI, J. C., AND D. R. BRUNO, 1982: Effects of the sub-surface bubble layer on sound propagation. *The Journal of the Acoustical Society of America*, **72**, 510–514.

OSBORN, T., D. M. FARMER, S. VAGLE, S. A. THORPE, AND M. CURE, 1992: Measurements of bubble plumes and turbulence from a submarine. *Atmosphere-Oceans*, **30**, 419–440.

PEDLOSKY, J., 1979: *Geophysical Fluid Dynamics*. Springer-Verlag. 564 pp.

PHILLIPS, O. M., 1981: *Dynamics of the Upper Ocean*. Second edition, Cambridge University Press, 336 pp.

PIERSON, W. J. JR., AND L. MOSKOWITZ, 1964: A proposed spectral form for fully developed wind seas based on the similarity theory of S. A. Kitaigorodskii. *Journal of Geophysical Research*, **69**, 5181–5190.

PINKEL R., AND J. A. SMITH, 1987: Open ocean surface wave measurements using Doppler sonar. *Journal of Geophysical Research*, **92**, 12967–12973.

PINKEL R., AND J. A. SMITH, 1992: Repeat sequence coding for improved precision of Doppler sonar and sodar. *Journal of Atmospheric and Oceanic Technology* **9**, 149–163.

PINKEL, R., MERRIFIELD, M., AND H. RAMM, 1995: Probing the interior of Arctic leads: investigations using high frequency sound. *Journal of Geophysical Research*, **100**, 4693–4705.

PLUEDDEMANN A. J., AND R. PINKEL, 1991: Biasing of the covariance-based spectral mean estimator in the presence of the band-limited noise. *Journal of Atmospheric and Oceanic Technology*, **8**, 172–178.

PLUEDDEMANN, A., J. A. SMITH, D. M. FARMER, R. A. WELLER, W. R. CRAWFORD, R. PINKEL,

S. VAGLE, AND A. GNANADESIKAN, 1996: Structure and variability of Langmuir circulation during the Surface Waves Processes Program, *Journal of Geophysical Research*, **101**, (C2), 3525–3543.

POLLARD R. T., 1977: Observations and theories of Langmuir circulations and their role in near surface mixing. In: M. Angel (Ed.): *A Voyage of Discovery: George Deacon 70th Anniversary Volume*. Oxford, 235–251.

POLONICHKO, V., 1992: Influence of multiple scattering on the bubble size distribution calculations. Paper presented at 39th PNAGU Meeting, Victoria, Canada, p. 14.

POLONICHKO, V., 1997: Generation of Langmuir circulation in case of wind-wave misalignment. *Journal of Geophysical Research*, **102**, (C7), 15773–1580.

PRICE, J. F., R. A. WELLER, AND R. P. PINKEL, 1986: Diurnal cycling: Observations and models of the upper ocean response to durinal heating, cooling and wind mixing. *Journal of Geophysical Research*, **91**, 8411–8427.

PROSPERETTI, A, N. Q. LU, AND H. S. KIM, 1993: Active and passive acoustic behavior of bubble clouds at the ocean's surface. *The Journal of the Acoustical Society of America*, **93**, 3117–3127.

RAMP, S. R., P. F. JENSSEN, K. H. BRINK, P. P. NIILER, F. L. DAGGETT, AND J. F. BEST, 1991: The physical structure of cold filaments near Point Arena, California during June 1987. *Journal of Geophysical Research*, **96**, 14859–14883.

RICHMAN, J., AND C. GARRETT, 1977: The transfer of energy and momentum by the wind to the surface mixed layer. *Journal of Physical Oceanography*, **7**, 876–881.

RJANZIN, S. V., 1980: On the energy and depth penetration of Langmuir circulation. *Izvestia All Union Geographical Society*, **112**, 46–54 (in Russian).

SARKAR, K, AND A. PROSPERETTI, 1993: Coherent and incoherent effects in underwater scattering of bubbles. *The Journal of the Acoustical Society of America*, **93**, 3128–3138.

SKOLNIK, M. I., 1980: *Introduction to Radar Systems*. Second edition, McGraw-Hill, 581 pp.

SKYLLINGSTAD, E. D., AND D. W. DENBO, 1995: An ocean large-eddy simulation of Langmuir circulations and convection in the surface mixed layer. *Journal of Geophysical Research*, **100**, 8501–8522.

SMITH, J. A., 1989: Doppler sonar and surface waves: Range and resolution. *Journal of*

Atmospheric and Oceanic Technology, **6**, 680–698.

SMITH, J. A., 1992: Observed growth of Langmuir circulation. *Journal of Geophysical Research*, **97**, 5651–5664.

SMITH, J. A., 1998: Evolution of Langmuir turbulence during a storm. *Journal of Geophysical Research*, (in press).

SMITH, J., R. PINKEL, AND R. WELLER, 1987: Velocity structure in the mixed layer during MILDEX. *Journal of Physical Oceanography*, **17**, 425–439.

SMITH, S. D., 1981: Coefficients for sea surface wind stress and heat exchange. *Bedford Institute of Oceanography Report Series/BI-R-81-19/December 1981*, 31 pp.

SOLOVIEV, A. V, N. V. VERSHINSKY, AND V. A. BEVERCHNII, 1988: Small-scale turbulence measurements in the thin surface layer of the ocean. *Deep-Sea Research* **35**, 1859–1874.

STEWART, R. W., 1961: The wave drag of wind over water. *Journal of Fluid Mechanics*, **10**, 189–194.

STOKES, G. G., 1847: On the theory of oscillatory wave. *Transactions of the Cambridge Philosophical Society*, **8**, 441–445.

STOMMEL, H., 1951: Streaks on natural water surfaces. *Weather*, **6**, 72–74.

STRUB, P. T., P. M. KORSO, AND A. HUYER, 1991: The nature of the cold filaments in the California current system. *Journal of Geophysical Research*, **96**, 14743–14768.

SUTCLIFFE, W. H., JR., E. R. BAYLOR, AND D. W MENZEL, 1963: Sea surface chemistry and Langmuir circulation. *Deep-Sea Research*, **10**, 233–243.

TANDON, A., AND S. LEIBOVICH, 1995: Simulations of three-dimensional Langmuir circulation water of constant density. *Journal of Geophysical Research*, **100**, 22613–22623.

THERIAULT, Y. B., 1986: Incoherent multi-beam Doppler current profiler performance. *IEEE Journal of Oceanic Engineering*, **OE–11**, 7–15.

THORPE, S. A., 1982: On the clouds of bubbles formed by breaking wind-waves in deep water, and their role in air-sea gas transfer. *Philosophical Transactions of the Royal Society of London, Series A*, **304**, 155–210.

THORPE, S. A., 1984: The effect of Langmuir circulation on the distribution of submerged bubbles caused by breaking wind waves. *Journal of Fluid Mechanics*, **114**, 237–250.

THORPE, S. A., 1986A: Measurements with an automatically recording inverted echo sounder: ARIES and the bubble clouds. *Journal of Physical Oceanography*, **16**, 1462–1478.

THORPE, S. A., 1986B: Bubble clouds: A review of their detection by sonar, of related models, and how $\mathcal{K}_v$ may be determined. In: E. C. Monahan and G. Mac Niocaill (Eds.), *Oceanic Whitecaps*, D. Riedel Publishing, 57–68.

THORPE, S. A., 1992A: Bubble clouds and the dynamics of the upper ocean. *Quarterly Journal of the Royal Meteorological Society*, **118**, 1–22.

THORPE, S. A., 1992B: The breakup of Langmuir circulation and instability of an array of vortices. *Journal of Physical Oceanography*, **22**, 350–359.

THORPE, S. A., 1993: Energy loss by breaking waves. *Journal of Physical Oceanography*, **23**, 2498–2502.

THORPE, S. A., 1995: Dynamical processes of transfer at the sea surface. *Progress in Oceanography*, **35**, 315–352.

THORPE, S. A., AND A. J. HALL, 1982: Observations of the thermal structure of Langmuir circulation. *Journal of Fluid Mechanics*, **114**, 237–250.

THORPE, S. A., AND A. J. HALL, 1983: The characteristics of bubble clouds, breaking waves and near-surface currents observed using side-scan sonars. *Continental Shelf Research*, **1**, 353–384.

THORPE, S. A., AND A. J. HALL, 1987: Bubble clouds and temperature anomalies in the upper ocean. *Nature*, **328**, 48–51.

THORPE, S. A., AND M. S. CURE, 1995: One-dimensional dispersion in a lake inferred from sonar observations. In: K. J. Beven, P. C. Chatwin and J. H. Millbank (Eds.): *Mixing and Transport in the Environment*. 17–27.

THORPE, S. A., A. R. STUBBS, A. J. HALL, AND R. J. TURNER, 1982: Wave-produced bubbles observed by side-scan sonar. *Nature*, **296**, 636–638.

THORPE, S. A., A. J. HALL, A. R. PACKWOOD, AND A. R. STUBBS, 1985: The use of a towed side-scan sonar to investigate processes near the sea surface. *Continental Shelf Research*, **4**, 597–607.

THORPE, S. A., M. S. CURE, AND A. GRAHAM, AND A. J. HALL, 1994: Sonar observations of

Langmuir circulation and estimation of dispersion of floating particles. *Journal of Atmospheric and Oceanic Technology*, **11**, 1273–1294.

TREVORROW, M. V., 1995: Measurements of ocean wave directional spectra using Doppler sidescan sonar arrays. *Journal of Atmospheric and Oceanic Technology*, **12**, 603–616.

TREVORROW, M. V., AND D. M. FARMER, 1992: The use of Barker codes in Doppler sonar measurements. *Journal of Atmospheric and Oceanic Technology*, **9**, 699–704.

TREVORROW, M. V., AND R. C. TEICHROB, 1994: Self-contained acoustic platforms for probing ocean surface processes. *IEEE Journal of Oceanic Engineering*, **19**, 483–492.

ULABY, F. T., R. K. MOORE, AND A. K. FUNG, 1981: *Microwave Remote Sensing: Active and Passive*. Addison-Wesley, Vol. **I**, 456 pp.

URIK, R. J., 1983: *Principles of Underwater Sound*. Third edition, McGraw-Hill, 423 pp.

VAGLE, S., AND D. M. FARMER, 1992: The measurements of bubble-size distributions by acoustical backscatter. *Journal of Atmospheric and Oceanic Technology*, **9**, 630–644.

WALSH A. L., AND M. J. MULHEARN, 1987: Photographic measurements of bubble populations from breaking wind waves at sea. *Journal of Geophysical Research*, **92**, 14553–14565.

WELANDER, P., 1963: On the generation of wind streaks on the sea surface by action of surface film. *Tellus*, **15**, 67–71.

WELLER, R. A., AND J. F. PRICE, 1988: Langmuir circulation within the oceanic mixed layer. *Deep-Sea Research*, **35**, 711–747.

WOLK F., AND R. LUECK, 1997: Direct heat flux measurements with a towed instrument. Paper presented at 12th Symposium on Boundary Layers and Turbulence, July 28-August 1, Vancouver, Canada.

ZEDEL, L., 1991: *Near Surface Ocean Processes: Acoustical Observations, Ambient Sound and Langmuir Circulation*. Ph.D. dissertation, Department of Oceanography, University of British Columbia, Vancouver, 187 pp.

ZEDEL, L., 1994: Deep ocean wave measurements using a vertically oriented sonar. *Journal of Atmospheric and Oceanic Technology*, **11**, 182–191.

ZEDEL, L., AND D. M. FARMER, 1991: Organized structures in subsurface bubble clouds: Langmuir circulation in the open ocean. *Journal of Geophysical Research*, **96**, 8889–8900.

APPENDIX A: COMPASS ERROR CORRECTION

As mentioned in Chapter 3, the mean rotation rate of the imaging sonar platform is between 0.1 and 0.5°/s with maximal spin reaching 2.5°/s. The compass used in SeaScan III has a time response of 3 s and a resolution of 1°. The rapid rotation will introduce an error in the apparent instrument heading. Under most conditions the instrument undergoes rotational oscillations with an average period of 50 s (Figure A.1, top). Compass-induced errors appear as sudden jumps in the image orientation which usually last for one frame. Unfortunately, due to slow compass response, laboratory tests aimed at deriving a compass response function and using it in a deconvolution to restore the original unbiased compass record, did not provide adequate results. Instead, a different

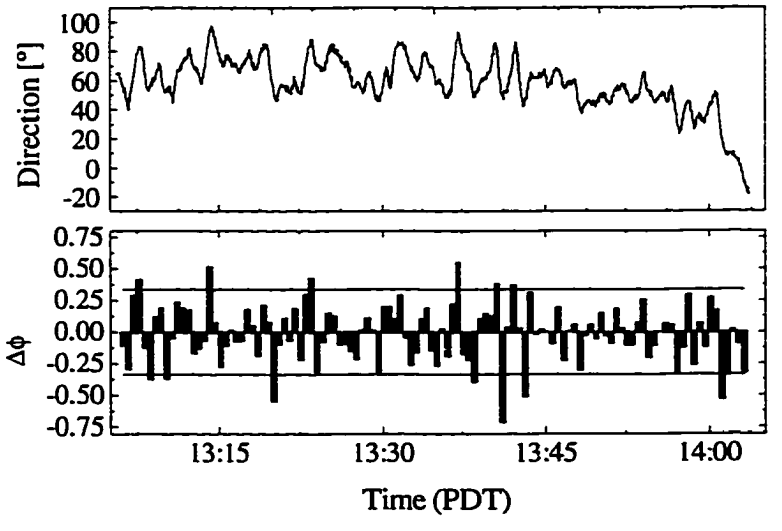

Figure A.1: Example of the compass correction using a mean spin rate. Top) raw compass record; bottom) cumulative spin rate.

technique was implemented. A cumulative spin rate, averaged over a sweep (50 transmissions or 30 s) was calculated as

$$d\phi_a = \frac{1}{N}\sum_{1}^{N}\frac{d\phi}{dt}. \tag{A.1}$$

Afterwards, a threshold of $\frac{1}{3}$ s^{-1} was used to locate frames which could be affected by the fast rotation (Figure A.1, bottom). The frame numbers inferred from this procedure were then used to correct the corresponding image orientation using a linear interpolation between the preceding and the successive images. This procedure improves the quality of the cell spacing estimate and Radon transform analysis.